Volume 66 • Number 1 • February 2018

Acta Geophysica

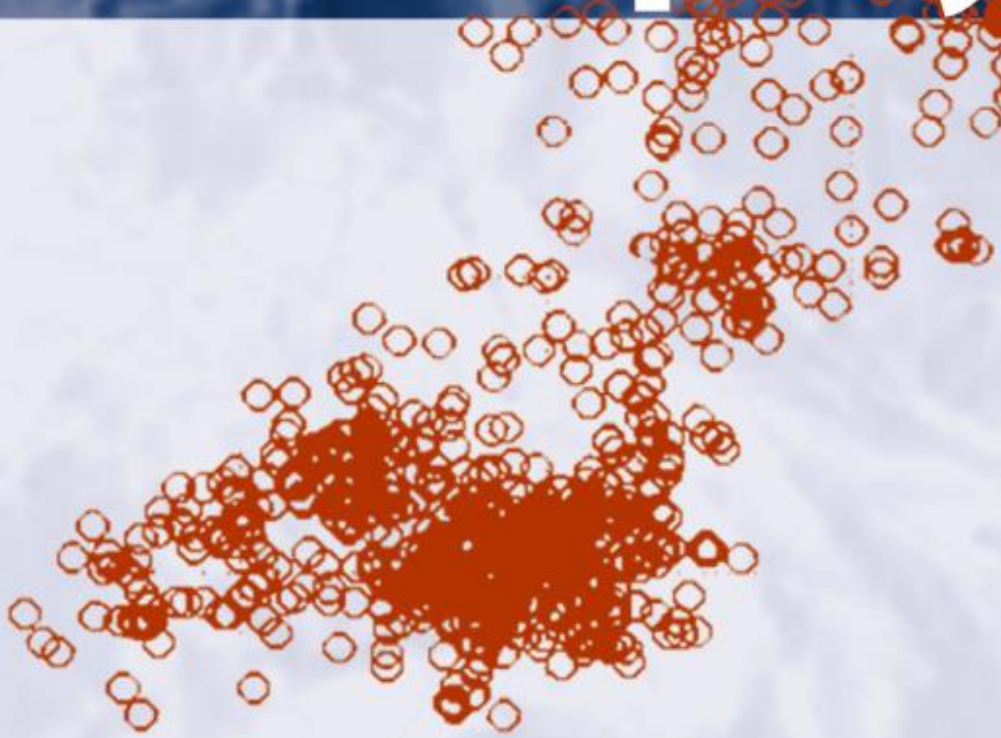

PAN
POLISH ACADEMY OF SCIENCES

Institute of Geophysics
Polish Academy of Sciences

Springer

Acta Geophysica (2018) 66:1–19
https://doi.org/10.1007/s11600-017-0108-8

RESEARCH ARTICLE - SOLID EARTH SCIENCES

Impact of inhomogeneity on SH-type wave propagation in an initially stressed composite structure

S. Saha[1] · A. Chattopadhyay[1] · A. K. Singh[1]

Received: 21 February 2017 / Accepted: 12 December 2017 / Published online: 27 December 2017

Abstract
The present analysis has been made on the influence of distinct form of inhomogeneity in a composite structure comprised of double superficial layers lying over a half-space, on the phase velocity of SH-type wave propagating through it. Propagation of SH-type wave in the said structure has been examined in four distinct cases of inhomogeneity viz. when inhomogeneity in double superficial layer is due to exponential variation in density only (Case I); when inhomogeneity in double superficial layers is due to exponential variation in rigidity only (Case II); when inhomogeneity in double superficial layer is due to exponential variation in rigidity, density and initial stress (Case III) and when inhomogeneity in double superficial layer is due to linear variation in rigidity, density and initial stress (Case IV). Closed-form expression of dispersion relation has been accomplished for all four aforementioned cases through extensive application of Debye asymptotic analysis. Deduced dispersion relations for all the cases are found in well-agreement to the classical Love-wave equation. Numerical computation has been carried out to graphically demonstrate the effect of inhomogeneity parameters, initial stress parameters as well as width ratio associated with double superficial layers in the composite structure for each of the four aforesaid cases on dispersion curve. Meticulous examination of distinct cases of inhomogeneity and initial stress in context of considered problem has been carried out with detailed analysis in a comparative approach.

Keywords Composite layered structure · Initial stress · Inhomogeneity · SH-type wave · Debye Asymptotic Approach

Introduction

Excavation of large quantity of raw materials, such as minerals, crude oils, coal, natural gases, etc., from inside of the earth surface is to accomplish the need of mounting population as well as the demand of growing industries, which contribute a lot to the increase in the frequency of earthquake. An earthquake is rapid and transient vibrations of earth produced by the sudden release of energy stored in an elastically strained rock and send waves of elastic energy throughout the earth. The investigations concerned with seismic waves generated during an earthquake are invaluable to study the interior of the Earth as well as to understand and predict the seismic behavior at the different margin of the earth. Also, the study of behavior of surface waves in layered structures is of prime importance due to its possible applications in geophysical prospecting, mechanical engineering, civil engineering construction and many other engineering branches. A detailed discussion and contribution to surface waves in layered medium are available in Ewing et al. (1957). The investigation made by many authors concerning the behavior of surface waves in layered medium can be quoted from Bullen (1963), Achenbach (1973), Pilant (1979), Bath (1968), Carcione (1992) and Pujol (2003).

Our Earth is extensively more complicated than the models presented earlier. Therefore, a more realistic representation of the Earth as a medium is required through which seismic waves propagate. The very well-known fact is that inhomogeneity lies in most of the

✉ S. Saha
shalinisaha.ism@gmail.com

A. Chattopadhyay
amares.c@gmail.com

A. K. Singh
abhi.5700@gmail.com

[1] Department of Applied Mathematics, Indian Institute of Technology (Indian School of Mines), Dhanbad, Jharkhand 826004, India

elastic bodies and also inside the earth where it is basically one dimensional which varies with depth. The continuous change in the material properties (rigidity and density) of the medium with the space co-ordinates (e.g. in the vertical direction of depth or thickness) contributes to inhomogeneity and it affects the waves (seismic) characteristics significantly propagating through the medium. Inhomogeneity inside earth or a body exists in various types and may be represented by distinct mathematical functions viz. linear, quadratic, exponential, trigonometric, etc. However, through the study of exponential type of inhomogeneity in a problem, effect of linear and quadratic type of heterogeneity may be realized in a problem when value of inhomogeneity parameter is very small. Also, Bullen (1940) suggested that the density varies at different rates with different layers within the Earth. The study of propagation of Love waves in a double superficial layer over heterogeneous medium by taking variation in rigidity has been studied by Sato (1952). Mal (1962) obtained the frequency equation for Love waves due to abrupt thickening of the crustal layer. Sinha (1967) investigated the propagation of love waves in a non-homogeneous layer of finite depth sandwiched between two semi-infinite isotropic media. Bhattacharya (1962, 1969) discussed the dispersion curves for Love-type wave propagation in a transversely isotropic crustal layer with an irregularity in thickness and further studied the possibility of the propagation of Love type waves in an intermediate heterogeneous layer lying between two semi-infinite isotropic homogeneous elastic layers. Chattopadhyay (1975) studied the propagation of Love-type wave considering nonhomogeneous intermediate layer lying between two semi-infinite homogeneous elastic media. Singh et al. (1976) investigated the propagation of Love waves in heterogeneous layered media. Kar (1977) studied the propagation of love type waves in a non-homogeneous internal stratum of finite thickness lying between two semi-infinite isotropic media. Sahu et al. (2014) further considered propagation of SH-waves in viscoelastic heterogeneous layer over half space with self-weight. Later on, Kumari et al. (2015) discussed influence of heterogeneity on the propagation behavior of Love-type waves in a layered isotropic media. Singh et al. (2015) considered the dispersion of shear wave propagating in vertically heterogeneous double layers overlying an initially stressed isotropic half-space. Recently, Chatterjee et al. (2016) showed that the initial stress has great influence on wave velocity; however, Kumari et al. (2016) has performed the modelling of magnetoelastic shear waves due to point source in a viscoelastic crustal layer over an inhomogeneous viscoelastic half space.

Our earth is considered to be an initially stressed medium because of a quantity of initial stress get raised due to many physical causes for example resulting from difference of temperature, process of quenching, shot peening and cold working, pressure due to over burden layer, differential external forces, gravity variations, etc. Thus it is a matter of great interest to study the propagation of waves in a medium under the influence of initial stresses. As discussed by Biot (1940) initial stress has a prominent influence on the propagation of elastic waves. Biot (1963) extended the surface instability of an elastic body under initial stress in finite strain to anisotropic elasticity. Further mechanics of incremental deformation has also been discussed (Biot 1965). Various works includes wave propagation in an initially stressed media can be cited (Dey and Addy 1978; Chattopadhyay et al. 2010; Kumari et al. 2017). Several authors have considered different forms of inhomogeneity and other geological parameter in their elastodynamic problems but the form of inhomogeneity in density as well as rigidity considered in the present study for its extensive mathematical analysis has not been attempted by any author till date.

In the present study an attempt has been made to highlight the impact of four different forms of inhomogeneity in a composite structure comprised of double superficial layers lying over a half-space, on the phase velocity of SH-type wave propagating through it. Four distinct cases of inhomogeneity which are taken into consideration are Case I (when inhomogeneity in double superficial layer is due to exponential variation in density only), Case II (when inhomogeneity in double superficial layers is due to exponential variation in rigidity only), Case III (when inhomogeneity in double superficial layer is due to exponential variation in rigidity, density and initial stress) and Case IV (when inhomogeneity in double superficial layer is due to linear variation in rigidity, density and initial stress). Dispersion relations for all four aforementioned cases are deduced through extensive application of Debye asymptotic analysis and are found in well-agreement to the classical Love-wave equation. Numerical computation and graphical demonstration have been carried out to unravel the effect of inhomogeneity parameters, initial stress parameters as well as width ratio associated with double superficial layers in the composite structure on dispersion curve for all four said cases. Comparative study has been carried out for the distinct cases of inhomogeneity and initial stress in context of present problem with detailed analysis.

Formulation and solution of the problem

The geometry of the current study consists of two isotropic heterogeneous initially stressed elastic layers (M_1 and M_2 respectively) lying over homogeneous isotropic elastic half-space (M_3). The two media M_1 and M_2 are of finite width h_1 and h_2 respectively. It is assumed that superficial layers (M_1) and (M_2) are acted upon by the horizontal initial stress P_1 and P_2, respectively. The rectangular coordinate system is chosen in such a way that x-axis is in the direction of wave propagation and along the common interface of medium M_1 and M_2.The z-axis is pointing vertically downward, as shown in Fig. 1. Let u_j, v_j and w_j denote the components of displacement for medium M_1, M_2 and M_3 where $(j = 1, 2, 3)$, respectively. Now, for the SH-type wave propagating in x-direction causing displacement only in the y-direction, the displacement components may be considered as

$$u_j = w_j = 0, \; v_j = v(x, z, t) \quad \text{for} \quad j = 1, 2, 3. \tag{1}$$

Let us consider μ_j μ_j and $\rho_j (j = 1, 2, 3)$ as the density and rigidity of the layers and half-space $(M_j)(j = 1, 2, 3)$. Inhomogeneity is a trivial characteristic in a material body and it is found in various ways which are being represented by different sort of mathematical function, for example exponential, linear, trigonometric, etc. It is also noted that variation in rigidity and density with respect to the space variable, leading to cause inhomogeneity, is not found similar in general. Further to explore the effects of inhomogeneity on shear type wave propagation in an extensive manner, four distinct following cases have been studied.

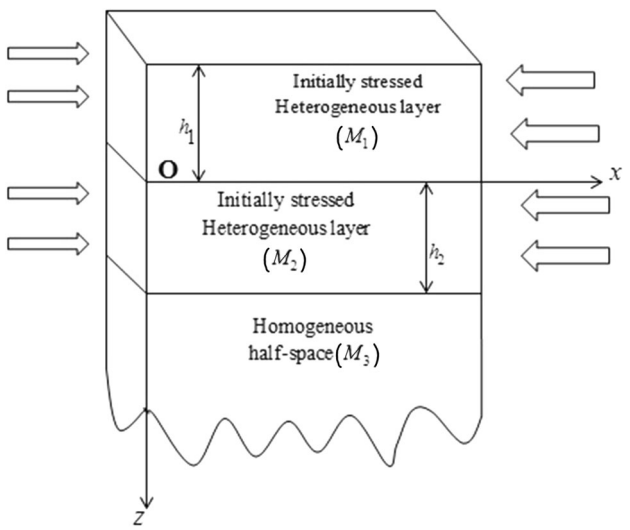

Fig. 1 Geometry of the problem

Case I: when inhomogeneity is caused in double superficial layers due to exponential variation in density only

In this case, we intend to explore the effect of inhomogeneity caused in double superficial layer due to exponential variations (with respect to space variable pointing vertically downwards) of density only on the propagation characteristics of SH type wave. Assumed inhomogeneity in this case for the layers (M_1) and (M_2) may mathematically be expressed as

$$\mu_j = \mu_j^{(1)}, \; \rho_j = \rho_j^{(1)} e^{2n_j z} \; (j = 1, 2), \tag{2}$$

where $\mu_1^{(1)}$ and $\mu_2^{(1)}$ denote the constants with dimension of rigidity; $\rho_1^{(1)}$ and $\rho_2^{(1)}$ denote the constants with dimension of rigidity; n_1 and n_2 denote the inhomogeneity parameter, associated with density of layer medium (M_1) and (M_2), respectively.

In view of Eq. (1), the non-vanishing equation of motion in the absence of body forces for isotropic heterogeneous initially stressed elastic layers M_1 and M_2 under initial stress (Biot 1940) can be, respectively given for $j = 1$ and 2 as

$$\frac{\partial}{\partial x}\left(\mu_j \frac{\partial v_j}{\partial x}\right) + \frac{\partial}{\partial z}\left(\mu_j \frac{\partial v_j}{\partial z}\right) - \frac{P_j}{2}\frac{\partial^2 v_j}{\partial x^2} = \rho_j \frac{\partial^2 v_j}{\partial t^2}, \tag{3}$$

whereas the non-vanishing equation of motion in the absence of body forces for isotropic homogeneous elastic half-space (M_3) is given by

$$\mu_3 \frac{\partial^2 v_3}{\partial x^2} + \mu_3 \frac{\partial^2 v_3}{\partial z^2} = \rho_3 \frac{\partial^2 v_3}{\partial t^2}. \tag{4}$$

For plane wave propagating in the x-direction with common velocity c and wave number k, we may consider the solution for Eqs. (3) and (4) in the form

$$v_j(x, z, t) = V_j(z) e^{ik(x - ct)}, \tag{5}$$

where above solution corresponds to layers and half-space (M_1), (M_2) and (M_3) for $j = 1$, 2 and 3.

In light of Eqs. (3, 5), for uppermost heterogeneous layer (M_1)(for $j = 1$) result in

$$\frac{\mathrm{d}^2 V_1}{\mathrm{d}z^2} + k^2 \left(\frac{c^2}{\left(\beta_1^{(1)}\right)^2} e^{2n_1 z} - 1 + \frac{P_1}{2\mu_1^{(1)}} \right) V_1 = 0, \tag{6}$$

where $\beta_1^{(1)} = \sqrt{\mu_1^{(1)} \Big/ \rho_1^{(1)}}$.

Now, setting $X_1 = e^{n_1 z}$, Eq. (6) yields

$$\frac{\mathrm{d}^2 V_1}{\mathrm{d}X_1^2} + \frac{1}{X_1}\frac{\mathrm{d}V_1}{\mathrm{d}X_1} + k^2 \left(\delta_1^2 - \frac{p_1^2}{X_1^2} \right) V_1 = 0, \tag{7}$$

where $\delta_1 = kc \Big/ n_1 \beta_1^{(1)}$, $\zeta_1^{(1)} = P_1 \Big/ 2\mu_1^{(1)}$ and $p_1 = k\sqrt{1 - \zeta_1^{(1)}} \Big/ n_1$.

Solution of Eq. (7) may be obtained as

$$V_1 = A_1 J_{p_1}(\delta_1 e^{n_1 z}) + B_1 Y_{p_1}(\delta_1 e^{n_1 z}), \tag{8}$$

where J_{p_1} and Y_{p_1} are the Bessel functions of the first kind and second kind, respectively, of order p_1, with A_1 and B_1 being arbitrary constants.

Therefore, the expression of non-vanishing displacement component for the uppermost heterogeneous layer (M_1) may be written as

$$v_1 = \left[A_1 J_{p_1}(\delta_1 e^{n_1 z}) + B_1 Y_{p_1}(\delta_1 e^{n_1 z})\right] e^{ik(x-ct)}. \tag{9}$$

In the similar fashion expression for non-vanishing displacement component for the intermediate heterogeneous layer M_2 may be obtained as

$$v_2 = \left[C_1 J_{p_2}(\delta_2 e^{n_2 z}) + D_1 Y_{p_2}(\delta_2 e^{n_2 z})\right] e^{ik(x-ct)}, \tag{10}$$

where J_{p_2} and Y_{p_2} are the Bessel functions of the first kind and second kind, respectively, of order p_2 with C_1 and D_1 being the arbitrary constants. Some newly introduced symbols appearing in Eq. (10) are as follows:

$$\beta_2^{(1)} = \sqrt{\mu_2^{(1)} \Big/ \rho_2^{(1)}}.\delta_2 = kc \Big/ n_2 \beta_2^{(1)},\ \zeta_2^{(1)} = P_2 \Big/ 2\mu_2^{(1)}$$
$$\text{and} \quad p_2 = k\sqrt{1-\zeta_2^{(1)}} \Big/ n_2.$$

With aid of Eq. (5), Eq. (4) (for $j = 3$) associated with M_3 takes the form

$$\frac{\mathrm{d}^2 V_3}{\mathrm{d}z^2} - k^2 r^2 V_3 = 0, \tag{11}$$

where $r = \sqrt{1-(c/\beta_3)^2}$ and $\beta_3 = \sqrt{\mu_3/\rho_3}$.

Now, the appropriate solution for the Eq. (11) may be written as

$$V_3 = E e^{-krz}. \tag{12}$$

where E is an arbitrary constant.

Therefore, non-vanishing displacement component for the lower half space M_3 can be expressed as

$$v_3 = E e^{-krz} e^{ik(x-ct)}. \tag{13}$$

Boundary conditions

1. The upper surface of the uppermost heterogeneous layer (M_1) is stress free, i.e.

$$\mu_1 \frac{\partial v_1}{\partial z} = 0 \quad \text{at} \quad z = -h_1, \tag{14}$$

2. The stress and displacement components are continuous at the common interface of the uppermost (M_1) and intermediate heterogeneous layers (M_2), i.e.

$$\mu_1 \frac{\partial v_1}{\partial z} = \mu_2 \frac{\partial v_2}{\partial z} \quad \text{at} \quad z = 0, \tag{15}$$

$$v_1 = v_2 \quad \text{at} \quad z = 0, \tag{16}$$

3. The stress and displacement components are continuous at the common interface of the intermediate heterogeneous layer (M_1) and isotropic half space (M_3), i.e.

$$\mu_2 \frac{\partial v_2}{\partial z} = \mu_3 \frac{\partial v_3}{\partial z} \quad \text{at} \quad z = h_2, \tag{17}$$

$$v_2 = v_3 \quad \text{at} \quad z = h_2. \tag{18}$$

Using Eqs. (9), (10) and (13) in the boundary conditions (14–18)yields

$$A_1 J'_{p_1}(\delta_1 e^{-n_1 h_1}) + B_1 Y'_{p_1}(\delta_1 e^{-n_1 h_1}) = 0, \tag{19}$$

$$\mu_1^{(1)} \delta_1 n_1 \left[A_1 J'_{p_1}(\delta_1) + B_1 Y'_{p_1}(\delta_1)\right] = \mu_2^{(1)} \delta_2 n_2 \left[C_1 J'_{p_2}(\delta_2) + D_1 Y'_{p_2}(\delta_2)\right], \tag{20}$$

$$A_1 J_{p_1}(\delta_1) + B_1 Y_{p_1}(\delta_1) = C_1 J_{p_2}(\delta_2) + D_1 Y_{p_2}(\delta_2), \tag{21}$$

$$\mu_2^{(1)} \delta_2 n_2 \left[C_1 J'_{p_2}(\delta_2 e^{n_2 h_2}) + D_1 Y'_{p_2}(\delta_2 e^{n_2 h_2})\right] = -kr\mu_3 E e^{-krh_2}, \tag{22}$$

$$C_1 J_{p_2}(\delta_2 e^{n_2 h_2}) + D_1 Y_{p_2}(\delta_2 e^{n_2 h_2}) = E e^{-krh_2}. \tag{23}$$

Eliminating arbitrary constants A_1, B_1, C_1, D_1 and E from the Eqs. (19–23) the dispersion relation is obtained as

$$\frac{R_1}{R_2} = \frac{\mu_1^{(1)} \delta_1 n_1 [\mu_2^{(1)} \delta_2 n_2 R_3 + kr\mu_3 R_4]}{\mu_2^{(1)} \delta_2 n_2 [\mu_2^{(1)} \delta_2 n_2 R_5 + kr\mu_3 R_6]}, \tag{24}$$

where the new terms $R_j (j = 1, 2\ldots 6)$ appearing in Eq. (24) contain Bessel functions and are defined in the "Appendix I".

Special case

When both of the superficial layers become homogeneous, i.e. inhomogeneity is absent in the two superficial layers, derived dispersion relation (24) must be further simplified for $n_1 \to 0$ and $n_2 \to 0$ and will be undertaken using Debye asymptotic expansion.

Now, considering $n_1 \to 0$ and $n_2 \to 0$ leads to $\delta_1 \to \infty$ and $\delta_2 \to \infty$. Further, it is to be noted that for large values of v, we have the following Debye asymptotic expansions (Watson 1958):

$$J_v(v \sec\theta) \sim \sqrt{\frac{2}{v\pi \tan\theta}} \cos\left(v \tan\theta - v\theta - \frac{\pi}{4}\right),$$

$$Y_v(v\sec\theta) \sim \sqrt{\frac{2}{v\pi\tan\theta}}\sin\left(v\tan\theta - v\theta - \frac{\pi}{4}\right).$$

Above asymptotic expansions can be used for the function appearing in Eq. (24) to yield the following:

$$\left[J_{p_1}(\delta_1 e^{-n_1h_1})Y_{p_1}(\delta_1) - Y_{p_1}(\delta_1 e^{-n_1h_1})J_{p_1}(\delta_1)\right] \approx \frac{-2\sin[p_1(\tan\phi_1 - \tan\phi_2) - p_1(\phi_1 - \phi_2)]}{\pi p_1\sqrt{\tan\phi_1\tan\phi_2}},$$

$$\left[J_{p_2}(\delta_2 e^{n_2h_2})Y_{p_2}(\delta_2) - Y_{p_2}(\delta_2 e^{n_2h_2})J_{p_2}(\delta_2)\right] \approx \frac{-2\sin[p_2(\tan\phi_3 - \tan\phi_4) - p_2(\phi_3 - \phi_4)]}{\pi p_2\sqrt{\tan\phi_3\tan\phi_4}},$$

$$\left[J_{p_1}(\delta_1 e^{-n_1h_1})Y'_{p_1}(\delta_1) - Y_{p_1}(\delta_1 e^{-n_1h_1})J'_{p_1}(\delta_1)\right] \approx \frac{2\sin\phi_2\cos[p_1(\tan\phi_1 - \tan\phi_2) - p_1(\phi_1 - \phi_2)]}{\pi p_1\sqrt{\tan\phi_1\tan\phi_2}},$$

$$\left[J_{p_2}(\delta_2 e^{n_2h_2})Y'_{p_2}(\delta_2) - Y_{p_2}(\delta_2 e^{n_2h_2})J'_{p_2}(\delta_2)\right] \approx \frac{2\sin\phi_4\cos[p_2(\tan\phi_3 - \tan\phi_4) - p_2(\phi_3 - \phi_4)]}{\pi p_2\sqrt{\tan\phi_3\tan\phi_4}},$$

$$\left[J'_{p_1}(\delta_1 e^{-n_1h_1})Y_{p_1}(\delta_1) - Y'_{p_1}(\delta_1 e^{-n_1h_1})J_{p_1}(\delta_1)\right] \approx \frac{-2\sin\phi_1\cos[p_1(\tan\phi_1 - \tan\phi_2) - p_1(\phi_1 - \phi_2)]}{\pi p_1\sqrt{\tan\phi_1\tan\phi_2}},$$

$$\left[J'_{p_2}(\delta_2 e^{n_2h_2})Y_{p_2}(\delta_2) - Y'_{p_2}(\delta_2 e^{n_2h_2})J_{p_2}(\delta_2)\right] \approx \frac{-2\sin\phi_3\cos[p_2(\tan\phi_3 - \tan\phi_4) - p_2(\phi_3 - \phi_4)]}{\pi p_2\sqrt{\tan\phi_3\tan\phi_4}},$$

$$\left[J'_{p_1}(\delta_1 e^{-n_1h_1})Y'_{p_1}(\delta_1) - Y'_{p_1}(\delta_1 e^{-n_1h_1})J'_{p_1}(\delta_1)\right] \approx \frac{-2\sin\phi_1\sin\phi_2\sin[p_1(\tan\phi_1 - \tan\phi_2) - p_1(\phi_1 - \phi_2)]}{\pi p_1\sqrt{\tan\phi_1\tan\phi_2}},$$

$$\left[J'_{p_2}(\delta_2 e^{n_2h_2})Y'_{p_2}(\delta_2) - Y'_{p_2}(\delta_2 e^{n_2h_2})J'_{p_2}(\delta_2)\right] \approx \frac{-2\sin\phi_3\sin\phi_4\sin[p_2(\tan\phi_3 - \tan\phi_4) - p_2(\phi_3 - \phi_4)]}{\pi p_2\sqrt{\tan\phi_3\tan\phi_4}},$$

where the relations for newly introduced functions appearing in above expansions are provided in "Appendix I".

Using the above Debye asymptotic expansion, dispersion relation (24) reduces to

$$\tan(ks_1^{(1)}h_1) = \frac{\mu_2^{(1)}\mu_3 r s_2^{(1)} - (\mu_2^{(1)}s_2^{(1)})^2\tan(ks_2^{(1)}h_2)}{\mu_1^{(1)}\mu_2^{(1)}s_1^{(1)}s_2^{(1)} + \mu_1^{(2)}\mu_3 r s_1^{(1)}\tan(ks_2^{(1)}h_2)}, \tag{25}$$

where $s_1^{(1)} = \sqrt{(c/\beta_1^{(1)})^2 - 1 + \zeta_1^{(1)}}$ and $s_2^{(1)} = \sqrt{(c/\beta_2^{(1)})^2 - 1 + \zeta_2^{(1)}}$.

Equation obtained in (25) represents dispersion relation for SH-type wave propagating in homogeneous double superficial layers (M_1 and M_2), both under the effect of initial stress, lying over an isotropic half- space (M_3).

Case II: when inhomogeneity is caused in double superficial layers due to exponential variation in rigidity only

In this case inhomogeneity is considered in double superficial layer due to exponential variation in rigidity only and the effect of such inhomogeneity on the propagation characteristics of SH-type wave is analyzed. Assumed inhomogeneity in this case for the layers (M_1) and (M_2) may mathematically be expressed as

$$\mu_j = \mu_j^{(2)}e^{2l_jz}, \quad \rho_j = \rho_j^{(2)} \quad (j = 1, 2), \tag{26}$$

where $\mu_1^{(2)}$ and $\mu_2^{(2)}$ denote the constants with dimension of rigidity, $\rho_1^{(2)}$ and $\rho_2^{(2)}$ denote the constants with dimension of density; l_1 and l_2 denote the inhomogeneity parameter, associated with rigidity of layer medium (M_1) and (M_2), respectively.

In view of Eqs. (1) and (26), the non-vanishing equation of motion in the absence of body forces for isotropic heterogeneous initially stressed elastic layers M_1 and M_2 under initial stress (Biot 1940) can be, respectively, given for $j = 1$ and 2 as

$$\left(\mu_j - \frac{P_j}{2}\right)\frac{\partial^2 v_j}{\partial x^2} + \mu_j\frac{\partial^2 v_j}{\partial z^2} + \frac{\partial\mu_j}{\partial z}\frac{\partial v_j}{\partial z} = \rho_j\frac{\partial^2 v_j}{\partial t^2} \quad j = 1, 2, \tag{27}$$

and non-vanishing equation of motion in the absence of body forces for isotropic homogeneous elastic half-space (M_3) is given by Eq. (4).

Now, we may consider the solution of Eqs. (27), as (5).

Then equation of motion (27) with the aid of Eq. (5) for the uppermost heterogeneous layer M_1 (for $j = 1$) results in

$$\frac{d^2V_1}{dz^2} + 2l_1\frac{dV_1}{dz} + k^2\left(\frac{c^2}{(\beta_1^{(2)})^2}e^{-2l_1z} - 1 + \zeta_1^{(2)}\right)V_1 = 0, \tag{28}$$

where $\beta_1^{(2)} = \sqrt{\mu_1^{(2)}/\rho_1^{(2)}}$ and $\zeta_1^{(2)} = P_1/2\mu_1^{(2)}$.

On substituting $V_1 = \sqrt{\xi}V_1'$ with $\xi = e^{-s_1z}$ and $s_1 = 2l_1$, in Eq. (28), we obtain

$$\frac{d^2V_1'}{d\xi^2} + \frac{1}{\xi}\frac{dV_1'}{d\xi} + \frac{k^2}{s_1^2}\left\{\frac{c^2}{(\beta_1^{(2)})^2}\frac{1}{\xi} - \left(1 - \zeta_1^{(2)} + \frac{s_1^2}{4k^2}\right)\frac{1}{\xi^2}\right\}V_1' = 0. \tag{29}$$

Further, using a transformation $\xi' = 2kc\sqrt{\xi}\Big/ s_1\beta_1^{(2)}$ in Eq. (29) following form may be instated:

$$\frac{d^2V_1'}{d\xi'^2} + \frac{1}{\xi'}\frac{dV_1'}{d\xi'} + \left(1 - \frac{q_1^2}{\xi'^2}\right)V_1' = 0, \tag{30}$$

where $q_1 = \sqrt{1 + \left\{k^2(1 - \zeta_1^{(2)})\Big/ l_1^2\right\}}$.

The solution of the Eq. (30) may be written as

$$V_1' = A_2 J_{q_1}(\gamma_1\sqrt{\xi}) + B_2 Y_{q_1}(\gamma_1\sqrt{\xi}),$$

where $\gamma_1 = kc\Big/ l_1\beta_1^{(2)}$, J_{q_1} and Y_{q_1} are the Bessel functions of the first kind and second kind, respectively, of order q_1 with A_2 and B_2 being the arbitrary constants, and, therefore, non-vanishing displacement component for the uppermost heterogeneous layer (M_1) may be written as

$$v_1 = e^{-l_1 z}[A_2 J_{q_1}(\gamma_1 e^{-l_1 z}) + B_2 Y_{q_1}(\gamma_1 e^{-l_1 z})]e^{ik(x-ct)}. \tag{31}$$

Adopting the similar mathematical treatment expression for non-vanishing displacement component for the intermediate heterogeneous layer (M_2) may be obtained as

$$v_2 = e^{-l_2 z}[C_2 J_{q_2}(\gamma_2 e^{-l_2 z}) + D_2 Y_{q_2}(\gamma_2 e^{-l_2 z})]e^{ik(x-ct)}, \tag{32}$$

where J_{q_2} and Y_{q_2} are the Bessel functions of the first kind and second kind, respectively, of order q_2 with C_2 and D_2 being the arbitrary constants. Other new symbols appearing in Eq. (32) are as follows:

$$\beta_2^{(2)} = \sqrt{\mu_2^{(2)}\Big/\rho_2^{(2)}}, \quad \gamma_2 = kc\Big/ l_2\beta_2^{(2)},$$

$$\zeta_2^{(1)} = P_2\Big/ 2\mu_2^{(2)}, \quad q_2 = \sqrt{1 + \left\{k^2\left(1 - \zeta_2^{(2)}\right)\Big/ l_2^2\right\}}.$$

For this case also the non-vanishing displacement component for the lower half space (M_3) is given by Eq. (13).

Using Eqs. (13), (31) and (32) in the boundary conditions (14–18), following equations may be instated:

$$\begin{aligned}&\left[l_1\left\{A_2 J_{q_1}(\gamma_1 e^{l_1 h_1}) + B_2 Y_{q_1}(\gamma_1 e^{l_1 h_1})\right\}\right.\\ &\left. + l_1\gamma_1\left\{A_2 J'_{q_1}(\gamma_1 e^{l_1 h_1}) + B_2 Y'_{q_1}(\gamma_1 e^{l_1 h_1})\right\}\right] = 0,\end{aligned} \tag{33}$$

$$\begin{aligned}&\mu_1^{(2)}\left[l_1\left\{A_2 J_{q_1}(\gamma_1) + B_2 Y_{q_1}(\gamma_1)\right\} + l_1\gamma_1\right.\\ &\left.\left\{A_2 J'_{q_1}(\gamma_1) + B_2 Y'_{q_1}(\gamma_1)\right\}\right]\\ &= \mu_2^{(2)}\left[l_2\left\{C_2 J_{q_2}(\gamma_2) + D_2 Y_{q_2}(\gamma_2)\right\}\right.\\ &\left. + l_2\gamma_2\left\{C_2 J'_{q_2}(\gamma_2) + D_2 Y'_{q_2}(\gamma_2)\right\}\right],\end{aligned} \tag{34}$$

$$A_2 J_{q_1}(\gamma_1) + B_2 Y_{q_1}(\gamma_1) = C_2 J_{q_2}(\gamma_2) + D_2 Y_{q_2}(\gamma_2), \tag{35}$$

$$\begin{aligned}&\mu_2^{(2)} e^{l_2 h_2}\left[l_2\left\{C_2 J_{q_2}(\gamma_2 e^{-l_2 h_2}) + D_2 Y_{q_2}(\gamma_2 e^{-l_2 h_2})\right\}\right.\\ &\left. + l_2\gamma_2\left\{C_2 J'_{q_2}(\gamma_2 e^{-l_2 h_2}) + D_2 Y'_{q_2}(\gamma_2 e^{-l_2 h_2})\right\}\right]\\ &= \mu_3 E k r e^{-krh_2},\end{aligned} \tag{36}$$

$$e^{-l_2 h_2}\left[C_2 J_{q_2}(\gamma_2 e^{-l_2 h_2}) + D_2 Y_{q_2}(\gamma_2 e^{-l_2 h_2})\right] = E e^{-krh_2}. \tag{37}$$

Now, eliminating arbitrary constant A_2, B_2, C_2, D_2, E from the above Eqs. (33–37), we arrive at the dispersion relation for the present case as

$$\begin{aligned}&\frac{\mu_1^{(2)} l_1^2[R_7 + \delta_1(R_8 + R_9) + \delta_1^2 R_{10}]}{\mu_2^{(2)} l_1[R_7 + \delta_1 R_8]}\\ &= \frac{(\mu_2^{(2)} l_2^2 e^{2l_2h_2} - \mu_3 krl_2)[R_{11} + \delta_2 R_{12}] + \mu_2^{(2)} l_2^2 e^{2l_2h_2}\delta_2(R_{13} + \delta_2 R_{14})}{(\mu_2^{(2)} e^{2l_2h_2} l_2 - \mu_3 kr)R_{11} + \mu_2^{(2)} e^{2l_2h_2} l_2\delta_2 R_{13}}.\end{aligned} \tag{38}$$

The newly introduced terms $R_{6+j}(j = 1, 2, \ldots 8)$ in (38) and are provided in terms of some relation of Bessel Functions in "Appendix II".

Special case

For the case, when both the superficial layers are homogeneous i.e. when $l_1 \to 0$ and $l_2 \to 0$.

Now, for $l_1 \to 0$, *and* $l_2 \to 0$ we have $\gamma_1 \to \infty$ and $\gamma_2 \to \infty$. Also, the terms $R_{6+j}(j = 1, 2, \ldots 8)$ of derived dispersion relation (38) are defined in terms of some relation of Bessel functions; the corresponding Debye asymptotic approximations are provided in "Appendix II". The employment of Debye asymptotic approximations in derived dispersion relation (38) reduces it to

$$\tan(ks_1^{(2)}h_1) = \frac{Numr_2}{Den\, r_2}, \tag{39}$$

$$\begin{aligned}Numr_2 &= (ks_1^{(2)}\Big/ l_1)\left[\left\{\left((\mu_2^{(2)} l_2^{(2)})^2 e^{2l_2h_2} - \mu_2^{(2)}\mu_3 krl_2^{(2)}\right)\right.\right.\\ &\left.\left. + (\mu_2^{(2)})^2 k^2 s_2^2 e^{2l_2h_2}\right\}\tan(ks_2^{(2)}h_2) + \mu_2^{(2)}\mu_3 k^2 r s_2^{(2)}\right],\end{aligned}$$

$$\begin{aligned}Den\, r_2 &= \left(\mu_1^{(2)} l_1 + \mu_1^{(2)}(ks_1^{(2)})^2\Big/ l_1\right)\\ &\left[\mu_2^{(2)} k e^{2l_2h_2} s_2^{(2)} + (\mu_2^{(2)} l_2 e^{2l_2h_2} - \mu_3 kr)\tan(ks_2^{(2)}h_2)\right]\\ &- \left[\left\{\left(\left(\mu_2^{(2)} l_2\right)^2 e^{2l_2h_2} - \mu_2^{(2)}\mu_3 krl_2\right)\tan(ks_2^{(2)}h_2)\right.\right.\\ &\left.\left. + \mu_2^2 k^2 s_2^2 e^{2l_2h_2}\right\} + \mu_2^{(2)}\mu_3 k^2 r s_2^{(2)}\right],\end{aligned}$$

with $s_1^{(2)} = \sqrt{\left(c\Big/\beta_1^{(2)}\right)^2 - 1 + \zeta_1^{(2)}}$, $s_2^{(2)} = \sqrt{\left(c\Big/\beta_2^{(2)}\right)^2 - 1 + \zeta_1^{(2)}}$.

Since $l_1 \to 0$ and $l_2 \to 0$, Eq. (39) finally becomes

$$\tan(ks_1^{(2)}h_1) = \frac{\mu_2^{(2)}\mu_3 rs_2^{(2)} - (\mu_2^{(2)}s_2^{(2)})^2\tan(s_2 kh_2)}{\mu_1^{(2)}\mu_2^{(2)}s_1^{(2)}s_2^{(2)} + \mu_1^{(2)}\mu_3 rs_1^{(2)}\tan(s_2^{(2)}kh_2)}, \tag{40}$$

Equation (40) represents dispersion relation for the propagation of SH-type wave in initially stressed homogeneous isotropic double superficial layer (M_1) and (M_2) lying over an isotropic half-space (M_3).

Case III: when inhomogeneity is caused in double superficial layer due to exponential variation in rigidity, density and initial stress

The present case discusses the exponential form of variation (with depth) of rigidity, density and initial stress associated with the uppermost and intermediate layers M_1 and M_2 of the composite structure. To serve the purpose, the following form of inhomogeneity are assumed:

$$\mu_j = \mu_j^{(3)}e^{\varsigma_j z}, \quad \rho_j = \rho_j^{(3)}e^{\sigma_j z}, \quad P_j = P_j^{(3)}e^{\varsigma_j z}, \quad (j = 1, 2), \tag{41}$$

where $\mu_j^{(3)}(j = 1, 2)$ are the constants with dimension of rigidity, $\rho_j^{(3)}(j = 1, 2)$ represent the constant with dimension of density, $P_j^{(3)}(j = 1, 2)$ denote the constants with dimension of stress, $\varsigma_j(j = 1, 2)$ represents the inhomogeneity parameters associated with rigidity and initial stress and $\sigma_j(j = 1, 2)$ are the inhomogeneity parameter associated with density, of the uppermost (M_1) and intermediate heterogeneous layer (M_2), respectively.

In light of Eqs. (1) and (41), for $j = 1$, the non-vanishing equation of motion for the upper heterogeneous layer (M_1) of the considered composite structure, we have,

$$\frac{d^2V_1}{dz^2} + \varsigma_1\frac{d^2V_1}{dz^2} + k^2\left(\left(c\Big/\beta_1^{(3)}\right)^2 e^{-2\hbar_1 z} - 1 + \frac{P_1^{(3)}}{2\mu_1}\right)V_1 = 0, \tag{42}$$

with the phase velocity $\beta_1^{(3)} = \sqrt{\mu_1^{(3)}\Big/\rho_1^{(3)}}$ and $2\hbar_1 = (\varsigma_1 - \sigma_1)$.

Considering $\hat{\lambda}_1 = e^{-2\hbar_1 z}$, Eq. (42) becomes

$$\frac{d^2V_1}{d\hat{\lambda}\hat{\lambda}_1^2} + \frac{4\hbar_1^2 - 2\varsigma_1\hbar_1}{4\hbar_1^2}\frac{1}{\hat{\lambda}_1}\frac{dV_1}{d\hat{\lambda}_1} + \frac{k^2}{4\hbar_1^2}\left[(c^2\Big/\beta_1^{(3)})^2\Big/\hat{\lambda}_1 - \frac{1-\zeta_1}{2\hat{\lambda}_1^2}\right]V_1 = 0. \tag{43}$$

where $\zeta_1^{(3)} = P_1^{(3)}\Big/2\mu_1^{(3)}$ is the dimensionless initial stress parameter associated with the uppermost layer (M_1)

Putting $V_1 = \hat{\lambda}_1^{\varsigma_1/4\hbar_1}Z_1$ in Eq. (43), we obtain,

$$\frac{d^2Z_1}{d\vec{\lambda}_1^2} + \frac{1}{\vec{\lambda}_1}\frac{d^2Z_1}{d\vec{\lambda}_1^2} + \left[\left(\frac{kc}{\hbar_1\beta_1^{(3)}}\right)^2\frac{1}{4\vec{\lambda}_1} - \left(\frac{\varsigma_1^2}{4\hbar_1^2} + k^2\frac{1-\zeta_1^{(3)}}{2\hbar_1^2}\right)\frac{1}{4\vec{\lambda}_1^2}\right]Z_1 = 0. \tag{44}$$

Substituting $\hat{\lambda}_1' = \left(kc\Big/\hbar\beta_1^{(3)}\right)\sqrt{\hat{\lambda}_1}$, Eq. (44) leads to

$$\frac{d^2Z_1}{d\hat{\lambda}_1'^2} + \frac{1}{\hat{\lambda}_1'}\frac{dZ_1}{d\hat{\lambda}_1'} + \left[1 - \frac{s_3^2}{\hat{\lambda}_1'^2}\right]Z_1 = 0, \tag{45}$$

with $s_3 = \left[(\varsigma_1/2\hbar_1)^2 + k^2(1-\zeta_1^{(3)})\Big/\hbar_1^2\right]^{1/2}$.

Therefore, the solution for Eq. (45) can be gained as (46)

$$V_1 = \hat{\lambda}^{\varsigma_1/4\hbar}[A_3J_{s_3}(\Omega_1\hat{\lambda}^{1/2}) + B_3Y_{s_3}(\Omega_1\hat{\lambda}^{1/2})], \tag{46}$$

where J_{s_3} and Y_{s_3} denote Bessel functions of the first kind and second kind, respectively, of order s_3 with $\Omega_1 = kc/\hbar_1\beta_1^{(3)}$. A_3 and B_3 are arbitrary constants.

Hence, the displacement components for the upper heterogeneous layer (M_1) is as follows

$$v_1 = e^{-\varsigma_1 z/2}[A_3J_{s_3}(\Omega_1 e^{-\hbar_1 z}) + B_3Y_{s_3}(\Omega_1 e^{-\hbar_1 z})]e^{ik(x-ct)}. \tag{47}$$

In order to obtain displacement component for the intermediate layer (M_2), similar steps can be followed. Therefore, displacement components for the intermediate layer may be obtained as

$$v_2 = e^{-\varsigma_2 z/2}[C_3J_{s_4}(\Omega_2 e^{-\hbar_2 z}) + D_3Y_{s_4}(\Omega_2 e^{-\hbar_2 z})]e^{ik(x-ct)}, \tag{48}$$

with $s_4 = [(\varsigma_2/2\hbar_2)^2 + k^2(1-\zeta_2^{(3)})\Big/\hbar_2^2]^{1/2}$, $2\hbar_2 = (\varsigma_2 - \sigma_2)$, $\Omega_2 = kc/\hbar_2\beta_2^{(3)}$, dimensionless initial stress parameter $\zeta_2^{(3)} = P_3^{(2)}\Big/2\mu_2^{(3)}$, dimensionless phase velocity $\beta_2^{(3)} = \sqrt{\mu_2^{(3)}\Big/\rho_2^{(3)}}$ associated with intermediate layer (M_1). Also, J_{s_4} and Y_{s_4} denote Bessel functions of the first kind and second kind, respectively, of order s_4. C_3 and D_3 are the arbitrary constants.

The displacement components for the lower isotropic half-space (M_3), will be same as of the two previous cases, given by Eq. (13).

Using Eqs. (13), (47) and (48) in the boundary conditions (14–18) for the present case, the following relations may be obtained as

$$A_3\left\{\frac{\varsigma_1}{2}J_{s_1}(\Omega_1 e^{\hbar_1 h_1})+\Omega_1\hbar_1 e^{\hbar_1 h_1}J'_{s_1}(\Omega_1 e^{\hbar_1 h_1})\right\}+B_3\left\{\frac{\varsigma_1}{2}Y_{s_1}(\Omega_1 e^{\hbar_1 h_1})+\Omega_1\hbar_1 e^{\hbar_1 h_1}Y'_{s_1}(\Omega_1 e^{\hbar_1 h_1})\right\}=0, \tag{49}$$

$$\mu_1^{(2)}\left[A_3\left\{\frac{\varsigma_1}{2}J_{s_1}(\Omega_1)+\Omega_1\hbar_1 J'_{s_1}(\Omega_1)\right\}+B_3\left\{\frac{\varsigma_1}{2}Y_{s_1}(\Omega_1)+\Omega_1\hbar_1 Y'_{s_1}(\Omega_1)\right\}\right]=\mu_1^{(2)}\left[C_3\left\{\frac{\varsigma_2}{2}J_{s_2}(\Omega_2)+\Omega_2\hbar_2 J'_{s_2}(\Omega_2)\right\}+D_3\left\{\frac{\varsigma_2}{2}Y_{s_2}(\Omega_2)+\Omega_2\hbar_2 Y'_{s_2}(\Omega_2)\right\}\right]. \tag{50}$$

$$A_3J_{s_1}(\Omega_1)+B_3Y_{s_1}(\Omega_1)=C_3J_{s_2}(\Omega_2)+D_3Y_{s_2}(\Omega_2), \tag{51}$$

$$\mu_2 e^{-\varsigma_2 h_2/2}\left[C_3\left\{\frac{\varsigma_2}{2}J_{s_2}(\Omega_2 e^{-\hbar_2 h_2})+\Omega_2\hbar_2 e^{-\hbar_2 h_2}J'_{s_2}(\Omega_2 e^{-\hbar_2 h_2})\right\}+D_3\left\{\frac{\varsigma_2}{2}Y_{s_2}(\Omega_2 e^{-\hbar_2 h_2})+\Omega_2\hbar_2 e^{-\hbar_2 h_2}Y'_{s_2}(\Omega_2 e^{-\hbar_2 h_2})\right\}\right]=kr\mu_3 E e^{-krh_2}, \tag{52}$$

$$\mu_2 e^{-\varsigma_2 h_2/2}\left\{C_3J_{s_2}(\Omega_2 e^{-\hbar_2 h_2})+D_3Y_{s_2}(\Omega_2 e^{-\hbar_2 h_2})\right\}=Ee^{-krh_2}. \tag{53}$$

The elimination of the arbitrary constants A_3, B_3, C_3, D_3 and E yield the following relation:

$$\frac{(\mu_1^{(3)}/\mu_2^{(3)})\frac{(\varsigma_1/2)^2R_{15}+\{\Omega_1\hbar_1\varsigma_1(R_{16}+R_{17})/2\}+(\Omega_1\hbar_1)^2R_{18}}{(\varsigma_1/2)R_{15}+\Omega_1\hbar_1R_{16}}}{=\frac{\mu_2^{(3)}(\varsigma_2/2)^2R_{19}+\left\{\mu_2^{(3)}\varsigma_2\Omega_2\hbar_2(R_{20}+R_{21})/2\right\}+\mu_2^{(3)}(\Omega_2\hbar_2)^2R_{22}+\mu_3kr\Omega_2\hbar_2R_{21}}{\left\{\mu_2^{(3)}e^{\hbar_2h_2}(\varsigma_2/2)+\mu_3kr\right\}R_{19}+\mu_2^{(3)}e^{\hbar_2h_2}\Omega_2\hbar_2R_{20}}}. \tag{54}$$

Equation (54) represents dispersion relation for SH-type wave propagating double superficial layers (M_1) and (M_2), having exponential form of variation associated with each of the rigidity, density and initial stress of the two layers, lying over an isotropic half-space. The terms $R_{14+j}\,(j=1,2,\ldots 8)$ appearing in Eq. (54) are new and provided in the "Appendix III".

Special case

When the two layers (M_1) and (M_2) become homogeneous, i.e. which require $\varsigma_1\to 0$, $\varsigma_2\to 0$ and $\sigma_1\to 0$, $\sigma_2\to 0$, the dispersion equation for this case can be obtained with the aid of Debye asymptotic expansions.

Now, for $\varsigma_1\to 0$, $\varsigma_1\to 0$ *and* $\sigma_1\to 0$, $\sigma_2\to 0$, we have $\hbar_1\to\infty$ and $\hbar_2\to\infty$. The relations in terms of Bessel functions are involved in the terms $R_{14+j}\,(j=1,2,\ldots 8)$ of deduced dispersion relation (54). Further in view of Debye asymptotic expansions, stated in the "Appendix III", the dispersion relation reduces to

$$\tan(ks_1^{(4)}h_1)=\frac{Numr_4}{Den\,r_4},$$

where

$$Numr_4=ks_1^{(4)}\left[\mu_2^2e^{\hbar_2h_2}\{(\varsigma_2^2/4)+k^2s_2^2\}\tan ks_2h_2-\mu_2\mu_3k^2rs_2\right],$$

$$Den\,r_4=\{(\varsigma_1^2/4)+k^2s_1^2\}\left[\mu_1\mu_2e^{\hbar_2h_2}((\varsigma_2/2)+ks_2)-\mu_1\mu_2kr\tan ks_2h_2\right](\varsigma_1/2)\left[\mu_2^2e^{\hbar_2h_2}\{(\varsigma_2^2/4)+k^2s_2^2\}\tan ks_2h_2-\mu_2\mu_3k^2rs_2\right],$$

with $s_1^{(3)}=\sqrt{(c/\beta_1^{(3)})^2-1+\zeta_1^{(3)}}$,

$s_2^{(3)}=\sqrt{(c/\beta_2^{(3)})^2-1+\zeta_2^{(3)}}$.

Since $\varsigma_1\to 0$ and $\varsigma_2\to 0$ therefore, in this view, Eq. (54) becomes

$$\tan(ks_1^{(3)}h_1)=\frac{\mu_2^{(3)}\mu_3rs_2^{(3)}-(\mu_2^{(3)}s_2^{(3)})^2tan(ks_2^{(3)}h_2)}{\mu_1^{(3)}\mu_2^{(3)}s_1^{(3)}s_2^{(3)}+\mu_2^{(3)}\mu_2^{(3)}s_1^{(3)}r\tan(ks_2^{(3)}h_2)}. \tag{55}$$

The above Eq. (55) constitutes the dispersion relation for the SH-type wave propagating in initially stressed homogeneous double layer (M_1 and M_2) lying over an isotropic half-space (M_3).

Case IV: when inhomogeneity is caused in double superficial layer due to linear variation in rigidity, density and initial stress

The present study considers the linear form of variation accompanying rigidity, density, initial stress of the uppermost layer (M_1) and intermediate layer (M_2) and are supposed as follows:

$$\mu_j=\mu_j^{(4)}(1+\varepsilon_jz),\quad \rho_j=\rho_j^{(4)}(1+\varepsilon_jz),\quad P_j=P_j^{(4)}(1+\varepsilon_jz);\quad j=1,2, \tag{56}$$

where $j=1$ and $j=2$ denotes distinct parameters corresponding to uppermost and intermediate heterogeneous layer (M_1) and (M_2), respectively.

Assuming

$$v_j=\left(V_j(x,z,t)/\sqrt{\mu_j}\right)e^{ik(x-ct)};\quad (j=1,2). \tag{57}$$

Then, with the aid of Eq. (1) and (57), for $j=1$, the reduced form of equation for the upper heterogeneous layer (M_1) may be taken as

$$\mu_1 \frac{\partial^2 V_1}{\partial z^2} + \left(\mu_1 - \frac{P_1}{2}\right)\frac{\partial^2 V_1}{\partial x^2} + \left[\frac{1}{4\mu_1}\left(\frac{\mathrm{d}\mu_1}{\mathrm{d}z}\right)^2 - \frac{1}{2}\frac{\mathrm{d}^2\mu_1}{\mathrm{d}z^2}\right]V_1 = \rho_1 \frac{\mathrm{d}^2\mu_1}{\mathrm{d}t^2}. \tag{58}$$

In view of (56), Eq. (58) becomes

$$(1+\varepsilon_1 z)^2 \frac{\mathrm{d}^2 V_1}{\mathrm{d}z^2} + \left[(1+\varepsilon_1 z)^2 k^2 \left\{\left(\frac{c}{\beta_1^{(4)}}\right)^2 - 1 + \zeta_1^{(4)}\right\} + \frac{\varepsilon_1^2}{4}\right]V_1 = 0, \tag{59}$$

where $\beta_1^{(4)} = \sqrt{\mu_1^{(4)}/\rho_1^{(4)}}$ and $\zeta_1^{(4)} = P_1^{(4)}/2\mu_1^{(4)}$ are phase velocity and dimensionless initial stress parameter of the uppermost heterogeneous layer (M_1) of the composite structure for the present case.

Substituting W_1 in place $(1+\varepsilon_1 z)$ in Eq. (59), we obtain

$$W_1^2 \frac{\mathrm{d}^2 V_1}{\mathrm{d}W_1^2} + (a + bW_1^2)V_1 = 0, \tag{60}$$

with $a = 1/4$, $b = (k^2/\varepsilon_1^2)[(c/\beta_1^{(4)})^2 - 1 + \zeta_1^{(4)}]$.

Further, using $V_1 = W^{\ell_1} V_1'$ in Eq. (52), it gives

$$W_1^2 \frac{\mathrm{d}^2 V_1'}{\mathrm{d}W_1^2} + 2\ell_1 W_1 \frac{\mathrm{d}V_1'}{\mathrm{d}W_1} + [\ell_1(\ell_1 - 1) + (a + bW_1^2)]V_1' = 0. \tag{61}$$

Choosing $\ell_1 = 1/2$ and $\sqrt{b}W_1 = i\Phi_1$

$$\Phi_1^2 \frac{\mathrm{d}^2 V_1'}{\mathrm{d}^2\Phi_1^2} + \Phi_1 \frac{\mathrm{d}V_1'}{\mathrm{d}\Phi_1} - \Phi_1^2 V_1' = 0, \tag{62}$$

Thus we can find the solution of Eq. (62) as

$$V_1' = A_4 I_0(\Phi_1) + B_4 K_0(\Phi_1), \tag{63}$$

I_0 and K_0 being the modified Bessel function of the first and third kinds, respectively, of zero order with arbitrary constants A_4 and B_4.

In view of (63), the solution for the upper heterogeneous layer (M_1) may be obtained as

$$v_1 = \left(1/\sqrt{\mu_1^{(4)}}\right)[A_4 I_0\{(t_1/i\varepsilon_1)(1+\varepsilon_1 z)\} + B_4 K_0\{(t_1/i\varepsilon_1)(1+\varepsilon_1 z)\}]e^{ik(x-ct)}, \tag{64}$$

with $t_1 = k\sqrt{\left(c/\beta_1^{(4)}\right)^2 - 1 + \zeta_1^{(4)}}$.

Similarly, solution for the intermediate heterogeneous layer (M_2) can be taken as

$$v_2 = \left(1/\sqrt{\mu_2^{(4)}}\right)[C_4 I_0\{(t_2/i\varepsilon_2)(1+\varepsilon_2 z)\} + D_4 K_0\{(t_2/i\varepsilon_2)(1+\varepsilon_2 z)\}]e^{ik(x-ct)}, \tag{65}$$

with A_4 and B_4 being arbitrary constants and $t_2 = k\sqrt{\left(c/\beta_2^{(4)}\right)^2 - 1 + \zeta_2^{(4)}}$.

The terms $\beta_2^{(4)} = \sqrt{\mu_2^{(4)}/\rho_2^{(4)}}$ and $\zeta_2 = P_2^{(4)}/2\mu_2^{(4)}$ represent phase velocity and initial stress parameter of the intermediate heterogeneous layer (M_2) for composite structure.

The displacement components for the lower isotropic half space (M_3) will be given by Eq. (13).

In view of (13), (64) and (65), the boundary conditions (14–18) yielding following relations may be obtained as

$$A_4 I_0'\left[\frac{t_1}{i\varepsilon_1}(1-\varepsilon_1 h_1)\right] + B_4 K_0'\left[\frac{t_1}{i\varepsilon_1}(1-\varepsilon_1 h_1)\right] = 0, \tag{66}$$

$$\sqrt{\mu_1^{(4)}}t_1\left[A_4 I_0'(t_1/i\varepsilon_1) + B_4 K_0'(t_1/i\varepsilon_1)\right] = \sqrt{\mu_2^{(4)}}t_2\left[C_4 I_0'(t_2/i\varepsilon_2) + D_4 K_0'(t_2/i\varepsilon_2)\right], \tag{67}$$

$$\sqrt{\mu_2^{(4)}}[A_4 I_0(t_1/i\varepsilon_1) + B_4 K_0(t_1/i\varepsilon_1)] = \sqrt{\mu_1^{(4)}}[C_4 I_0(t_2/i\varepsilon_2) + D_4 K_0(t_2/i\varepsilon_2)], \tag{68}$$

$$\sqrt{\mu_2^{(4)}}(1+\varepsilon_2 h_2)t_2\left[C_4 I_0'\left\{\frac{t_2}{i\varepsilon_2}(1+\varepsilon_2 h_2)\right\} + D_4 K_0'\left\{\frac{t_2}{i\varepsilon_2}(1+\varepsilon_2 h_2)\right\}\right] = -i\mu_3 krE^{-krh_2}, \tag{69}$$

$$\sqrt{\mu_2^{(4)}}\left[C_4 I_0\left\{\frac{t_2}{i\varepsilon_2}(1+\varepsilon_2 h_2)\right\} + D_4 K_0\left\{\frac{t_2}{i\varepsilon_2}(1+\varepsilon_2 h_2)\right\}\right] = E^{-krh_2}. \tag{70}$$

Eliminating the arbitrary constants A_4, B_4, C_4, D_4 and E from the relations (66–70) gives the dispersion relation for the propagation of SH-type wave in the considered geometry (Case IV) as:

$$\frac{\mu_1^{(4)}t_1}{\mu_2^{(4)}t_2}\frac{R_{23}}{R_{24}} = \frac{\mu_2^{(4)}t_2(1+\varepsilon_2 h_2)R_{25} + i\mu_3 krR_{26}}{\mu_2^{(4)}t_2(1+\varepsilon_2 h_2)R_{27} + i\mu_3 krR_{28}}, \tag{71}$$

where $R_{22+j}(j = 1, 2, \ldots 6)$ are provided in the "Appendix IV".

Considering following relations

$$I_v(z) = e^{-1/i2\pi v}J_v(iz), \quad K_v(z) = \frac{1}{2}i\pi e^{1/i2\pi v}[J_v(iz) + iY_v(iz)]. \tag{72}$$

the dispersion equation in (71) can be rewritten as

$$\frac{\mu_1 t_1}{\mu_2 t_2}\frac{R_{29}}{R_{30}} = \frac{\mu_2 t_2(1+\varepsilon_2 h_2)R_{31} - \mu_3 krR_{32}}{\mu_2 t_2(1+\varepsilon_2 h_2)R_{33} + \mu_3 krR_{34}}, \tag{73}$$

with all the new terms $R_{28+j}(j = 1, 2, \ldots 6)$ of Eq. (73) provided in the "Appendix IV".

Again, using following asymptotic expansion of Bessel function, we have

$$J_0(\lambda) \approx \frac{2}{3\sqrt{\pi\lambda}}(\cos\lambda + \sin\lambda), Y_0(\lambda) \approx \frac{2}{3\sqrt{\pi\lambda}}(\cos\lambda + \sin\lambda),$$
$$J_0'(\lambda) \approx \frac{2}{3\sqrt{\pi\lambda}}\left[\left(1 - \frac{1}{2\lambda}\right)\cos\lambda + \left(1 + \frac{1}{2\lambda}\right)\sin\lambda\right],$$
$$Y_0'(\lambda) \approx \frac{-2}{3\sqrt{\pi\lambda}}\left[\left(1 - \frac{1}{2\lambda}\right)\sin\lambda - \left(1 + \frac{1}{2\lambda}\right)\cos\lambda\right]. \tag{74}$$

Using above relations mentioned in (74), we have the following results:

$$Y_0'(\lambda_2)J_0'(\lambda_1) - Y_0'(\lambda_1)J_0'(\lambda_2)$$
$$\approx \frac{-4}{9\pi\sqrt{\lambda_1\lambda_2}}[2\cos(\lambda_2)\sin(\lambda_1) - 2\cos(\lambda_1)\sin(\lambda_2)],$$
$$Y_0'(\lambda_2)J_0(\lambda_1) - Y_0(\lambda_1)J_0'(\lambda_2) \tag{75}$$
$$\approx \frac{-4}{9\pi\sqrt{\lambda_1\lambda_2}}[2\sin(\lambda_2)\sin(\lambda_1) - 2\cos(\lambda_1)\cos(\lambda_2)],$$

Using results of (75), in Eq. (73), we obtain

$$\frac{\mu_1^{(4)}t_1}{\mu_2^{(4)}t_2}\frac{\tan(\lambda_1) - \tan(\lambda_2)}{1 + \tan(\lambda_1)\tan(\lambda_2)} =$$
$$\frac{\mu_2^{(4)}t_2(1 + \varepsilon_2 h_2)\{\tan(\lambda_3) - \tan(\lambda_4)\} + \mu_3 kr\{1 + \tan(\lambda_3)\tan(\lambda_4)\}}{\mu_3 kr\{\tan(\lambda_3) - \tan(\lambda_4)\} - \mu_2^{(4)}t_2(1 + \varepsilon_2 h_2)\{1 + \tan(\lambda_3)\tan(\lambda_4)\}}, \tag{76}$$

taking $\lambda_1 = t_1/\varepsilon_1$, $\lambda_2 = t_1(1 - \varepsilon_1 h_1)/\varepsilon_1$, $\lambda_3 = t_2(1 + \varepsilon_2 h_2)/\varepsilon_2$, $\lambda_2 = t_2/\varepsilon_2$,which further reduces to

$$\tan(t_1 h_1) = \frac{\mu_2^{(4)}\mu_3 krt_2 - (\mu_2^{(4)}t_2)^2(1 + \varepsilon_2 h_2)\tan(t_2 h_2)}{\mu_1^{(4)}\mu_2^{(4)}t_1 t_2 + \mu_1^{(2)}\mu_3 krt_1(1 + \varepsilon_2 h_2)\tan(t_2 h_2)}, \tag{77}$$

Special case

When both of the upper and intermediate layers becomes homogeneous, i.e. $\varepsilon_1 \to 0$, $\varepsilon_2 \to 0$; then deduced dispersion relation in (77) yields

$$\tan(t_1 h_1) = \frac{\mu_2^{(4)}\mu_3 krt_2 - (\mu_2^{(4)}t_2)^2\tan(t_2 h_2)}{\mu_1^{(4)}\mu_2^{(4)}t_1 t_2 + \mu_1^{(2)}\mu_3 rt_1\tan(t_2 h_2)}. \tag{78}$$

Validation with the classical case

In each case, if intermediate layer of composite structure vanishes and corresponding initial stress associated with upper layer is assumed to be absent, which mathematically may be represented as $h_2 \to 0$ and $\zeta_1^{(1)} = 0$ in Case I, $h_2 \to 0$ and $\zeta_1^{(2)} = 0$ in Case II, $h_2 \to 0$ and $\zeta_1^{(3)} = 0$ in Case III and $h_2 \to 0$ and $\zeta_1^{(4)} = 0$ in Case IV. Then, dispersion relation obtained in Eqs. (25), (39), (55) and (77), for Case I, Case II, Case III and Case IV associated with each of the four distinct cases reduce to

$$\tan\left(kh_1\sqrt{\left(c\Big/\beta_1^{(j)}\right)^2 - 1}\right) = \frac{\mu_3\sqrt{1 - (c/\beta_3)^2}}{\mu_1^{(j)}\sqrt{\left(c\Big/\beta_1^{(j)}\right)^2 - 1}}, \tag{79}$$

for $j = 1, 2, 3,$ and 4, respectively. Equation (79) represents classical Love wave equation with $\beta_1^{(j)}\left(= \sqrt{\mu_1^{(j)}/\rho_1}\right)$ being the shear wave velocity associated with uppermost layer for Case j. This validates the result accomplished in each of the four distinct cases in view of classical results.

Analysis through numerical results

For the purpose of graphical depicture of the results, numerical computation has been carried out for deduced dispersion relations (24), (38), (54) and (73) for the propagation of SH-type wave in composite structure with inhomogeneous double superficial layers with initial stress and an isotropic half-space for Cases I, II, III and IV, respectively. Each of the considered cases deals with a distinct with form of inhomogeneity viz. when inhomogeneity in double superficial layer is due to exponential variation in density only (Case I); when inhomogeneity in double superficial layers is due to exponential variation in rigidity only (Case II); when inhomogeneity in double superficial layer is due to exponential variation in rigidity, density and initial stress (Case III) and when inhomogeneity in double superficial layer is due to linear variation in rigidity, density and initial stress (Case IV). The effect of the inhomogeneity parameters, initial stress parameters and width ratio associated with the two layers in the composite structure for each of the four aforesaid cases on dispersion curve (representing the variation of dimensionless phase velocity $c/\beta(c\Big/\beta_1^{(j)}; = j = 1, 2, 3, 4)$, against wavenumber, kh_1) of SH-type wave has been analyzed and their pictorial delineation has been accomplished through Figs. 2a, b, 3a, b, 4a, b, 5a, b, 6a and b.

For simplicity of the graphical representation, we have considered the following notations for all the figures as below:

In Figs. 2a, 3a, 4a, 5a and 6a: (1) Case I: replacing $\beta_1^{(1)}$ by β. (2) Case II: replacing $\beta_1^{(2)}$ by β.

In Figs. 2b, 3b, 4b, 5b and 6b: (1) Case III: replacing $\beta_1^{(3)}$ by β. (2) Case IV: replacing $\beta_1^{(4)}$ by β.

Following data (Gubbins 1990) have been taken into the account for numerical computation:

For the uppermost layer (M_1):

$$\mu_1^{(1)} = \mu_1^{(2)} = \mu_1^{(3)} = \mu_1^{(4)} = 3.23 \times 10^{10}\ \text{N/m}^2,$$
$$\rho_1^{(1)} = \rho_1^{(2)} = \rho_1^{(3)} = \rho_1^{(4)} = 2802\ \text{Kg/m}^3,$$

for the intermediate layer (M_2):

$$\mu_2^{(1)} = \mu_2^{(2)} = \mu_2^{(3)} = \mu_2^{(4)} = 6.54 \times 10^{10}\ \text{N/m}^2,$$
$$\rho_1^{(1)} = \rho_1^{(2)} = \rho_1^{(3)} = \rho_1^{(4)} = 3409\ \text{Kg/m}^3,$$

for the lowermost half-space (M_3):

$$\mu_3 = 29.17 \times 10^{10}\ \text{N/m}^2, \quad \rho_3 = 5563\ \text{Kg/m}^3.$$

Moreover, following values (unless otherwise stated) have also been taken into consideration:

$$n_1h_1 = 0.1, 0.2, 0.3; \quad n_2h_2 = 0.1, 0.2, 0.3;$$
$$l_1h_1 = 0.1, 0.2, 0.3; \quad l_2h_2 = 0.1, 0.2, 0.3;$$
$$\varsigma_1h_1 = 0.13, 0.15, 0.17;$$

$$\varsigma_1h_1 = 0.13, 0.15, 0.17; \quad \varsigma_2h_2 = 0.13, 0.15, 0.17;$$
$$\sigma_1h_1 = 0.01, 0.02, 0.03; \quad \sigma_2h_2 = 0.01, 0.02, 0.03;$$

$$\sigma_2h_2 = 0.01, 0.02, 0.03; \quad \varepsilon_1h_1 = 0.13, 0.15, 0.17;$$
$$\varepsilon_2h_2 = 0.13, 0.15, 0.17; \quad \zeta_1^{(1)} = 0, \pm 0.2;$$
$$\zeta_2^{(1)} = 0, \pm 0.2;$$

$$\zeta_1^{(2)} = 0, \pm 0.2; \quad \zeta_2^{(2)} = 0, \pm 0.2\ \zeta_1^{(3)} = 0, \pm 0.2;$$
$$\zeta_2^{(3)} = 0, \pm 0.2;\ \zeta_1^{(4)} = 0, \pm 0.2; \quad \zeta_2^{(4)} = 0, \pm 0.2.$$

To unravel the effect of different form of inhomogeneity in uppermost layer due to consideration of Case I, II, III and IV, Fig. 2a, b has been portrayed. In Fig. 2a curves 1, 2 and 3 reflect the effect of exponential inhomogeneity parameter (n_1h_1) of the uppermost layer associated with Case I, whereas curves 4, 5 and 6 are concerned with variation of exponential inhomogeneity parameter (l_1h_1) of uppermost layer associated with Case II, on phase velocity of SH-type wave. In view of the consideration of very small value of n_1h_1, curve 1 corresponds to the situation of linear heterogeneity, in close approximation, in density and rigidity being constant in uppermost layer, whereas for small value of l_1h_1, curve 4 realizes the situation of the uppermost layer to be Gibson layer (Gibson 1967) in close approximation, as it will correspond to the existence of linear inhomogeneity in rigidity and constant density. It is examined through this figure that exponential inhomogeneity parameter associated with density (n_1h_1) encourages the phase velocity; on the other hand, exponential inhomogeneity parameter associated with rigidity (l_1h_1)

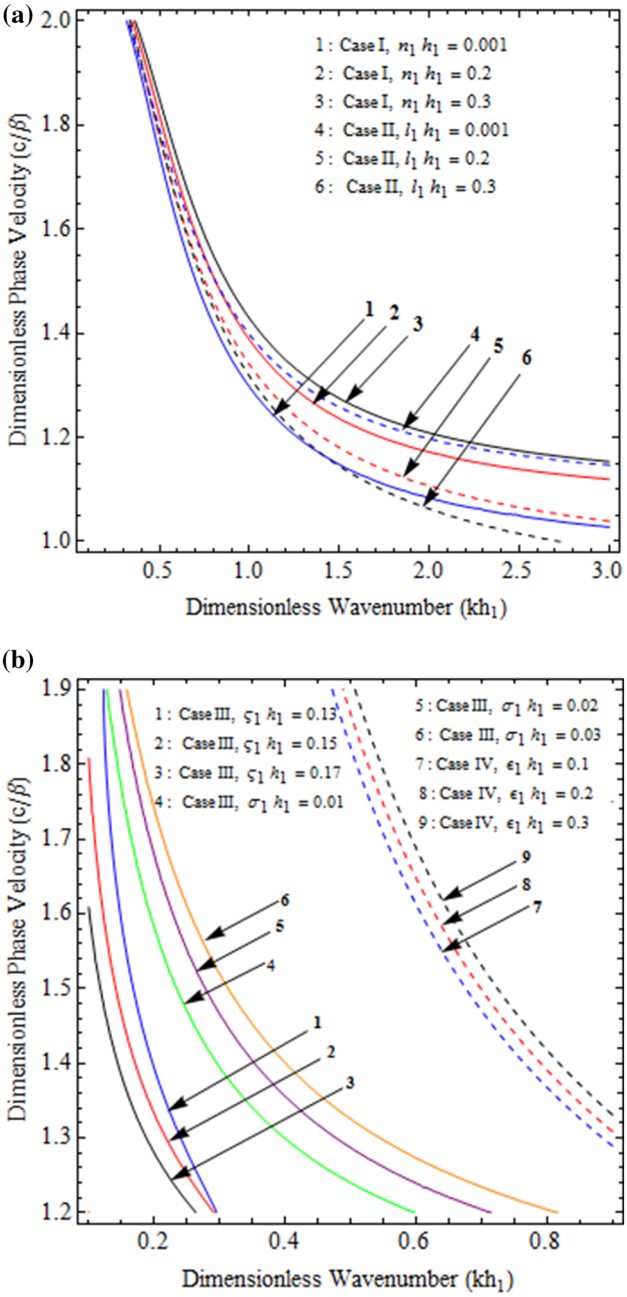

Fig. 2 Variation of dimensionless phase velocity (c/β) of SH-type wave against dimensionless wave number (kh_1) for different values of distinct heterogeneity parameter of the uppermost layer (M_1) **a** for Case I $(\beta = \beta_1^{(1)})$ and Case II $(\beta = \beta_1^{(2)})$ **b** for Case III $(\beta = \beta_1^{(3)})$ and Case IV $(\beta = \beta_1^{(4)})$

discourages the phase velocity of SH-type wave propagating in the considered structure.

On the other hand, in Fig. 2b, curves 1, 2 and 3 manifest the effect of exponential inhomogeneity parameter (σ_1h_1) associated with rigidity and initial stress of uppermost layer, whereas curves 4, 5 and 6 correspond to the variation of distinct exponential inhomogeneity parameter associated

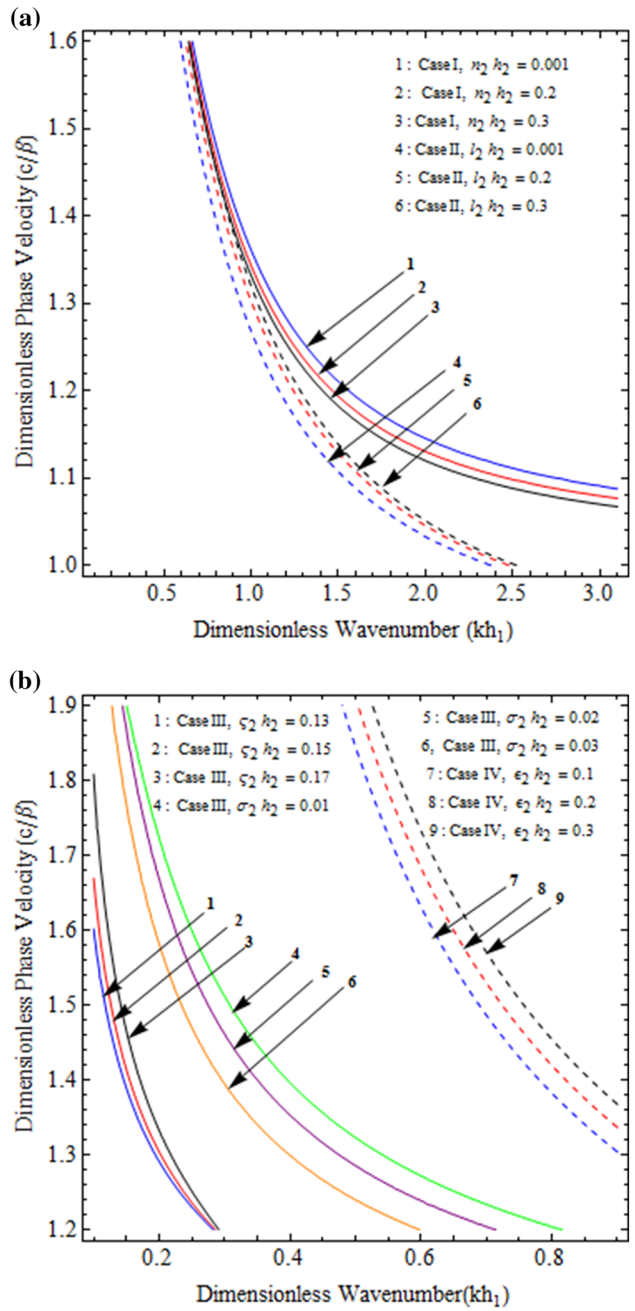

Fig. 3 Variation of dimensionless phase velocity (c/β) of SH-type wave against dimensionless wave number (kh_1) for different values distinct heterogeneity parameter of the intermediate layer (M_2) **a** for Case I $(\beta = \beta_1^{(1)})$ and Case II $(\beta = \beta_1^{(2)})$ **b** for Case III $(\beta = \beta_1^{(3)})$ and Case IV $(\beta = \beta_1^{(4)})$

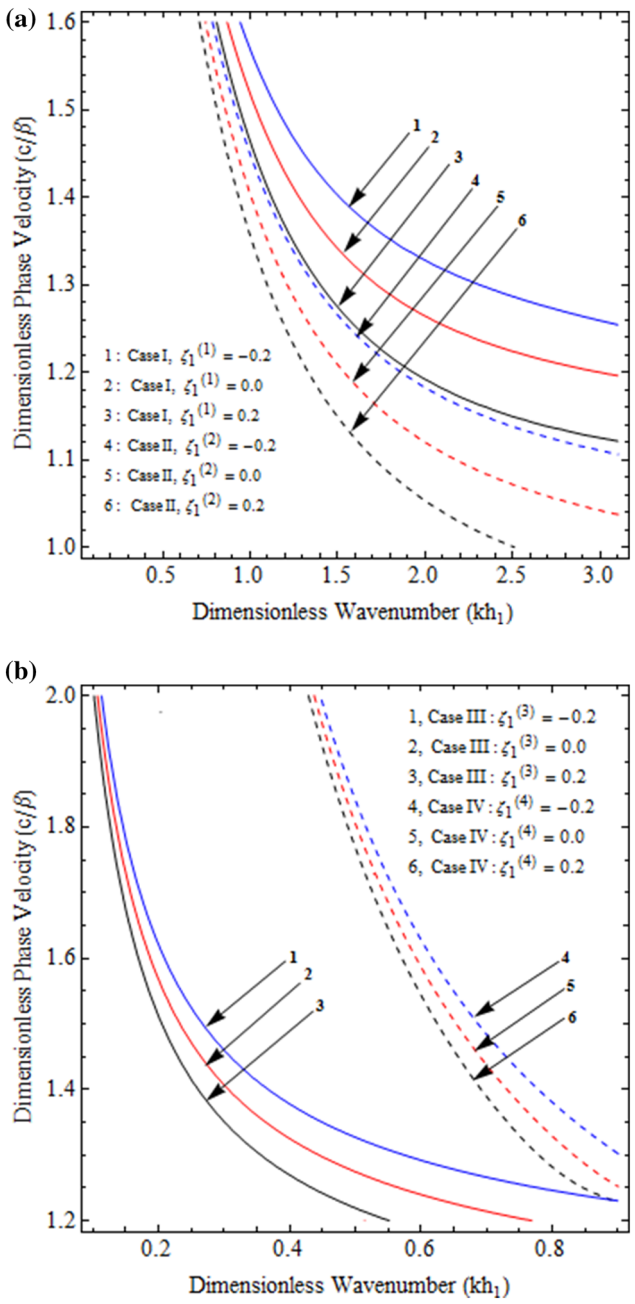

Fig. 4 Variation of dimensionless phase velocity (c/β) of SH-type wave against dimensionless wave number (kh_1) for different values initial stress (comressive/tensile) parameter of the uppermost layer (M_1) **a** for Case I $(\beta = \beta_1^{(1)})$ and Case II $(\beta = \beta_1^{(2)})$ **b** for Case III $(\beta = \beta_1^{(3)})$ and Case IV $(\beta = \beta_1^{(4)})$

with the density of the uppermost layer on the phase velocity of SH-type wave for Case III. Further, curves 7, 8 and 9 represent the influence of linear inhomogeneity parameter associated with rigidity, density and initial stress on the phase velocity of SH-type wave in Case IV. It is exhibited in Fig. 2b that for Case III, exponential inhomogeneity parameter associated with rigidity and initial stress disfavors whereas distinct exponential inhomogeneity parameter associated with density favors significantly the phase velocity of SH-type with increment in their magnitude. This observed trend in phase velocity of SH-type wave with concerned inhomogeneity parameter for Case III is found to be fairly compliant with the trend found for the associated inhomogeneity parameters in Case I and

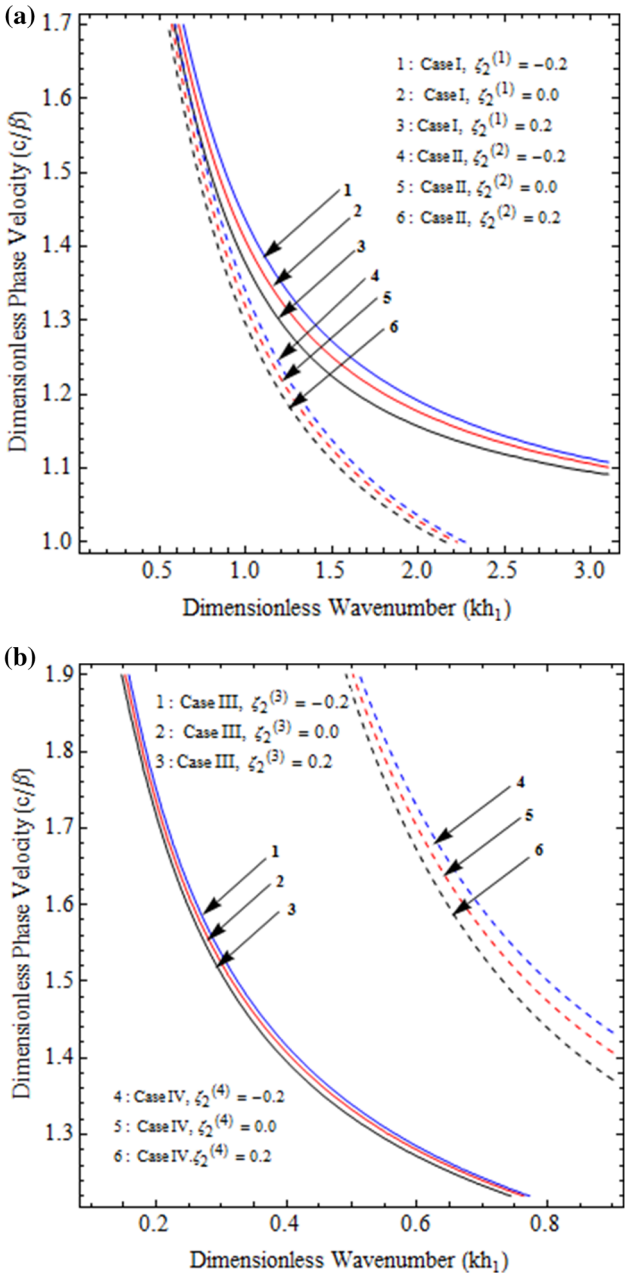

Fig. 5 Variation of dimensionless phase velocity (c/β) of SH-type wave against dimensionless wave number (kh_1) for different values of initial stress (comressive/tensile) parameter of the intermediate layer (M_2) **a** for Case I $(\beta = \beta_1^{(1)})$ and Case II $(\beta = \beta_1^{(2)})$ **b** for Case III $(\beta = \beta_1^{(3)})$ and Case IV $(\beta = \beta_1^{(4)})$

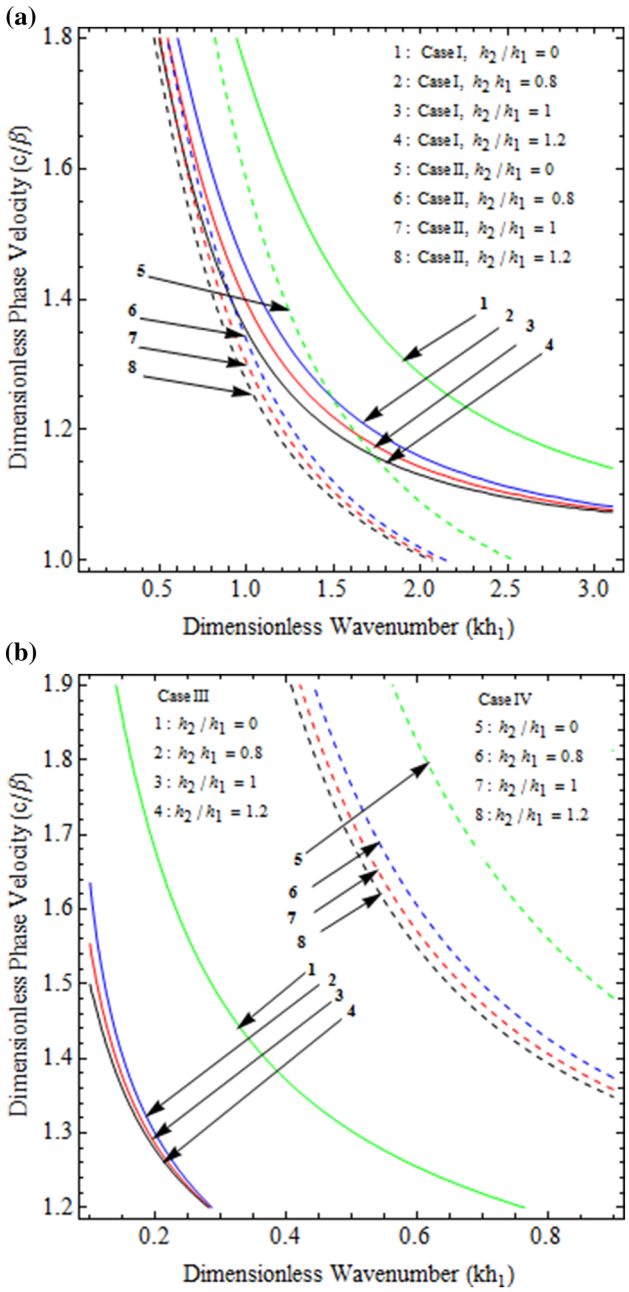

Fig. 6 Variation of dimensionless phase velocity (c/β) of SH-type wave against dimensionless wave number (kh_1) for different values of width ratio **a** for Case I $(\beta = \beta_1^{(1)})$ and Case II $(\beta = \beta_1^{(2)})$ **b** for Case III $(\beta = \beta_1^{(3)})$ and Case IV $(\beta = \beta_1^{(4)})$

Case II. However, the magnitude-wise deviation is being observed. Further, in Case IV, linear inhomogeneity $(\varepsilon_1 h_1)$ parameter associated with density, rigidity and initial stress affects favorably the phase velocity of SH-type wave. Meticulous examination of curves in Fig. 2a reveals that the presence of Gibson layer as an uppermost layer in the considered composite structure supports the phase velocity of SH-type wave.

The influence of distinct form of inhomogeneity, which has been taken into consideration in Cases I, II, III and IV, for intermediate layer, is demonstrated graphically in Figs. 3a, b. The variation of inhomogeneity parameter associated with material property of intermediate layer for Case I and Case II has been manifested through Fig. 3a, whereas that for Case III and Case IV has been delineated through Fig. 3b. Again curve 1 closely represents the linear

heterogeneity in density and a constant rigidity in intermediate layer as n_2h_2 is taken very small, whereas curve 4 accounts for Gibson intermediate layer for l_2h_2 being very small. More precisely, in Fig. 3a, the curves 1, 2 and 3 show the pronounced discouraging influence of exponential inhomogeneity parameter (n_2h_2) associated with Case I of intermediate layer on the phase velocity of SH-type wave. On the contrary curves 4, 5 and 6 show the significant encouraging effect of exponential inhomogeneity parameter l_2h_2 associated with Case II of intermediate layer on the same. Again in Fig. 3b, curves 1, 2 and 3 reflect the favorable effect of exponential inhomogeneity parameter associated with rigidity and initial stress (σ_2h_2) of intermediate layer, on the phase velocity of SH-type wave, for Case III. However, curves 4, 5 and 6 account for the discouraging effect of exponential inhomogeneity parameter associated with density of intermediate layer on the same for Case III. Besides this, the curves 7, 8 and 9 indicate the substantial increasing effect of linear inhomogeneity (ε_2h_2) parameter associated with rigidity, density and initial stress for intermediate layer on the phase velocity of SH-type wave in Case IV. Subtle analysis establishes that presence of Gibson layer as intermediate layer in the considered composite structures discourages the phase velocity of SH-type wave.

To demonstrate the effect of compressive as well as tensile initial stress acting in the uppermost layer for Case I and Case II Fig. 4a is portrayed, whereas for Case III and Case IV, Fig. 4b is plotted. In Fig. 4a, b, curves 1 and 4 correspond to the presence of tensile initial stress; curves 2 and 5 correspond to the presence of no initial stress; and curves 3 and 6 indicate the presence of compressive initial stress in the uppermost layer for the Case I and II, respectively. On the other hand, in Fig. 4b, curves 1 and 4 represent the presence of tensile initial stress; curves 2 and 5 represent no initial stress; and curves 3 and 6 account for compressive initial stress, associated with the uppermost layer, of Case III and Case IV. It is established through Fig. 4a, b that initial stress acting in uppermost layer has a disfavoring influence on phase velocity of SH-type wave in all four aforementioned cases. Specifically, as compressive initial stress grows in the uppermost layer, phase velocity of SH-type wave gets decreased, whereas as tensile initial stress increases in the uppermost layer, phase velocity of SH-type wave get increased in all four cases.

Figure 5a, b manifests the impact of dimensionless initial stress parameter associated with intermediate layer of composite structure for Case I & Case II and Case III & Case IV, respectively. The association of the case with the numbering of curves in Fig. 5a, b follows the same fashion, which is followed in Fig. 4a, b but for intermediate layer. It is examined that for intermediate layer, with the growth of compressive initial stress, phase velocity of SH-type wave diminishes, whereas with the growth of tensile initial stress in the same leads to the increase in phase velocity of SH-type wave in all four considered cases. Although the same trend has been exhibited for initial stress acting in the uppermost layer and intermediate layer for all four said cases yet the effect in terms of magnitude may easily be observed.

Effect of width ratio associated with double superficial layer in the considered composite structure on the phase velocity of SH-type wave is described graphically for Case I (Curves 1, 2, 3, 4) and Case II (Curves 5, 6, 7, 8) in Fig. 6a and for Case III (Curves 1, 2, 3, 4) and Case IV (Curves 5, 6, 7, 8) in Fig. 6b. In Fig. 6a, b, curve 1 corresponds to Case I and Case III, respectively, when there exists only uppermost layer over half-space (i.e. intermediate layer is absent); curve 2 is associated with the Case I and Case III, respectively, when thickness of the uppermost layer greater than the intermediate layer; curve 3 associated with the Case I and III, respectively, when thickness of the uppermost layer is equal to the thickness of the intermediate one; curve 4 is associated with the Case I and III, respectively, when thickness of the uppermost layer is smaller than the thickness of the intermediate one; curve 5 corresponds to Case II and IV, respectively, when there intermediate layer is absent in the considered composite structure; curve 6 corresponds to Case II and IV, respectively, when thickness of the uppermost layer greater than the intermediate layer; curve 7 indicates Case II and IV, respectively, when thickness of the uppermost layer is equal to the thickness of the intermediate one and curve 8 is associated with the Case II and IV, respectively, when thickness of the uppermost layer is smaller than the thickness of the intermediate one. It is reported from these two figures that phase velocity of SH-type wave decreases with the increase in the width ratio of double superficial layers for all aforesaid cases. Subtle examination of these curves in both the figures suggest that phase velocity of SH-type is maximum, when intermediate layer is absent in the considered composite structure and minimum when thickness of uppermost layer is less than that of intermediate one among all considered cases of width ratio.

The comparative study of all the figures concludes that the phase velocity of SH-type wave is maximum when heterogeneity is considered in composite structure as per case IV and minimum when it is considered as per case III, among all four studied cases. Besides this, phase velocity is found to be more when heterogeneity is considered as per case I as compared to the situation when it is according to the case II. The meticulous examination of these figures establishes that the influence of heterogeneity parameter associated with density dominates over the effect of heterogeneity parameter associated with rigidity on the phase velocity of SH-type wave. In addition to this,

it may be concluded that the linear heterogeneity in the material properties of the medium favors more to the phase velocity as compared to the exponential heterogeneity in material property of the medium. This may be cause due to the reason that extent of heterogeneity is more in case of exponential heterogeneity as compared to linear heterogeneity and as prevalence of heterogeneity is more in a medium, phase velocity is greater.

Conclusion

Analysis on the influence of different form of inhomogeneity in a composite structure comprised of double superficial layers lying over a half-space, on the phase velocity of propagating SH-type wave has been accomplished through present study using Debye asymptotic analysis. Propagation of SH-type wave in a composite structure has been examined in four distinct cases of inhomogeneity viz. when inhomogeneity in double superficial layer is due to exponential variation in density only (Case I); when inhomogeneity in double superficial layers is due to exponential variation in rigidity only (Case II); when inhomogeneity in double superficial layer is due to exponential variation in rigidity, density and initial stress (Case III) and when inhomogeneity in double superficial layer is due to linear variation in rigidity, density and initial stress (Case IV). Closed-form expression of dispersion relation has been obtained for all four aforementioned cases. Numerical computation has been carried out to graphically demonstrate the effect of inhomogeneity parameters, initial stress parameters as well as width ratio associated with double superficial layers in the composite structure for each of the four aforesaid cases on dispersion curve. Meticulous examination of distinct cases of inhomogeneity and initial stress in context of considered problem has been carried out with extensive analysis in a comparative approach. Following points may be encapsulated through the analysis undertaken in present paper:

1. Dispersion equations of SH-type wave have been deduced in closed-form through analytical treatment with extensive application of Debye asymptotic analysis for all four said cases and they are found in well-agreement with the classical Love-wave equation as well.
2. The substantial effect of wave number has been reported on phase velocity of SH-type wave in all four said cases. Phase velocity decreases significantly with the increase in wave number.
3. It may be stated through the comparative study of Case I and Case II that, the influence of heterogeneity parameters associated with rigidity is of opposite nature to the influence of heterogeneity parameters associated with density, accompanying either of the superficial layers M_1 and M_2 are of the conflicting nature. More precisely, the influence of heterogeneity parameter present in the upper layer follows a completely opposite trend in contrast to that of the intermediate layer for each of Case I and Case II.
4. Comparative study of Case III and Case IV emphasized that linear form of inhomogeneity (Case III) assumed in both the superficial layers favors the phase velocity of SH-type wave, However, the inhomogeneity contributing to exponential variation in corresponding density of each of the two superficial layers disfavors the phase velocity of SH-type wave. On the other hand, the exponential form of inhomogeneity existing in the upper layer and intermediate layer, accompanying rigidity and that of initial stress favors and disfavors the phase velocity significantly.
5. It can be stated through minute contemplation of all four cases that the phase velocity of SH-type wave is maximum when heterogeneity is considered in composite structure as per case IV and minimum when it is considered as per case III, among all four studied cases. Besides this, phase velocity is found to be more when heterogeneity is considered as per case I as compared to the situation when it is according to the case II.
6. The meticulous examination carried out in comparative manner establishes that the influence of heterogeneity parameter associated with density dominates over the effect of heterogeneity parameter associated with rigidity on the phase velocity of SH-type wave. In addition to this, it may also be concluded that the linear heterogeneity in the material properties of the medium favors more the phase velocity as compared to the exponential heterogeneity in material property of the medium.
7. It is revealed that the presence of Gibson layer as an uppermost layer in the considered composite structure encourages, whereas presence of Gibson layer as an intermediate layer in the considered composite structure discourages the phase velocity of SH-type wave.
8. It is established that as compressive initial stress grows in the uppermost as well as intermediate layer, phase velocity of SH-type wave gets decreased, whereas as tensile initial stress increases in the uppermost as well as intermediate layer, phase velocity of SH-type wave gets increased in all four said cases.
9. It is reported that phase velocity of SH-type wave decreases with the increase in the width ratio of double superficial layers for all aforesaid cases. Subtle examination establishes that phase velocity of SH-type is maximum, when intermediate layer is absent in the considered composite structure and minimum when thickness of uppermost layer is less than that of intermediate one among all considered cases of width ratio.

The earth is considered to be consisting of a sequence of horizontal layers bearing different elastic properties. The study of propagation of seismic waves is done extensively to predict and understand the behavior of the earth's interior. Therefore, the present study may find its worthy applications in the sphere of seismology, engineering geology, earthquake engineering and geophysics: specifically, in the problems affiliated to waves and vibrations through heterogeneous media.

Acknowledgements The authors convey their sincere thanks to Indian Institute of Technology (Indian School of Mines), Dhanbad, for providing JRF to Ms. Shalini Saha and also for facilitating them with its best facility for research.

Compliance with ethical standards

Conflict of interest On behalf of all authors, the corresponding author states that there is no conflict of interest.

Appendix I

$$R_1 = J'_{p_1}(\delta_1 e^{-n_1 h_1}) Y_{p_1}(\delta_1) - Y'_{p_1}(\delta_1 e^{-n_1 h_1}) J_{p_1}(\delta_1),$$
$$R_2 = J'_{p_1}(\delta_1 e^{-n_1 h_1}) Y'_{p_1}(\delta_1) - Y'_{p_1}(\delta_1 e^{-n_1 h_1}) J'_{p_1}(\delta_1),$$
$$R_3 = J'_{p_2}(\delta_2 e^{n_2 h_2}) Y_{p_2}(\delta_2) - Y'_{p_2}(\delta_2 e^{n_2 h_2}) J_{p_2}(\delta_2),$$
$$R_4 = J_{p_2}(\delta_2 e^{n_2 h_2}) Y_{p_2}(\delta_2) - Y_{p_2}(\delta_2 e^{n_2 h_2}) J_{p_2}(\delta_2),$$
$$R_5 = J'_{p_2}(\delta_2 e^{n_2 h_2}) Y'_{p_2}(\delta_2) - Y'_{p_2}(\delta_2 e^{n_2 h_2}) J'_{p_2}(\delta_2),$$
$$R_6 = J_{p_2}(\delta_2 e^{n_2 h_2}) Y'_{p_2}(\delta_2) - Y_{p_2}(\delta_2 e^{n_2 h_2}) J'_{p_2}(\delta_2),$$

$$p_1 \sec\phi_1 = \frac{kc}{n_1 \beta_1^{(1)}} e^{-n_1 h_1}, \quad p_2 \sec\phi_2 = \frac{kc}{n_1 \beta_1^{(1)}},$$
$$p_1 \tan\phi_1 = \frac{k}{n_1}\sqrt{\frac{c^2}{(\beta_1^{(1)})^2} - 1 + \zeta_1^{(1)}}\left[1 - \frac{c^2 n_1 h_1}{c^2 - (\beta_1^{(1)})^2}\right],$$
$$p_1 \tan\phi_2 = \frac{k}{n_1}\sqrt{\frac{c^2}{(\beta_1^{(1)})^2} - 1 + \zeta_1^{(1)}}, (\phi_1 - \phi_2) \sim n_1 h_1 \frac{\sqrt{1-\zeta_1^{(1)}}}{\sqrt{\frac{c^2}{(\beta_1^{(1)})^2} - 1 + \zeta_1^{(1)}}},$$
$$p_1(\tan\phi_1 - \tan\phi_2) - p_1(\phi_1 - \phi_2) \sim -kh_1\sqrt{\frac{c^2}{(\beta_1^{(1)})^2} - 1 + \zeta_1^{(1)}},$$
$$\sin\phi_1 \sim \frac{\beta_1^{(1)}}{c}\sqrt{\frac{c^2}{(\beta_1^{(1)})^2} - 1 + \zeta_1^{(1)}} \sim \sin\phi_2,$$
$$p_2 \sec\phi_3 = \frac{kc}{n_2 \beta_2^{(1)}} e^{n_2 h_2}, \quad p_2 \sec\phi_4 = \frac{kc}{n_2 \beta_2^{(1)}},$$
$$p_2 \tan\phi_3 = \frac{k}{n_2}\sqrt{\frac{c^2}{(\beta_2^{(1)})^2} - 1 + \zeta_2^{(1)}},$$
$$p_2 \tan\phi_4 = \frac{k}{n_2}\sqrt{\frac{c^2}{(\beta_2^{(1)})^2} - 1 + \zeta_2^{(1)}}\left[1 + \frac{c^2 n_2 h_2}{c^2 - (\beta_2^{(1)})^2}\right],$$
$$(\phi_3 - \phi_4) \sim n_2 h_2 \frac{\sqrt{1-\zeta_2^{(1)}}}{\sqrt{\frac{c^2}{(\beta_2^{(1)})^2} - 1 + \zeta_2^{(1)}}},$$
$$p_2(\tan\phi_3 - \tan\phi_4) - p_2(\phi_3 - \phi_4) \sim kh_2\sqrt{\frac{c^2}{(\beta_2^{(1)})^2} - 1 + \zeta_2^{(1)}},$$
$$\text{and } \sin\phi_3 \sim \frac{\beta_2^{(1)}}{c}\sqrt{\frac{c^2}{\left(\beta_2^{(1)}\right)^2} - 1 + \zeta_2^{(1)}} \sim \sin\phi_4.$$

Appendix II

$$R_7 = J_{q_1}(\delta_1 e^{l_1 h_1}) Y_{q_1}(\delta_1) - J_{q_1}(\delta_1) Y_{q_1}(\delta_1 e^{l_1 h_1}),$$
$$R_8 = J'_{q_1}(\delta_1 e^{l_1 h_1}) Y_{q_1}(\delta_1) - J_{q_1}(\delta_1) Y'_{q_1}(\delta_1 e^{l_1 h_1}),$$
$$R_9 = J_{q_1}(\delta_1 e^{l_1 h_1}) Y'_{q_1}(\delta_1) - J'_{q_1}(\delta_1) Y_{q_1}(\delta_1 e^{l_1 h_1}),$$
$$R_{10} = J'_{q_1}(\delta_1 e^{l_1 h_1}) Y'_{q_1}(\delta_1) - J'_{q_1}(\delta_1) Y'_{q_1}(\delta_1 e^{l_1 h_1}),$$

$$R_{11} = J_{q_2}(\delta_2 e^{-l_2 h_2}) Y_{q_2}(\delta_2) - J_{q_2}(\delta_2) Y_{q_2}(\delta_2 e^{-l_2 h_2}),$$
$$R_{12} = J_{q_2}(\delta_2 e^{-l_2 h_2}) Y'_{q_2}(\delta_2) - J'_{q_2}(\delta_2) Y_{q_2}(\delta_2 e^{-l_2 h_2}),$$
$$R_{13} = J'_{q_2}(\delta_2 e^{-l_2 h_2}) Y_{q_2}(\delta_2) - J_{q_2}(\delta_2) Y'_{q_2}(\delta_2 e^{-l_2 h_2}),$$
$$R_{14} = J'_{q_2}(\delta_2 e^{-l_2 h_2}) Y'_{q_2}(\delta_2) - J'_{q_2}(\delta_2) Y'_{q_2}(\delta_2 e^{-l_2 h_2}).$$

$$\left[J_{q_1}(\gamma_1 e^{l_1 h_1}) Y_{q_1}(\gamma_1) - Y_{q_1}(\delta\gamma_1 e^{l_1 h_1}) J_{q_1}(\gamma_1)\right] \approx \frac{-2\sin[q_1(\tan\psi_1 - \tan\psi_2) - q_1(\psi_1 - \psi_2)]}{\pi q_1 \sqrt{\tan\psi_1 \tan\psi_2}},$$

$$\left[J_{q_2}(\gamma_2 e^{-l_2 h_2}) Y_{q_2}(\delta_2) - Y_{q_2}(\gamma_2 e^{-l_2 h_2}) J_{q_2}(\gamma_2)\right] \approx \frac{-2\sin[q_2(\tan\psi_3 - \tan\psi_4) - q_2(\psi_3 - \psi_4)]}{\pi q_2 \sqrt{\tan\psi_3 \tan\psi_4}},$$

$$\left[J_{q_1}(\gamma_1 e^{l_1 h_1}) Y'_{q_1}(\gamma_1) - Y_{q_1}(\gamma_1 e^{l_1 h_1}) J'_{q_1}(\gamma_1)\right] \approx \frac{2\sin\psi_2 \cos[q_1(\tan\psi_1 - \tan\psi_2) - q_1(\psi_1 - \psi_2)]}{\pi q_1 \sqrt{\tan\psi_1 \tan\psi_2}},$$

$$\left[J_{q_2}(\gamma_2 e^{-l_2 h_2}) Y'_{q_2}(\gamma_2) - Y_{q_2}(\gamma_2 e^{-l_2 h_2}) J'_{q_2}(\gamma_2)\right] \approx \frac{2\sin\psi_4 \cos[q_2(\tan\psi_3 - \tan\psi_4) - q_2(\psi_3 - \psi_4)]}{\pi q_2 \sqrt{\tan\psi_3 \tan\psi_4}},$$

$$\left[J'_{q_1}(\gamma_1 e^{l_1 h_1})Y_{q_1}(\gamma_1) - Y'_{q_1}(\gamma_1 e^{l_1 h_1})J_{q_1}(\gamma_1)\right] \approx \frac{-2sin\psi_1 \cos[q_1(\tan\psi_1 - \tan\psi_2) - q_1(\psi_1 - \psi_2)]}{\pi q_1 \sqrt{\tan\psi_1 \tan\psi_2}},$$

$$\left[J'_{q_2}(\gamma_2 e^{-l_2 h_2})Y_{q_2}(\gamma_2) - Y'_{q_2}(\gamma_2 e^{-l_2 h_2})J_{q_2}(\gamma_2)\right] \approx \frac{-2\sin\psi_3 \cos[q_2(\tan\psi_3 - \tan\psi_4) - q_2(\psi_3 - \psi_4)]}{\pi q_2 \sqrt{\tan\psi_3 \tan\psi_4}},$$

$$\left[J'_{q_1}(\gamma_1 e^{l_1 h_1})Y'_{q_1}(\gamma_1) - Y'_{q_1}(\gamma_1 e^{l_1 h_1})J'_{q_1}(\gamma_1)\right] \approx \frac{-2\sin\psi_1 \sin\psi_2 \sin[q_1(\tan\psi_1 - \tan\psi_2) - q_1(\psi_1 - \psi_2)]}{\pi q_1 \sqrt{\tan\psi_1 \tan\psi_2}},$$

$$\left[J'_{q_2}(\gamma_2 e^{-l_2 h_2})Y'_{q_2}(\gamma_2) - Y'_{q_2}(\gamma_2 e^{-l_2 h_2})J'_{q_2}(\gamma_2)\right] \approx \frac{-2\sin\psi_3 \sin\psi_4 \sin[q_2(\tan\psi_3 - \tan\psi_4) - q_2(\psi_3 - \psi_4)]}{\pi q_2 \sqrt{\tan\psi_3 \tan\psi_4}},$$

$$q_1 \sec\psi_1 = \frac{kc}{l_1 \beta_1^{(2)}} e^{l_1 h_1}, \quad q_1 \sec\psi_2 = \frac{kc}{l_1 \beta_1^{(2)}},$$

$$q_1 \tan\psi_1 = \frac{k}{l_1}\sqrt{\frac{c^2}{(\beta_1^{(2)})^2} - 1 + \zeta_1^{(1)}}\left[1 + \frac{c^2 l_1 h_1}{c^2 - (\beta_1^{(2)})^2}\right],$$

$$q_1 \tan\psi_2 = \frac{k}{l_1}\sqrt{\frac{c^2}{\left(\beta_1^{(2)}\right)^2} - 1 + \zeta_1^{(2)}},$$

$$\psi_1 - \psi_2 \sim l_1 h_1 \frac{\sqrt{1 - \zeta_1^{(2)}}}{\sqrt{\frac{c^2}{(\beta_1^{(2)})^2} - 1 + \zeta_1^{(2)}}},$$

$$q_1(\tan\psi_1 - \tan\psi_2) - q_1(\psi_1 - \psi_2) \sim kh_1\sqrt{\frac{c^2}{\left(\beta_1^{(2)}\right)^2} - 1 + \zeta_1^{(2)}},$$

$$\sin\psi_1 \sim \frac{\beta_1^{(2)}}{c}\sqrt{\frac{c^2}{\left(\beta_1^{(2)}\right)^2} - 1 + \zeta_1^{(2)}} \sim \sin\psi_2.$$

$$q_2 \sec\psi_3 = \frac{kc}{l_2 \beta_2^{(1)}} e^{-l_2 h_2}, \quad q_2 \sec\psi_4 = \frac{kc}{l_2 \beta_2^{(2)}},$$

$$q_2 \tan\psi_3 = \frac{k}{l_2}\sqrt{\frac{c^2}{(\beta_2^{(2)})^2} - 1 + \zeta_2^{(2)}}\left[1 - \frac{c^2 l_2 h_2}{c^2 - (\beta_2^{(2)})^2}\right],$$

$$q_2 \tan\psi_4 = \frac{k}{l_2}\sqrt{\frac{c^2}{(\beta_2^{(2)})^2} - 1 + \zeta_2^{(2)}},$$

$$q_2(\tan\psi_3 - \tan\psi_4) - q_2(\psi_3 - \psi_4) \sim -kh_2\sqrt{\frac{c^2}{(\beta_2^{(2)})^2} - 1 + \zeta_2^{(2)}},$$

$$\psi_3 - \psi_4 \sim l_2 h_2 \frac{\sqrt{1 - \zeta_2^{(2)}}}{\sqrt{\frac{c^2}{(\beta_2^{(2)})^2} - 1 + \zeta_2^{(2)}}} \quad \text{and}$$

$$\sin\psi_3 \sim \frac{\beta_2^{(2)}}{c}\sqrt{\frac{c^2}{\left(\beta_2^{(2)}\right)^2} - 1 + \zeta_2^{(2)}} \sim \sin\psi_4.$$

Appendix III

$$R_{15} = J_{s_3}(\Omega_1 e^{\hbar_1 h_1})Y_{s_1}(\Omega_1) - J_{s_3}(\Omega_1)Y_{s_3}(\Omega_1 e^{\hbar_1 h_1}),$$
$$R_{16} = J'_{s_3}(\Omega_1 e^{\hbar_1 h_1})Y_{s_3}(\Omega_1) - J_{s_3}(\Omega_1)Y'_{s_3}(\Omega_1 e^{\hbar_1 h_1}),$$
$$R_{17} = J_{s_3}(\Omega_1 e^{\hbar_1 h_1})Y'_{s_3}(\Omega_1) - J'_{s_3}(\Omega_1)Y_{s_3}(\Omega_1 e^{\hbar_1 h_1}),$$
$$R_{18} = J'_{s_3}(\Omega_1 e^{\hbar_1 h_1})Y'_{s_3}(\Omega_1) - J'_{s_3}(\Omega_1)Y'_{s_3}(\Omega_1 e^{\hbar_1 h_1}),$$

$$R_{19} = J_{s_4}(\Omega_2 e^{-\hbar_2 h_2})Y_{s_4}(\Omega_2) - J_{s_4}(\Omega_2)Y_{s_4}(\Omega_2 e^{-\hbar_2 h_2}),$$
$$R_{20} = J'_{s_4}(\Omega_2 e^{-\hbar_2 h_2})Y_{s_4}(\Omega_2) - J_{s_4}(\Omega_2)Y'_{s_4}(\Omega_2 e^{-\hbar_2 h_2}),$$
$$R_{21} = J_{s_4}(\Omega_2 e^{-\hbar_2 h_2})Y'_{s_4}(\Omega_2) - J'_{s_4}(\Omega_2)Y_{s_4}(\Omega_2 e^{-\hbar_2 h_2}),$$
$$R_{22} = J'_{s_4}(\Omega_2 e^{-\hbar_2 h_2})Y'_{s_4}(\Omega_2) - J'_{s_4}(\Omega_2)Y'_{s_4}(\Omega_2 e^{-\hbar_2 h_2}),$$

$$\left[J_{s_3}(\Omega_1 e^{\hbar_1 h_1})Y_{s_3}(\Omega_1) - Y_{s_3}(\Omega_1 e^{\hbar_1 h_1})J_{s_3}(\Omega_1)\right] \approx \frac{-2\sin[s_3(\tan\phi_{21} - \tan\phi_{22}) - s_3(\phi_{21} - \phi_{22})]}{\pi s_3 \sqrt{\tan\phi_{21}\tan\phi_{22}}},$$

$$\left[J_{s_4}(\Omega_2 e^{-\hbar_2 h_2})Y_{s_4}(\Omega_2) - Y_{s_4}(\Omega_2 e^{-\hbar_2 h_2})J_{s_2}(\Omega_2)\right] \approx \frac{-2\sin[s_4(\tan\phi_{23} - \tan\phi_{24}) - s_4(\phi_{23} - \phi_{24})]}{\pi s_4 \sqrt{\tan\phi_{23}\tan\phi_{24}}},$$

$$\left[J_{s_3}(\Omega_1 e^{\hbar_1 h_1})Y'_{s_3}(\Omega_1) - Y_{s_3}(\Omega_1 e^{\hbar_1 h_1})J'_{s_3}(\Omega_1)\right] \approx \frac{2\sin\phi_{21}\sin[s_3(\tan\phi_{21} - \tan\phi_{22}) - s_3(\phi_{21} - \phi_{22})]}{\pi s_3 \sqrt{\tan\phi_{21}\tan\phi_{22}}},$$

$$\left[J_{s_4}(\Omega_2 e^{-\hbar_2 h_2})Y'_{s_4}(\Omega_2) - Y_{s_4}(\Omega_2 e^{-\hbar_2 h_2})J'_{s_4}(\Omega_2)\right] \approx \frac{2\sin\phi_{24}\cos[s_4(\tan\phi_{23} - \tan\phi_{24}) - s_4(\phi_{23} - \phi_{24})]}{\pi s_4 \sqrt{\tan\phi_{23}\tan\phi_{24}}},$$

$$\left[J'_{s_3}(\Omega_1 e^{\hbar_1 h_1})Y_{s_3}(\Omega_1) - Y'_{s_3}(\Omega_1 e^{\hbar_1 h_1})J_{s_3}(\Omega_1)\right] \approx \frac{-2\sin\phi_{21}\cos[s_3(\tan\phi_{21} - \tan\phi_{22}) - s_3(\phi_{21} - \phi_{22})]}{\pi s_3 \sqrt{\tan\phi_{21}\tan\phi_{22}}},$$

$$\left[J'_{s_4}(\Omega_2 e^{-\hbar_2 h_2})Y_{s_4}(\Omega_2) - Y'_{s_4}(\Omega_2 e^{-\hbar_2 h_2})J_{s_4}(\Omega_2)\right] \approx \frac{-2\sin\phi_{23}\cos[s_4(\tan\phi_{23} - \tan\phi_{24}) - s_4(\phi_{23} - \phi_{24})]}{\pi s_4 \sqrt{\tan\phi_{23}\tan\phi_{24}}},$$

$$\left[J'_{s_3}(\Omega_1 e^{\hbar_1 h_1})Y'_{s_3}(\Omega_1) - Y'_{s_3}(\Omega_1 e^{\hbar_1 h_1})J'_{s_3}(\Omega_1)\right] \approx \frac{-2\sin\phi_{21}\sin\phi_{22}\sin[s_3(\tan\phi_{21}-\tan\phi_{22}) - s_3(\phi_{21}-\phi_{22})]}{\pi s_3\sqrt{\tan\phi_{21}\tan\phi_{22}}},$$

$$\left[J'_{s_4}(\Omega_2 e^{-\hbar_2 h_2})Y'_{s_4}(\Omega_2) - Y'_{s_4}(\Omega_2 e^{-\hbar_2 h_2})J'_{s_4}(\Omega_2)\right] \approx \frac{-2\sin\phi_{23}\cos[s_4(\tan\phi_{23}-\tan\phi_{24}) - s_4(\phi_{23}-\phi_{24})]}{\pi s_4\sqrt{\tan\phi_{23}\tan\phi_{24}}},$$

$$s_3\sec\varphi_{21} = \frac{kc}{\hbar_1\beta_1^{(3)}}e^{\hbar_1 h_1}, \quad s_3\sec\varphi_{22} = \frac{kc}{\hbar_1\beta_1^{(3)}},$$

$$s_3\tan\varphi_{21} = \frac{k}{\hbar_1}\sqrt{\frac{c^2}{(\beta_1^{(3)})^2} - 1 + \zeta_1^{(3)}}\left[1 - \frac{c^2\hbar_1 h_1}{c^2 - (\beta_1^{(3)})^2}\right],$$

$$s_3\tan\phi_{22} = \frac{k}{\hbar_1}\sqrt{\frac{c^2}{\left(\beta_1^{(3)}\right)^2} - 1 + \zeta_1^{(3)}},$$

$$(\phi_{21}-\phi_{22}) \sim \hbar_1 h_1\frac{\sqrt{1-\zeta_1^{(3)}}}{\sqrt{\frac{c^2}{(\beta_1^{(3)})^2} - 1 + \zeta_1^{(3)}}},$$

$$s_3(\tan\phi_{21}-\tan\phi_{22}) - s_3(\phi_{21} - \phi_{22}) \sim kh_1\sqrt{\frac{c^2}{(\beta_1^{(3)})^2} - 1 + \zeta_1^{(3)}},$$

$$\sin\phi_{21} \sim \frac{\beta_1^{(3)}}{c}\sqrt{\frac{c^2}{(\beta_1^{(3)})^2} - 1 + \zeta_1^{(3)}} \sim \sin\phi_{22},$$

$$s_4\sec\phi_{23} = \frac{kc}{\hbar_2\beta_2^{(3)}}e^{\hbar_2 h_2}, \quad s_4\sec\phi_{24} = \frac{kc}{\hbar_2\beta_2^{(3)}},$$

$$s_4\tan\phi_{23} = \frac{k}{\hbar_2}\sqrt{\frac{c^2}{(\beta_2^{(3)})^2} - 1 + \zeta_2^{(3)}},$$

$$s_4\tan\phi_{24} = \frac{k}{\hbar_2}\sqrt{\frac{c^2}{(\beta_2^{(3)})^2} - 1 + \zeta_2^{(3)}}\left[1 + \frac{c^2\hbar_2 h_2}{c^2 - (\beta_2^{(3)})^2}\right],$$

$$(\phi_{23}-\phi_{24}) \sim \hbar_2 h_2\frac{\sqrt{1-\zeta_2^{(3)}}}{\sqrt{\frac{c^2}{(\beta_2^{(3)})^2} - 1 + \zeta_2^{(3)}}}, s_4(tan\phi_{23} - tan\phi_{24}) - s_4(\phi_{23}-\phi_{24}) \sim \hbar_2 h_2\sqrt{\frac{c^2}{\left(\beta_2^{(3)}\right)^2} - 1 + \zeta_2^{(3)}},$$

and $\sin\phi_{23} \sim \frac{\beta_2^{(3)}}{c}\sqrt{\frac{c^2}{(\beta_2^{(3)})^2} - 1 + \zeta_2^{(3)}} \sim \sin\phi_{24}.$

Appendix IV

$$\begin{aligned}
R_{23} &= I_0'\{t_1(1-\varepsilon_1 h_1)/i\varepsilon_1\}K_0'(t_1/i\varepsilon_1) - K_0'\{t_1(1-\varepsilon_1 h_1)/i\varepsilon_1\}I_0'(t_1/i\varepsilon_1),\\
R_{24} &= I_0'\{t_1(1-\varepsilon_1 h_1)/i\varepsilon_1\}K_0(t_1/i\varepsilon_1) - K_0'\{t_1(1-\varepsilon_1 h_1)/i\varepsilon_1\}I_0(t_1/i\varepsilon_1),\\
R_{25} &= I_0'\{t_2(1+\varepsilon_2 h_2)/i\varepsilon_2\}K_0'(t_2/i\varepsilon_2) - K_0'\{t_2(1+\varepsilon_2 h_2)/i\varepsilon_2\}I_0'(t_2/i\varepsilon_2),\\
R_{26} &= I_0\{t_2(1+\varepsilon_2 h_2)/i\varepsilon_2\}K_0'(t_2/i\varepsilon_2) - K_0\{t_2(1+\varepsilon_2 h_2)/i\varepsilon_2\}I_0'(t_2/i\varepsilon_2),\\
R_{27} &= I_0'\{t_2(1+\varepsilon_2 h_2)/i\varepsilon_2\}K_0(t_2/i\varepsilon_2) - K_0'\{t_2(1+\varepsilon_2 h_2)/i\varepsilon_2\}I_0(t_2/i\varepsilon_2),\\
R_{28} &= I_0\{t_2(1+\varepsilon_2 h_2)/i\varepsilon_2\}K_0(t_2/i\varepsilon_2) - K_0\{t_2(1+\varepsilon_2 h_2)/i\varepsilon_2\}I_0(t_2/i\varepsilon_2),\\
R_{29} &= J_0'(t_1/\varepsilon_1)Y_0'\{t_1(1-\varepsilon_1 h_1)/\varepsilon_1\} - J_0'\{t_1(1-\varepsilon_1 h_1)/\varepsilon_1\}Y_0'(t_1/\varepsilon_1),\\
R_{30} &= J_0'\{t_1(1-\varepsilon_1 h_1)/\varepsilon_1\}Y_0(t_1/\varepsilon_1) - J_0(t_1/\varepsilon_1)Y_0'\{t_1(1-\varepsilon_1 h_1)/\varepsilon_1\},\\
R_{31} &= J_0'(t_2/\varepsilon_2)Y_0'\{t_2(1+\varepsilon_2 h_2)/\varepsilon_2\} - J_0'\{t_2(1+\varepsilon_2 h_2)/\varepsilon_2\}Y_0'(t_2/\varepsilon_2),\\
R_{32} &= J_0\{t_2(1+\varepsilon_2 h_2)/\varepsilon_2\}Y_0'(t_2/\varepsilon_2) - J_0'(t_2/\varepsilon_2)Y_0\{t_2(1+\varepsilon_2 h_2)/\varepsilon_2\},\\
R_{33} &= J_0'\{t_2(1+\varepsilon_2 h_2)/\varepsilon_2\}Y_0(t_2/\varepsilon_2) - J_0(t_2/\varepsilon_2)Y_0'\{t_2(1+\varepsilon_2 h_2)/\varepsilon_2\},\\
R_{34} &= J_0\{t_2(1+\varepsilon_2 h_2)/\varepsilon_2\}Y_0(t_2/\varepsilon_2) - J_0(t_2/\varepsilon_2)Y_0\{t_2(1+\varepsilon_2 h_2)/\varepsilon_2\},
\end{aligned}$$

References

Achenbach JD (1973) Wave propagation in elastic solids. North Holland Publishing Co., NewYork

Bath MA (1968) Mathematical aspects of seismology. Elsevier Publishing Co., New York

Bhattacharya J (1962) On the dispersion curve for Love wave due to irregularity in the thickness of the transversely isotropic crustal layer. Gerlands Beitr Geophys 6:324–334

Bhattacharya J (1969) The possibility of the propagation of Love type waves in an intermediate heterogeneous layer lying between two semi-infinite isotropic homogeneous elastic layers. Pure Appl Geophys 72(1):61–71

Biot MA (1940) The influence of initial stress on elastic waves. J Appl Phys 11(8):522–530

Biot MA (1963) Surface instability in finite anisotropic elasticity under initial stress. Proceed R Soc Lond A Math Phys Eng Sci 273:329–339

Biot MA (1965) Mechanics of incremental deformations. John Wiley and Sons Inc., New York

Bullen KE (1940) The problem of the Earth's density variation. Bull Seismol Soc Am 30:235–250

Bullen KE (1963) An introduction to the theory of seismology. Cambridge University Press, Cambridge

Carcione JM (1992) Modeling anelastic singular surface waves in the Earth. Geophysics 57:781–792

Chatterjee M, Dhua S, Chattopadhyay A, Sahu SA (2016) Seismic waves in heterogeneous crustmantle layers under initial stresses. J Earthquake Eng 20(1):39–61

Chattopadhyay A (1975) On the propagation of Love types waves in an intermediate non-homogeneous layer lying between two semi-infinite homogeneous elastic media. Gerlands Beitr Geophys 84(3–4):327–334

Chattopadhyay A, Gupta S, Sharma VK, Kumari P (2010) Propagation of Shear waves in viscoelastic medium at irregular boundaries. Acta Geophys 58(2):195–214

Dey S, Addy SK (1978) Love waves under initial stresses. Acta Geophys Polonica 26(1):7

Ewing WM, Jardetzky WS, Press F, Beiser A (1957) Elastic waves in layered media. Phys Today 10:27

Gibson RE (1967) Some results concerning displacements and stresses in a non-homogeneous elastic half-space. Geotechnique 17(1):58–67

Gubbins D (1990) Seismology and Plate Tectonics. Cambridge University Press, Cambridge

Kar BK (1977) On the propagation of Love type waves in a non-homogeneous internal stratum of finite thickness lying between two semi-infinite isotropic elastic media Gerlands Beitr. Geophys Leipz 86(5):407–412

Kumari N, Anand Sahu S, Chattopadhyay A, Kumar Singh A (2015) Influence of heterogeneity on the propagation behavior of love-type waves in a layered isotropic structure. Int J Geomech 16(2):04015062

Kumari P, Kumar Sharma V, Modi C (2016) Modeling of magnetoelastic shear waves due to point source in a viscoelastic crustal layer over an inhomogeneous viscoelastic half space. Waves Random Compl Media 26(2):101–120

Kumari N, Chattopadhyay A, Kumar Singh A, Anand Sahu S (2017) Magnetoelastic shear wave propagation in pre-stressed anisotropic media under gravity. Acta Geophys. https://doi.org/10.1007/s11600-017-0016-y

Mal AK (1962) On the frequency equation for Love waves due to abrupt thickening of the crustal layer. Geofis Pura e Appl 52(1):59–68

Pilant WL (1979) Elastic waves in the Earth, Vol. 11 of developments in solid earth geophysics. Series

Pujol J (2003) Elastic wave propagation and generation in seismology. Cambridge University Press, Cambridge

Sahu SA, Saroj PK, Dewangan N (2014) SH-waves in viscoelastic heterogeneous layer over half space with self weight. Arch Appl Mech 84(2):235–245

Sato Y (1952) Love waves propagated upon heterogeneous medium. Bull Earthq Res Inst Univ Tokyo 30:1–12

Singh BM, Singh SJ, Chopra SD, Gogna ML (1976) On love waves in laterally and vertically heterogeneous layered media. Geophys J Int 45(2):357–370

Singh AK, Das A, Chattopadhyay A, Dhua S (2015) Dispersion of shear wave propagating in vertically heterogeneous double layers overlying an initially stressed isotropic half-space. Soil Dyn Earthq Eng 6(9):16–27

Sinha NK (1967) Propagation of Love waves in a non-homogeneous stratum of finite depth sandwiched between two semi-infinite isotropic media. Pure Appl Geophys 67(1):65–70

Watson GN (1958) A treatise on the theory of Bessel functions. Cambridge University Press, New York

Acta Geophysica (2018) 66:21–38
https://doi.org/10.1007/s11600-017-0103-0

RESEARCH ARTICLE - APPLIED GEOPHYSICS

Comparison of SPT and V_s-based liquefaction analyses: a case study in Erciş (Van, Turkey)

İsmail Akkaya[1] · Ali Özvan[2] · Mutluhan Akin[3] · Müge K. Akin[4] · Uğur Övün[2]

Received: 4 June 2017 / Accepted: 1 December 2017 / Published online: 8 December 2017

Abstract
Liquefaction which is one of the most destructive ground deformations occurs during an earthquake in saturated or partially saturated silty and sandy soils, which may cause serious damages such as settlement and tilting of structures due to shear strength loss of soils. Standard (SPT) and cone (CPT) penetration tests as well as the shear wave velocity (V_s)-based methods are commonly used for the determination of liquefaction potential. In this research, it was aimed to compare the SPT and V_s-based liquefaction analysis methods by generating different earthquake scenarios. Accordingly, the Erciş residential area, which was mostly affected by the 2011 Van earthquake ($M_w = 7.1$), was chosen as the model site. Erciş (Van, Turkey) and its surroundings settle on an alluvial plain which consists of silty and sandy layers with shallow groundwater level. Moreover, Çaldıran, Erciş–Kocapınar and Van Fault Zones are the major seismic sources of the region which have a significant potential of producing large magnitude earthquakes. After liquefaction assessments, the liquefaction potential in the western part of the region and in the coastal regions nearby the Lake Van is found to be higher than the other locations. Thus, it can be stated that the soil tightness and groundwater level dominantly control the liquefaction potential. In addition, the lateral spreading and sand boiling spots observed after the 23rd October 2011 Van earthquake overlap the scenario boundaries predicted in this study. Eventually, the use of V_s-based liquefaction analysis in collaboration with the SPT results is quite advantageous to assess the rate of liquefaction in a specific area.

Keywords Liquefaction · SPT · Shear wave velocity (V_s) · LPI · LSI · Erciş

Introduction

In addition to the structural quality, surface deformations (liquefaction, lateral spreading, etc.) which occur due to adverse soil properties, have a significant role in the loss of life and property during earthquakes. Liquefaction occurs as a result of earthquakes in loose sandy, silty soils and areas with shallow groundwater level. Pore water pressure between the soil particles increases due to earthquake waves during liquefaction. Once, the pore water pressure and the total stress are equal, the frictional force between the soil particles, in other words, the effective stress reaches to zero. Thus, bearing capacity and sudden settlement problems occur in the foundation ground and there may be significant structural problems such as overturning of structures. Liquefaction is mostly observed after moderate to high magnitude earthquakes. It is very important to determine the liquefaction potential of the ground under dynamic loads to prevent damage due to liquefaction.

Following the 1964 earthquake in Japan, lots of studies have been carried out to explain soil liquefaction. Shear wave velocity measurements, CPT and SPT, have been used by many researchers for determining the liquefaction potential of soils (Seed and Idriss 1971; Dobry et al. 1982; Iwasaki et al. 1982; Tokimatsu and Yoshimi 1983; Ishihara 1996; Kramer 1996; Robertson and Wride 1998; Juang et al. 2003; Cetin et al. 2004; Idriss and Boulanger

✉ İsmail Akkaya
iakkaya@yyu.edu.tr; iakkaya79@gmail.com

[1] Department of Geophysical Engineering, Engineering Faculty, Van Yüzüncü Yıl University, 65080 Van, Turkey

[2] Department of Geological Engineering, Van Yüzüncü Yıl University, Van, Turkey

[3] Department of Geological Engineering, Nevşehir Hacı Bektaş Veli University, Nevşehir, Turkey

[4] Department of Civil Engineering, Abdullah Gül University, Kayseri, Turkey

2006, 2008; Yi 2010). In addition, Andrus and Stokoe (2000), Uyanık (2002), Uyanik and Taktak (2009), Uyanik et al. (2013a) developed liquefaction analysis methods that depend upon the S wave velocity. Several empirical formulas were developed to determine the liquefaction potential using SPT-N values and V_s data using Seed and Idriss (1971) method (Dikmen 2009; Akın et al. 2011; Hasançebi and Ulusay 2007). V_s which is an important parameter used in earthquake engineering, is mainly used for determining the dynamic properties and liquefaction potential of soils (Karastathis et al. 2002; Soupios et al. 2005; Uyanık et al. 2006; Tezcan et al. 2006; Bozcu et al. 2007; Dadashpour et al. 2009; Uyanık and Ulugergerli 2008; Uyanik 2010, 2011; Uyanik et al. 2013b).

The SPT-N and V_s values are important physical parameters that may vary depending on porosity, effective stress, and relative density. V_s velocity is considered to be an easy and fast method as it can be applied both in the field and in the laboratory. In particular, liquefaction analysis based on V_s data, which can be easily obtained in environments where the SPT and CPT measurements cannot be performed, has been frequently used in recent years (Dobry et al. 1981b; Seed et al. 1983; Tokimatsu and Uchida 1990; Kayen et al. 1992; Andrus and Stokoe 2000; Uyanık 2002, 2006; Uyanik and Taktak 2009; Uyanik et al. 2013a; Duman and Ikizler 2014; Pekkan et al. 2015).

The liquefaction analysis methods based on SPT and laboratory data are frequently used. The studies in which liquefaction analysis methods based on SPT and V_s wave velocities coexist are limited.

In this study, Erciş (Van, Turkey) settlement area, which is under the effect of three different major fault zones, is selected as the study location. Erciş residential area is the largest district of the region located at the north of Lake Van, with more than 150,000 inhabitants (Fig. 1). A catastrophic earthquake of 7.1(M_w) shook the study area on 23rd October, 2011 at 13:41 local time (KOERI 2011). As a result of this earthquake, lateral spreading and liquefaction occured in the Erciş settlement area and in the close vicinity (Akın et al. 2013, 2015a, b; Aydan et al. 2012, 2013). The earthquake heavily damaged hundreds of buildings in Van and Erciş city, rendering them unusable. The Erciş settlement is classified in the first-degree seismic hazard zone of Turkey (ABYYHY 1997).

In this study, the grain size distribution of recent loose sediments and the presence of groundwater as well as the seismicity of the region were jointly investigated to determine the liquefaction potential of the subsurface soil. Liquefaction analysis was conducted using the V_s velocities and SPT-N values. Moreover, the advantages and disadvantages of these methods were highlighted by performing liquefaction analyses using both SPT and V_s data in a model area. Four different methodologies (SPT-based LPI and LSI, V_s-based threshold acceleration and safety factor) used for the assessment of liquefaction potential were taken into consideration. Moreover, the results of both methods were compared. Additionally, the liquefaction potential of the study area was determined on the basis of different magnitude earthquakes using the seismic data complied from 21 different sites along with the SPT values collected from a total of 165 different boreholes (Fig. 1). Finally, maps presenting the liquefaction potential were prepared and the results of the analyses were discussed. Different earthquake scenarios for three different active faults that can produce large earthquakes in the selected area were considered in these analyses.

Geology of the study area

The Lake Van basin, involving the Erciş settlement, consists of Late Cretaceous ophiolites and Tertiary marine sediments (Fig. 2a). A number of dissimilar rock masses and alluvium are traced in some locations of the Lake Van as shown in the geological map illustrated in Fig. 2b.

The Erciş province and its surroundings consist of three main geological units which are the basement rocks of the Erciş region. The limestone unit which is also known as the Lower Miocene aged Adilcevaz limestone, Pliocene–Pleistocene aged volcanics and volcano-sedimentary clasts and Quaternary–Holocene aged recent, and old alluviums and old lake sediments are the major geological units in the study area (Fig. 2). Volcanism occurred in various stages from Pliocene to Quaternary with different volcanic units in the region (Özdemir et al. 2006, 2016; Özdemir and Güleç 2014; Oyan et al. 2016). Erciş settlement is covered by old alluvial deposits of Quaternary age and the recent alluvium around Zilan Creek with Holocene age. This unit is comprised of loose and soft clay, sand, silt and gravels.

The groundwater level is shallow particularly around the Lake Van considering the borehole data (Fig. 3). While the groundwater level in the study area is generally observed after 5 m in old lake sediments, it is shallower than 5 m in the coastal sections of Lake Van and around Zilan Creek in recent alluvial deposits (Özvan et al. 2008; Akın et al. 2015a, b) (Fig. 3).

Seismic characteristics of the region

Erciş and its surroundings is located in the Lake Van basin at the Eastern Anatolian Plateau, that was formed due to the collision of Arabian and Eurasian Plates in Late Miocene (Şengör and Yılmaz 1981; Şengör and Kidd 1979; Koçyiğit et al. 2001). Attributable to these crustal movements, north–south direction compression in the region,

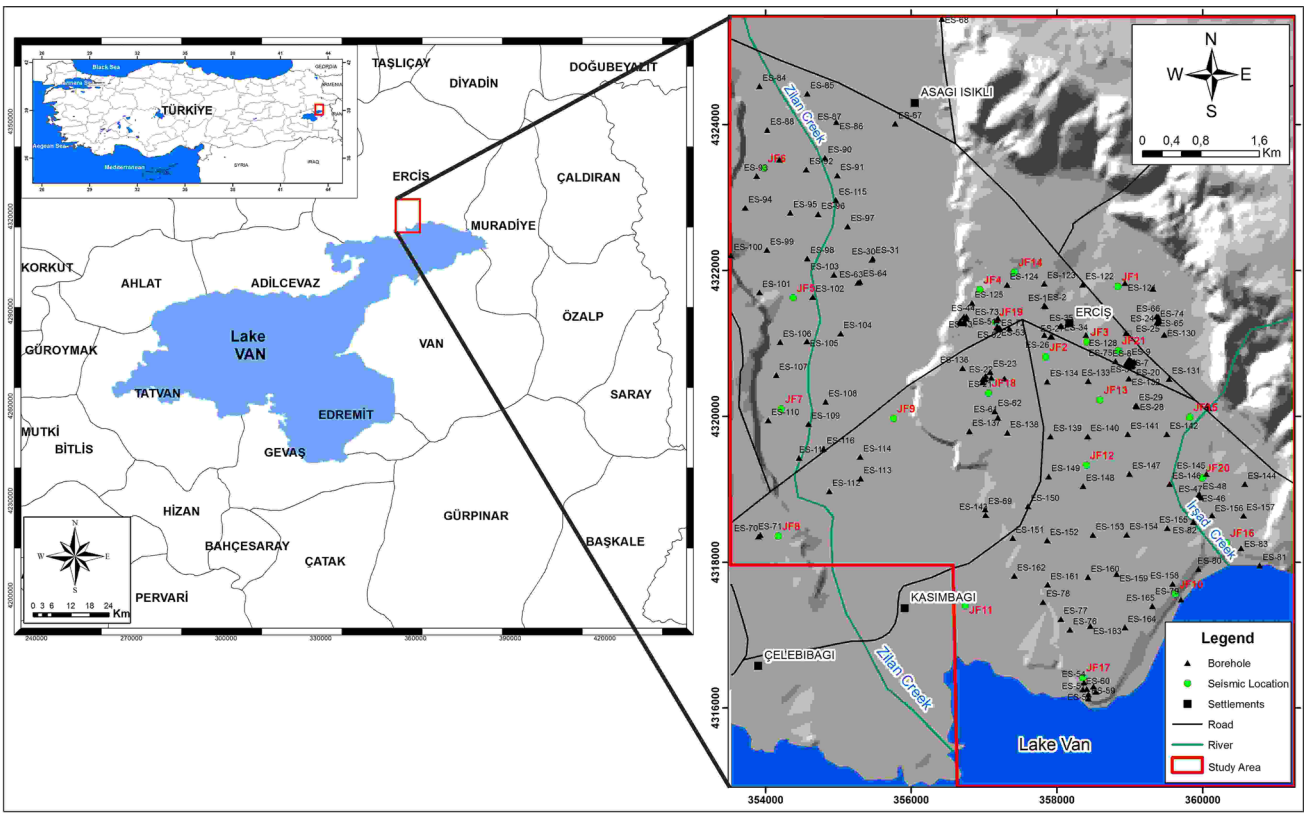

Fig. 1 Location map of the study area

east–west trending reverse faults and main folding axis and northeast–southwest left-lateral and northwest–southeast right-lateral strike-slip faults and north–south trending normal faults were developed (Şaroğlu and Yılmaz 1986; Koçyiğit et al. 2001; Bozkurt 2001; Koçyiğit 2013). The activity of all these tectonic structures supports the ongoing seismic activity in the region (Fig. 4, Table 1).

The Lake Van basin and its surrounding area has a very complex seismotectonic setting and active fault zones, such as Çaldiran fault zone, Çolpan fault, Erciş–Kocapınar fault zone, Süphan fault, Everek fault, Alaköy fault, Özalp fault, Gürpınar fault zone and Van thrust fault (Koçyiğit 2013; Selçuk 2016) (Fig. 4). Numerous devastating earthquakes have been documented around the Lake Van basin in the last century, such as 1941 Erciş ($M_s = 5.9$); 1945 Van ($M_s = 5.8$); 1966 Varto ($M_s = 6.8$); 1903 Malazgirt ($M_s = 6.3$); 1976 Çaldıran ($M_s = 7.3$); 2011 Van ($M_w = 7.1$) and 2011 Van ($M_w = 5.6$) earthquakes (Ambraseys 2001; Koçyiğit 2013). Erciş–Kocapınar Fault, Çaldıran Fault and Van Fault are important fault zones that can adversely affect the study area.

Liquefaction analyses

In the study area, liquefaction analyses were carried out according to different liquefaction analysis methods as well as dissimilar magnitude and acceleration values that can be produced by three different active faults. Experimental data of 165 boreholes drilled in the study area were used to evaluate Liquefaction Potential (LPI) and Liquefaction Severity (LSI) Index (Table 2). LPI (Iwasaki et al. 1982) and LSI (Sonmez and Gokceoglu 2005) values were calculated using the liquefaction safety factor of every geotechnical borehole. Idriss and Boulanger (2008) method, which depends on the ratio between cyclic stress ratio (CSR) and cyclic resistance ratio (CRR), was utilized for the determination of safety factor against liquefaction.

It is inevitable to use V_s as a parameter for the determination of liquefaction resistance. In this sense, seismic surface wave measurements (MASW) were performed at 21 points in the study area (Table 3). In this study, liquefaction analyses based on calculated V_s values and geotechnical data were performed.

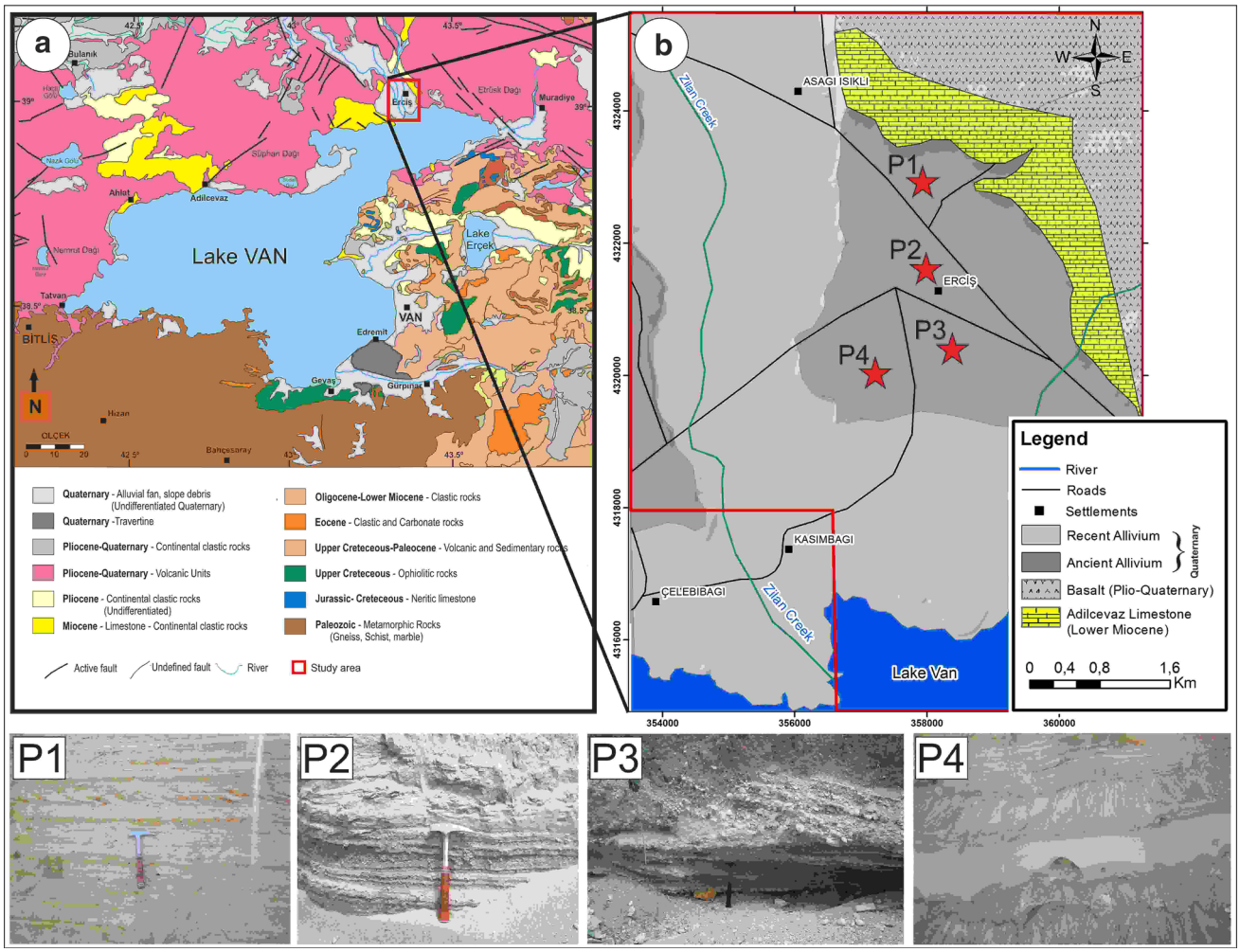

Fig. 2 The general geological map of Lake Van basin (modified from MTA, 2007) (**a**), geological map of Erciş (**b**) (Picture 1, 2, 3 and 4 refers to Quaternary aged alluvium units)

Calculated LPI, LSI, V_{s30} distribution, liquefaction potential according to threshold acceleration criteria, and safety factor liquefaction potential maps obtained according to V_s velocities were prepared using ArcMap10 Geographic Information Systems software. Inverse Distance Weighting (IDW) statistical method was utilized during the preparation of the maps. IDW interpolation designates cell values using weighted combination of sample points (Watson and Philip 1985).

Attenuation relationship for the determination of peak ground acceleration (a_{max})

In this study, scenario earthquakes were initially designed, and then liquefaction analyses were performed. Equations of liquefaction analyses are highly dependent on the peak ground acceleration (a_{max}) which is an important parameter for the scenario earthquakes.

In the liquefaction analyses based on SPT and V_s, active faults that may affect and/or affected the Erciş settlement area and the largest earthquakes that occurred in the region were considered. As a result of these analyses, magnitude (M), distance (R) and acceleration calculations were performed for three different active faults (Erciş–Kocapınar, Çaldıran and Van fault) that can adversely affect the study area (Table 4, Fig. 5). Major earthquakes that hit the region were gathered from the Kandilli Observatory and Earthquake Research Institute (KOERI) earthquake data. Each earthquake was expressed in terms of M_w using the magnitude conversion relations suggested by Kadirioğlu and Kartal (2016) after determining the largest earthquakes that occurred on three active faults (Table 4). Kadirioğlu and Kartal (2016) proposed M_S to M_w conversion as follows;

$$\begin{aligned} M_w &= 0.5716\,(\pm 0.024927)\,M_s \\ &\quad + 2.4980\,(\pm 0.117197) \qquad 3.4 \le M_s \le 5.4 \\ M_w &= 0.8126\,(\pm 0.034602)\,M_s \\ &\quad + 1.1723\,(\pm 0.208173) \qquad M_s \ge 5.5. \end{aligned} \tag{1}$$

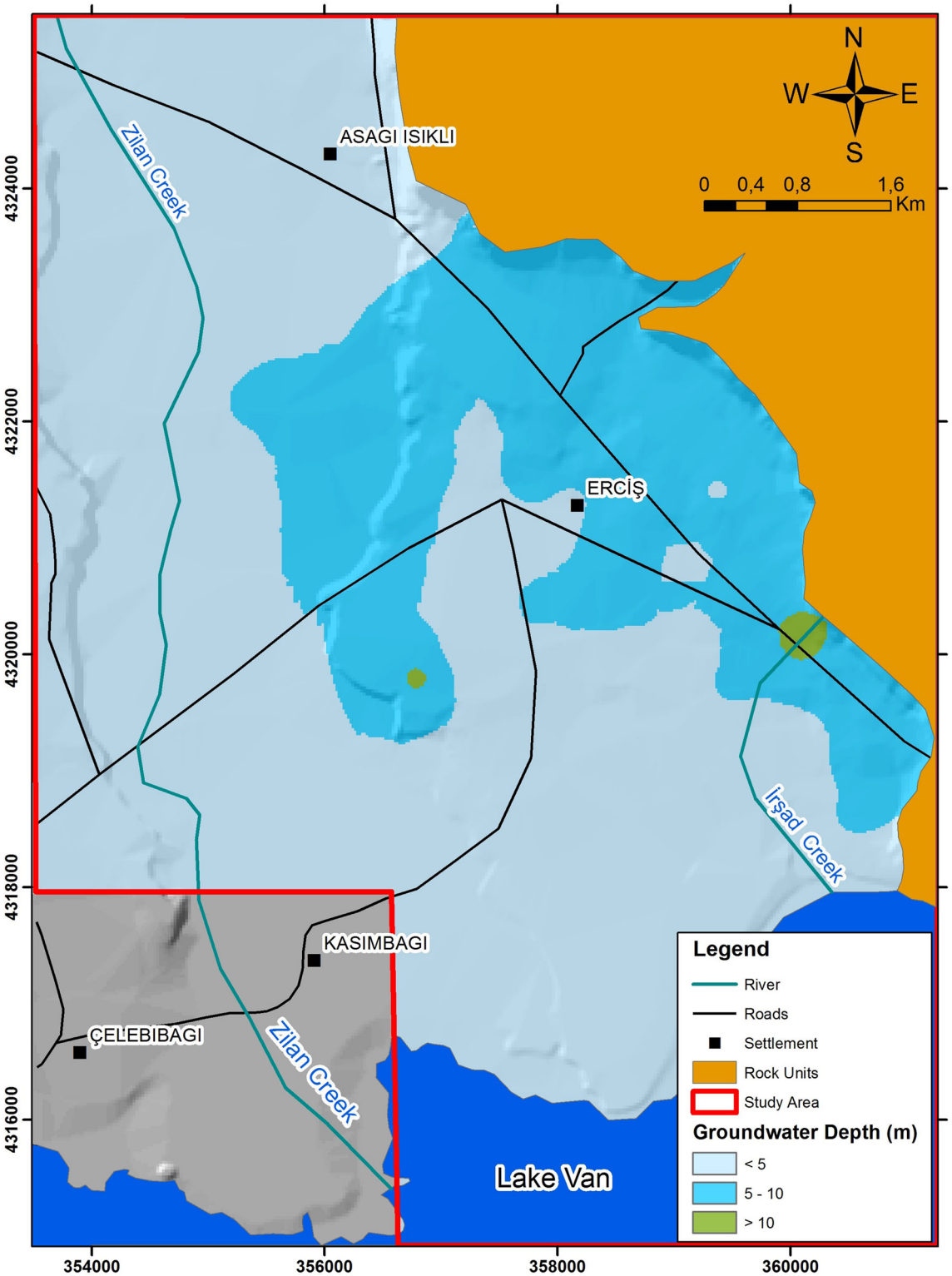

Fig. 3 Depth to groundwater level map of the study area

Using the magnitude and distance parameters obtained from the analyses, accelerations were calculated with the ground motion prediction model proposed by Graizer and Kalkan (2015). The obtained data were used as scenario earthquakes in SPT and V_s-based liquefaction analyses. Ground motion prediction equation (GMPE) developed by Graizer and Kalkan (2015) is as follows;

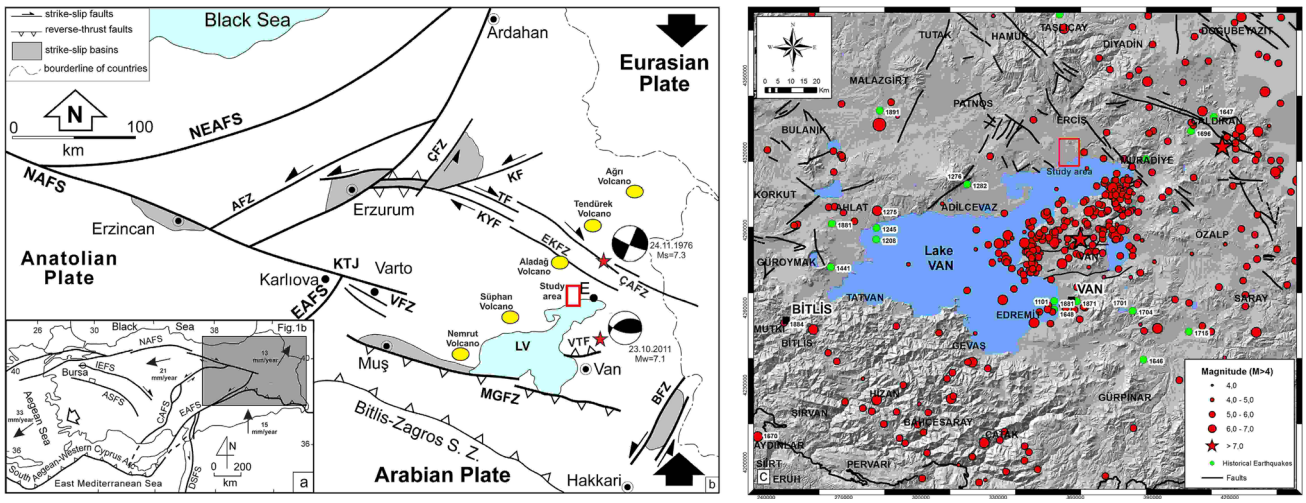

Fig. 4 **a** Tectonic map of Turkey. **b** Simplified tectonic map of Eastern Anatolia (*AFZ* Aşkale fault zone, *BFZ* Başkale fault zone, *ÇFZ* Çobandede fault zone, *ÇAFZ* Çaldıran fault zone, *EAFS* East Anatolian fault zone, *EKFZ* Erciş–Kocapınar fault zone, *NAFS* North Anatolian fault zone, *KF* Kağızman fault zone, *MGFZ* Muş–Gevaş thrust to reverse fault zone, *TF* Tutak fault, *VTF* Van thrust fault, VFZ: Varto fault zone) (modified from Koçyiğit, 2013) **c** the distribution of earthquakes ($M > 4.0$) around the Lake Van

$$\ln(Y) = \ln(G_1) + \ln(G_2) + \ln(G_3) + \ln(G_4) + \ln(G_5) + \sigma_{\ln(\mathrm{PGA})}, \tag{2}$$

where $\sigma_{\ln(\mathrm{PGA})}$ is the random variability and Y is the PGA. The formulations of G_1, G_2, G_3, G_4, and G_5 are given,

$$\begin{aligned}
\ln(G_1) &= \ln[(c_1 \cdot \arctan(M + c_2) + c_3) \cdot F] \\
\ln(G_2) &= -0.5 \cdot \ln\Big[(1 - R/(c_4.M + c_5))^2 \\
&\quad + 4.(c_6 \cdot \cos[c_7 \cdot (M + c_8)] + c_9)^2 \cdot (R/(c_4 \cdot M + c_5))\Big] \\
\ln(G_3) &= -c_{10} \cdot R/Q_0 \ln(G_4) \\
&= b_v \cdot \ln(V_{s30}/V_A) \ln(G_5) \\
&= \ln\left[1 + A_{B\mathrm{dist}} \cdot A_{B\mathrm{depth}}\right] \\
A_{B\mathrm{depth}} &= 1.077/\sqrt{\left[1 - (1.5/(B_{\mathrm{depth}} + 0.1))^2\right]^2 + 4 \cdot 0.7^2 \cdot (1.5/(B_{\mathrm{depth}} + 0.1))^2} \\
A_{B\mathrm{dist}} &= 1/\sqrt{\left[1 - (40/(R + 0.1))^2\right]^2 + 4 \cdot 0.7^2 \cdot (40/(R + 0.1))^2}
\end{aligned} \tag{3}$$

where M is moment magnitude, F is the style of faulting, and R is the nearest distance to fault rupture plane (km). Q_0 is regional quality factor, and B_{depth} basin depth under the site (km). c_{1-10}, b_v and V_A are coefficients. The model established by Graizer and Kalkan (2015) may be employed for the earthquakes with moment magnitudes of 5.0–8.0, distances from 0 to 250 km, spectral periods of 0.01–5 s and average V_s from 200 to 1300 m/s.

SPT-based liquefaction analyses

Liquefaction analyses were carried out according to the cyclic stress approach. The method proposed by Idriss and Boulanger (2006, 2008) and based on SPT was used in the present research. The liquefaction safety factor is explained as the ratio of the CRR that results in liquefaction for a certain cycle number, to the CSR, generated in the soil as a result of earthquake motion.

During the SPT, the blow counts are highly sensitive to the length of rods, hammer energy, sampler type, borehole diameter and overburden stress (Idriss and Boulanger 2008, 2010). Thus, a corrected penetration resistance is obtained using raw SPT data and a number of correction factors as shown in equation,

$$(N1)_{60} = C_N C_E C_R C_B C_S N_m, \tag{4}$$

where C_N, C_E, C_R, C_B, and C_S are the correction parameters whereas N_m is the SPT blow count obtained in situ (Idriss and Boulanger 2008, 2010).

The safety factor (FS) against liquefaction is determined considering the influence of the magnitude scaling factor (MSF). The corrected SPT-$(N_1)_{60}$ values are taken into consideration in the factor of safety analysis as suggested by Youd et al. (2001) and Idriss and Boulanger (2008).

$$\mathrm{FS} = \frac{\mathrm{CRR}}{\mathrm{CSR}}\,\mathrm{MSF}, \tag{5}$$

FS is the ratio of CRR to CSR, which is an indication of the shear resistance of the soil deposit to liquefaction (CRR) under the influence of the maximum shear stress (CSR) generated by an earthquake. Since the Eq. 5 is appropriate for the magnitude 7.5 earthquakes; a MSF developed by Seed and Idriss (1982) for the earthquakes of diverse magnitudes are used in this study. The soils are assumed to be liquefiable if the safety factor ≤ 1; potentially liquefiable between 1 and 1.2 and non-liquefiable if the safety factor > 1.2 (Seed and Idriss 1982).

Table 1 Major Earthquakes ($M \geq 5$) around the Lake Van between 1900 and 2017 (KOERI http://www.koeri.boun.edu.tr/sismo/2/en/)

Date	Latitude	Longitude	Depth (km)	M	Date	Latitude	Longitude	Depth (km)	M
28.04.1903	39.1	42.5	30	6.3	24.11.1976	39.1	44.2	63	5.5
29.01.1907	39.1	42.5	30	5.2	24.11.1976	39.17	43.95	33	5.1
31.03.1907	39.1	42.5	30	5.4	24.11.1976	39.05	44.04	10	7.3
28.09.1908	38	44	30	6	25.11.1976	38.96	44.28	38	5.1
27.01.1913	38.38	42.23	10	5.5	17.01.1977	39.27	43.7	39	5.3
14.02.1915	38.8	42.5	30	5.7	26.05.1977	38.93	44.38	38	5.4
25.07.1924	38	43	30	5.2	03.12.1984	37.94	43.18	55	5
06.09.1924	39.67	42.81	10	5.2	20.04.1988	39.11	44.12	48	5.1
07.05.1930	38	44.5	30	5.2	25.06.1988	38.5	43.07	49	5.3
08.05.1930	38	44.5	30	5.5	03.06.1991	40.04	42.85	28	5
10.05.1930	37.55	44.25	10	5.2	14.02.1995	37.75	42.96	0	5.4
23.05.1930	38	44.5	30	5.4	15.11.2000	38.28	42.94	8	5.2
29.05.1930	38	44.5	30	5.6	01.07.2004	39.63	43.94	10	5.4
09.07.1930	38	44.5	30	5.2	25.01.2005	37.57	43.68	22	5.9
03.08.1930	38.46	44.7	80	5.3	21.01.2007	39.60	42.82	5	5.1
15.03.1932	39.7	44	15	5.5	23.10.2011	38.63	43.08	5	5.9
18.08.1935	39.6	43.1	30	5.3	23.10.2011	38.70	43.29	2.1	5.1
01.05.1936	39.6	43.1	30	5.7	23.10.2011	38.80	43.25	5	5.7
02.05.1936	39.8	43.5	30	5.3	23.10.2011	38.69	43.04	4.4	5.2
18.10.1940	39.6	42.2	15	5.7	23.10.2011	38.81	43.44	5	5.6
10.09.1941	39.45	43.32	20	5.9	23.10.2011	38.75	43.59	9	5.1
15.01.1945	38.4	44.2	32	5.3	23.10.2011	38.72	43.41	5	7.1
29.07.1945	38	43	30	5.2	24.10.2011	38.73	43.28	5	5
20.11.1945	38.63	43.33	10	5.4	25.10.2011	38.72	43.56	5.2	5.6
03.10.1946	39.5	44.12	50	5.2	27.10.2011	37.20	44.08	10	5.4
19.04.1947	37.8	43.31	40	5.3	29.10.2011	38.89	43.55	10	5.1
04.09.1962	39.96	44.13	40	5.5	08.11.2011	38.72	43.08	6	5.4
27.04.1966	38.14	42.52	28	5.2	09.11.2011	38.42	43.21	6	5.6
02.05.1966	38.1	42.5	50	5	14.11.2011	38.69	43.16	8	5.3
17.05.1967	38.69	44.29	54	5	18.11.2011	38.82	43.83	5	5
29.04.1968	39.24	44.23	17	5.6	30.11.2011	38.47	43.43	4.1	5
11.06.1968	38.15	42.85	53	5.1	26.03.2012	39.16	42.32	5	5
16.07.1972	38.23	43.86	46	5	14.06.2012	37.24	42.42	5	5.5
24.11.1976	39.08	44.13	55	5	05.08.2012	37.41	42.95	8.1	5.4
24.11.1976	39	44.19	62	5					

The liquefaction resistance of soils is represented by the CRR following some essential corrections. The CRR of a soil is affected by the duration time of earthquake as well as the effective overburden stress which is expressed by a K_σ factor. The K_σ is commonly small for shallow ground conditions (Idriss and Boulanger 2008, 2010).

CRR is required to determine the liquefaction safety factor and is calculated as a function of SPT values (Seed and Idriss 1982; Seed et al. 1983; Idriss and Boulanger 2008). Idriss and Boulanger (2008, 2010) expressed the subsequent formula for the determination of CRR, corrected for overburden pressure and magnitude.

$$\mathrm{CRR}_{\sigma=1} = \exp\left(\left(\frac{(N_1)_{60\mathrm{cs}}}{14.1}\right) + \left(\frac{(N_1)_{60\mathrm{cs}}}{126}\right)^2 - \left(\frac{(N_1)_{60\mathrm{cs}}}{23.6}\right)^3 + \left(\frac{(N_1)_{60\mathrm{cs}}}{25.4}\right)^4 - 2.8\right)$$
$$(N1)_{60\mathrm{cs}} < 37.5 \ \mathrm{CRR}_{\sigma=1,M=7.5} = 2 \qquad (N1)_{60\mathrm{cs}} > 37.5 \,. \tag{6}$$

The following methods for the calculation of CRR are for $\mathrm{CRR}_{7.5}$ and K_σ correction factors should still be applied.

$$\mathrm{CRR} = \mathrm{CRR}_{7.5} K_\sigma \tag{7}$$

Table 2 The utilized data of the geotechnical boreholes within the study area

Borehole no	Coordinate		Depth (m)	Groundwater Level	*Average SPT-N	Borehole no	Coordinate		Depth (m)	Groundwater Level	*Average SPT-N	Borehole no	Coordinate		Depth (m)	Groundwater level	*Average SPT-N
	X	*Y*					*X*	*Y*					*X*	*Y*			
ES-1	357838	4321511	15	9	32	ES-56	358498	4316294	24	2.5	20	ES-111	354458	4319433	20	1	34
ES-2	357826	4321522	10	9	33	ES-57	358429	4316189	24	2.5	24	ES-112	354874	4318973	35	0.5	49
ES-3	358992	4320777	16	5	36	ES-58	358532	4316223	27	2	28	ES-113	355303	4319146	20	0.7	16
ES-4	359014	4320764	15	5	40	ES-59	358430	4316130	27	2	28	ES-114	355300	4319447	25	1	37
ES-5	359029	4320754	15	5	40	ES-60	358354	4316255	20	1.5	31	ES-115	354962	4322970	30	1	43
ES-6	359059	4320749	15	5	40	ES-61	357188	4319984	15	4.5	46	ES-116	354796	4319557	30	1	19
ES-7	358954	4320732	20	4.5	46	ES-62	357145	4320071	15	4.5	48	ES-117	356980	4320512	20	5	21
ES-8	358967	4320752	17	4.5	44	ES-63	355267	4321835	15	4.5	43	ES-118	356980	4320471	20	5	21
ES-9	358985	4320775	20	4.5	40	ES-64	355297	4321846	15	4.5	53	ES-119	357015	4320509	20	5	26
ES-10	358969	4320717	18	4.7	37	ES-65	359367	4321371	15	2	37	ES-120	359316	4321752	20	10	25
ES-11	358985	4320738	19	4.7	44	ES-66	359394	4321364	15	2	38	ES-121	358931	4321831	25	8	19
ES-12	359003	4320760	20	5	46	ES-67	355779	4324017	15	2	47	ES-122	358350	4321809	20	8	35
ES-13	358992	4320702	19	5	45	ES-68	356419	4325453	15	2.5	46	ES-123	357826	4321823	25	8	18
ES-14	359006	4320722	20	4.7	44	ES-69	357014	4318726	15	4	31	ES-124	357315	4321804	20	3	22
ES-15	359018	4320747	18	5	42	ES-70	353901	4318353	15	4.5	35	ES-125	356833	4321555	25	10	20
ES-16	359009	4320692	18	5	44	ES-71	353925	4318379	15	4.5	37	ES-126	357348	4321207	25	2	18
ES-17	359021	4320713	19	5	44	ES-72	357191	4321344	15	4	29	ES-127	357827	4321115	20	2	21
ES-18	359036	4320737	18	5	42	ES-73	357170	4321320	15	4	31	ES-128	358396	4321116	22	8	30
ES-19	359025	4320683	20	5	44	ES-74	359374	4321294	10	8.5	49	ES-129	358946	4321140	20	8	24
ES-20	359042	4320703	19	5	41	ES-75	358801	4320760	10	9	49	ES-130	359472	4321121	15	10	22
ES-21	357020	4320555	15	4.5	42	ES-76	358178	4317074	40	1	28	ES-131	359538	4320512	25	10	28
ES-22	357099	4320532	15	4.5	41	ES-77	358051	4317219	20	1.5	27	ES-132	358984	4320520	25	7	19
ES-23	357079	4320608	10	4.5	40	ES-78	357808	4317454	20	0.8	29	ES-133	358427	4320486	30	7	35
ES-24	359376	4321288	10	9	41	ES-79	359702	4317488	20	0.8	18	ES-134	357865	4320478	25	6	18
ES-25	359406	4321313	10	9	44	ES-80	359940	4317906	20	0.2	18	ES-135	357278	4320522	20	3	16
ES-26	357928	4321091	15	4.5	38	ES-81	360781	4317956	20	0.8	24	ES-136	356704	4320663	20	6	15
ES-27	357910	4321092	10	4.5	34	ES-82	359872	4318550	20	2.2	22	ES-137	356795	4319798	20	11	22
ES-28	359096	4320136	10	2.5	39	ES-83	360527	4318194	40	2	25	ES-138	357317	4319777	20	3.5	21
ES-29	359082	4320147	10	2.5	42	ES-84	353917	4324531	30	0.5	45	ES-139	357912	4319726	20	3	21
ES-30	355460	4322150	10	9	54	ES-85	354573	4324427	20	1	38	ES-140	358420	4319727	25	1.5	21
ES-31	355468	4322168	10	9	49	ES-86	354969	4324036	30	1	32	ES-141	358970	4319757	35	0.5	21
ES-32	360084	4320111	15	11	43	ES-87	354670	4323997	20	0.5	46	ES-142	359508	4319756	20	6	21
ES-33	360064	4320151	11	11	37	ES-88	354023	4323932	20	0.5	44	ES-143	357019	4318647	20	4	21
ES-34	358058	4321236	15	3	50	ES-89	354190	4323523	20	0.7	50	ES-144	360580	4319072	20	10	21

Table 2 continued

Borehole no	Coordinate		Depth (m)	Groundwater Level	*Average SPT-N	Borehole no	Coordinate		Depth (m)	Groundwater Level	*Average SPT-N	Borehole no	Coordinate		Depth (m)	Groundwater level	*Average SPT-N
	X	*Y*					*X*	*Y*					*X*	*Y*			
ES-35	358047	4321239	15	3	50	ES-90	354812	4323548	20	0.5	46	ES-145	360051	4319213	25	4	21
ES-36	356669	4321287	20	6	22	ES-91	354983	4323306	25	1	46	ES-146	359545	4319074	20	1	21
ES-37	356688	4321280	20	7.5	24	ES-92	354559	4323387	20	1	48	ES-147	358993	4319210	30	2	16
ES-38	356714	4321278	20	7.5	27	ES-93	353875	4323299	20	1	39	ES-148	358356	4319044	20	1	19
ES-39	356723	4321301	20	10.5	20	ES-94	353719	4322862	30	1	42	ES-149	357885	4319174	20	1	16
ES-40	356667	4321305	20	10.5	21	ES-95	354339	4322794	20	0.5	48	ES-150	357603	4318769	20	1	16
ES-41	356718	4321362	20	10	20	ES-96	354721	4322775	20	1	50	ES-151	357392	4318330	20	1	31
ES-42	356756	4321341	20	10	22	ES-97	355126	4322607	20	1	23	ES-152	357865	4318298	25	2	18
ES-43	356757	4321372	20	10	22	ES-98	354573	4322167	23	1	38	ES-153	358492	4318374	30	2	17
ES-44	356721	4321371	20	7.5	26	ES-99	354018	4322284	20	1	33	ES-154	358956	4318376	35	1.5	30
ES-45	359941	4318919	20	2.5	37	ES-100	353523	4322211	20	1	39	ES-155	359515	4318468	20	4	18
ES-46	359946	4318889	20	2.5	43	ES-101	353914	4321701	20	1	32	ES-156	360127	4318645	20	1	20
ES-47	359972	4318891	20	2.5	45	ES-102	354647	4321637	20	1	41	ES-157	360560	4318641	20	8	36
ES-48	359957	4318926	20	2.5	37	ES-103	354937	4321945	20	1	16	ES-158	359586	4317703	20	1	15
ES-49	357169	4321219	20	3	64	ES-104	355029	4321138	24	1	21	ES-159	358818	4317838	20	1.5	17
ES-50	357201	4321200	20	3	64	ES-105	354567	4321032	30	1	34	ES-160	358426	4317796	20	1	16
ES-51	357211	4321216	20	3	64	ES-106	354200	4321020	20	1	34	ES-161	357871	4317693	20	1	18
ES-52	357178	4321232	20	3	64	ES-107	354147	4320567	20	1.5	43	ES-162	357414	4317813	25	1	18
ES-53	357192	4321214	20	3	64	ES-108	354824	4320202	20	1	20	ES-163	358457	4317124	20	1	20
ES-54	358372	4316353	24	3.5	24	ES-109	354589	4319896	20	1	44	ES-164	358931	4317107	20	1	19
ES-55	358409	4316261	24	3.5	21	ES-110	354037	4319947	20	1	48	ES-165	359309	4317398	25	4	21

*Average of all tests in borehole

Table 3 Seismic measurement points in Erciş settlement area

Measurement point	Coordinates		V_s	$V_{s_{30}}$	Measurement point	Coordinates		V_s	$V_{s_{30}}$
	X	*Y*				*X*	*Y*		
JF-1	358834	4321780	257	303	JF-12	358403	4319327	210	266
JF-2	357845	4320814	226	261	JF-13	358589	4320226	228	289
JF-3	358412	4321020	235	284	JF-14	357419	4321976	249	270
JF-4	356938	4321736	224	254	JF-15	359824	4319987	232	264
JF-5	354377	4321624	251	263	JF-16	360328	4318263	210	250
JF-6	353979	4323405	245	278	JF-17	358353	4316416	184	201
JF-7	354213	4320100	250	281	JF-18	357059	4320320	234	275
JF-8	354174	4318355	234	265	JF-19	357154	4321295	248	298
JF-9	355755	4319970	213	268	JF-20	359992	4319155	210	275
JF-10	359625	4317561	210	243	JF-21	358840	4320901	247	291
JF-11	356741	4317401	221	274					

*The V_s value beneath the groundwater level is used in liquefaction analysis

Table 4 Scenario earthquake parameters used in liquefaction analyses

	Earthquake date	M_s	M_w	R (km)	a_{max} (g)
Erciş fault	1941	5.9	6	11	0.53
Çaldıran fault	1976	7.3	7.1	32	0.28
Van fault	2011	–	7.1	38	0.29

Several expressions using different correction factors have been proposed by various researchers. The most recent one is the work by Idriss and Boulanger (2008). It suggests that the value of K_σ should be less than 1.0 for loose and shallow sediments, and greater than 1.0 for tight grounds (Seed and Harder 1990). Idriss and Boulanger (2006) suggest the following relation for the K_σ and C_σ correction factors.

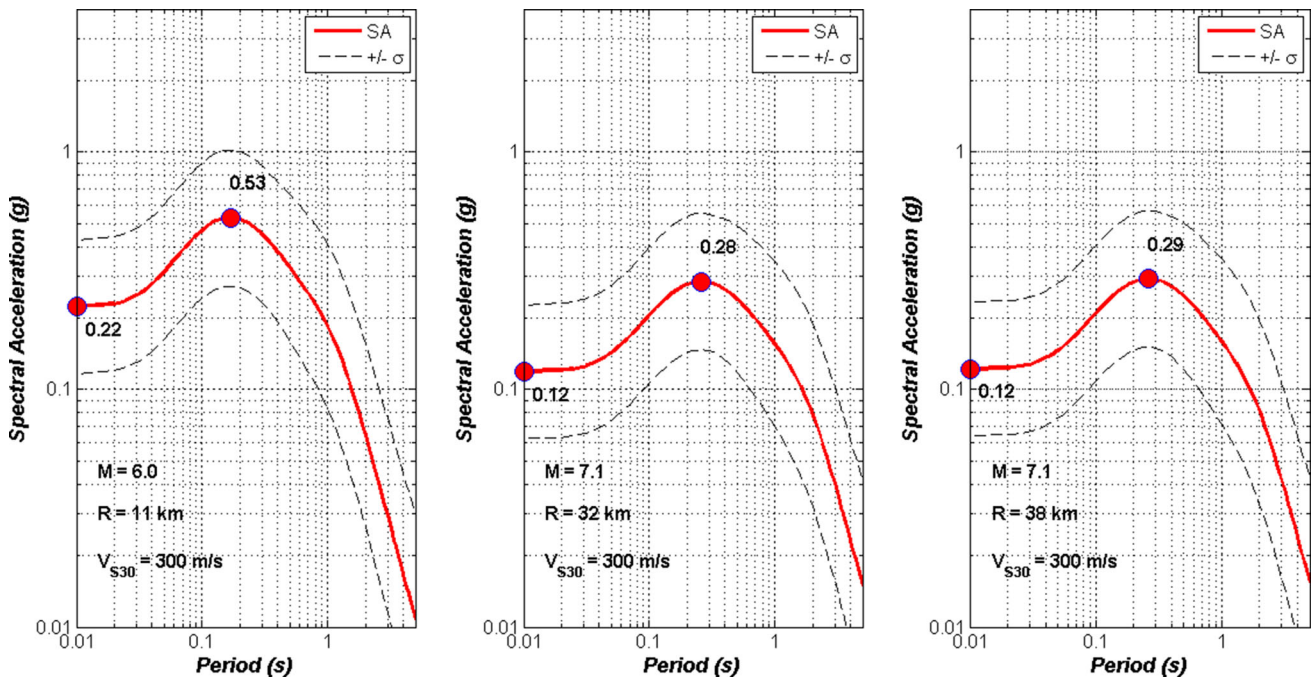

Fig. 5 Peak ground accelerations of Erciş, Çaldıran and Van faults that may affect the study area

$$K_\sigma = 1 - C_\sigma \ln\left(\frac{\sigma'_{vo}}{P_a}\right)$$
$$C_\sigma = \frac{1}{18.9 - 2.55\sqrt{(N1)_{60}}} \quad (8)$$

Idriss and Boulanger (2008, 2010) introduced a new and up-to-date analytical approach to cyclic resistance ratio by creating a large database of liquefaction analyses. Details of this approach are listed below.

$$(N1)_{60CS} = (N1)_{60} + \Delta(N1)_{60CS}$$
$$\Delta(N1)_{60CS} = \exp\left[1.63 + \left(\frac{9.7}{FC + 0.01}\right) - \left(\frac{15.7}{FC + 0.01}\right)^2\right] \quad (9)$$

$$CRR_{7.5} = \exp\left[\frac{(N1)_{60CS}}{14.1} + \left(\frac{(N1)_{60CS}}{126}\right)^2 - \left(\frac{(N1)_{60CS}}{23.6}\right)^3 + \left(\frac{(N1)_{60CS}}{23.6}\right)^4 - 2.8\right]. \quad (10)$$

The CSR under earthquake loads is usually explained as a characteristic rate corresponding to 65% of the maximum cyclic shear stress at a certain depth, z. The CSR is calculated by an equation that considers acceleration, total and effective stresses at various depths, non-rigidity of the deposit, and several assumptions. Seed and Idriss (1971) presented an equation for the calculation of CSR as follows.

$$CSR = \frac{\tau_{av}}{\sigma^t_{vo}} = 0.65\left(\frac{a_{max}}{g}\right)\left(\frac{\sigma_{vo}}{\sigma^t_{vo}}\right) r_d \quad (11)$$

where τ_{av} is the mean cyclic shear stress triggered by earthquake and is accepted to be 65% of the maximum induced stress, g is the acceleration of gravity, a_{max} is the peak ground acceleration (g), σ_{v0} and σ'_{v0} are total and effective stresses at depth z, respectively, and r_d is a stress reduction coefficient.

MSF and reduction factor (r_d) were determined by means of the formulations suggested by Golesorkhi (1989) and Idriss (1999), respectively.

$$Ln(r_d) = \alpha(z) + \beta(z)M_w$$
$$\alpha(z) = -1.012 - 1.126\sin\left(\left(\frac{z}{11.73}\right) + 5.133\right)$$
$$\beta(z) = 0.106 + 0.118\sin\left(\left(\frac{z}{11.28}\right) + 5.142\right), \quad (12)$$

$$MSF = 6.9\exp\left(\frac{-M_w}{4}\right) - 0.058 \qquad M_w > 5.2 \quad (13)$$

where; M_w is the earthquake moment magnitude, z is the depth (m).

LPI and LSI calculations

The LPI method was first introduced by Iwasaki et al. (1978, 1982). LPI depends upon the thickness, depth and liquefaction safety factor of the liquefiable and non-liquefiable layers. LPI provides values for evaluating the liquefaction potentials of liquefiable layers. The equation of LPI is presented in Eq. (14).

$$LPI = \int_0^z F(z)W(z)dz \quad (14)$$

$$W(z) = 10 - 0.5z \qquad z < 20 \text{ m}, \quad (15)$$

where $F(z)$ is the liquefaction safety factor that points out the degree of severity whereas $W(z)$ signifies the depth-based weighting factor. Severity factor [$F(z)$] is designated by the quantitative FS (Sonmez 2003) as follows:

$$F(z) = \begin{cases} FS \le 0.95 & F(z) = 1 - FS \\ 0.95 < FS < 1.2 & F(z) = 2.106\, e^{-18.427\,FS} \\ FS \ge 1.2 & \text{non - liquefaction} \end{cases}. \quad (16)$$

In a sequence with different ground levels, the LPI value is calculated separately for each level. The total LPI value found for each soil level is the sum of the LPI values of the other levels above this level. The total LPI value, in other words the liquefaction potential index of the investigated location specifies the liquefaction risk of the ground (Table 5) (Iwasaki et al. 1982).

The LSI approach has quite different boundary values compared to the LPI method. The maximum value of liquefaction is assumed to be 1.411 in this method (Sonmez and Gokceoglu 2005). According to Sonmez and Gokceoglu (2005), the equation required for the calculation of LSI is presented below.

$$LSI = \int_0^x P(L)W(z)dz \quad (17)$$

The liquefaction probability (P_L) given in the above equation is calculated as follows.

Table 5 Degrees of LPI (Iwasaki et al. 1982)

Liquefaction potential index (LPI)	Liquefaction potential
0	Very low liquefiable
0 < LPI ≤ 5	Low liquefiable
5 < LPI ≤ 15	High liquefiable
15 > LPI	Very high liquefiable

$$P_L = \frac{1}{1+(F_L/0.96)^{4.5}} \quad FL \le 1.411$$
$$P_L(z) = 0 \quad FL > 1.411 \tag{18}$$

On the other hand, $W_{(z)}$ is calculated as in the LPI method. Liquefaction potential classes for the LSI method are given in Table 6.

V_s-based liquefaction analyses

In this study, seismic wave velocity was revealed using seismic refraction and Multichannel Analysis of Surface Waves (MASW) techniques developed by Park et al. (1999). The seismic data can be gathered by this technique and the V_s of soil deposits can be determined using multichannel receivers (Foti 2000; Dikmen et al. 2010a, b). Active source seismograph (12 channels) and 4.5 Hz geophones were employed to acquire data from 21 recording locations in Erciş. Geophone ranges were 3 m, sampling range was 1 ms, as well as record lengths were selected to be 2 s during measurements.

In addition, the V_s values were also calculated for each borehole location depending on the SPT values using the Eq. 19 proposed by Akın et al. (2011) considering the SPT blow counts (N) and depth (z).

$$V_s = 121.75\,N^{-0.101}\,z^{0.216} \quad r = 0.94. \tag{19}$$

In the V_s-based liquefaction analyses, liquefaction potential is determined using acceleration with V_s (Dobry et al. 1981a). The liquefaction potential is defined to be high if the acceleration experienced during an earthquake is greater than 60% of the acceleration that the earth can withstand without being subjected to deformation.

The factor of safety F_a account for the threshold acceleration criteria is as follows:

$$F_a = 1.6\left(\frac{a_t}{a_{max}}\right) \tag{20}$$

where F_a is the safety factor in threshold acceleration criteria, a_t is the threshold acceleration required to start liquefaction, a_{max} is peak ground acceleration of the earthquake. From calculated F_a values obtained using the above mentioned equation, $F_a < 1$ is considered as high liquefaction potential and liquefaction potential is classified as low when $F_a \ge 1$ (Dobry et al. 1981a).

Table 6 Degrees of LSI (Sonmez and Gokceoglu 2005)

Liquefaction severity index (LSI)	Liquefaction potential
0	Non-liquefiable
0 < LSI < 15	Very low liquefiable
15 ≤ LSI < 35	Low liquefiable
35 ≤ LSI < 65	Moderate liquefiable
65 ≤ LSI < 85	High liquefiable
85 ≤ LSI < 100	Very high liquefiable

For the calculation of the threshold acceleration value, $\gamma t = 0.0001$ is adopted and the following formula is used by taking into account the corresponding G/G_{max} value as 0.8 (Hardin and Drnevich 1972).

$$\left(\frac{a_t}{g}\right) = \frac{\left[\gamma t\,\left(\frac{G}{G_{max}}\right) t\,V_s^2\right]}{g\,z\,r_d}$$
$$r_d = 1 - 0.015\,z, \tag{21}$$

where, G_{max} refers to shear modulus, γ is the density of soil, g is the gravity and z is the depth (m).

Andrus and Stokoe (1997, 2000), Uyanık (2002), Uyanık and Taktak (2009) and Uyanik et al. (2013a) suggested several V_s-based liquefaction analyses. FS is generally used for the determination of liquefaction potential using both SPT and V_s data. Seed and Idriss (1971), Uyanık and Taktak (2009) and Uyanik et al. (2013a) formulated the following equation for the calculation of safety factor.

$$FS_{V_s} = \frac{CRR_{V_s}}{CSR_{V_s}} = \frac{SRR}{SSR}. \tag{22}$$

Shear resistance ratio (SRR) is determined as a function of V_s. The SRR and corrected V_s were formulated by Andrus and Stokoe (1997, 2000), Youd et al. (2001), Uyanık (2006) and Uyanık and Taktak (2009).

$$SRR = \left[a\left(\frac{Vs_c}{100}\right)^2 + b\left(\frac{1}{Vs_{max} - Vs_c} - \frac{1}{Vs_{max}}\right)\right] MSF \tag{23}$$

$$V_{s_{max}} = 250 \text{ m/s} \quad FC \le \%5$$
$$V_{s_{max}} = 250 - (FC - 5) \text{ m/s} \quad \%5 < FC < \%35 \tag{24}$$
$$V_{s_{max}} = 220 \text{ m/s} \quad FC \ge \%35,$$

where V_{s_c} is the corrected V_s; $V_{s_{max}}$ is the upper limit of the V_{s_c} and FC is fine content of the soil (Uyanık and Taktak 2009; Uyanik et al. 2013a). MSF is the magnitude scaling factor. a and b are regression coefficients.

Andrus and Stokoe (2000) suggest the values of $V_{s_{max}} = 215$ m/s, $a = 0.022$ and $b = 2.8$ in Eq. 23. Uyanık (2002, 2006) suggests these values as 0.025, 4 and 250 m/s, respectively. Furthermore, Uyanık and Taktak (2009) defined $V_{s_{max}}$ values ranging from 220 to 250 m/s which are related to the fine content of soil.

MSF is a correction coefficient calculated according to earthquake magnitude. The equation developed by Youd et al. (1997) is expressed by the following formula:

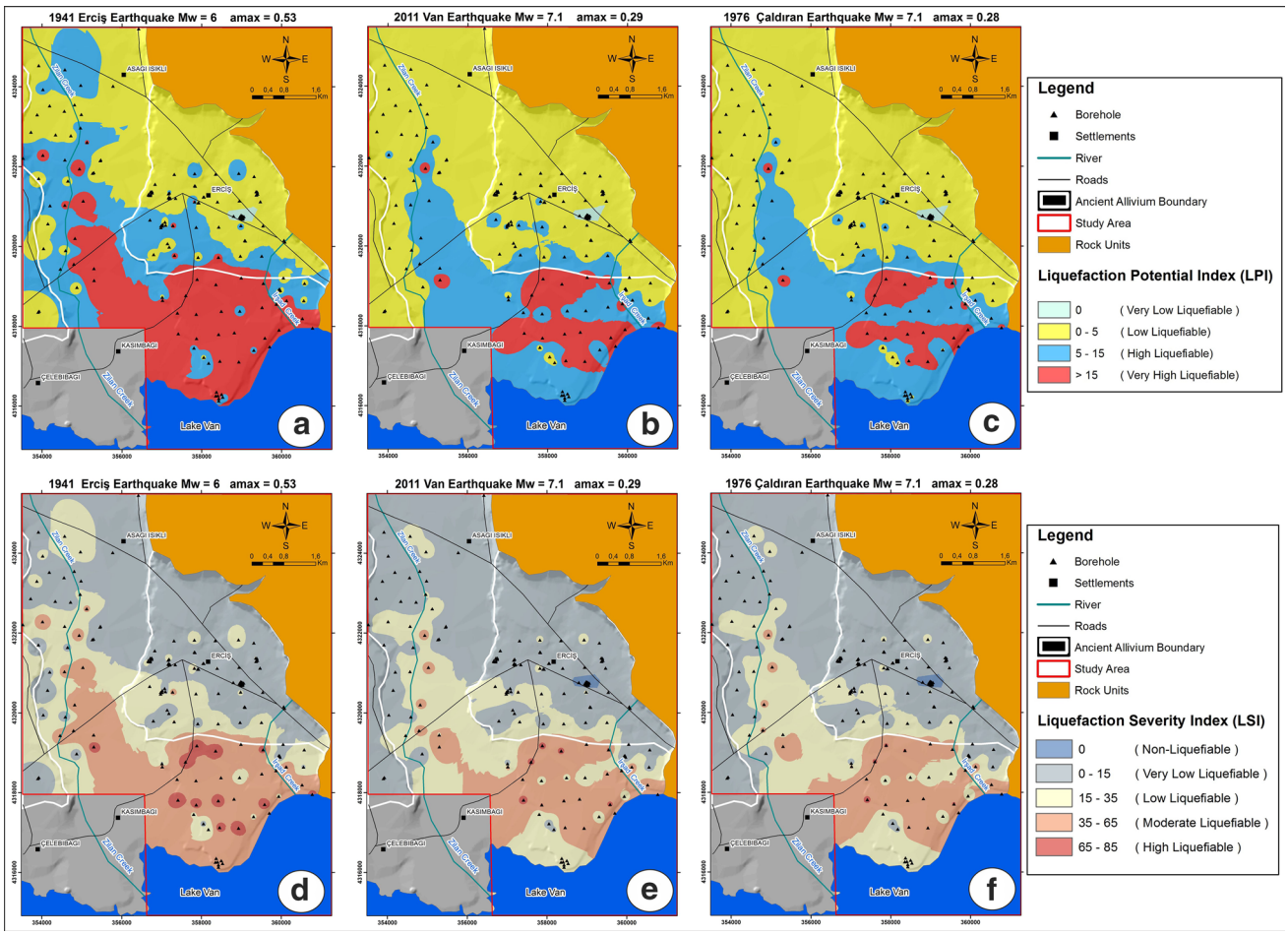

Fig. 6 Liquefaction potential maps of Erciş and its surrounding according to LPI (**a**–**c**) and LSI (**d**–**f**) methods

$$\mathrm{MSF} = \left(\frac{M_w}{7.5}\right)^n \qquad (n = -2.56 \;\; M_\mathrm{w} > 7.5 \;\; \text{and} \;\; n = -3.3 \;\; M_\mathrm{w} \leq 7.5 \;\;), \tag{25}$$

where n is exponential constant. Andrus and Stokoe (1997, 2000) propose the following values for the exponential constant (n) obtained depending on the magnitude of the earthquake.

Shear stress ratio (SSR) is the other term required to calculate the factor of safety in terms of liquefaction potential as a function of V_s. CSR and SSR are physically in similar meaning. Nevertheless, the SSR relies on the V_s of the soil deposit and the acceleration as well as the period of the earthquake. The CSR term (in Eq. 11), suggested by Seed and Idriss (1971), is modified as follows using V_s by Uyanık (2002, 2006) and Uyanik et al. (2013a).

$$\mathrm{SSR} = \left(\frac{a_\mathrm{max}}{g}\right)\left(\frac{\sigma_{V_\mathrm{s}}}{\sigma'_{V_\mathrm{s}}}\right) r_\mathrm{d} \tag{26}$$

$$\sigma_{V_\mathrm{s}} = 0.25T\left(\sum_{i=1}^{n} \gamma_i V_{\mathrm{s}_i}\right)$$
$$\sigma'_{V_\mathrm{s}} = \sigma_{V_\mathrm{s}} - u = 0.25T\left(\sum_{i=1}^{n} \gamma_i V_{\mathrm{s}_i} - V_{\mathrm{s}_n}(\gamma_\mathrm{sa} - \gamma_\mathrm{d})\right) \tag{27}$$
$$r_\mathrm{d} = 1 - 0.00765z \quad z \leq 9.15 \text{ m}$$
$$r_\mathrm{d} = 1.174 - 0.0267z \quad 9.15 < z \leq 23 \text{ m}$$
$$r_\mathrm{d} = 0.744 - 0.008z \quad 23 < z \leq 30 \text{ m},$$

where σ'_{V_s} is the effective vertical stress (kN/m^2); σ_{V_s} is the dynamic vertical stress at the investigated depth defined by V_s and earthquake wave period (kN/m^2); a_max is the peak ground acceleration (g), g is the acceleration of gravity, T is the dominant period of the earthquake (s); γ_i is the unit weight of soil layers (kN/m^3); γ_sa saturated unit weight of soil (kN/m^3); γ_d unit weight of unsaturated soil (kN/m^3); V_{s_i} is the V_s velocities of soil unit (m/s); n is the number of layers; z is the depth of layer considered in liquefaction analyses (m) (Uyanık 2002; Uyanık and Taktak 2009; Uyanik et al. 2013a); r_d is a stress reduction coefficient

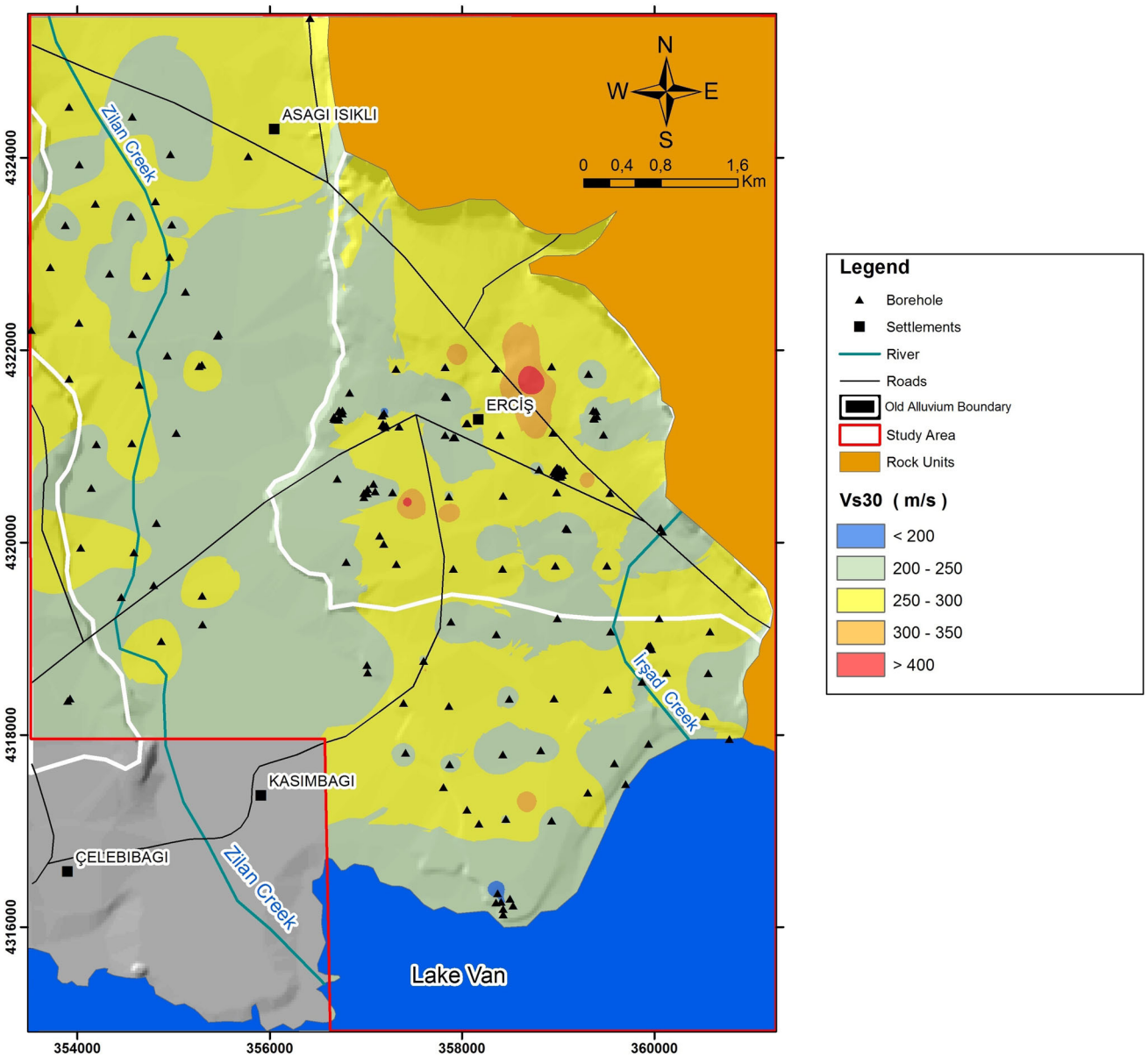

Fig. 7 V_{s30} map of the study area

dependent to depth (Robertson and Wride, 1997; Liao and Whitman, 1986).

To obtain the SSR values from V_s, the V_s values measured in the field should be corrected by a reference overburden stress using the correction factor (Andrus and Stokoe 1997, 2000; Uyanık 2006; Uyanik et al. 2013a).

$$V_{s_c} = V_s \left(\frac{P_a}{\sigma'_{vo}} \right)^{0.25}, \tag{28}$$

where σ'_{V_o} is the effective vertical stress in kPa; V_{s_s} is the corrected V_s (m/s) and P_a is the reference stress which is accepted to be 100 kPa. The SSR is calculated using the earthquake period and V_s values as well as the earthquake acceleration. The SSR value reveals more accurate results when these parameters are used. In this study, the relationships developed by Uyanik et al. (2013a) are used for the calculation of SSR and SRR values.

Results of the liquefaction analyses

Using the SPT, V_s, soil type, groundwater level and earthquake scenarios, the units in the first 20 m in the study area were evaluated in terms of liquefaction potential. As can be seen from the liquefaction potential maps prepared according to the LPI and LSI methods (Fig. 6a–f), the liquefaction potential is determined to be high to very high in all three earthquake scenarios in the coastal sections of

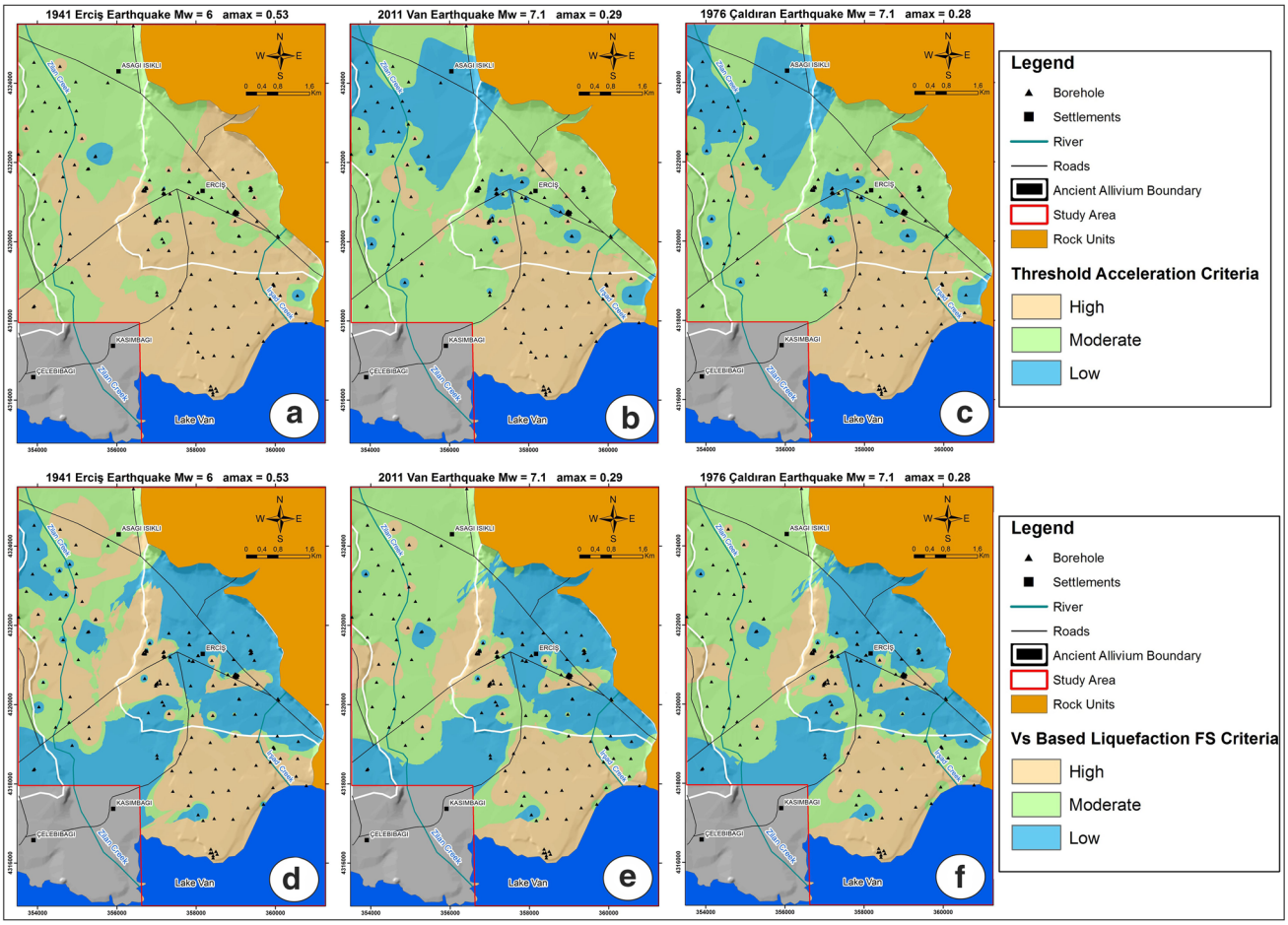

Fig. 8 V_s-based threshold acceleration criteria (**a**–**c**) and safety factor (**d**–**f**) liquefaction potential maps of Erciş and its surrounding

the Lake Van as well as the Zilan Creek in the western part of Erciş and Irşat Creek. However, LPI and LSI values are determined to be low in the western and northern parts of the study area.

$V_{s_{30}}$ value for a depth of 30 m was calculated using seismic methods in the study area, as well (Eq. 28). The $V_{s_{30}}$ velocities in the study area are generally between 200 and 250 m/s in recent alluvial deposits; however, they vary between 250 and 300 m/s in old lacustrine sediments (Fig. 7).

$$V_{s_{30}} = \frac{30}{\sum_{i=1}^{n} \frac{h_i}{V_{s_i}}}. \tag{29}$$

where h_i is the thickness (m) and V_{s_i} is the V_s of the ith layer.

V_s-based threshold acceleration criteria and safety factor were also used to signify the liquefaction potential of the research area (Fig. 8a–f). Similar to the results of LPI and LSI, it was determined that the liquefaction potential is medium to high nearby the Lake Van and in the western region.

Discussion and results

According to four different methodologies (SPT-based LPI and LSI, V_s-based threshold acceleration and safety factor) and three different earthquake scenarios, the liquefaction potential was evaluated for the Erciş district, which suffered the most damage in 2011 Van earthquake. After all these evaluations, it was determined in all four methods that the liquefaction potential of the study area near the coastal parts of the Lake Van and the western part of the study area is higher than the other regions. This indicates that the soil tightness and groundwater level control the liquefaction potential. When three different earthquake scenarios are examined, a high liquefaction potential in Erciş settlement area is determined if Erciş–Kocapınar fault creates an earthquake, which is the closest fault to the study area and there is high-moderate liquefaction potential in the scenarios considering the Çaldıran and Van faults. When all results obtained from those analyses are considered, it is concluded that the LPI and LSI values calculated according to the borehole data and the safety factor liquefaction analyses calculated on the basis of V_s are more

compatible than the threshold acceleration criteria. In addition, it was determined that the location of lateral spreading and sand boils observed in the field after the 23rd October 2011 Van earthquake overlap with the scenario boundaries in this study. Since seismic work can be performed quickly and easily in all types of soil conditions, the use of V_s-based safety factor liquefaction analyses, which reveals consistent results with the SPT-based analyses, is also recommended for the liquefaction assessments.

When liquefaction potential is evaluated according to the methods used in this study, it can be derived that liquefaction type surface deformations may occur after a possible large earthquake in the vicinity of Erciş, especially near the Lake Van from Erciş–Patnos road and in areas close to the rivers. For this reason, considering that the present research is a comprehensive study of the region, liquefaction potential should be evaluated in detail during geotechnical studies carried out for new constructions and soil improvement studies should be executed in areas where liquefaction potential exists.

The raw SPT-N blow counts beneath the groundwater level vary between 4 and 32 when the borehole data and the results of SPT-based liquefaction analyses are considered. Furthermore, it is also concluded that the shallow soils having low shear wave velocity values reveal high liquefaction potential which are compatible with the SPT data. Thus, the use of V_s-based liquefaction analysis in collaboration with the SPT results is quite advantageous to determine the liquefaction potential of a specific site. On the other hand, the SPT data may be misleading where gravelly layers exist within a liquefiable soil whilst the collection of V_s data is rapid and practical.

Acknowledgements This research has been funded by Van Yüzüncü Yıl University the Scientific and Technical Research Council of Turkey (Project No 2014-HIZ-MIM167 and 2015-FBE-YL271). The authors would also like to thank the reviewers for their constructive comments, which enhance the quality of the paper.

References

ABYYHY (1997). Afet Bölgelerinde Yapılacak Yapılar Hakkında Yönetmelik, Aydınoğlu, M. M., Bayındırlık ve İskan Bakanlığı (in Turkish)

Akın, M, Akın MK, Akkaya İ, Özvan A, Şengül MA (2015a) Erciş (Van) Yerleşim Alanındaki Zeminlerin Sıvılaşma Potansiyelinin Değerlendirilmesi, No: 2014-HIZ-MİM167 Yüzüncü Yıl Üniversitesi Bilimsel Araştırma Projeleri Başkanlığı, 46 s (**in Turkish**)

Akın KM, Kramer SL, Topal T (2011) Empirical correlations of shear wave velocity (V_s) and penetration resistance (SPT-N) for different soils in an earthquake-prone area (Erbaa-Turkey). Eng Geol 119(1–2):1–17

Akın M, Özvan A, Akın M, Topal T (2013) Evaluation of liquefaction in Karasu River floodplain after the October 23, 2011, Van (Turkey) earthquake. Nat Hazards 69:1551–1575

Akın M, Akın MK, Akkaya İ, Özvan A, Şengül MA (2015b) Erciş (Van) yerleşim alanındaki zeminlerin sıvılaşma potansiyelinin değerlendirilmesi, Ulusal Mühendislik Jeolojisi Sempozyumu, 3-5 Eylül 2015, KTÜ, Trabzon. s 208-215(**in Turkish**)

Ambraseys NN (2001) Reassessment of earthquakes 1900–1999 in the Eastern Mediterranean and Middle East. Geophys J Int 145:471–485

Andrus RD, Stokoe KH II (2000) Liquefaction resistance of soils from shear-wave velocity. J Geotech Geoenviron Eng (ASCE) 126:1015–1025

Andrus RD and Stokoe II KH (1997) Liquefaction Resistance Based on Shear Wave Velocity. In: NCEER Workshop on Evaluation of Liquefaction Resistance Of Soils, Technical Report NCEER-97-0022, T.L.Youd and I.M. Idriss (Eds.), Held (1996), Salt Lake City, UT, Buffalo, NY, pp 89–128

Aydan Ö, Ulusay R, Kumsar H, Konagai K (2012) Site investigation and engineering evaluation of the Van earthquakes of October 23 and November 9, 2011. Japan Society of Civil Engineers

Aydan Ö, Ulusay R, Kumsar H (2013) Seismic, ground motion and geotechnical characteristics of the 2011 Van-Ercis¸ and Van-Edremit earthquakes of Turkey, and assessment of geotechnical damages. Bull Eng Geol Environ. https://doi.org/10.1007/s10064-013-0526-z

Bozcu M, Uyanık O, Çakmak O, Türker AE (2007) Geotechnical properties of Esen I HEPP Project Field. Süleyman Demirel University. J Nat Appl Sci 11(1):75–83

Bozkurt E (2001) Neotectonics of Turkey-a synthesis. Geodin Acta 14:3–30

Cetin KO, Seed RB, Der Kiureghian A, Tokimatsu K, Harder LF, Kayen RE, Moss RES (2004) Standard penetration test-based probabilistic and deterministic assessment of seismic soil liquefaction potential. J Geotech Geoenviron Eng ASCE 130(12):1314–1340

Dadashpour M, Echeverria-Ciaurri D, Kleppe J, Landro M (2009) Porosity and permeability estimation by integration of production and time-lapse near and far offset seismic data. J Geophys Eng 6:325–344

Dikmen U (2009) Statistical correlations of shear wave velocity and penetration resistance for soils. J Geophys Eng 6:61–72

Dikmen Ü, Arısoy MÖ, Akkaya İ (2010a) Offset and linear spread geometry in MASW method. J Geophy Eng 7:211–222

Dikmen Ü, Başokur AT, Akkaya İ, Arısoy MÖ (2010b) Yüzey dalgalarının çok-kanallı analizi yönteminde uygun atış mesafesinin seçimi. Yerbilimleri 31(1):23–32 **(in Turkish)**

Dobry R, Powell DJ, Yokel FY, Ladd RS (1981a) Geotechnical aspect. Liquefaction potential of saturated sand—the stiffness method. In: Proceeding of the Seventh World Conference on Earthquake Engineering Istanbul, Turkey

Dobry R, Stokoe KHII, Ladd RS, Youd TL (1981b) Liquefaction susceptibility from S-Wave Velocity. In: Proceedings, In Situ Tests to Evaluate Liquefaction Susceptibility, ASCE National Convertion, held 1981, St. Louis, MO

Dobry R, Ladd RS, Yokel FY, Chung RM, Powell D (1982) Prediction of pore water pressure buildup and liquefaction of sands during earthquakes by the cyclic strain method. Building Science Series 138, National Bureau of Standards, US, p 182

Duman ES, Ikizler SB (2014) Assessment of liquefaction potential of Erzincan Province and its vicinity, Turkey. Nat Hazards 73:1863–1887

Foti S (2000) Multistation Methods for Geotechnical Characterization using Surface Waves, Ph.D. Diss., Politecnico di Torino, p 230, Milano

Golesorkhi R (1989) Factors Influencing the Computational Determination of Earthquake-Induced Shear Stresses in Sandy Soils, Ph.D. thesis, University of California at Berkeley, p 395

Graizer V, Kalkan E (2015) Update of the Graizer-Kalkan ground-motion prediction equations for shallow crustal continental earthquakes. USGS Open-File Rep 2015–1009:79

Hardin BO, Drnevich VP (1972) Shear modulus and damping in soils: measurement and parameter effects. J Soil Mech Found Div ASCE. 98(6):603–624

Hasançebi N, Ulusay R (2007) Empirical correlations between shear wave velocity and penetration resistance for ground shaking assessments. Bull Eng Geol Env 66:203–213

Idriss IM (1999) An update to the Seed-Idriss simplified procedure for evaluating liquefaction potential. In: Proceedings, TRB Workshop on New Approaches to Liquefaction, Publication No. FHWARD-99-165, Federal Highway Administration, January

Idriss IM, Boulanger RW (2006) Semi-empirical procedures for evaluating liquefaction potential during earthquakes. Soil Dyn Earthq Eng 26:115–130

Idriss IM, Boulanger RW (2008) Soil liquefaction during earthquakes. Monograph MNO-12, Earthquake Engineering Research Institute, Oakland, p 261

Idriss IM and Boulanger RW (2010) SPT-based Liquefaction Triggering Procedures, Report No. UCD/CGM-10/02, department of Civil & Environmental Engineering College of Engineering University of California, pp 259

Ishihara K (1996) Soil behaviour in earthquake geotechnics. The Oxford Engineering Science Series, Oxford

Iwasaki T, Tokida K, Tatsuko F and Yasuda S (1978) A practical method for assessing soil liquefaction potential based on case studies at various site in Japan. In: 2nd International Conference on Microzonation, San Francisco, pp 885–896

Iwasaki T, Tokida K, Tatsuoka F, Watanabe S, Yasuda S, Sato H (1982) Microzonation for soil liquefaction potential using simplified methods. In: Proceedings of the 3rd international conference on microzonation, Seattle, vol 3, pp 1310–1330

Juang CH, Yuan H, Lee DH, Lin PS (2003) Simplified cone penetration test based method for evaluating liquefaction resistance of soils. J Geotech Geoenviron Eng 129(1):66–80

Kadirioğlu FT, Kartal RF (2016) The new empirical magnitude conversion relations using an improved earthquake catalogue for Turkey and its near vicinity (1900–2012). Turk J of Earth Sc 25:300–310

Karastathis VK, Karmis PN, Draskatos G, Stavrakakis G (2002) Geophysical methods contributing to the testing of concrete dams. Application at the Marathon Dam. J Appl Geophys 50:247–260

Kayen RE, Mitchell JK, Seed RB, Lodge A, Nishio S and Coutinho R (1992) Evaluation of SPT-,CPT-, and shear wave-based methods for liquefaction potential assessment using Loma Prieta data, Fourth Japan-U.S. In: Workshop on Earthquake Resistant Design of Lifeline Facilities and Countermeasures for Soil Liquefaction, Honolulu, Hawaii, Proceedings, Technical Rep. NCEER-92-0019, M. Hamada and T. D. O'Rourke, eds., National Center for Earthquake Engineering Research, Buffalo, NY, 1, pp 177–204

Koçyiğit A (2013) New field and seismic data about the intraplate strike-slip deformation in Van region, East Anatolian plateau, E Turkey. J Asian Earth Sci 62:586–605

Koçyiğit A, Yılmaz A, Adamia S, Kuloshvili S (2001) Neotectonics of East Anotolian Plateau transition from thrusting to strike-slip faulting. Geodin Acta 14:177–195

KOERI (2011) Probabilistic assessment of the seismic hazard for the Lake Van basin, October, 23 2011. www.koeri.boun.edu.tr. Accessed 23 Dec 2011

Kramer SL (1996) Geotechnical earthquake engineering. Prentice-Hall International Series in Civil Engineering and Engineering Mechanics, p 653

Liao SSC, Whitman RV (1986) Overburden correction factors for SPT in sands. J Geotech Eng (ASCE) 112:337–373

MTA (2007) Van İlinin Yer Bilim Verileri, Ankara, s. 69 (**in Turkish**)

Oyan V, Keskin M, Lebedev VA, Chugaev AV, Sharkov EV (2016) Magmatic evolution of the Early Pliocene Etrüsk stratovolcano, Eastern Anatolia collision zone, Turkey. Lithos 256–257:88–108

Özdemir Y, Güleç N (2014) Geological and geochemical evolution of the quaternary Süphan stratovolcano, eastern Anatolia, Turkey: evidence for the lithosphere-asthenosphere interaction in post-collisional volcanism. J Petrol 55:37–62

Özdemir Y, Karaoğlu Ö, Tolluoğlu AÜ, Guleç N (2006) Volcanostratigraphy and petrogenesis of the Nemrutstratovolcano (East Anatolian Plateau): the most recent post-collisional volcanism in Turkey. Chem Geol 226:189–211

Özdemir Y, Akkaya İ, Oyan V, Kelfoun K (2016) A Debris avalanche at Süphan Stratovolcano (Turkey) and implications for hazard evaluation. Bull Volcanol 78(9). https://doi.org/10.1007/s00445-016-1007-6

Özvan A, Şengül MA, Tapan M (2008) Van Gölü havzası Neojen çökellerinin jeoteknik özelliklerine bir bakış: erciş yerleşkesi. Geosound 52:297–310 **(in Turkish)**

Park CB, Miller RD, Xia J (1999) Multichannel analysis of surface waves. Geophysics 64(3):800–808

Pekkan E, Tun M, Guney Y, Mutlu S (2015) Integrated seismic risk analysis using simple weighting method: the case of residential Eskişehir, Turkey. Nat Hazards Earth Syst Sci 15:1123–1133

Robertson PK and Wride CE (1997) Cyclic Liquefaction and Evaluation Based on the SPT and CPT, NCEER Workshop on Evaluation of Liquefaction Resistance of Soils (NCEER-97-0022)

Robertson PK, Wride CE (1998) Evaluating cyclic liquefaction potential using the cone penetration test. Can Geotech J 35(3):442–459

Şaroğlu F, Yilmaz Y (1986) Doğu Anadolu'da Neotektonik Dönemdeki Jeolojik Evrim ve Havza Modelleri. MTA Dergisi 107:73–94 **(Ankara (in Turkish))**

Seed RB and Harder LF (1990) SPT-based analysis of cyclic pore pressure generation and undrained residual strength. In: Froc., HB. Seed Memorial Symp., Hi-Tech Publishing Ltd., vol 2, pp 351–376

Seed HB, Idriss IM (1971) Simplified procedure for evaluating soil liquefaction potential. J Soil Mech Found Div 97:1249–1273

Seed HB, Idriss IM (1982) Ground motions and soil liquefaction during earthquakes. Earthquake Engineering Resarch Institute, Berkeley

Seed HB, Idriss IM, Arango I (1983) Evaluation of liquefaction potential using field performance data. J Geotech Eng ASCE 109:458–482

Selçuk AS (2016) Evaluation of the relative tectonic activity in the eastern Lake Van basin, East Turkey. Geomorphology 270:9–21

Şengör AMC, Kidd WSF (1979) Post-collisional tectonics of the Turkish-Iranian plateau and a comparison with Tibet. Tectonophys. 55:361–376

Şengör AMC, Yılmaz Y (1981) Tethyan evolution of Turkey: a plate tectonic approach. Tectonophysics 75:181–241

Sonmez H (2003) Modification of the liquefaction potential index and liquefaction susceptibility mapping for a liquefactionprone area (Inegol, Turkey). Environ Geol 44:862–871. https://doi.org/10.1007/s00254-003-0831-0

Sonmez H, Gokceoglu C (2005) A liquefaction severity index suggested for engineering practice. Environ Geol 48:81–91

Soupios PM, Papazachos CB, Vargemezis G, Fikos I (2005) Application of Modern Seismic Methods for Geotechnical Site Characterization. In: Πρακτικά του International Workshop in Geoenvironment and Geotechnics 12-14 September 2005, Milos island, Greece, ISBN 960-88153-7-1, σ_λ, pp 163–170

Tezcan SS, Keceli A, Ozdemir Z (2006) Allowable bearing capacity of shallow foundations based on shear wave velocity. J Geotech Geol Eng 24:203–218

Tokimatsu K, Uchida A (1990) Correlation between liquefaction resistance and shear wave velocity. Soils Found 30(2):33–42

Tokimatsu K, Yoshimi Y (1983) Empirical Correlation of Soil Liquefaction Based on SPT N-Value and Fine Content. Soils Found 23(4):56–74

Uyanik O (2010) Compressional and shear-wave velocity measurements in unconsolidated top-soil and comparison of the results. Int J Phys Sci 5(7):1034–1039

Uyanık O (2002) Kayma Dalga Hızına Baglı Potansiyel Sıvılasma Analiz Yöntemi, Doktora Tezi, DEÜ. Fen Bilimleri Enstitüsü, İzmir, 200 s (**in Turkish**)

Uyanık O (2006) Sıvılaşır yada Sıvılaşmaz Zeminlerin Yinelemeli Gerilme Oranına Bir Seçenek, DEÜ Mühendislik Fakültesi Fen ve Mühendislik Dergisi Cilt:8. Sayı 2:79–91 **(in Turkish)**

Uyanık O (2011) The porosity of saturated shallow sediments from seismic compressional and shear wave velocities. J Appl Geophys 73(1):16–24

Uyanık O, Taktak AG (2009) Kayma Dalga Hızı ve Etkin Titresim Periyodundan Sıvılasma Çözümlemesi için Yeni Bir Yöntem. Süleyman Demirel Üniversitesi Fen Bilimleri Enstitüsü Dergisi 13(1):74–81 **(in Turkish)**

Uyanık O, Ulugergerli EU (2008) Quality control of compacted grounds using seismic velocities. Near Surface Geophys 6(5):299–306

Uyanık O, Ekinci B, Uyanık NA (2013a) Liquefaction analysis from seismic velocities and determination of lagoon limits Kumluca/Antalya example. J Appl Geophys 95:90–103

Uyanık O, Türker E, İsmailov T (2006) Sığ Sismik Mikro-Bölgeleme ve Burdur/Türkiye Örneği. Ekologiya ve Su Teserrufatı 1(8):9–15 **(in Turkish)**

Uyanık AN, Uyanık O, Akkurt İ (2013b) Micro-zoning of the natural radioactivity levels and seismic velocities of potential residential areas in volcanic fields: the case of Isparta (Turkey). J Appl Geophys 98:191–204

Watson DF, Philip GM (1985) A refinement of inverse distance weighted interpolation. Geoprocessing 2:315–327

Yi F (2010) Procedure to evaluate liquefaction-induced lateral spreading based on shear wave velocity. In: Fifth International Conference on Recent Advances in Geotechnical Earthquake Engineering and Soil Dynamic, San Diego, California, USA

Youd TL, Idriss IM, Andrus RD, Arango I, Castro G, Christian JT, Dobry R, Finn WDL, Harder Jr LF, Hynes ME, Ishihara K, Koester JP, Liao SSC, Marcuson III WF, Martin GR, Mitchell JK, Moriwaki Y, Power MS, Robertson PK, Seed RB, Stokoe II KH (1997) Summary Report, NCEER Workshop on Evaluation of Liquefaction Resistance of Soils, Technical Report NCEER-97-0022, T.L. Youd and I.M. Idriss, (Eds.), Buffalo, NY, 1-40

Youd TL, Idriss IM, Andrus RD, Arango I, Castro G, Christian JT, Dobry R, Finn WDL, Harder LF Jr, Hynes ME, Ishihara K, Koester JP, Liao SSC, Marcusan WF III, Martin GR, Mitchell JK, Moriwaki Y, Power MS, Robertson PK, Seed RB, Stokoe KH II (2001) Liquefaction resistance of soils: summary report from the 1996 NCEER and 1998 NCEER/NSF Workshops on Evaluation of Liquefaction Resistance of Soils. J Geotech Geoenviron Eng ASCE 127:10

Acta Geophysica (2018) 66:39–49
https://doi.org/10.1007/s11600-017-0104-z

RESEARCH ARTICLE - APPLIED GEOPHYSICS

Lineaments in the Shamakhy–Gobustan and Absheron hydrocarbon containing areas using gravity data

Ali Elmas[1] · Hakan Karsli[1] · Fakhraddin A. Kadirov[2]

Received: 25 July 2017 / Accepted: 2 December 2017 / Published online: 7 December 2017

Abstract
In this study, we purposed to investigate the edge of geostructures and position of existing faults of the Shamakhy–Gobustan and Absheron hydrocarbon containing regions in Azerbaijan. For this purpose, the horizontal gradient, analytic signal, tilt angle, and hyperbolic of tilt angle methods were applied to the first vertical derivative of gravity data instead of Bouguer gravity data. We obtained the maps that show the previous lineaments which were designated by considering the maximum contours of horizontal gradient, analytic signal maps, and zero values of tilt angle, hyperbolic of tilt angle maps. The geometry of basement interface was also modeled utilizing the Parker–Oldenburg algorithm to understand the sediment thickness and coherency or incoherency between the gravity values and basement topography. The lineaments were held a candle to most current tectonic structure map of the study area. It was seen that the techniques used in this study are very effective to determine the old and new lineaments in the Shamakhy–Gobustan and Absheron regions. The epicenter distribution of earthquakes within the study area supports the new lineaments which are extracted by our interpretation. We concluded that better comprehension of Azerbaijan geostructures and its effect on the large scale works will be provided by means of this study.

Keywords First vertical derivative · Horizontal gradient · Analytic signal · Tilt angle · Hyperbolic of tilt angle

Introduction

Shamakhy–Gobustan and Absheron located in the eastern part of Azerbaijan are important hydrocarbon reservoir and also a seismically active regions. In addition, these regions are located in the eastern part of the Greater Caucasus belt (Bochud 2011). The Greater Caucasus belt forms a morphological barrier along the southern margin of the Scythian Platform, lying down from the northern margin of the Eastern Black Sea Basin to the South Caspian Basin. It improved during several phases of deformation in Mesozoic–Cenozoic times (Brunet et al. 2009; Saintot et al. 2006). It is localized within the active convergence zone between the Arabian and Eurasian plates. Based on the study of Vincent et al. (2007), the partitioning of Arabian–Eurasian plate convergence is divided between right-lateral strike–slip faulting on NW–SE striking faults in eastern Turkey and thrusting along the Caucasus thrust front. The NW–SE-oriented geological structures are the dominant in the tectonic regime of the study area (Kadirov et al. 2015). On the other hand, a number of earthquakes related to the geostructures in the region have been occured and caused severe damages in the Azerbaijan since ancient time (Kadirov 2000).

Many studies by Radjabov (1978), Kadirov (2000, 2012a, b, 2015) and Alizadeh et al. (2016) have been done to understand the geotectonic structures of the region. Although diapir folds and mud volcanoes which contain hydrocarbon are widespread in the region, the main geotectonic elements are consist of the Tengi–Beshbarmag

✉ Ali Elmas
aeaeelmas@gmail.com

Hakan Karsli
hkarsli@ktu.edu.tr

Fakhraddin A. Kadirov
kadirovf@gmail.com

[1] Department of Geophysics, Engineering Faculty, Karadeniz Technical University, 61080 Trabzon, Turkey

[2] Department of Geodynamics and Seismology, Institute of Geology and Geophysics, Azerbaijan National Academy of Sciences, Baku, Azerbaijan

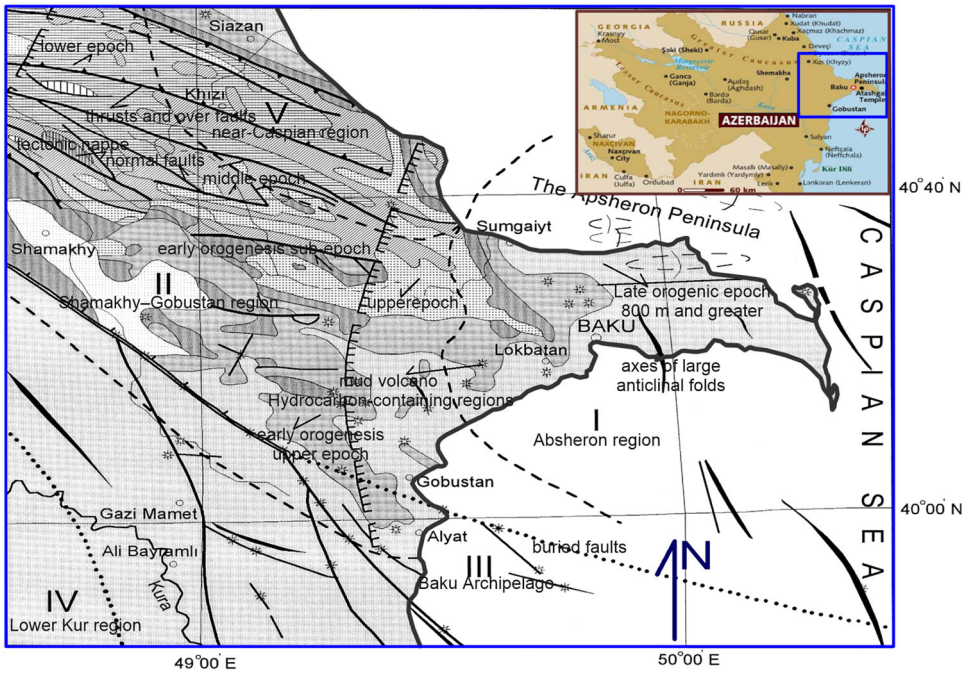

Fig. 1 Geological and tectonic map of the study region (Kadirov et al. 2015)

anticlinoria, Zakatala–Govdag, Shahdag–Khyzy, Shamakhy–Gobustan synclinorium, Lower Kura, and Absheron reservoirs (Shikhalibeyli 1972). The Lower Kura basin is the deepest structure in the Kura basin system. The geological and tectonic units of the region are shown in Fig. 1.

The determination of the boundaries (or lineaments) of the geostructure is of vital attention in many practices of geosciences such as investigation of basement topography, hydrocarbon reservoirs, fault mechanisms, and seismotectonic structures. The lineaments of Shamakhy–Gobustan and Absheron regions have been in advance examined by Kadirov (2000, 2012a, b, 2015) utilizing several data groups like seismic and gravity data, which is not adequate to figure out the lineaments of the study area. Among the geophysical data, the gravity data are very useful to study the position of subsurface geostructures. Recently, edge analysis techniques have been widely applied to gravity data to extract the details of the lineaments of the geostructures. For example, Oruç et al. (2013) have successfully used the edge analysis techniques to obtain the boundaries of the geostructures of Kozaklı in the Central Anatolia Region, Turkey.

This study mainly aims to delineate the lineaments of the geostructures which characterized by the Tengi–Beshbarmag anticlinoria, Zakatala–Govdag, Shahdag–Khyzy, Shamakhy–Gobustan synclinorium, Lower Kura, and Absheron reservoirs and to provide an updated lineament map of the region using Horizontal Gradient (HG), Analytic Signal (AS), Tilt Angle (TI), and Hyperbolic of Tilt Angle (HTA) calculated from the First Vertical Derivative (FVD) of the regional gravity data of the region.

Data and methods

The data used in this study were digitized and prepared by Kadirov (2000) from Bouguer gravity anomaly map of Azerbaijan (1:500000). The negative gravity anomalies dominate within the most part of the area and increase from SW to NE in the Bouguer gravity anomaly map, as shown in Fig. 2. It is generally known that the gravity maps illustrate positive anomaly in the marine while negative anomaly in the land. For this reason, it is important to calculate the basement topography by inversion as well as to determine the lineaments in the region. Thus, it will be investigated the compatibility between the Bouguer gravity anomalies and the basement topography to be calculated.

In this study, the data were processed and evaluated using the computer programmes such as 3DINVER (Gomez-Ortiz and Agarwal 2005) and POTENSOFT (Arısoy and Dikmen 2011). The 3DINVER based on Parker–Oldenburg algorithm and POTENSOFT were utilized to display 3D geometry of basement interface, and to perform some preprocesses and extract the lineaments of geostructure in the study area, respectively.

We use the radial power spectrum technique based on Fourier Transform (FT) technique and given by Spector and Grant (1970) to estimate the average basement topography of the area. The calculated power spectrum curves shown in Fig. 3 display that wavenumber increases with decreasing amplitude. In the analysis of the spectrum, the vertical axis is taken as logarithmic and the tilt change points are considered as the distinct layers having different densities.

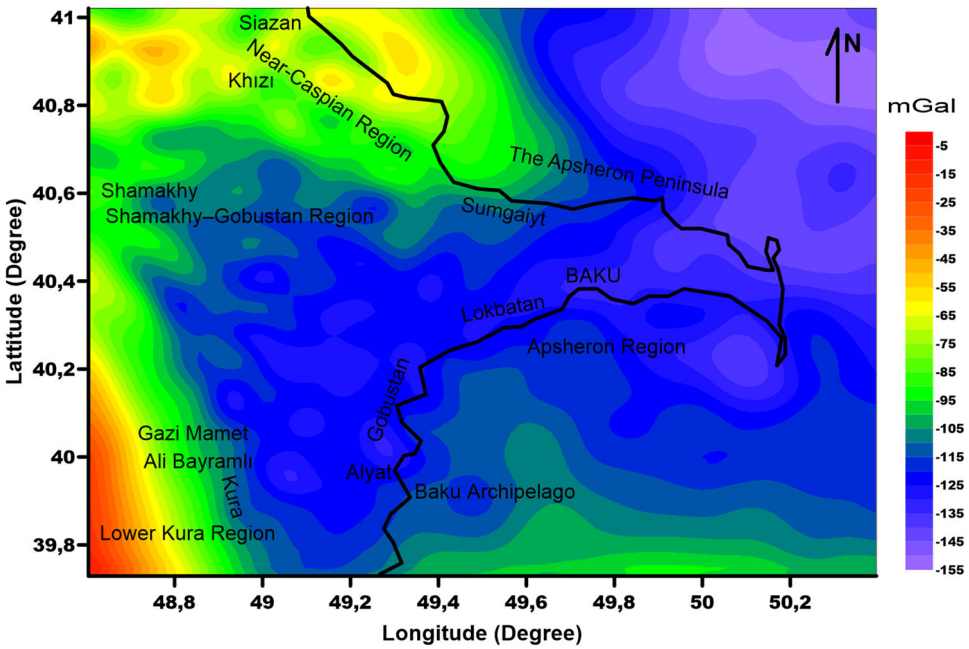

Fig. 2 Bouguer gravity anomaly map of the region (after Kadirov 2000)

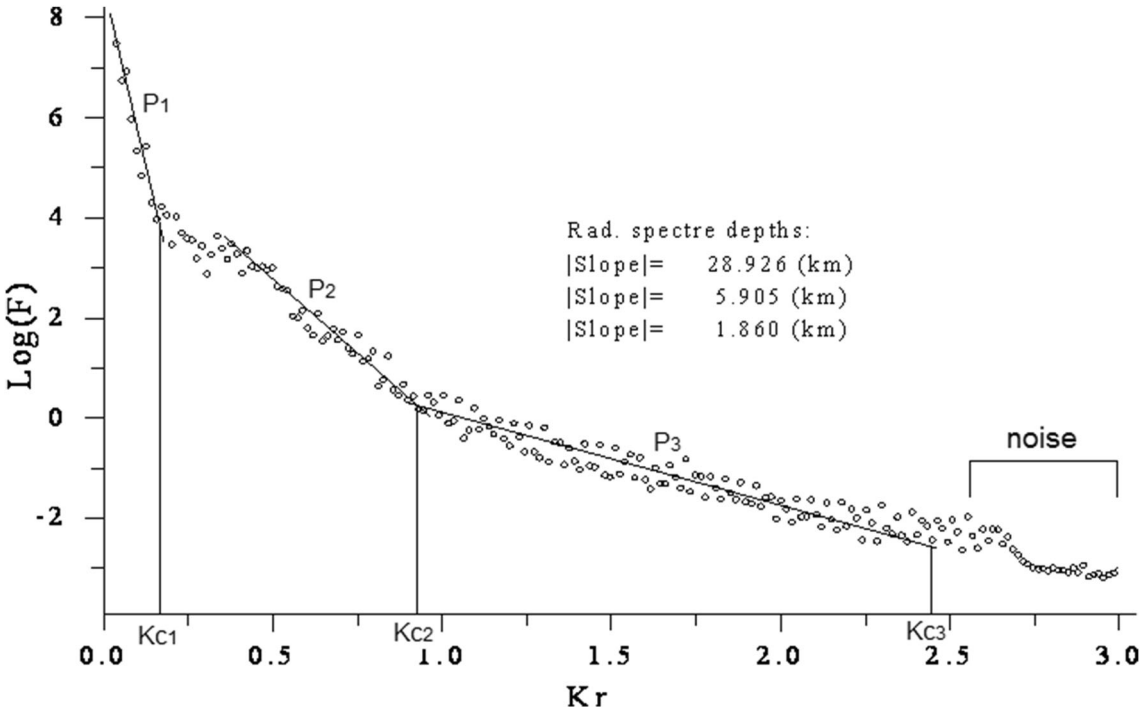

Fig. 3 Power spectrum of the Bouguer gravity data

Parker–Oldenburg algorithm provides a link between the sum of interface topography's Fourier transformation and Fourier transform of Bouguer gravity data. On the other hand, a formulation including depth and density of each layer interface is iteratively, as given in Eq. (1) (Parker 1973; Oldenburg 1974). The formulation uses the FT and can be used to calculate the gravity anomalies of homogeneous layers with terrain topography as follows:

$$f[z_1(x)] = -\frac{f[\Delta g(x)]e^{|k|z_0}}{2\pi G g} - \sum_{n=2}^{\infty} \frac{|k|^{n-1}}{n!} f\left[z_1^n(x)\right], \quad (1)$$

where $f[\Delta g(x)], G, g, k, z_1(x)$ and z_0 are the FT of the gravity data, gravity constant, density difference between layers, wavenumber, depths to geometry of interface obtained from inversion at each survey position, and average depth calculated from power spectrum,

respectively. Equation (1) works iteratively to calculate the density interface topography using $\Delta g(x)$ and z_0. Altınoğlu et al. (2015) simply have explained the iterative usage of Eq. (1) as follows: in the iteration, first, $z_1 = 0$ or an approximate value is taken and obtained a solution. The inverse FT of the solution ensures the first prediction of interface geometry. Then, the interface geometry information can be repeatedly utilized to designate the right side of Eq. (1). The recapitulation proceeding pursues until the convergence criteria are reached.

Techniques for lineaments

In gravitational studies in the literature, HG, AS, TI, and HTA techniques are generally organized to delineate the lineaments according to Bouguer gravity data (Cooper and Cowan 2006; Bilim 2007; Salem et al. 2008; Kumar et al. 2009; Altınoğlu et al. 2015). However, all equations in this study are rearranged according to the FVD of gravity data. Evjen (1936) pointed out the first time the benefits of utilizing the FVD of gravity data. Oruç and Keskinsezer (2008) and Oruç (2010) carried out the first application of TI techniques leading to image linear geological structure in interpretation of FVD of gravity data after low-pass filtering. We also applied these equations to FVD of regional gravity data. For this reason, Butterworth low-pass filter was used to separate the residual and regional gravity data from the Bouguer gravity data. Next, the fast Fourier transform (FFT) technique was used to calculate the FVD of regional gravity data as introduced by Gunn (1975). By considering the FVD of regional gravity data, the brief explanations of the methods used in the study are following.

The HG technique was developed by Cordell and Grauch (1985) and is given in Eq. (2). The highest amplitude values of HG depict edges of anomaly sources. On the other hand, HG is powerful to monitor the correlation of FVD of regional gravity anomalies with surface and covered faults:

$$\mathrm{HG} = \sqrt{\left(\frac{\partial^2 g}{\partial x \partial z}\right)^2 + \left(\frac{\partial^2 g}{\partial y \partial z}\right)^2}. \tag{2}$$

The AS technique can be defined by Eq. (3) and the amplitude of the AS is a widely utilized technique that generates bell-shaped curves above subsurface anomalous targets and is the maximum on the edges of the targets (Nabighian 1972). In Eq. (3), horizontal derivative detects lateral edges, vertical derivative localizes anomaly to a certain location, and finally, AS generates the largest amplitude at the edges of the structure which have highly density contrast:

$$\mathrm{AS} = \sqrt{\left(\frac{\partial^2 g}{\partial x \partial z}\right)^2 + \left(\frac{\partial^2 g}{\partial y \partial z}\right)^2 + \left(\frac{\partial^2 g}{\partial z^2}\right)^2}. \tag{3}$$

It is reported (Miller and Singh 1994; Cooper and Cowan 2006) that HG and AS techniques give poor information about deep structures because of lower density contrast. Another weakness of both techniques is that it cannot be resolved when structures overlap, because the overlapping causes that edges of all structures appear to such an edge (Ansari and Alamdar 2011). To partly overcome these weaknesses, Miller and Singh (1994), and Cooper and Cowan (2006) have developed more effective techniques in recent years. One of these techniques is TI technique which gives better results from both shallow and deep structures. Miller and Singh (1994) introduced the TI equation with normalization, as given in

$$\mathrm{TI} = \tan^{-1}\left(\frac{\frac{\partial^2 g}{\partial z^2}}{\sqrt{\left(\frac{\partial^2 g}{\partial x \partial z}\right)^2 + \left(\frac{\partial^2 g}{\partial y \partial z}\right)^2}}\right). \tag{4}$$

TI technique works also well when density contrast is either strong or weak. If the density contrast is positive, the sign of TI value is plus, zero, and minus when above, edge, and outside of the anomalous mass, respectively. The values of TI change between -0.785 ($-\pi/4$) and $+0.785$ ($+\pi/4$). Oruç (2010) suggested that the half distance between the contours of -0.785 and $+0.785$ radians

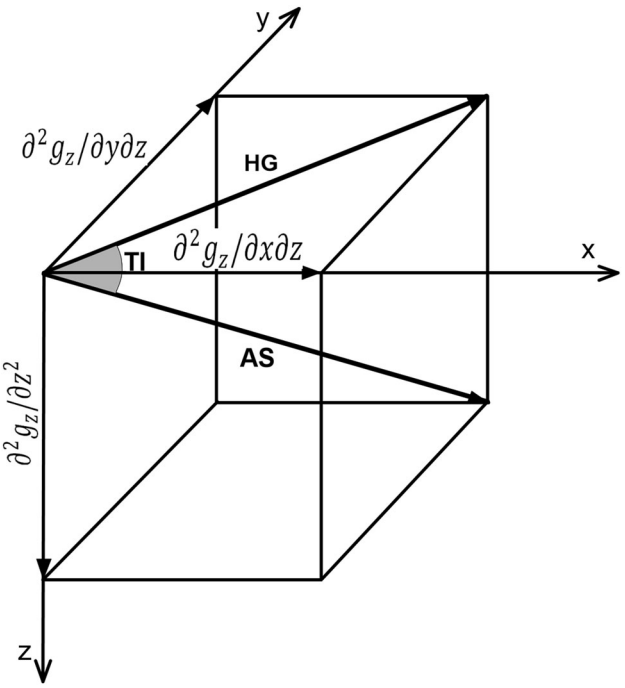

Fig. 4 Schematic diagram illustrating the geometrical meaning of all equations in this paper (redesigned after Oruç 2010)

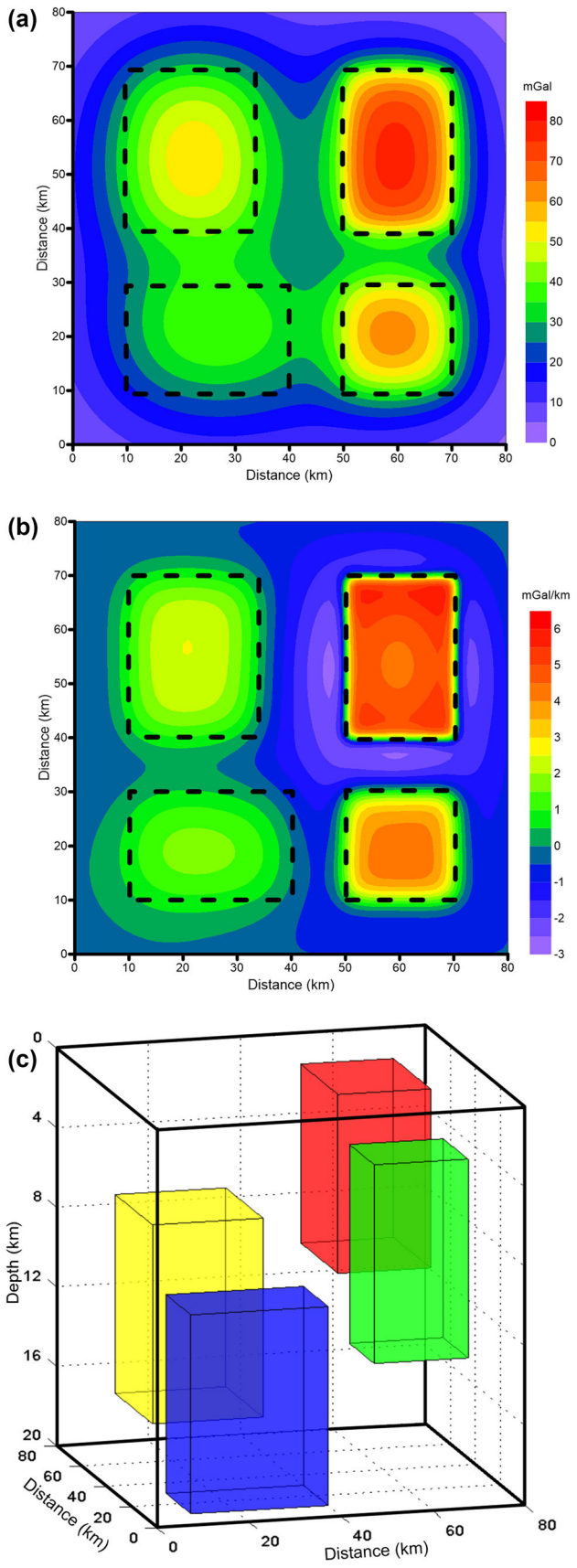

◀**Fig. 5** **a** Gravity data of the model, **b** FVD data of the gravity data, and **c** position of the prisms. Dashed lines in **a** and **b** show the edges of upper surface of the prisms

corresponds to the depth of the top of the structure from surface.

The last technique used in this study is the HTA which was proposed by Cooper and Cowan (2006) to determine the source edges effectively. Since the HTA as in written in Eq. (5) is hyperbolic expression unlike the standard TI technique in Eq. (4), the value of HTA is not an angular value but a scalar quantity. It is used real component of HTA values because of complex character. On the other hand, the HTA technique is less susceptible to shallower source effects (considered as noise), and provides more detailed results for buried targets. HTA values take positive, zero, and negative values, respectively, over, edge, and outside of source (Cooper and Cowan 2006). The HTA is given by the following formula:

$$\mathrm{HTA} = R\left[\tanh^{-1}\left(\frac{\frac{\partial^2 g}{\partial z^2}}{\sqrt{\left(\frac{\partial^2 g}{\partial x \partial z}\right)^2+\left(\frac{\partial^2 g}{\partial y \partial z}\right)^2}}\right)\right] \quad (5)$$

where R shows real component.

The geometrical means of the equations mentioned from Eqs. (2–5) are drawn in Fig. 4.

To show the effectiveness and reliability of the use of FVD of gravity data instead of gravity data and of the methods, we calculate a synthetic gravity data (Fig. 5a) and it is FVD of gravity data (Fig. 5b) for the earth model shown in Fig. 5c using the POTENSOFT software.

In the earth model, there are four vertical prisms which have 0.3 g/cm^3 density contrasts; in the meanwhile, the depths of synthetic prisms are 1, 3, 7, and 10 km, as given in Fig. 5c. The HG, AS, TI, and HTA techniques were performed to FVD of gravity data in Fig. 5b and obtained results were presented in Fig. 6.

As it is seen well from Fig. 6a, the locations and edges of the prisms are purely determined by the HG method. However, the highest magnitude of HG anomalies is observed from the shallower prism (red color in Fig. 5c). Therefore, this means that the HG magnitude is sensitive to depth of prisms and we easily recognize the prism depth by tracing the amplitudes of anomalies in HG map. It is obtained the same result with HG results when applied the AS method to FVD of gravity data. Therefore, it can be said that AS technique smears the boundaries of the prisms when compared HG technique. Calculated TI and HTA maps are shown in Fig. 6c, d, respectively. On the maps, zero contours show the edges (or boundaries) of the prisms. On the other hand, the maximum and minimum values of

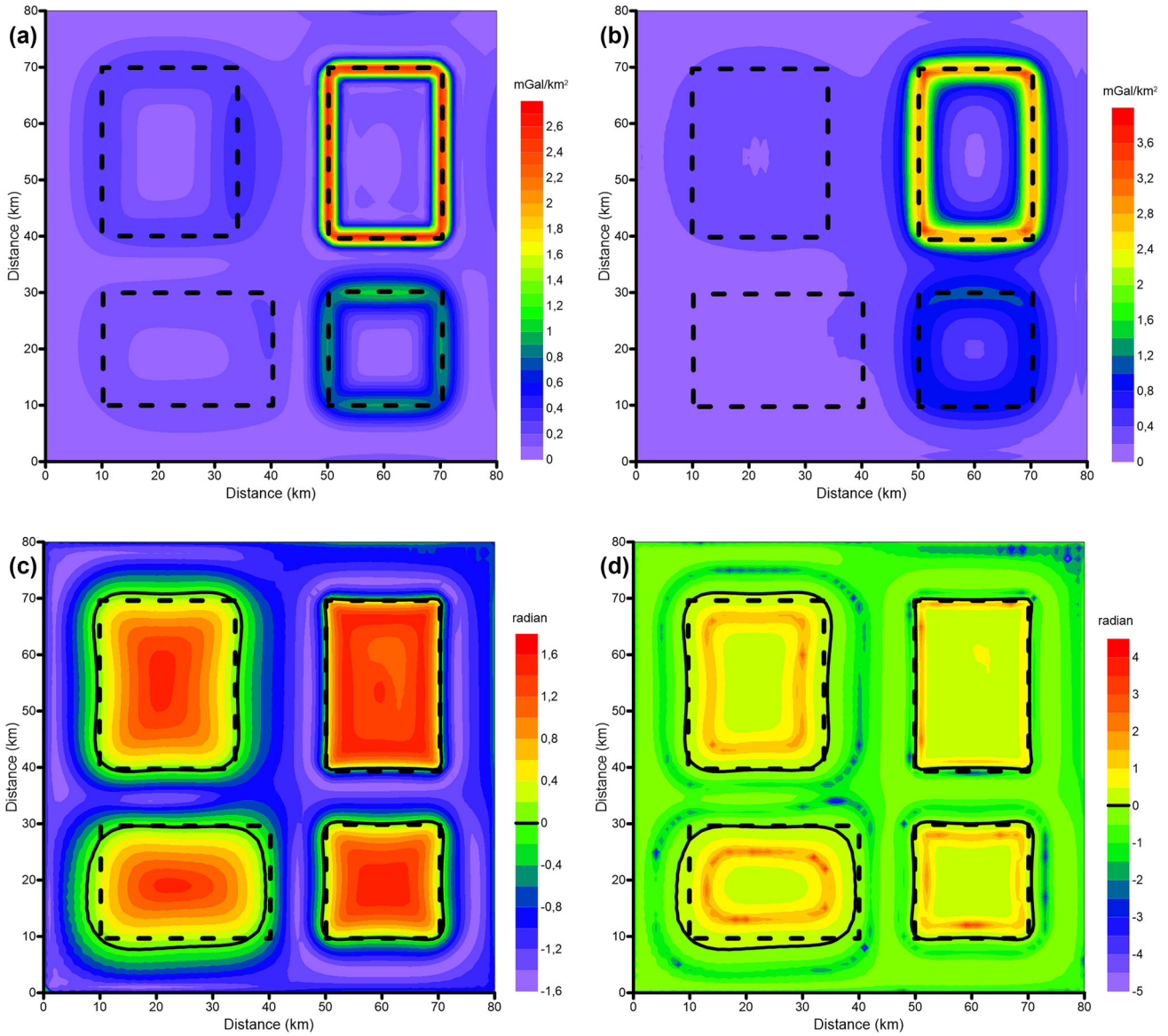

Fig. 6 **a** Horizontal gradient map, **b** analytic signal map, **c** tilt angle map, and **d** hyperbolic of tilt angle map of the model. Black dashed lines show the real boundaries of prisms, while solid lines show zero contours in **c** and **d** which mark the edge of prisms

TI and HTA are placed in inside and outside of the prisms. According to that, it can be understood that TI and HTA techniques are very useful to determine the edges of subsurface structures that have different densities and depths. From the synthetic tests, it could be excluded that it can be obtained lineaments of subsurface structures when all methods applied to the FVD of gravity data. However, among these methods, TI and HTA methods are more proper to get better findings that define the edges of subsurface structures, because these are sensitive to either depth or shallow targets, whereas HG and AS are sensitive to shallow units more.

Results

As seen from gravity anomalies of the region shown in Fig. 2, it is observed the NE–SW trending which is coherent well with the syncline-basement topography developed in eastern part of Azerbaijan. On the other hand, if it is locally evaluated, we see that the crust is thicker in NE part and is thinner in SW part of the region. This is controversial case when compared with general gravity anomalies between continental and oceanic crust. Kadirov (2000), Kadirov et al. (2012a, b, 2015) and Alizadeh et al. (2016) declared that the Shamakhy–Gobustan synclinoria can be characterized with large negative anomalies in the

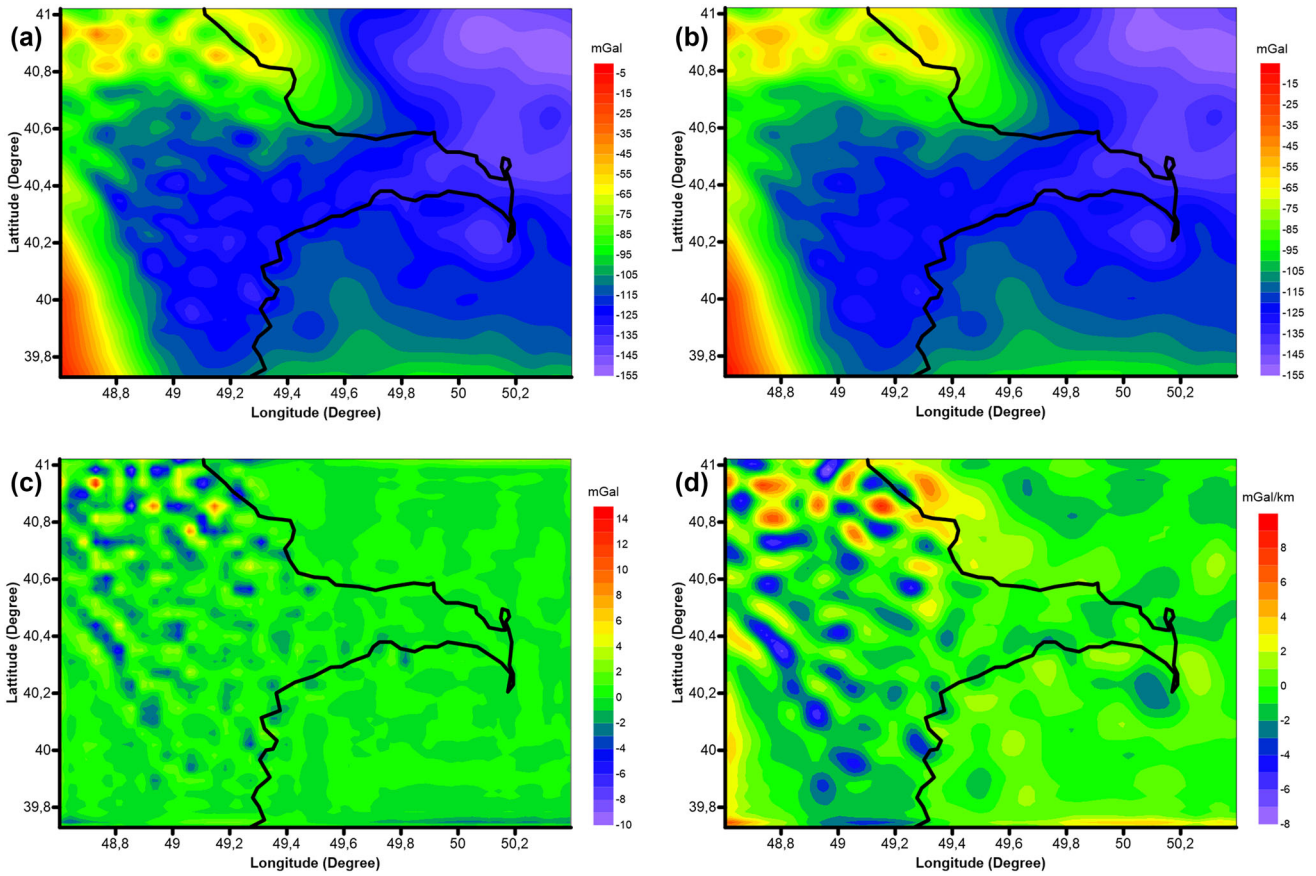

Fig. 7 **a** Bouguer gravity, **b** regional gravity, **c** residual gravity, and **d** FVD of regional gravity map of the study area

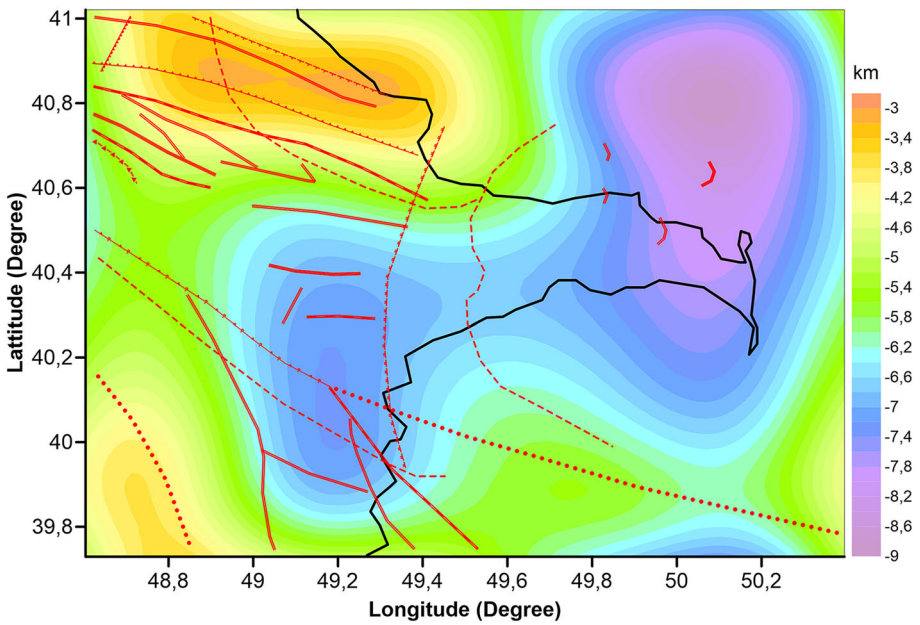

Fig. 8 Geometry of basement interface (red solid and dotted lines show the lineaments, as illustrated in Fig. 1)

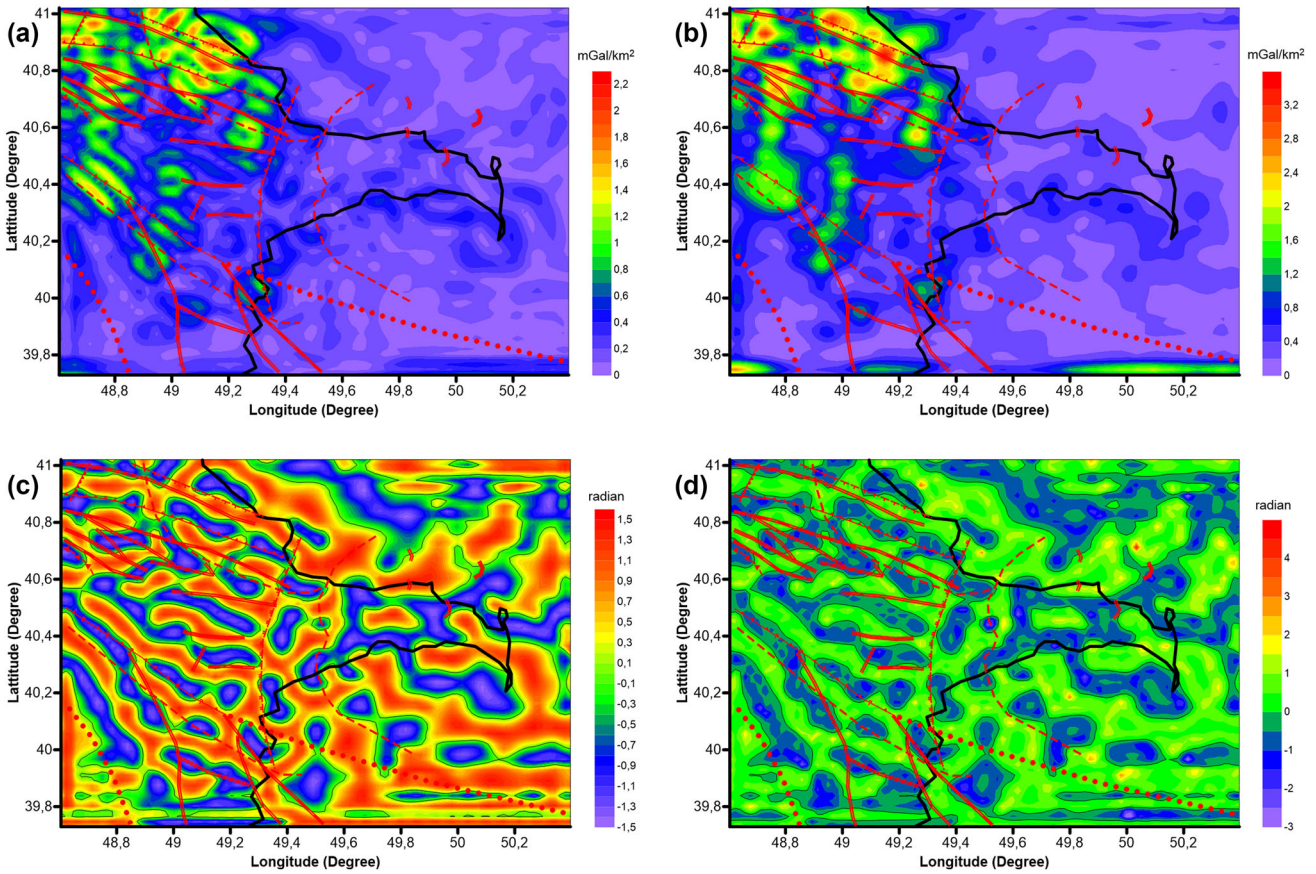

Fig. 9 **a** Horizontal gradient, **b** analytic signal, **c** tilt angle, AND **d** hyperbolic of tilt angle map of the study area. The lineaments on the maps are known lineaments (red lines)

mid and northeast parts of Bouguer anomalies because of thick sediment deposition.

We first obtained the depth level for region by evaluating the power spectrum of the gravity values. These are calculated as 1.86, 5.91, and 28.93 km for the interface between hard and soft sediment layers, the basement depth, and the mean continental Moho depth, respectively.

Geometry of basement interface

To understand how to vary the basement topography of the region, 3D modeling was performed and this also leads to delineate the geostructural boundaries in the region. On the other hand, Kadirov (2000) determined that the upper surface of the Mesozoic level of the region varies from 1 to 10 km from the previous studies such as geophysical and borehole data belonging to the region. The regional gravity anomaly map in Fig. 7b, necessary to inversion process, was obtained by applying a low-pass filter (Kc = 0.93 km^{-1}) to Bouguer gravity map in Fig. 7a. The FVD of regional gravity map in Fig. 7d was produced from regional gravity map and the residual gravity data in Fig. 7c.

The inversion process was performed using the 3DINVER software based on the Parker–Oldenburg algorithm iteratively. An initial depth is taken as 5.91 km to reproduce the geometry of basement interface and a density contrast (0.3 g/cm^3) was determined by considering the densities of sediment until basement depth ($\sim$ 2.4 g/cm^3) and metamorphic unit ($\sim$ 2.7 g/cm^3). Besides, the convergence criterion was utilized as 0.01 km, cut-off wavenumbers are taken as 0.15 and 0.93 km^{-1} from power spectrum, respectively. The geometry of basement interface obtained from inversion is shown in Fig. 8. According to the results, the sediments in NE part of region are thicker than that of SW part of region. The thinnest sediment layer is in the NW of the study area. This shows that both the depths of basement and Moho discontinuity toward NE of the region increase. In addition, we concluded that this sediment thickening and topographic undulation of basement is related to the main tectonic structure of investigated region.

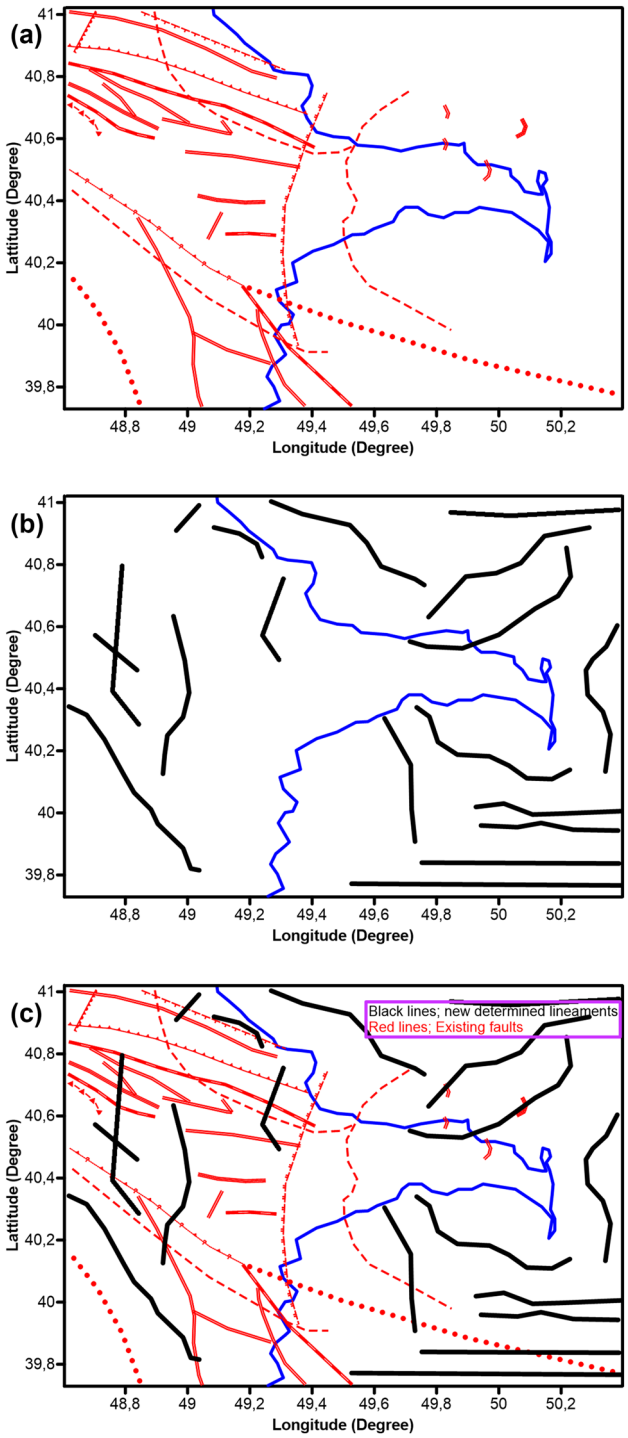

Fig. 10 **a** Known faults (Kadirov et al. 2015) (red solid and dotted lines), **b** Determined lineaments (black solid lines), and **c** Tectonic structure of the study field

It is well known the edges between the anticlinals and synclinals in geometry of basement interface undulation are involved to the faults (Oruç et al. 2013). Our results are compatible with the previous studies as we expected. The high uplift of interface is located at NE of the Apsheron Peninsula. The geometry of basement interface is shallower to NW and SW parts of the study area. Furthermore, the familiar lineaments and the geometry of basement interface undulation are in good agreement with the sediment topography as suggested by Kadirov et al. (2015).

Detection of the lineaments

The edges of the geostructures and tectonic lineaments in the region are nearly related to the maxima of the HG and AS contours, and zero value of TI and HTA of FVD of regional gravity anomalies, as shown in Fig. 9.

The maxima contours of HG and AS show basically NW–SE and NE–SW directed discontinuities, as shown in Fig. 9a, b. On the other hand, when look closer to map of the AS, a lineament is seen as east–west trending in south-east part of study area. The maxima of HG and AS illustrate generally significantly boundaries of structures and faults. The TI and HTA maps have zero values on the lineaments, whereas HG and AS maps have maxima values, as shown in Fig. 9c, d. By tracing the zero values of TI and HTA maps, we observed that most of lineaments show NW–SE and NE–SW trending and particularly flat lineaments in direction of E–W in the SE part of the region, as shown in Fig. 9c, d. When we interpret together these four maps, the lineaments which are east–west trending in south-east part of the study area are never seen on HG map, while only one is seen on AS. Besides, several lineaments are seen on TI and HTA maps. As explained by synthetic model calculations, this can be interpreted that these lineaments correspond to deep faults in the area. It is clearly observed that the all lineaments newly marked are fairly

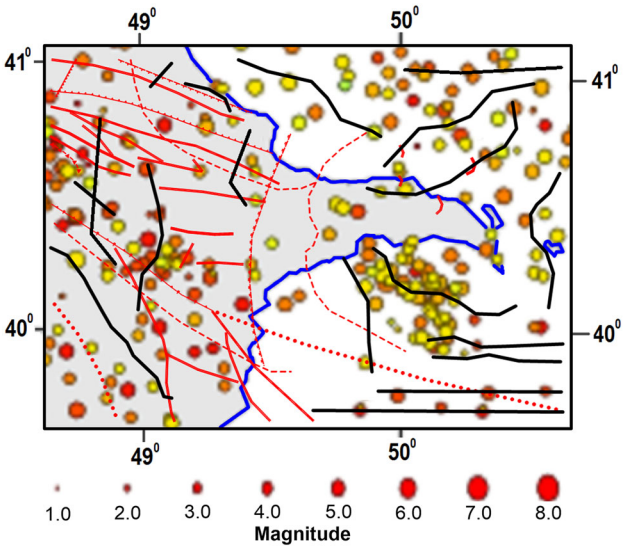

Fig. 11 Distribution of the epicenters of the earthquakes from 1980 to 2015 around the study area (ISC 2014)

compatible with each other in the four maps (Fig. 9a–d). Therefore, besides the previous known lineaments, as shown in Fig. 10a, we determined the new lineaments, as shown in Fig. 10b, by interpreting the new maps in Fig. 9. Both old (red lines) and new (black lines) lineaments have been combined and given in Fig. 10c.

According to the International Seismological Centre (ISC 2014), distribution of the epicenters of the earthquakes from 1980 to 2015 around the study area is shown in Fig. 11. The epicenter distribution of the earthquakes, whose magnitudes are greater than 1, is shown in this figure. According to the map, the earthquake epicenter distribution supports the new lineaments estimated with this study.

Discussion

In this study, we used the HG, AS, TI, and HTA techniques to extract new lineaments. These techniques are old, but they have been applied for the first time to FVD of regional gravity values of Shamakhy–Gobustan and Absheron region. Using the maps produced from these techniques, we determined new lineaments situated in Shamakhy–Gobustan synclinorium. Especially, we defined the uplift of basement tomography, NW of study area in Fig. 8, related to Shamakhy–Gobustan synclinorium. Furthermore, the thickness of sediment of the study area has been found as 3–9 km. Whereas we cannot see the maxima in some parts of HG and AS maps (Fig. 9a, b), zero contour values on TI and HTA maps (Fig. 9c, d) provide us to reveal the new lineaments. It is remarked that there is no lineament (red lines in Fig. 10c) detected by the previous studies (Radjabov 1978; Kadirov et al. 2012a, b, 2015 and Alizadeh et al. 2016) in the some parts of the study area; in this study, the new lineaments (black lines in Fig. 10c) in the study area have been determined.

Conclusions

The Shamakhy–Gobustan and Absheron regions are an important areas due to its tectonically structure hydrocarbon. In this study, the new lineaments which have not been discovered so far were determined by interpreting the HG, AS, TI, and HTA maps obtained from first vertical derivative of the regional gravity data. These new lineaments are coherent with the epicenters of the earthquakes. According to our findings, a new lineament map of the region has been firstly presented in this paper. Synthetic gravity data for an earth model including four prisms having different sizes and depths were calculated to compare the techniques used and to understand their responses. On the other hand, the topography of the basement was modeled to see sediment thickness and to understand the controversial case of Bouguer gravity data. The locations of the new lineaments were determined utilizing the relations with the maximum values of HG and AS, and zero contours of TI and HTA maps. TI and HTA maps provided to image the deep faults, especially. The lineaments were controlled by comparing with the known tectonic units of area and the new lineaments were defined for the first time. It was seen that the techniques used in this study are very effective to determine and to image the old and new lineaments in the Shamakhy–Gobustan and Absheron regions. As a result, the new lineaments would be tested by new studies to be performed in the future and provide a new look to seismologic events which will likely be occurred in the area. The results of this study should be supported by other geophysical studies and data sets after this time. Therefore, the parts which have high earthquake hazards were existed in the area before, but not discovered yet could easily be determined.

References

Alizadeh AA, Guliyev IS, Kadirov FA, Eppelbaum LV (2016) Geosciences of Azerbaijan. Geology 1:237

Altınoğlu FF, Sarı M, Aydın A (2015) Detection of lineaments in Denizli Basin of Western Anatolia region using bouguer gravity data. Pure Appl Geophys 172:415–425

Ansari AH, Alamdar K (2011) A new edge detection method based on the analytic signal of tilt angle (ASTA) for magnetic and gravity anomalies. Iran J Sci Technol 35(A2):81–88

Arısoy MÖ, Dikmen Ü (2011) Potensoft: MATLAB-based Software for potential field data processing, modelling and mapping. Comput Geosci 37:935–942

Bilim F (2007) Investigation into the lineaments and thermal structure of Kütahya-Denizli Region Western Anatolia from using aeromagnetic, gravity and seismological data. Phys Earth Planet Inter 165:135–146

Bochud M (2011) Tectonics of the eastern greater caucasus in Azerbaijan. In: GeoFocus, Vol 30, thesis No: 1733, PhD thesis in tectonics and general geology at the University of Fribourg (25 Oct 2011), Switzerland

Brunet MF, Granath JW, Wilmsen M (2009) South Caspian to Central Iran basins: introduction. In: Brunet MF, Wilmsen M, Granath JW (eds) South Caspian to Central Iran basins, vol 312. The Geological Society of London, London, pp 1–10 **(Special publication)**

Cooper GRJ, Cowan DR (2006) Enhancing potential field data using filters based on the local phase. Comput Geosci 32(10):1585–1591

Cordell L, Grauch VJS (1985) Mapping basement magnetization zones from aeromagnetic data in the San Juan Basin, New Mexico. In: Hinze WJ (ed) The utility of regional gravity and magnetic anomaly maps. Society of Exploration Geophysicists, Tulsa, pp 181–197

Evjen HM (1936) The place of the vertical gradient in gravitational interpretations. Geophysics 1:127–136

Gomez-Ortiz D, Agarwal BNP (2005) 3DINVER.M: a MATLAB program to invert the gravity anomaly over a 3-D horizontal

density interface by Parker–Oldenburg's algorithm. Compu Geosci 31:513–520
Gunn PJ (1975) Linear transformations of gravity and magnetic fields. Geophys Prospect 23(2):300–312
International Seismological Centre (ISC) (2014), On-line Bulletin, http://www.isc.ac.uk, Internatl. Seismol. Cent., Thatcham, United Kingdom. Accessed 04 April 2017
Kadirov FA (2000) Application of the Hartley transform for interpretation of gravity anomalies in the Shamakhy-Gobustan and Absheron oil- and gas-bearing regions Azerbaijan. J Appl Geophys 45:49–61
Kadirov FA, Babayev G, Gadirov A (2012a) Analysis of horizontal to vertical spectra of microseismics for Baku City. In: Problems of Cybernetics and Informatics (PCI), 2012 IV International Conference
Kadirov FA, Babayev G, Gadirov A, Safarov RT, Mukhtarov AS (2012b) Microzonation of the Baku city using miktrotremor measurements, In: Problems of reduction of natural hazards and risks, International scientific and practical conference "GEORISK 2012". In 2 Vols. Volume 1. Moscow. Peoples' Friendship University of Russia (PFUR), 384:94-98
Kadirov FA, Ahadov BG, Gadirov AH, Babayev GR, Mammadov SG, Safarov RT (2015) Microtremor survey and spectral analyses of H/V ratio for Baku city (Azerbaijan). In: Proceedings of Azerbaijan national academy of sciences, the sciences of earth, no:3
Kumar NJ, Singh AP, Rao MRKP, Chandrasekhar DV, Singh B (2009) Gravity signatures derived crustal structure and tectonics of Achankovil shear zone Southern India. Gondwana Res 16:45–55
Miller HG, Singh V (1994) Potential field tilt -a new concept for location of potential field sources. J Appl Geophys 32:213–217
Nabighian MN (1972) The Analytic Signal of two dimensional magnetic bodies with polygonal cross section: its properties and use for automated anomaly interpretation. Geophysics 37:507–517
Oldenburg DW (1974) The inversion and interpretation of gravity anomalies. Geophysics 39:526–536
Oruç B (2010) Edge detection and depth estimation using a tilt angle map from gravity gradient data of the Kozaklı-Central Anatolia Region Turkey. Pure Appl Geophys. https://doi.org/10.1007/s00024-010-0211-0
Oruç B, Keskinsezer A (2008) Structural setting of the northeastern Biga Peninsula (Turkey) from tilt derivatives of gravity gradient tensors and magnitude of horizontal gravity components. Pure Appl Geophys 165:1913–1927
Oruç B, Sertçelik İ, Kafadar Ö, Selim HH (2013) Structural interpretation of the Erzurum Basin Eastern Turkey, using curvature gravity gradient tensor and gravity inversion of basement relief. J Appl Geophys 88:105–113
Parker RL (1973) The rapid calculation of potential anomalies. Geophys J R Astr Soc 31:447–455
Radjabov MM (1978) Study of the structure of the earth's crust-consolidated complex of the Azerbaijan using deep seismic sounding and refracted wave-correlation method data the Structure of the Earth's Crust and Upper Mantle in the Central and East Europe. Naukova Dumka, Kiev, pp 205–211 **(In Russian)**
Saintot A, Brunet M-F, Yakovlev F, Sebrier M, Stephenson RA, Ershov AV, Chalot-Prat F, Mccann T (2006) The Mesozoic-Cenozoic tectonic evolution of the Greater Caucasus. Geol Soc Lond Mem 32:277–289
Salem A, Williams S, Fairhead D (2008) Interpretation of magnetic data using tilt-angle derivatives. Geophysics 73:1–10
Shikhalibeyli ESh (1972) Location of Azerbaijan in general structure of the Caucasus and surrounding folded region. In: Azizbekov ShA (ed) Geology of the USSR Azerbaijan, vol XLVII. Nedra, Moscow, pp 286–290
Spector A, Grant FS (1970) Statistical models for interpreting aeromagnetic data. Geophysics 35:293–302
Vincent SJ, Morton AC, Carter A, Gibbs S, Barabadze TG (2007) Oligocene uplift of the western Gre ater Caucasus: an effect of initial Arabia-Eurasia collision. Terra Nova 19:160–166

Acta Geophysica (2018) 66:51–70
https://doi.org/10.1007/s11600-017-0105-y

RESEARCH ARTICLE - APPLIED GEOPHYSICS

Unbiased total electron content (UTEC), their fluctuations, and correlation with seismic activity over Japan

Pierre-Richard Cornely[1] · John Hughes[2]

Received: 27 December 2016 / Accepted: 2 December 2017 / Published online: 16 December 2017

Abstract
Earthquakes are among the most dangerous events that occur on earth and many scientists have been investigating the underlying processes that take place before earthquakes occur. These investigations are fueling efforts towards developing both single and multiple parameter earthquake forecasting methods based on earthquake precursors. One potential earthquake precursor parameter that has received significant attention within the last few years is the ionospheric total electron content (TEC). Despite its growing popularity as an earthquake precursor, TEC has been under great scrutiny because of the underlying biases associated with the process of acquiring and processing TEC data. Future work in the field will need to demonstrate our ability to acquire TEC data with the least amount of biases possible thereby preserving the integrity of the data. This paper describes a process for removing biases using raw TEC data from the standard Rinex files obtained from any global positioning satellites system. The process is based on developing an unbiased TEC (UTEC) data and model that can be more adaptable to serving as a precursor signal for earthquake forecasting. The model was used during the days and hours leading to the earthquake off the coast of Tohoku, Japan on March 11, 2011 with interesting results. The model takes advantage of the large amount of data available from the GPS Earth Observation Network of Japan to display near real-time UTEC data as the earthquake approaches and for a period of time after the earthquake occurred.

Keywords Seismic ionospheric events · Unbiased total electron content · Pre-earthquake signals · Earthquake precursor signal · ELF–ULF electromagnetic waves

Introduction

Earthquake physics is a very complex and broad topic. It involves many scales of the earth's crustal structure starting from tectonic plates and finishing with the microscopic processes involved in the friction and generation of electric charge and ensuing chemical reactions. Collision of tectonic plates leads to a geometrical change in tectonic plate distribution. This geometrical change leads to strain accumulations within the earth's crust and subsequently to mechanical deformations and crust rupture. The process of rupture is a process best described by greater than normal tectonic shifts and the subsequent effects that are felt on earth as earthquakes. The science behind earthquakes is, therefore, an important topic, but yet, it is not well understood. The primary reason for this lack of understanding is that a real pursuit of earthquake science will require inputs from various disciplines, ranging from chemistry and pure mechanics to geology and space plasma physics, demanding simultaneous knowledge of many special disciplines such as plate tectonics, seismology, atmosphere and ionosphere physics and chemistry, and atmospheric electricity. Atmospheric electricity emerges from the atmospheric plasma that lives above the earth's surface from ~ 90 to 1000 km. The atmospheric plasma concept postulates that a section of the earth's atmosphere becomes chemically active as a result of processes originally taking place deep beneath the earth. These processes include rock configurations in the earth's crust changing as

✉ Pierre-Richard Cornely
pierre-richard.cornely@enc.edu

[1] Science and Tecnology Division Chair, Eastern Nazarene College, Quincy, MA, USA

[2] Department of Physics and Engineering, Chair, Eastern Nazarene College, 23 East Elm Avenue, Quincy, MA, USA

a result of the abnormal tectonic plate movements. These movements create stress within these rocks and start a series of processes leading to readily observable parameters at the earth surface. This concept is one of the links in the chain of the physical processes, from tectonic movements to tectonic shifts to the tectonic plate ruptures, leading to the concept of seismic–ionosphere coupling, the main purpose of this paper. This link was first described by Freund et al. (2006) and Freund (2010) after conducting a laboratory experiment which showed that igneous and high-grade metamorphic rocks contain defects, known as peroxy defects or holes are released in the oxygen anion sub-lattice when under stress. These positive charge carriers are highly mobile, able to flow out of stressed rocks, deep within the earth crust, into surrounding unstressed rocks closer to the earth surface. This change in chemical dynamics can create a difference in potential between sections of the earth crust, setting the stage for various ionization processes on the earth surface, immediately beneath and well above the earth surface. Several authors have also reported about changes in lithosphere–atmosphere–ionosphere coupling dynamics due to seismic and pre-earthquake activities. These reports include but are not limited to: electromagnetic phenomena related to earthquake prediction (Hayakawa and Fujinawa 1994; Hayakawa and Molchanov 2002); correlation analysis techniques revealing ionosphere precursors of earthquakes (Pulinets et al. 2004); and atmospheric and ionospheric coupling phenomena related to large earthquakes (Parrot et al. 2016). The majority of these previous discoveries point to the fact that changes in lithosphere–atmosphere–ionosphere coupling dynamics due to seismic and pre-earthquake activities are complex, multi-faceted, and multi-dimensional. These changes are not isolated and can be readily traced back to lower subsections of the earth such as the earth's inner and outer core. The earth core has been the center of most of the investigations, often revealing unexpected and interesting anomalies that seem to be related to seismological events. For example, in addition to its global North–South anisotropy, there are two other enigmatic seismological observations (Poupinet et al. 1983) related to the earth's inner core: the asymmetry between its eastern and western hemispheres (Yu et al. 2005; Souriau and Poupinet 1991; Souriau and Roudil 1995; Kennett and Engdahl 1991; Kennett et al. 1995; Song and Helmberger 1995; Zou et al. 2008) and the presence of a layer of reduced seismic velocity at the base of the outer core. The resulting strong asymmetry of buoyancy flux caused by light elements is anticipated to have an important impact on the dynamics of the outer core and on the geo-dynamo. Karato (1999) reported that based on geodynamic and mineral physics considerations, flow induced by the stress due to the magnetic field, known as the Maxwell stress, near the inner core boundary produces an asymmetric fabric responsible for the currently observed seismic anisotropy. This seismic anisotropy is responsible for the geometry of the magnetic field near the inner core boundary, and therefore, seismological observations might provide constraints on the geo-dynamo and vice versa. The flow induced by the stress due to this magnetic field also causes a non-uniform release of energy at the inner core boundary, associated with solidification and melting which affect the pattern of convection in the outer core. All of these observations imply that there is a fundamental connection between the seismic and pre-earthquake dynamics taking place in the earth inner and outer cores and the related observables on and below the earth crust and well beyond the earth surface (troposphere, and ionosphere). As a result, our hypothesis about seismic–ionospheric coupling is based on the following:

(a) Seismic anisotropy can change the geometry of the magnetic field near the earth inner core boundary. This change can be the genesis of electromagnetic forces within the earth inner and outer cores believed to generate special electromagnetic fields, additional to fields currently known to naturally contribute to the earth average magnetic field, that are related to seismic and pre-earthquake activities.
(b) Seismic and pre-earthquake electromagnetic fields can either be constant or time varying and can propagate up to the earth surface and beyond.
(c) Positive holes born from chemical and other dynamics within rocks under stress can flow out of stressed rocks and make it to the earth surface.
(d) Positive holes trapped at the earth surface create a surface potential, which in turn creates a short range but steep electric (E) field perpendicular to the surface.
(e) At the ground-to-air interface, this E field can ionize air molecules, most likely O_2 turning into airborne O_2^+ and changes in air chemistry. At the ground-to-water interface, this E field leads to the electrochemical oxidation of H_2O to H_2O_2 (hydrogen peroxide) and thereby changes in water chemistry.
(f) These positive charges also initiate combination and recombination processes between ion species in the troposphere and ionosphere that will ultimately create tropospheric and ionospheric disturbances.
(g) The ionospheric disturbances, as seen from the point of view of variations in UTEC correlated with seismic and pre-earthquake activities in Japan, are the subject of the investigation in this paper.

The ionosphere

The ionosphere is a frequency dispersive, inhomogeneous, stochastic, anisotropic, and non-linear medium in general, although some of these effects may be neglected under restricted conditions. Furthermore, the ionosphere is a dynamic gas and is subject to transport phenomena, such as winds and diffusion in several regions, which can redistribute the ionization over time. Since the ionosphere is such a complex medium, an overview of its behavior clearly cannot do justice to the myriad of effects that it is known to produce. This section attempts to describe some of the more significant and well-understood ionospheric phenomena. We will begin with a set of simplifying assumptions characteristic of an average ionosphere:

(a) The ionization in the upper atmosphere occurs primarily due to incident solar extreme ultraviolet (EUV) and X-ray radiation.
(b) The ionization in the ionosphere responds uniformly to all frequencies of energetic solar radiation.
(c) The ionization in the ionosphere is generally considered to be homogeneous.
(d) As the radiation enters the ionosphere, it is absorbed by ionospheric gas molecules at a rate proportional to the gas concentration (i.e., less absorption in sparse gas concentration).
(e) Deeper into the ionosphere, the concentration increases and the radiation is absorbed more rapidly.
(f) The ionization is proportional to the rate of absorption and as such, starting from the top of the ionosphere (higher altitudes), the ion density gradually increases to a maximum.
(g) At altitudes below the maximum ion density, the ion density drops off sharply because the solar ionizing radiation is almost completely attenuated by ionospheric gas molecules.
(h) Temperature is constant at all altitudes and there is no diffusion.

Based on (a)–(h), the composition of the ionosphere will vary with height and the primary constituents of each layer absorb different frequencies. One important factor in the formation of the ionosphere is the ion production rate. This is a fairly complicated process which involves several chemical and physical dynamics. As such, to compute the rate of ion production, several simplifying assumptions are also made such as:

1. The ionizing radiation is monochromatic and the ionosphere is homogeneous. That is, the ionosphere contains a single absorbing constituent and responds to the sole frequency of solar radiation being considered.
2. The curvature of the ionosphere is assumed to be planar, as shown in Fig. 1. In Fig. 1, the angle of incidence χ indicates the angle at which the incident solar radiation hits the earth's atmosphere. When χ is zero degrees, the sun is overhead, indicating maximum radiation from the sun and highest ion production rate.

To compute the electron density as a function of radius (or height above the earth's surface) $\mathbf{N}(r)$, the dynamics of the free electrons must be considered. In terms of electron density, the continuity equation for free electrons in the ionosphere is

$$\frac{\partial N}{\partial t} = q - l(N) - \nabla \cdot (N\vec{V}). \tag{1}$$

Basically, Eq. (1) states that the time rate of change of the electron density $\mathbf{N}$ is equal to the production rate $\boldsymbol{q}$ minus the loss rate $\boldsymbol{l}(\mathbf{N})$ and the loss due to transport mechanism, estimated to be traveling at a mean drift velocity vector $\mathbf{V}$. Under equilibrium and where transport can be neglected (1) reduces to

$$q = l(N). \tag{2}$$

When the positive ions are largely molecular, the production rate is proportional to $\mathbf{N}$ allowing us to modify (2) as

$$l(N) = \alpha N^2 \tag{3}$$

where α being the recombination coefficient. Thus, under the above restrictions, applying (2) and (3) results in $\mathbf{N}$ being expressed as follows:

$$N(r) = \begin{cases} N_{\mathrm{m}} \exp\left[1/2\left(1 - \left(\frac{r - r_{\mathrm{m}}}{y_{\mathrm{m}}}\right) - \exp\left(-\left(\frac{r - r_{\mathrm{m}}}{y_{\mathrm{m}}}\right)\right)\right) * \sec(\chi)\right], & r_{\mathrm{b}} < r < r_{\mathrm{m}}\left(\frac{r_{\mathrm{b}}}{r_{\mathrm{b}} - y_{\mathrm{m}}}\right) \\ 0, & \text{otherwise} \end{cases} \tag{4}$$

where $\mathbf{N}(r)$ electron density at radial distance r from the earth center, $\mathbf{N_m}$ peak electron density at the layer, r_{b} radial base height of the layer, r_{m} radial height of the peak density, y_{m} layer's semi-layer thickness (typically referred to as the scale height that relates height to temperature), χ zenith angle.

Equation (4) is a version of the Chapman layer profile of the ionosphere called the "Chapman alpha" distribution.

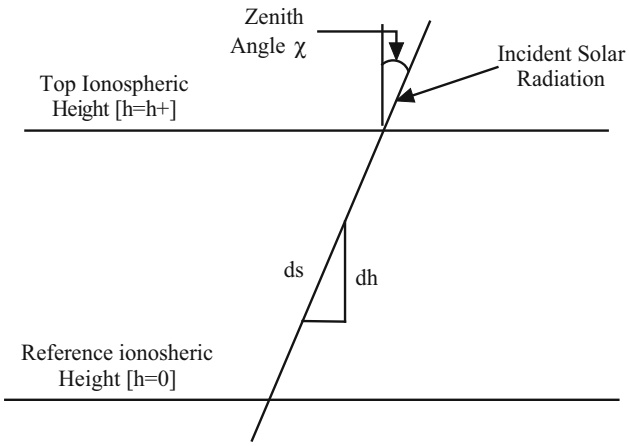

Fig. 1 Simplified Chapman Geometry

Naturally, it assumes that the solar zenith angle is small and incorporates all of the assumptions stated in (a)–(g) in Sect. 1. Given the large number of assumptions involved in the derivation of (4), the Chapman layer is not a completely accurate model of electron concentration in the ionosphere. First, the ionosphere is not chemically homogeneous and subject to monochromatic radiation. Second, temperature and thus scale height y_m vary with altitude.

Third, the mean velocity of the particles in the gravitationally stratified ionosphere, and hence, their temperature also varies with altitude. Fourth, transport mechanisms, affecting the electron–ion generation/recombination rate in the ionosphere, are not negligible in the F_2 layer. Fifth, the electron–ion recombination rate does not always follow a square law as in (3).

Finally, and more seriously perhaps, the Chapman theory does not explain the existence of ionized layers at night, in the absence of solar radiation, nor does it account for the fact that the maximum electron density is frequently reached several hours after local noon when the solar zenith angle is greater than zero. Nevertheless, the basic shape of the Chapman distribution, i.e., a pronounced peak with a sharp drop-off, gradually tapering off thereafter, is still preserved and, therefore, a very good approximation of the average behavior of the ionosphere. Thus, it is safe to assume that at the very least, we can begin with this average behavior in support of our analysis. It is also clear that when the ionosphere deviates from this average behavior, we should be able to identify the external forces responsible for the changes in ionization dynamics. There are many external forces known to exist, such as solar flares and magnetic storms (related to the sunspot cycle) that can influence the dynamics of ionization. These phenomena have been studied by scientists in very great details for a very long time (Ohl 1966; Simon et al. 2014), with a lot of available observations. The current sunspot cycle (cycle 24) reached a peak around 2014 (Ng 2016). As a result, we would expect the years 2013, 2014, and 2015 to be very active solar years. Active solar years result in higher than usual energy in the ultraviolet rays which can affect ionization in the ionosphere. More discussion on this subject will follow in upcoming sections.

Rock under stress and associated chemical processes

Freund (2010, 2011) described the chemical processes resulting from rocks under stress. He reports that during cooling from high temperatures, igneous rocks acquire O^- through an oxidation–reduction (red–ox) reaction. Redox reactions have a number of similarities to acid–base reactions. Fundamentally, redox reactions are a family of reactions that are concerned with the transfer of electrons between species. Like acid–base reactions, redox reactions are a matched set in the sense that an oxidation reaction does not typically occur without a reduction reaction happening at the same time. Oxidation refers to the loss of electrons, while reduction refers to the gain of electrons. Each reaction by itself is called a "half-reaction", simply because we need two of such half-reactions to form the whole reaction. A commonly known redox reaction is the ferrous hydroxides conversion into magnetite, hydrogen, and water as written in (5):

$$3\mathrm{Fe}\,(\mathrm{OH})_2 \rightarrow \mathrm{Fe_3O_4} + \mathrm{H_2} + 2\mathrm{H_2O}. \tag{5}$$

This reaction can be decomposed in half-redox reactions which begin with the oxidation of iron ions as in (6):

$$2\,(\mathrm{Fe}^{2+} \rightarrow \mathrm{Fe}^{3+} + \mathrm{e}^-) \tag{6}$$

and continue with the reduction of two water protons as in (7):

$$2\left(\mathrm{H_2O} + \mathrm{e}^- \rightarrow \frac{1}{2}\mathrm{H_2} + \mathrm{OH}^-\right). \tag{7}$$

In the case of igneous rocks under stress, an O^- acquired in an O^{2-} matrix becomes a defect electron, also known as a hole. O^{2-} matrix forms O^- pairs, equivalent to peroxy links $O^{\cdot}$. The symbol ($^{\cdot}$) represents a peroxy link that is typically electrically inactive in its native state. However, under stress, peroxy links can break and become active such as illustrated in (8):

$$\mathrm{O_3S_iO^{\cdot}OS_iO_3} + [\mathrm{S_iO_4}]^{4-} \rightarrow \mathrm{O_3S_iO^{\cdot e^-}OS_iO_3} + [\mathrm{S_iO_4}]^{3-} \tag{8}$$

where $[S_iO_4]^{3-}$ is actually a hole, because it has one less electron than $[S_iO_4]^{4-}$. This is the simple process where an electron (e^-) moves from $[S_iO_4]^{4-}$ to the activated peroxy

link $O^{\cdot}$ thereby creating a hole $[S_iO_4]^{3-}$, as illustrated in (9):

$$O_3S_iO^{\cdot\cdot}OS_iO_3 + [S_iO_4]^{4-} - e^- \rightarrow O_3S_iO^{\cdot\cdot e^-}OS_iO_3 + \text{hole}. \quad (9)$$

The electric (positive hole) currents can flow deep beneath the earth surface and can fluctuate thereby creating extremely low and ultralow frequency (ELF, ULF, below $\sim$ 10–20 Hz) electromagnetic waves that can propagate upward through the rocks. The ULF waves reach the earth surface and can further propagate upward to the troposphere and the ionosphere. The positive hole charge carriers are also highly mobile charge carriers. They can travel very far and very fast into surrounding unstressed rocks and can subsequently disturb the distribution of electrons in the ionosphere.

Ionospheric disturbances can be displayed using the variations in the number of electrons per meter's cube (called the electron density) above the earth surface. Ionospheric disturbances can also be displayed using the variations in the number of electrons per meters square [called the total electron content (TEC)] in a thin cylindrical tube along the line of sight between a Global Positioning Satellite (GPS) and a receiver on the ground. The TEC can be computed using the line integral from a GPS satellite (st) and a receiver (rx), as described in (10):

$$\text{TEC}\,(r,\theta,\phi,t) = \int_{\text{rx}}^{\text{st}} \text{d}(r,\theta,\phi,t)\,d_{\text{rs}} \quad (10)$$

where $\text{d}(r,\theta,\phi,t)$ is the electron density as a function of range, altitude, and longitude, r is range or radial position (m), θ is latitude (°), ϕ is longitude (°), t is time (s), d_{rs} is the slant TEC path from receiver to satellite.

In this paper, the first point in these paths is a GPS satellite, and the second point is a GPS receiver in Japan. The TEC as computed in (10) is the raw slant TEC data. The raw slant TEC data are not corrected for various errors in the GPS measurements. These errors include: slight changes in satellite orbits, signal propagation delays due to interaction between ion species in the ionosphere and troposphere, and timing errors in the receivers due to inaccurate timing clocks. A procedure is described in Sect. 4 that discusses removing all biases except those due to the troposphere. Tropospheric biases will be considered as a delta in the final value of the corrected TEC.

Computation of unbiased TEC

The Japan GPS Earth Observation Network (GEONET) was set up by the Geographical Survey Institute (GSI) of Japan. It has more than 1000 GPS receivers spread over Japan, about 209 of which give precise code pseudo-ranges at both GPS frequencies. Equation (11) depicts the basic computation of the raw slant TEC data from uncorrected pseudo-range information (Jin et al. 2012a, b). One of the first contribution of this paper is to convert the raw slant TEC data into Unbiased TEC (UTEC) data. To estimate precise UTEC from GPS pseudo-range measurements data, we need to remove the errors due to the Differential Code Biases (DCBs), as well as propagation errors due to the ionosphere, using (11):

$$P_{\text{td}} = 40.3 * \left(\frac{1}{f_1} - \frac{1}{f_2}\right) * \text{TEC} + \text{DCB}^i + \text{DCB}_j + P\_\text{Tropo} + P\_\text{Iono}, \quad (11)$$

where P_{td} is the differential pseudo-range measurements, f_1, f_2 are GPS measurement frequencies: 1575.42 and 1227.60 MHz, TEC is total electron content (m/s^2), DCB^i is the ith satellite bias, DCB_j is the jth receiver bias, $P_$Tropo is the tropospheric bias, $P_$Iono is the ionospheric bias.

The UTEC can then be found using (11) as

$$\text{UTEC} = -\frac{f_1^2 f_2^2}{40.3\,(f_1^2 - f_2^2)}\left(P_{\text{td}} - c\text{DCB}^i - c\text{DCB}_j - P\_\text{Tropo} - P\_\text{Iono}\right). \quad (12)$$

DCB estimates for GPS satellites and ground receivers are typically not known and often difficult to compute for a given receiver network. A Matlab code was developed to estimate GPS satellite and receiver DCBs for time intervals from hours to days. The primary function of this Matlab code is the following:

(a) Read the pseudo-range and carrier phase measurements P_1, P_2, L_1, and L_2 from the RINEX files.
(b) Compute the DCB estimates (as shown in Fig. 3), using the Standard Product #3 (SP3) files.
(c) Check computed DCBs for consistency using the IONospheric EXchange (IONEX) files.
(d) Correct raw slant TEC data using DCBs and ionospheric propagation delay estimates to create UTEC data.

The calculated DCB estimates show good agreement with equivalent DCB estimates from IGS analysis centers with a mean difference of less than 0.7 ns and an RMS error of less than 0.4 ns, even for a single station DCB estimate (Jin et al. 2012a, b).

Once single UTEC site data are computed, another MATLAB data processing program, designed to convert single site UTEC data into a UTEC map, as a function of Longitude, Latitude and Time, is used, as shown in Fig. 4. This MATLAB program takes the data points for each single GPS UTEC site as a function of time, and averages

them out resulting in a single UTEC data point for each site every 30 s, which is the sampling period of the GPS receivers. The average UTEC is subsequently interpolated using a linear triangulation method, resulting in one mesh of data over Japan at each sampled time. The data meshes are turned into contour plots and each plot is used to create a video Frame. The video frames are assembled to create a video file. The individual frames, which are similar to the Japan GEONET-TEC maps (discussed in more details Sect. 5), will be used to follow the UTEC evolution and variations over Japan, at the time of the March 11, 2011 earthquake.

Japan GEONET-TEC data

In this section, we discuss the average TEC behavior over Japan. The National Institute of Information and Communications Technology (NICT) in Japan aims to develop a monitoring system of the earth's ionosphere to provide ionospheric observation data and early warnings of ionospheric disturbances. Consistent with this vision, the Japan GEONET was set up by the Geographical Survey Institute (GSI) of Japan. TEC over Japan for each day is being computed, in near real time, and archived. NICT provides three versions of GEONET-TEC maps:

(a) Final version with delay of several days: http://seg-web.nict.go.jp/GPS/GEONET/AMAP/.
(b) Quasi-real-time version with delay of a few hours: http://seg-web.nict.go.jp/GPS/QR_GEONET/AMAP/.
(c) Real-time version with delay of a few minutes: http://seg-web.nict.go.jp/GPS/RT_GEONET/AMAP/.

As a result, it is possible to obtain real-time two-dimensional TEC maps recorded all over Japan for each day, month, and year. These two-dimensional maps are of absolute vertical TEC and derived with time resolution of 30 s and spatial resolution of 0.15° × 0.15° in latitude and longitude. The method used to derive these maps was validated by (Otsuka et al. 2002; Mannucci et al. 1998; Ma and Maruyama 2003). Although the primary purpose of this GPS network was to measure crustal deformations, the two-dimensional TEC maps provided additional benefits for understanding potential correlations between these deformations and variations in the ionosphere over Japan. Their high spatial density (typical horizontal separations are 15–25 km) and time resolution (regularly sampled every 30 s) make these maps an ideal tool to image the evolution of TEC with time all over Japan. Using the existing Japan TEC maps, we can study the general behavior of the Japan background TEC with time. We assume that a ∼ 10-year time period covering March 2007–March 2016 would provide a good indicator for the average behavior of the TEC over Japan. We also assume that over this time period, deviations from the average behavior of the TEC over Japan should be observable when they exist. These deviations should, therefore, be supported by ionospheric phenomena readily known to have produced such deviations in the past. When deviations occur that are not expected in the average behavior of the TEC, and not related to other known phenomena, we should assume that they are coming from an unknown source (more specifically, a source not readily identified in the past). In particular, when these deviations occur at time periods which correlate with seismic and pre-earthquake activities, the results in this paper will show that the potential likelihood is significant that they are partly a result of activities in the earth's magnetic field due to seismic and pre-earthquake activities.

We begin with hourly Japan TEC maps, typically provided from 00:00 to 23:00-UT, 9:00 AM-JST to 08:00 AM-JST. We have chosen to study Japan TEC maps of March 11, the day of the earthquake over a 10-year period. As discussed in Sect. 2, the ion production rate function behaves like a skewed Gaussian, as a function of altitude. In addition, the ion production rate grows progressively as we approach noon time, typically coinciding with the time the sun is overhead, at zenith (as shown in Fig. 2). Then, as we pass by zenith through the afternoon hours, the production rate progressively fades until the night hours when ion production rate is minimal. Given this average ion production rate paradigm, we should be able to observe a similar behavior in the TEC maps in the absence

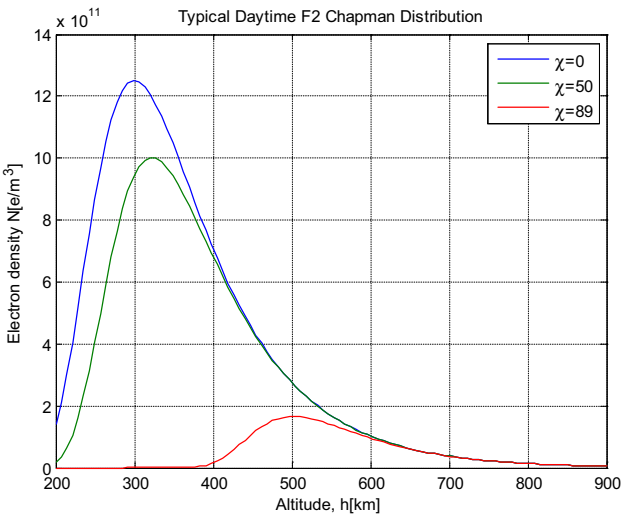

Fig. 2 Typical daytime F_2 Chapman layer model of the ionosphere for zenith angles ($\chi = 0°$, $\chi = 50°$, $\chi = 89°$), max electron density $N_m = [12.51 \times 10^5$ e/cm$^3]$; base height $y_m = 50$ km, and max density radial height $r_m = 300$ km

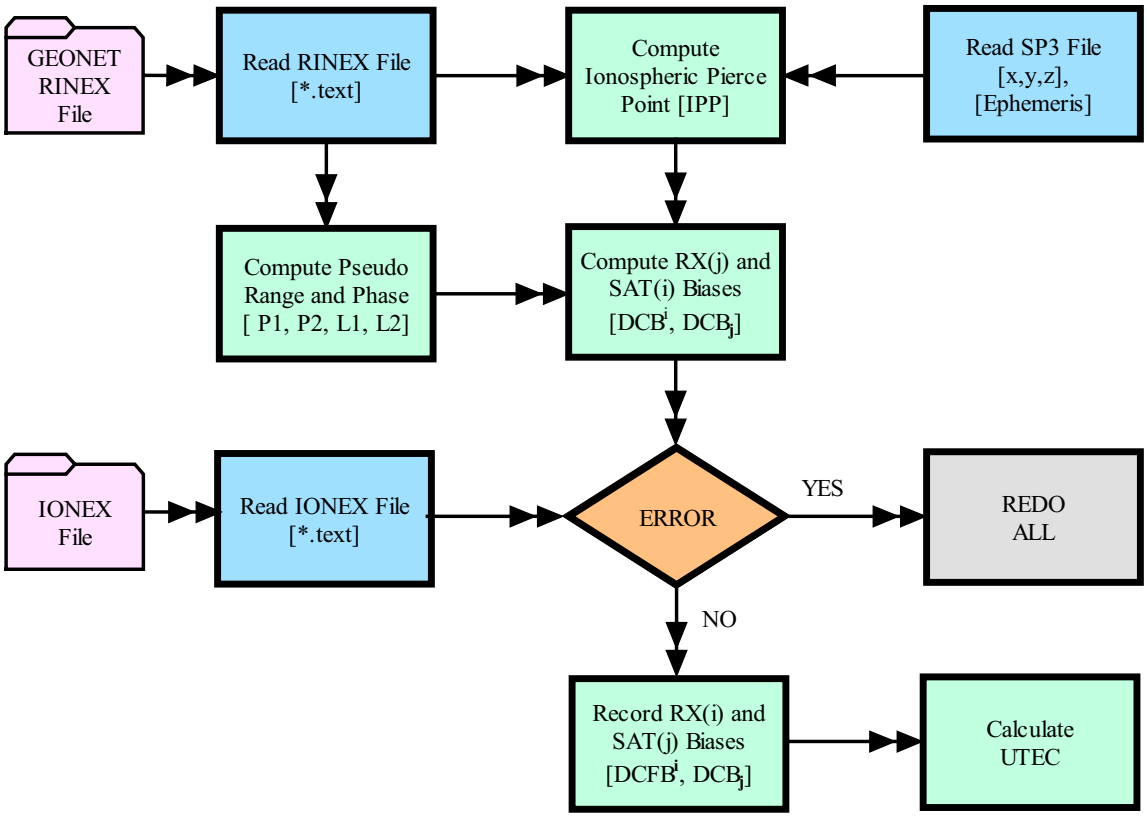

Fig. 3 GPS UTEC data processing block diagram

of other phenomena affecting the TEC. Since the Japan TEC maps are readily available, we can look at the progression of the Japan TEC data for each month starting in March 2007. The daily Japan TEC maps are provided in sets of six maps per hour (e.g., every 10 min) for a total of $(6 \times 24 = 144)$ maps per day. In this study, we have chosen to look at the Japan TEC maps for every hour which will represent the first column of the daily Japan TEC map matrices provided online.

We begin this analysis with the Japan TEC maps of March 11, 2007 and 2011, as shown in Fig. 5. Both maps depict TEC values spanning 24°–48°N in latitude and 124°–148°E in longitude. Both maps show the variations in the TEC to be from 0 to 20 TECU.

The only real difference between these two maps is in the minimum and maximum values of the TEC, as shown in Fig. 5a, where TEC data vary from 0 to ~ 10 TECU, while in Fig. 5b, TEC data vary from 0 to ~ 20 TECU, as well as the distribution of the TEC values. In analyzing the Japan TEC maps, it will be important to follow the differences in the variations of the TEC values as a prime discriminator between maps. Data for March 11, 2007 (TEC ranging from 0 to 20 TECU) show TEC maps starting 00:00 UT, 9:00a JST and ending at 23:00 UT, 8:00p JST. As expected, as we move towards noon 12:00p JST on that day, we can see that the TEC reaches a peak, progressively decreasing until 8:00p JST. A similar behavior is observed in the data for March 11, 2008 (TEC ranging from 0 to 20 TECU). In the data for March 11, 2009, the peak TEC drifts slightly to 2:00p JST. This behavior is accounted for by the skewed Gaussian ion production rate model discussed earlier. We also notice a significant depletion change in the maximum value of the TEC from 2007 to 2008 (~ 20 TECU in 2007–2008 to ~ 13 TECU in 2009). In the data for March 11, 2010 (TEC ranging from 0 to 60 TECU), the overall expected trend is the same as that seen from 2007 to 2010, this time with a slight change in the maximum value of the TEC (from ~ 20 TECU in 2009 to ~ 25 TECU in 2010). Data for March 11, 2011, the month of the Tohoku Japan earthquake (TEC ranging from 0 to 20 TECU), show significant enhancements starting 9:00a JST and persisting through ~ 6:00p JST. In addition, the behavior of the TEC departs sharply from expected averages seen in the data from 2007 to 2010. Data for March 11, 2012 (TECU maximum values ~ 20 TECU) also show persistent TEC enhancements all over Japan from ~ 11:00a JST to ~ 4:00p JST. The Japan Tohoku earthquake was considered a challenging event to analyze in many ways, since it took place not too distant from a solar maximum. Solar

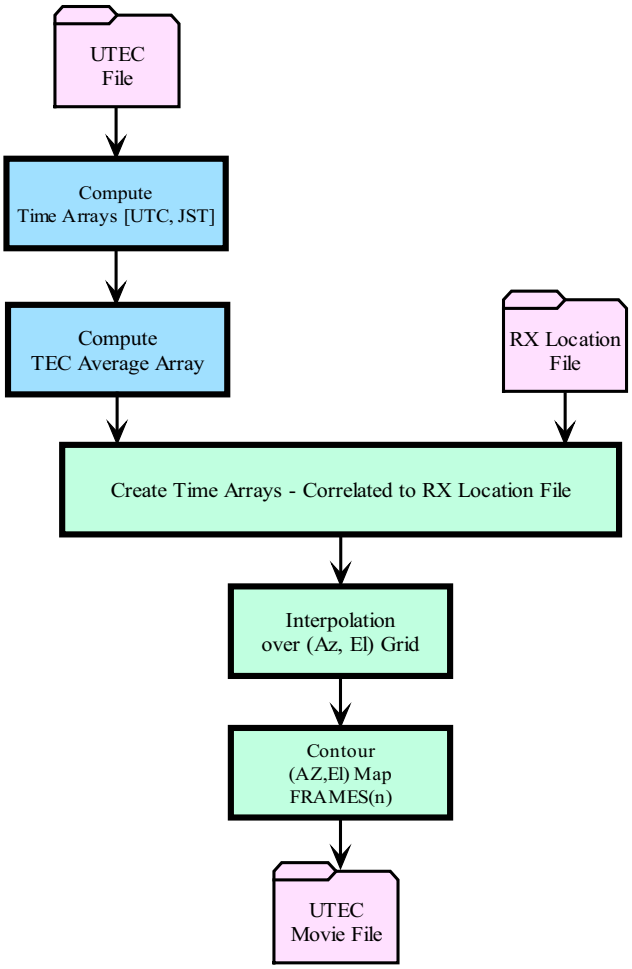

Fig. 4 UTEC–UTEC movie–map data processing block diagram

cycle 24 peaked near 2014, and as such, we would expect 2011, 2012, 2013, and 2014 and potentially 2015 to have greater solar flux than usual. This greater input in solar flux would significantly affect ion production rate, as discussed earlier, and should, therefore, be reflected in the TEC data. Data from March 11, 2013—1 year before solar maximum—(TECU ranges from 0 to ~ 20 TECU) continue to show persistent TEC enhancements all over Japan from ~ 9:00a JST to ~ 4:00p JST. In 2013, differences in the maximum values of the TEC from expected averages reach as high as ~ 10–15 TECU. Similarly, in the data from March 11, 2014—the year of solar maximum (TEC ranging from 0 to 20 TECU) shows that TEC enhancements are quite evident from 9:00a JST to 6:00p JST. The enhancements seen in the March 11, 2011–2014 are consistent with TEC data from solar maximum. Most importantly, maximum values of TEC (20 TECU) are seen literally covering Japan during that time period, underlying the fact that solar maximum does produce more solar flux which in turns, affects the TEC in rather predictable ways (Russell et al. 2010; Chakrabarty et al. 2012). However, we find no real discontinuities in the TEC data over that time period. In the data from March 11, 2015 and March 11, 2016 (TEC ranging from 0 to 20 TECU), the TEC data go back to an expected average behavior similar to what is seen in the data for March 11, 2007 (TEC ranging from 0 to 20 TECU), providing more evidence supporting the fact that the background TEC over Japan can be reasonably predicted from yearly observations. This is another important fact, in support of the results presented in this paper, since it provides a framework for identifying departures from an average behavior of the Japan TEC when they occur. This also provides evidence supporting the fact that while the Chapman layer model is far from perfect, it is yet a reasonable representation of the average behavior of the electron density, which in turns reflects quite well in the TEC.

The unbiased TEC model

One primary objective of this paper is to study UTEC data as a potential earthquake precursor parameter. The basic idea is to study the correlation between the disturbances in the ionosphere and pre-earthquake and seismic activities. Ionospheric disturbances due to seismic and pre-earthquake activities were previously reported by several authors. These reports include, but are not limited to: atomic oxygen ion density anomalies from the 1981, $M = 7.5$ earthquake at -33.1^{o} in geographic latitude and -73.1^{o} in geographic longitude (Oyama et al. 2011); GPS TEC data from the 1999, Taiwan $M = 7.6$ earthquake (Liu et al. 2010); GPS TEC and Doppler soundings data from the Sumatra–Andaman $M = 9.3$ earthquake (Astafyeva and Afraimovich 2004); digital sounder data from the 2005, Sumatra–Andaman $M = 9.3$ earthquake (Liu et al. 2006a, b); GPS TEC and magnetometer data from the 2005, Sumatran $M = 8.6$ earthquake (Hasbi et al. 2009); Japan GEONET GPS TEC and HF radar data from the 2011, Japan $M = 9.0$ earthquake (Astafyeva et al. 2009); Japan GEONET GPS TEC from the 2011, Japan $M = 9.0$ earthquake (Heki 2011); ion and electron density as well as TEC variations using the Detection of Electromagnetic Emissions Transmitted from Earthquake Regions (DEMETER) satellite data, from the 2010, Chile $M = 8.8$ earthquake (Ho et al. 2013); DEMETER satellite electron density data from the 2010, Haiti $M = 7.6$ earthquake (Cornely and Daniell 2013); GPS TEC from Japan GEONET from the 2011, Japan $M = 9.0$ earthquake (Hammerstrom and Cornely 2016); GPS TEC data from the 2008, China $M = 7.9$ earthquake (Song et al. 2015); DEMETER satellite electron density data from the 2010, Haiti $M = 7.6$ earthquake (O'Brien and Cornely 2015); GPS TEC from Japan GEONET and GNSS radio

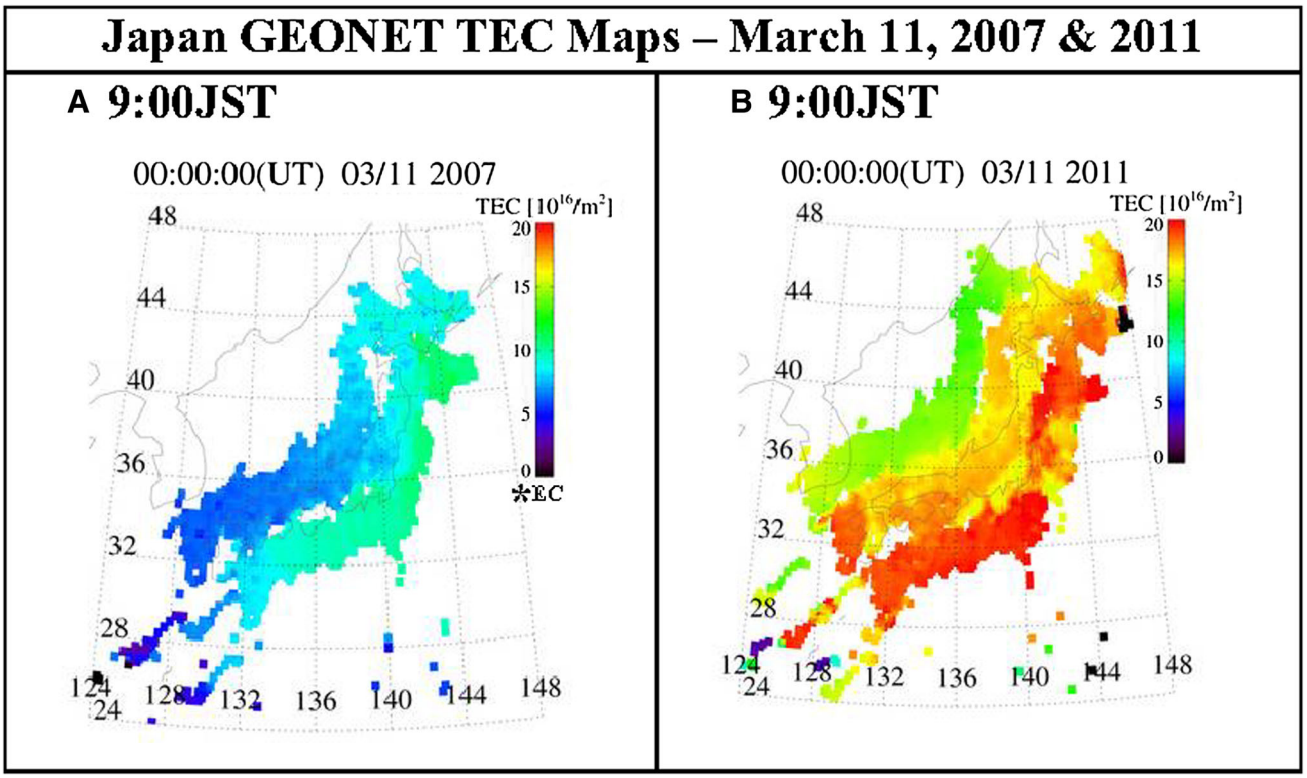

Fig. 5 Japan GEONET-TEC maps show two typical days one with low TEC (**a** March 2007) and the other with high TEC (**b** March 2011) values. Notice the high TEC values coinciding with the day and month of the earthquake

occultation data from the 2011, Japan $M = 9.0$ earthquake (Jin et al. 2015). These previous works cover a wide array of investigations using GPS TEC data, at times with other independent observables from radar, satellite, and digital sounder data. This body of work points to various instances of disturbances in the ionosphere, days to hours before and after several earthquakes, starting in 1981. In this paper, we seek to introduce more definitive correlations between UTEC behaviors and seismic and pre-earthquake activities. We also propose a first-order model that captures important aspects of these correlations.

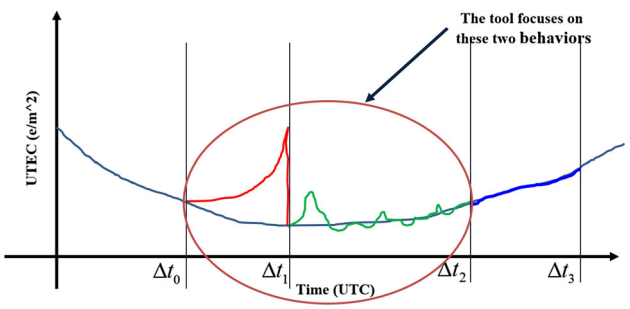

Fig. 6 Cartoon showing the difference in UTEC time series before and after an earthquake. UTEC enhancement appears for a period ($\Delta t_1 - \Delta t_0$) before the earthquake followed by UTEC fluctuations for a period ($\Delta t_2 - \Delta t_1$) during the earthquake and finally UTEC settling back to normal levels over a period ($\Delta t_3 - \Delta t_2$) after the earthquake

An analysis of the overall behavior of the UTEC, before, during and after earthquakes, reveals that the UTEC disturbances manifest as a sudden rise in UTEC levels (as shown in the red portions of the curve in Fig. 6) followed by a sudden drop in UTEC and UTEC oscillations (as shown in the green portion of the curve in Fig. 6). Eventually, the UTEC levels slowly settle back down to their average expected levels (as shown in the blue portion of the curve). The UTEC disturbances seem to begin suddenly and proceed in sequence, with changes in UTEC levels both above and below the average UTEC (blue curve of Fig. 6). This behavior of the UTEC is not consistent with changes expected under normal ionospheric conditions. Heki (2011) reports UTEC anomalies, related to these ionospheric changes, to be much larger, closer to the epicenter reaching $\sim$ 4 TECU (1 TECU is 10^{16} electrons/m^2). Other earthquakes were also investigated by (Heki 2011) including the 2010 Central Chilean earthquake (Mw 8.8, 3–4 TECU change lasting $\sim$ 50 min), the 2004 Sumatra–Andaman earthquake (Mw 9.2, $>$ 5 TECU lasting $\sim$ 90 min), and the 1994 Hokkaido-Toho-Oki earthquake (Mw 8.3, 2–3 TECU anomaly lasting $\sim$ 60 min). The plurality of cases showing the same UTEC anomalies within comparable time periods before, during, and after earthquakes suggest the existence of a distinct possibility that we might be able to model these UTEC anomalies. In

this paper, the UTEC calculated in (12) is modeled with two components: the first component ($UTEC_a$) contains the time varying background UTEC (descriptive of the average behavior of the UTEC) and possibly other smooth variations in UTEC (including UTEC associated with smooth increases in solar flux). The second component ($UTEC_s$) contains sudden changes (disturbances) in the UTEC due to seismic and pre-earthquake activities:

$$\mathrm{UTEC} = \mathrm{UTEC_a}(t) + \mathrm{UTEC_s}(t). \quad (13)$$

Assuming a time varying average behavior of the UTEC, designated as $UTEC_a(t)$ (as for an example, the average behavior of the Japan GEONET-TEC data) known to contain only minimal fluctuations, a first-order representation of the disturbances in the UTEC is proposed that uses a constant percentage change in the UTEC data from a nominal average, $\Delta UTEC_s$. This fixed component is designed to account for the constant changes in the average UTEC background due to seismic and pre-earthquake activities. This model was used very effectively in the past to represent enhancements and depletion phenomena that affect the nature of the peak electron density in the F layer (Cornely 2003). Enhancements and depletions, before and after earthquakes, were observed in the past studies, and are quite representative in the UTEC data under current study, as they accurately model part of the sudden variations of the UTEC [the $\Delta UTEC_s$ term of (14)]. In addition to the constant change from an average behavior $\Delta UTEC_s$, we have also included small but, non-negligible UTEC variations as a function of time, represented by $UTEC_s(t)$. This variable component of the UTEC is designed to account for changes in the average UTEC background (as shown in the green portion of the curve in Fig. 5). As a result, we have a follow-up to (13):

$$\mathrm{UTEC} = \mathrm{UTEC_a}(t) \pm \Delta\mathrm{UTEC_s} + \mathrm{UTEC_s}(t) \quad (14)$$

where $UTEC_a(t)$ is the UTEC contribution from the ionosphere, $\pm\Delta UTEC_s$ is the UTEC enhancement and depletion due to seismic and pre-earthquake activities, $UTEC_s(t)$ is the variable UTEC contribution from seismic and pre-earthquake activities.

Equation (14) is a simplistic first-order model describing some of the couplings between ionospheric dynamics and their correlations with seismic and pre-earthquake activities. Equation (14) assumes that departure from the first term in the equation, though not necessarily deterministic, can be approximated deterministically once a set of seismic, pre-earthquake, and earthquake parameters are fixed including but not limited to: local time and geographic location (plate boundary, geology, fault history, etc). The formulation in (14) is also consistent with our current knowledge from observations and previous works, namely, that preceding an earthquake, we notice the following: a sudden discrete jump in UTEC: $+\Delta_1$UTEC $(\Delta t_1 - \Delta t_0)$ time lapse before the earthquake, followed by a recovery jump Δ_2UTEC at Δt_1, UTEC fluctuations $(\Delta t_2 - \Delta t_1)$ time lapse after the recovery at Δt_1 and finally, the UTEC settling back down to average level $\sim (\Delta t_3 - \Delta t_2)$ after the UTEC fluctuations time period. The time lapses associated with $(\Delta t_1 - \Delta t_0)$, $(\Delta t_2 - \Delta t_1)$, and $(\Delta t_3 - \Delta t_2)$ are currently not well known and not yet well understood. $(\Delta t_1 - \Delta t_0)$ lapse time is especially important, because it begins to open a window on the kinds of earthquake precursor timelines that will be essential to understanding and refining the UTEC data as a potential contributor to the future of earthquake forecasting.

Results and discussion

The primary method used in this paper is a visualization tool. This visualization tool allows means to observe the correlation between UTEC data and seismic as well as pre-earthquake activities. The primary input to this tool is raw slant TEC data over Japan leading to a set of unbiased TEC (UTEC) data that are converted into UTEC maps. For this experiment, a cluster of GEONET GPS receivers was selected facing the earthquake epicenter. Figure 7 shows the network of receivers used in this study (red), as compared to the entire GEONET network (green), along with the earthquake epicenter (blue dot on the right inside). The UTEC visualization technique takes GPS readings (RINEX files) from Japan GEONET using the method, as described in Sect. 4 and Fig 4. Figure 8 shows instances of the raw slant TEC input data from the GPS receiver at site 65,

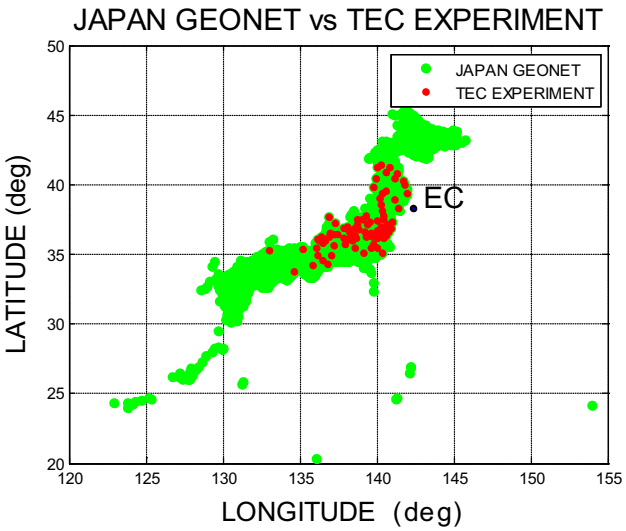

Fig. 7 Japan GEONET network (green dots) and the GPS network used for conducting the experiment (red dots), and the epicenter (blue dot)

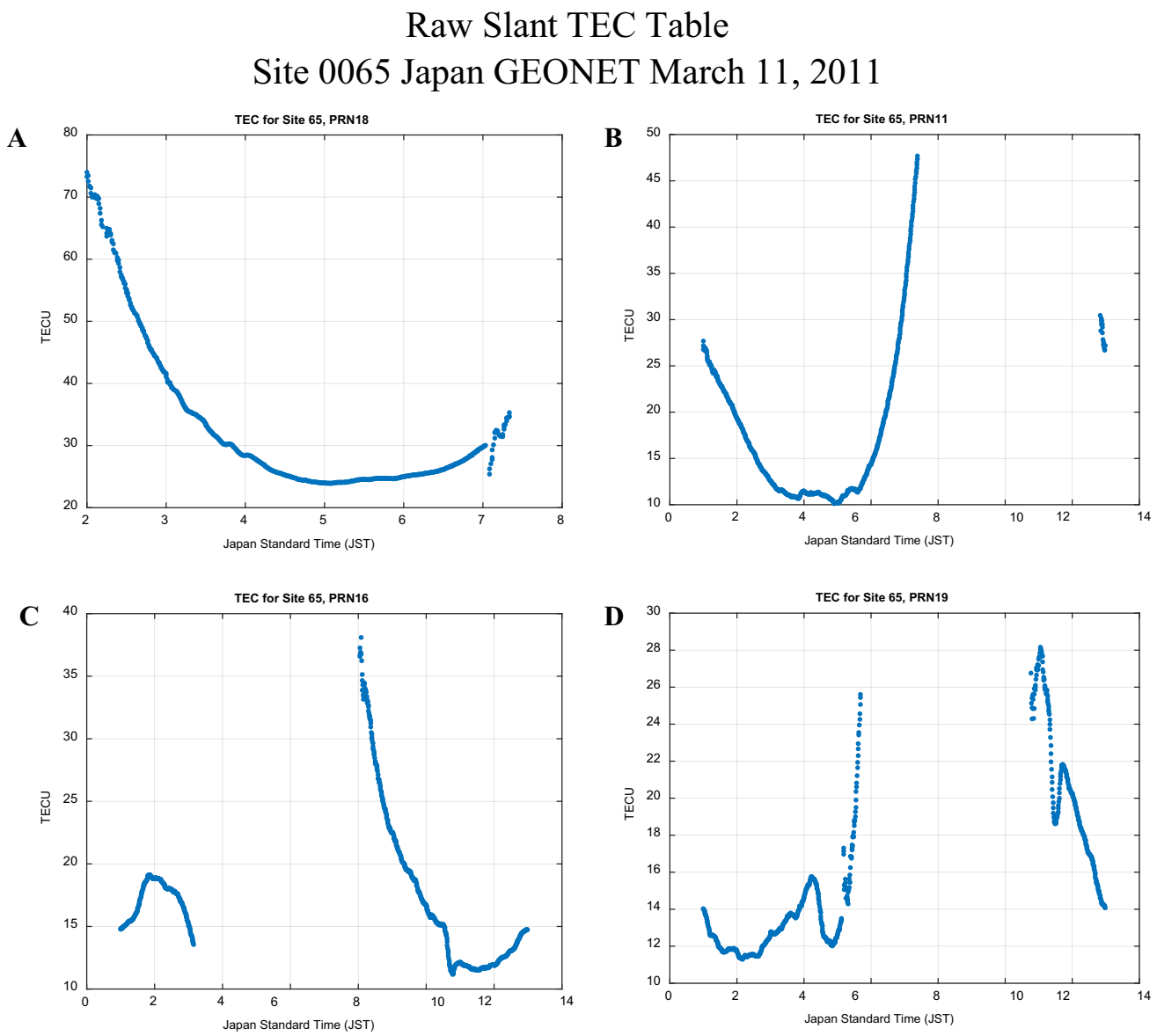

Fig. 8 Four frames of the UTEC data from a receiver at site 0065 observing four different satellites PRN11, PRN16, PRN18, and PRN19 on March 11, 2011

while it was observing four different GPS satellites PRN11, PRN16, PRN18, and PRN19. Figure 8 shows a representation of four different data acquisition instances providing observations from GPS receivers crossing different regions of the ionospheric sky at slightly different time periods on the same day. Figure 8a shows the raw slant TEC from 2:00p JST to 7:30p JST. Several aspects of the slant TEC data from PRN18 need to be discussed. First, the sudden drop near 7:00p JST. This sudden drop is repaired via interpolation. Second, the concavity of the slant TEC curve as a function of time. Such concavity is one of the known primary features of the slant TEC. The concavity structure of the slant TEC data, displayed in Fig. 8a, is well understood and is the primary reason why it has been relatively easy to depict deviations from this basic concavity structure. We also observe the high values of the slant TEC in Fig. 8a ($\sim$ 30–75 TECU), not reflected in the average behavior of the Japan TEC, as discussed in Sect. 5. Figure 8b: $\sim$ 12:30a JST to $\sim$ 8:00a JST begins to show some slight departure from the basic concavity structure of the slant TEC data.

Specifically, we can see some slight fluctuations around 4:00–6:00a JST. We also observe the values of the raw slant TEC ($\sim$ 30–45 TECU) going down as expected for this time of the day, as discussed in Sect. 5. In Fig. 8c: $\sim$ 8:00p JST to 2:30a JST, the departure from the basic structure becomes more evident, especially around 10:00–12:00p JST. In Fig. 8d, more

Japan UTEC Maps Before and After EQ – March 11, 2011

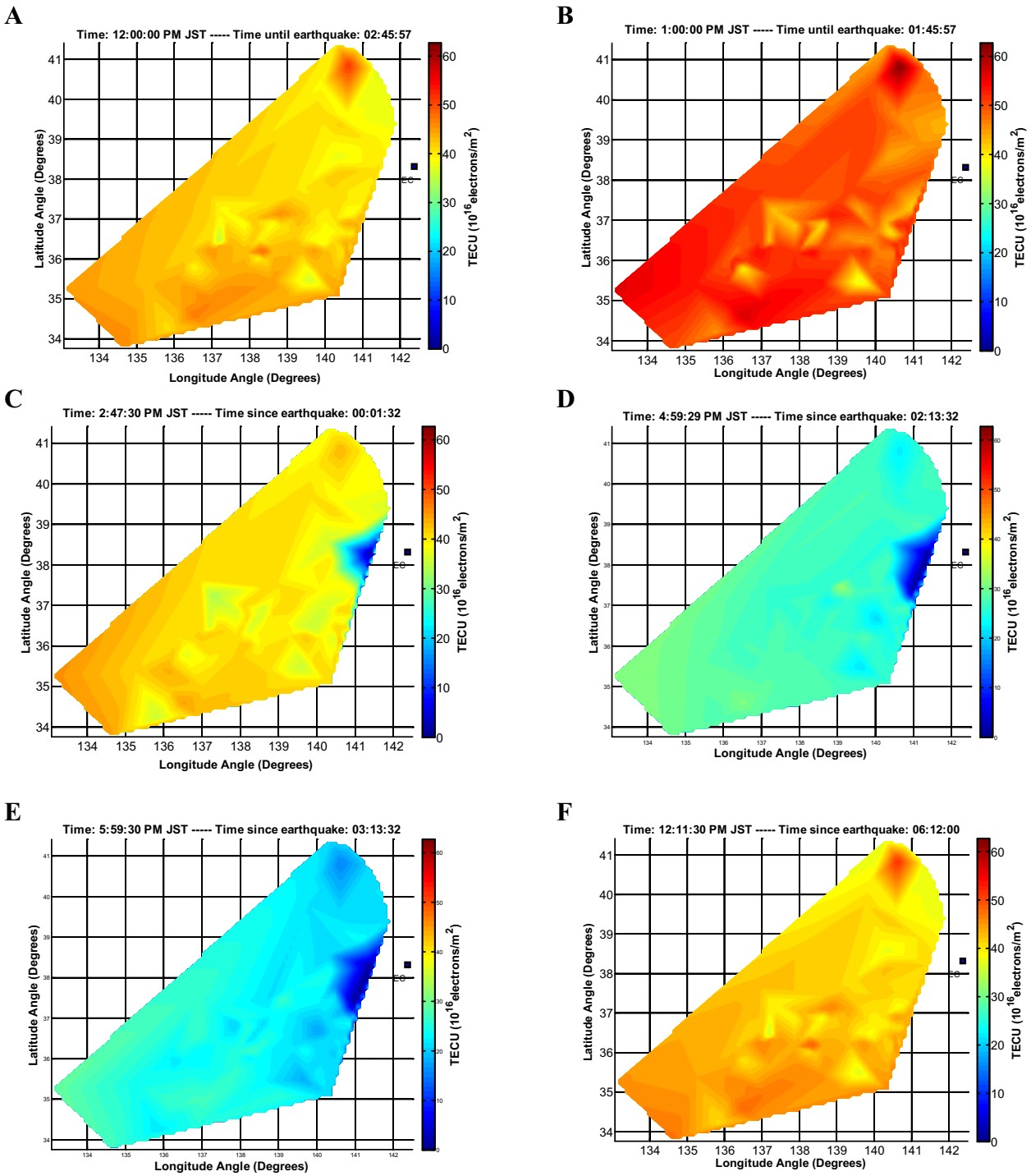

Fig. 9 Six UTEC frames taken over an 3°27′ window around the earthquake from 2°45′ before the earthquake to 6°12′ after the earthquake

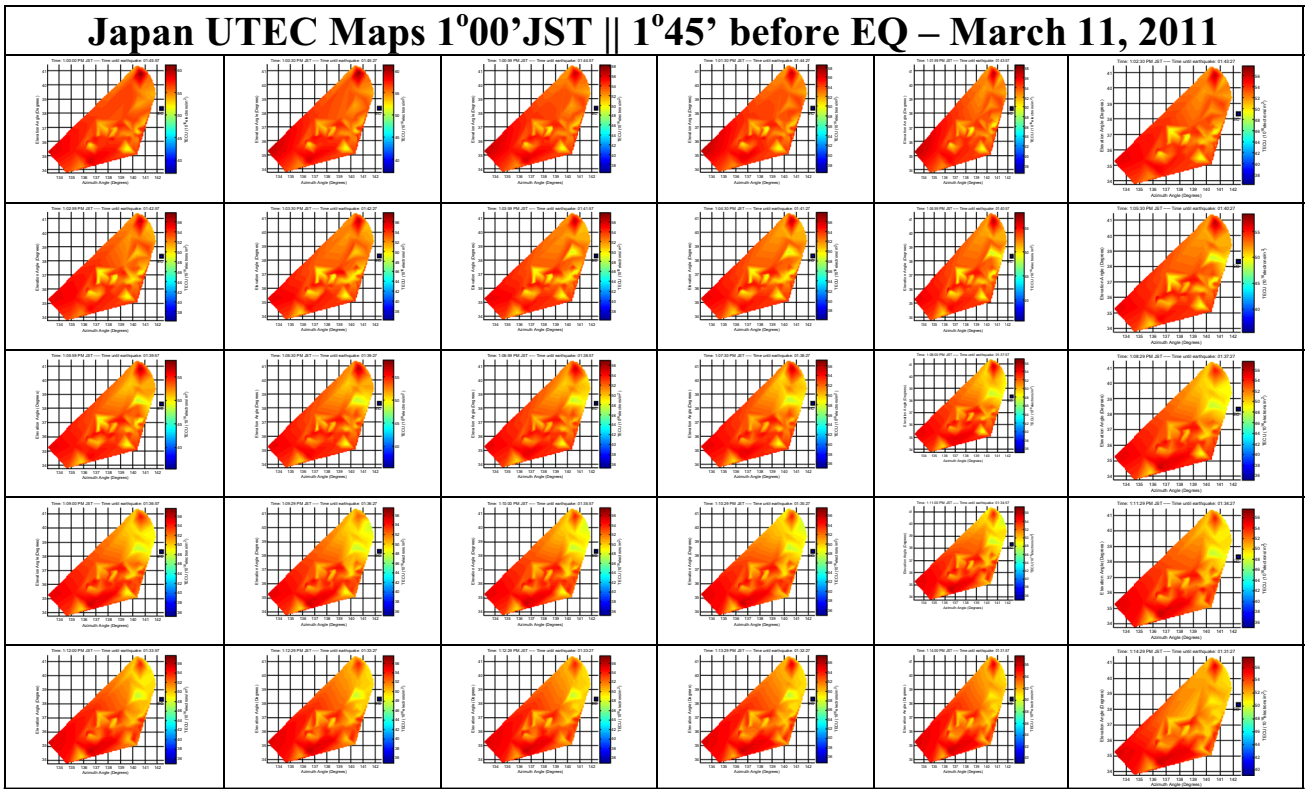

Fig. 10 Family 1, frames of the UTEC movie from 1°00′ to 1°14′ JST, 1°45′ before the earthquake

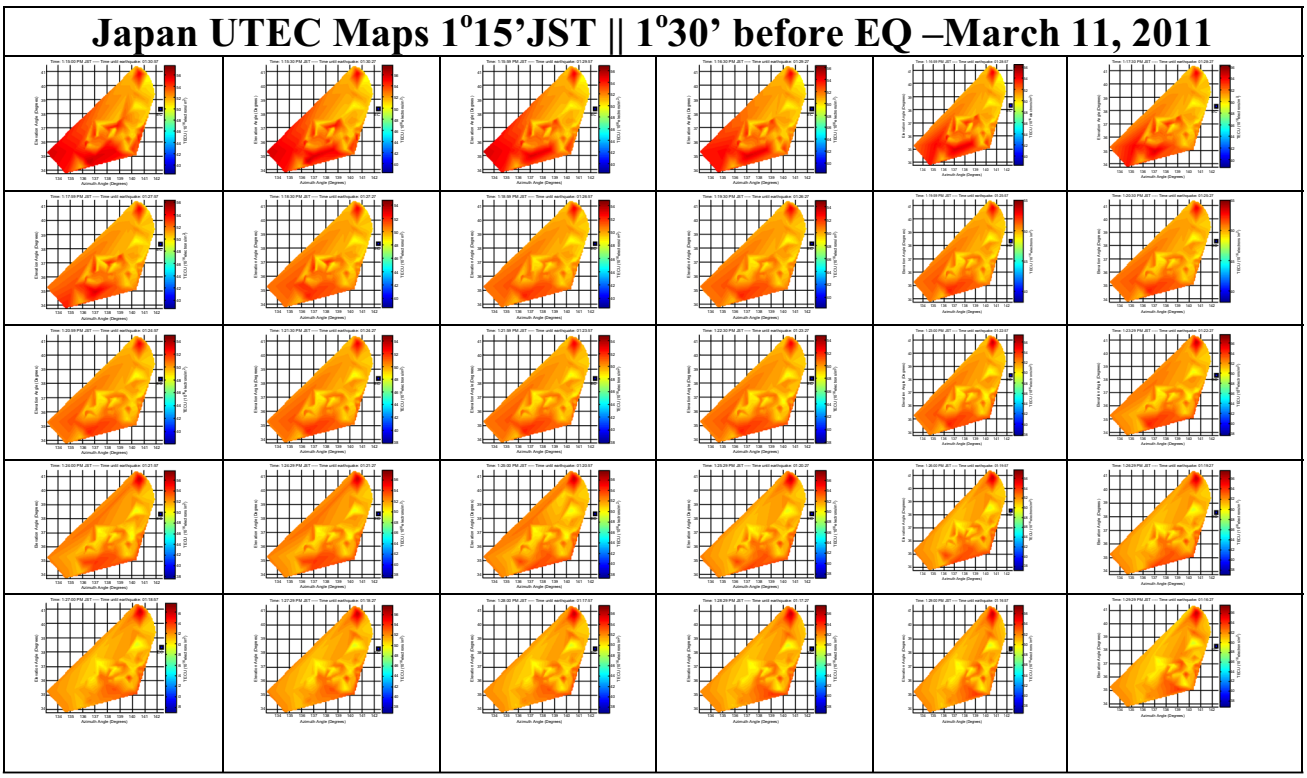

Fig. 11 Family 2, frames of the UTEC movie from 1°15′ to 1°29′JST, 1°30′ before the earthquake

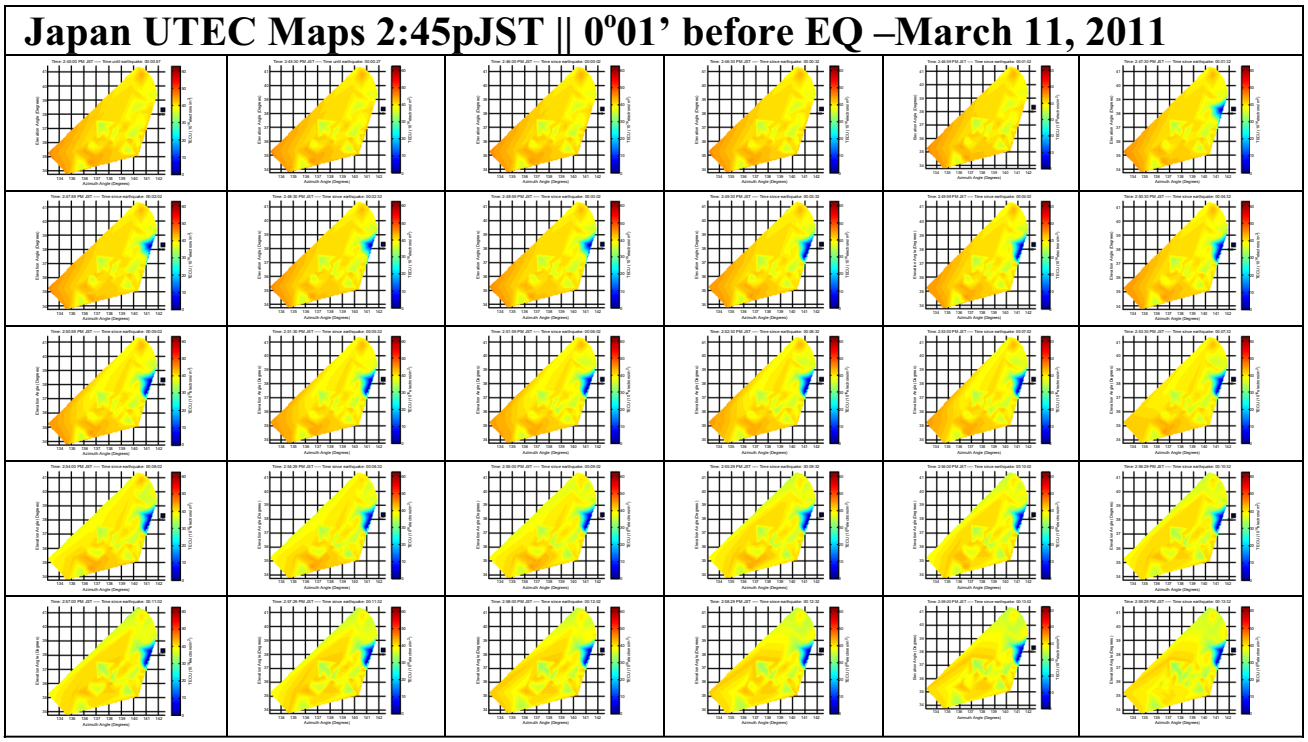

Fig. 12 Family 8, frames of the UTEC movie from 2°45 to 2°59′ JST, 0°1′ before the earthquake

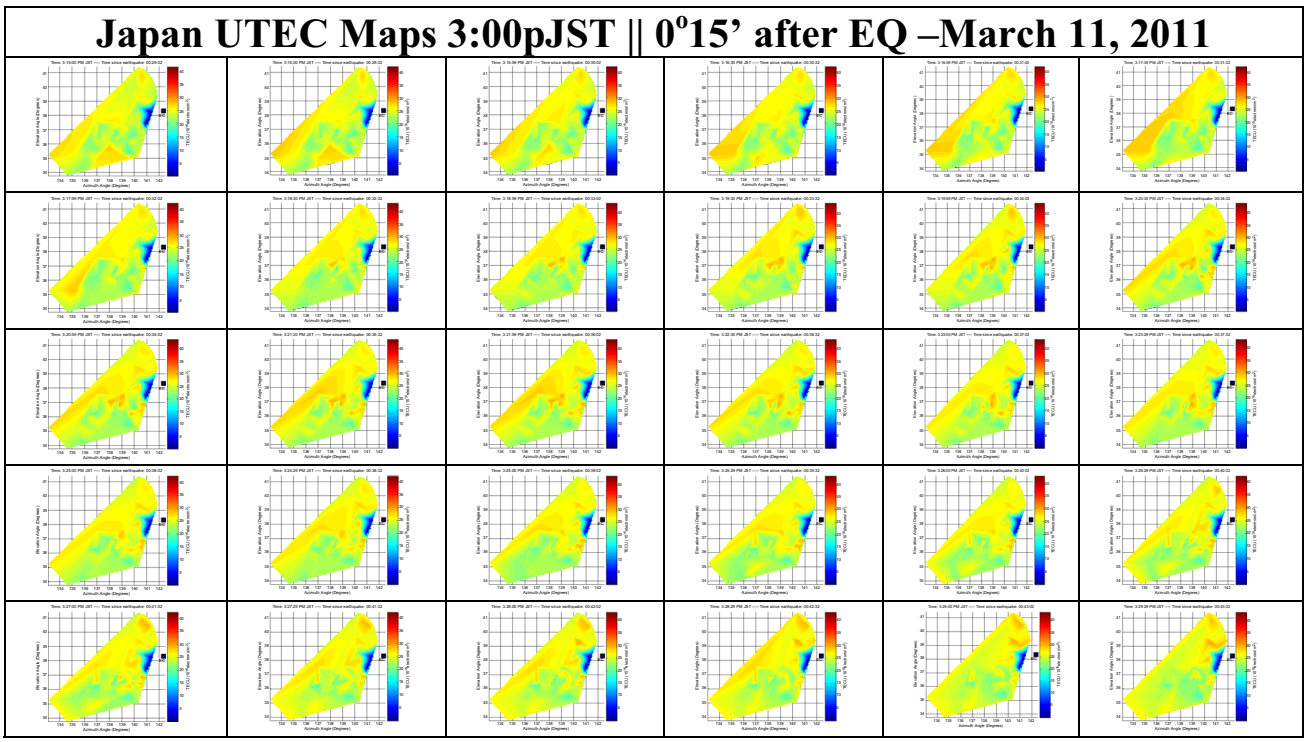

Fig. 13 Family 9, frames of the UTEC movie from 3°00′ to 3°14′ JST, 0°14′ after the earthquake

specifically, while the behavior around 5:00a JST is surely a drop, the behavior around 11:30p JST is obviously not. These observations continue to underscore the sensitivity of the TEC data to reflecting changes in the structure of the ionospheric electron density when they occur.

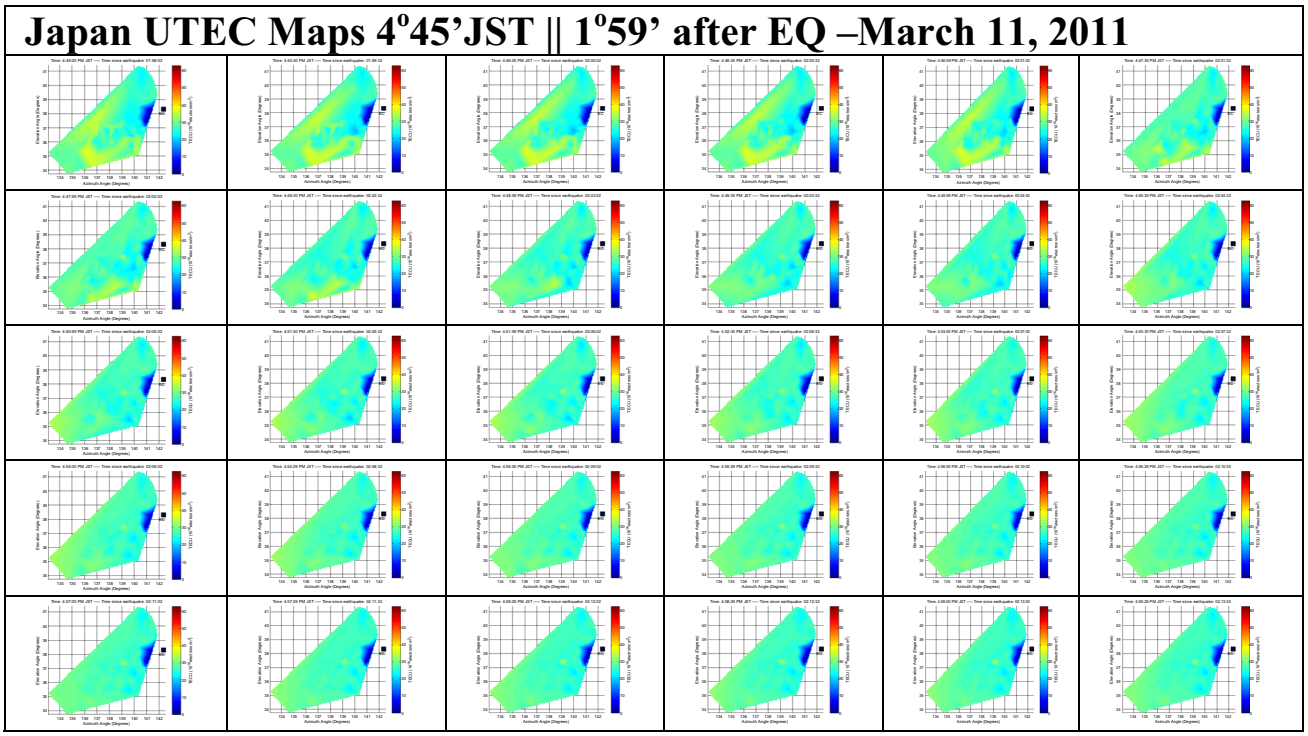

Fig. 14 Family 16, frames of the UTEC movie from, from 4°45′ to 4°59′ JST, 1°59′ after the earthquake

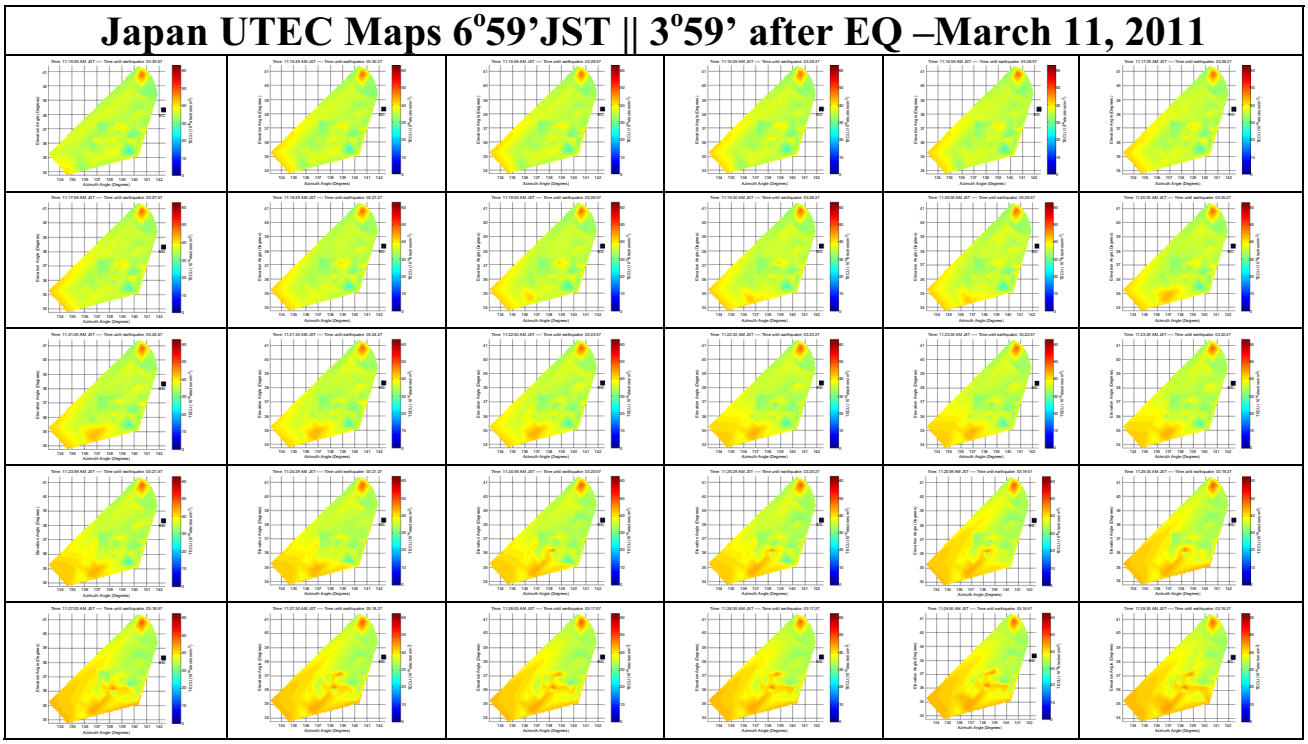

Fig. 15 Family 34, frames of the UTEC movie from 11°15′ to 11°29′ JST, 8°14′ after the earthquake

Examples of the raw slant TEC data in Fig. 8 converted into UTEC map data are shown in Fig. 9. Figure 9 depicts six examples of UTEC frames which provide a glimpse into the behavior of the UTEC data: the noticeable UTEC enhancements in Fig. 9a (1°45′ before the earthquake), followed by a sudden UTEC enhancement in Fig. 9b

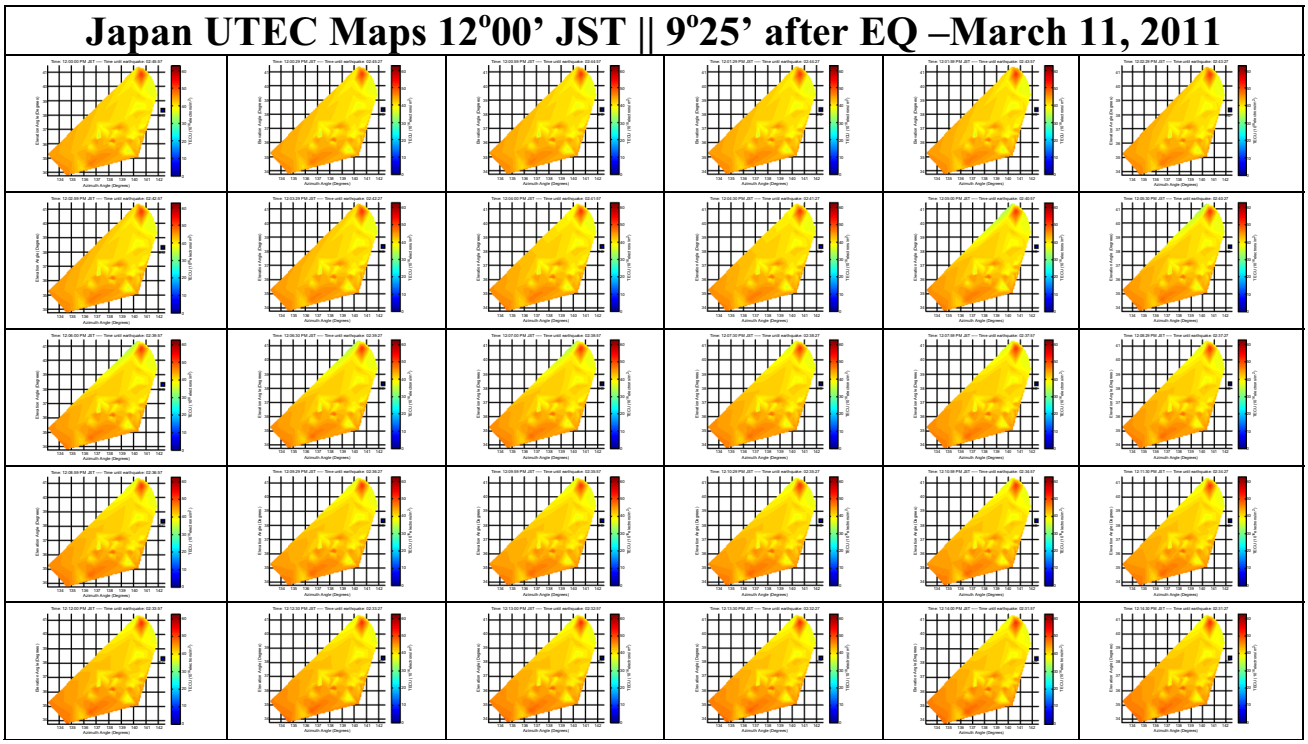

Fig. 16 Family 37, frames of the UTEC movie from 12°00′ to 12°14′ JST, 9°25′ after the earthquake

(1°45′after the earthquake). In Fig. 9c (0°01′32″ since the earthquake begun), we see the first sign of UTEC depletion, directly facing the epicenter. The UTEC continues to show signs of greater depletions for the next ∼ 2–3 h, first in Fig. 9d (2°13′ since the earthquake begun), and continuing in Fig. 9e (2°13′ since the earthquake begun). Finally, the UTEC begins to slowly go back to average levels in Fig. 9f (6°05′ since the earthquake begun). The period of UTEC oscillations is definitely evident from Fig. 9b through Fig. 9f, for about a 6-h time period. The UTEC behavior in the six frames of Fig. 9 is consistent with the behavior expected using data from a single GPS receiver, as described in the cartoon of Fig. 5.

Figure 9 shows a good top-level summary of the behavior of the UTEC data, as earthquakes approach. It mimics and is consistent with the expected behavior of the UTEC reported by several authors, as described in the previous sections. The visualization tool, developed in this study, shows the overall behavior of the UTEC data, all in the form of UTEC frames similar to the ones in Fig. 9, for a time period before during and after the earthquake. The tool creates the UTEC frames as a function of latitude, longitude, and time with UTEC intensities given in TEC Units (TECU). The UTEC frames contain the UTEC data for March 11, stretching over a time period Δt_1 starting from 1:00p JST to 2:46p JST (1 h and minutes to the time of the earthquake) and time periods Δt_2 to Δt_3 (∼ 6 h and 5 min during and after the time of the earthquake). Thirteen UTEC families are provided that show the progression of the UTEC frames before, during, and after the earthquake. Figure 10: Family-1, from 1°00′ to 1°14′ JST shows very high UTEC values (∼ 60 TECU) when compared with average levels, as discussed in Sect. 5. The UTEC values start to drop in Fig. 11: Family-2, ∼ 1°15′ to 1°29′JST (1°30′ before the earthquake). In Fig.12: Family-8, ∼ 2°45′ to 2°59′ JST, 0°1′ before the earthquake, we observe the first real sign of a severe drop in UTEC levels (down to ∼ 0 UTEC) with a depletion region facing the earthquake epicenter. From Fig. 13: Family-9, ∼ 3°00′ to 3°14′ JST, 0°29′ after the earthquake to Fig. 14: Family-16, ∼ 4°45′ to 4°59′ JST, 1°59′ after the earthquake, the UTEC levels begin to recover to the point where in Fig. 15: Family-34, ∼ 6°45′to 6°59′ JST, 3°59′ after the earthquake, the UTEC levels are starting to become much closer to expected levels. The UTEC variations from Family-1 to Family-34 (∼ 60 to 25 UTEC) are significant variations in UTEC levels to occur in less than ∼ 6 h. In Fig. 16: Family-37, ∼ 12°00′ to 12°14′ JST, 9°25′ after the earthquake, the UTEC data are completely back to average levels.

Figure 17 shows a synthesis of the variations in UTEC from frame to frame and as a function of time before, during, and after the earthquake for a total of 1200 UTEC frames over a 9-h period. In this synthesis, we specifically looked at the first- and second-order statistics of the variations in UTEC from frame to frame, as compared to an

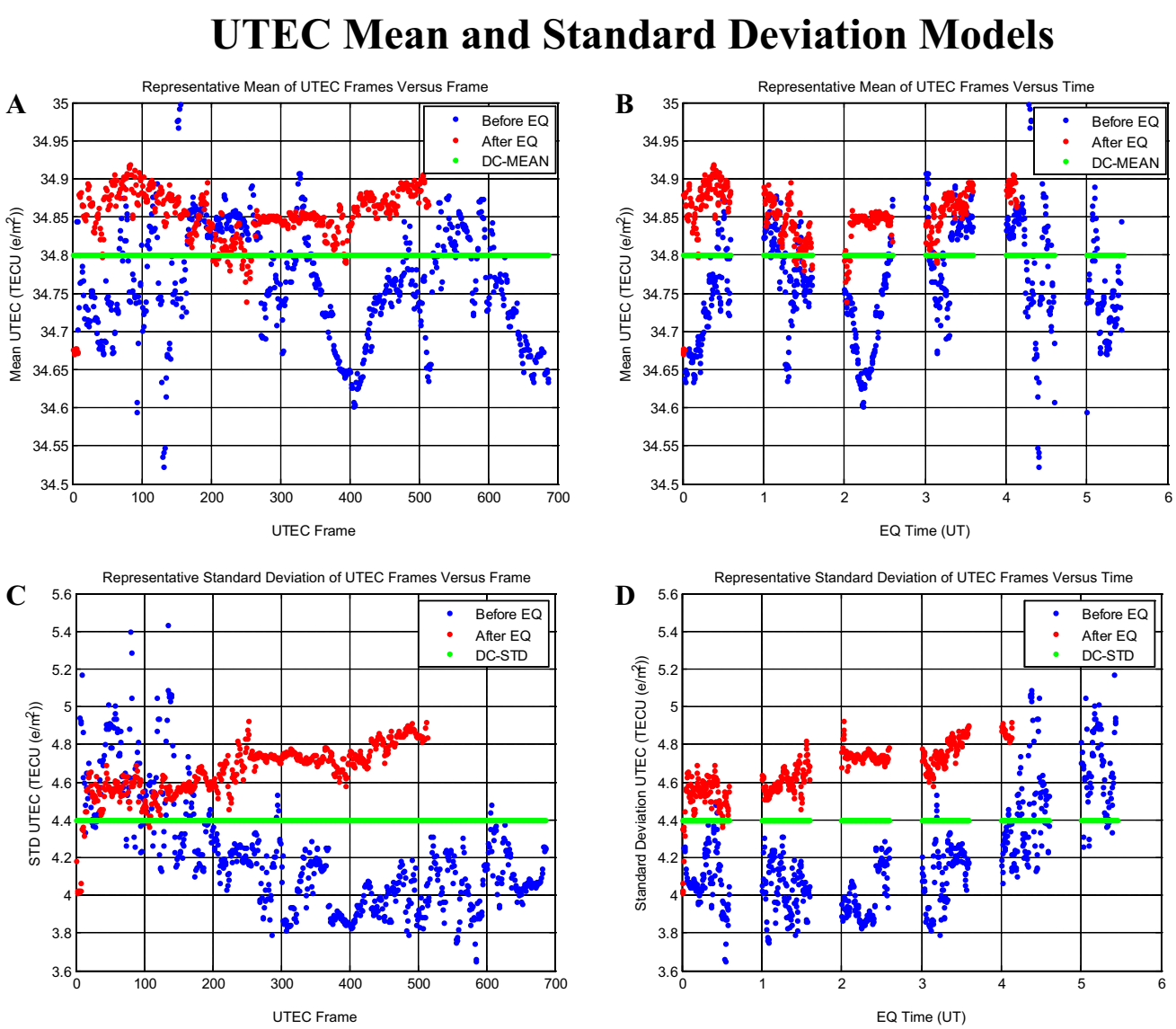

Fig. 17 Representative means and standard deviations of UTEC data as a function of time before and after the earthquake. **a** Variations in the means UTEC as a function of frame. **b** Variations in the means UTEC as a function of time. **c** Variations in the standard deviations UTEC as a function of frame. **d** Variations in the standard deviations UTEC as a function of time

overall mean over all 1200 frames (called DC-MEAN). Figure 17a shows the time varying mean of the UTEC (in TEC units, TECU) from frame to frame before the earthquake (blue curve). We observe the largest mean UTEC variation of (34.8–34.63) = 0.17 TECU within the first ∼ 60 frames (not including the obvious outlier points around frame 130). Beyond frame-60, we begin to see UTEC fluctuations, as discussed earlier, on either side of the DC-MEAN, the largest of which takes place at ∼ frame-400 (34.8–34.6) = 0.20 TECU. Figure 17a also shows that the variations in UTEC from frame to frame after the earthquake (red curve), the largest of which occurs before frame-100 and right after frame-500, are much less severe. In either case, the variation in mean UTEC does not exceed (34.92–34.80) = 0.12 TECU. In Fig. 17b, the same variations in mean UTEC are shown as a function of time before and after the earthquake. Except for a few outliers between 4:00 and 5:00 UT, we can see the largest variations in mean UTEC at 2.23 UT (0.25 TECU) and right before the earthquake at 0.00 UT (0.26 TECU). Figure 17c shows the time varying standard deviation of the UTEC from frame to frame and as a function of time before, during, and after the earthquakes (time axis is to be read from right to left). For example, in the first 150 frames, we see large variations in the standard deviation (5.1–4.4 = 0.7 TECU) from an overall average standard deviation (called DC-STD) of 4.4 TECU. In addition, as we move from frame-200 to frame-600, we see

the deviation from the DC-STD increase progressively. This increase in the standard deviation, as a function of time, is shown more definitively in Fig. 17d (time axis from right to left).

In Fig. 17d, 5 h before the earthquake, we see the largest variations in the standard deviation from the DC-STD. These variations in the standard deviation increase progressively as we approach the earthquake at 0.0UT. More specifically, we can see large variations (4.93–3.8 = 1.13 TECU) starting 3 h before the earthquake. The variations in UTEC mean and standard deviations clearly illustrate the nature of the variations of the UTEC, as a function of time, as the earthquake approaches and for some time after. In addition, the variations in mean and standard deviations would seem to support our assertion that while the average behavior of the UTEC is well known, variations in UTEC data due to seismic and pre-earthquake activities can change the UTEC dynamics with readily observable changes in the standard deviations of the UTEC from a known average background. This realization opens the door for more in depth investigations in UTEC data correlation with seismic and pre-earthquake activities. In particular, more investigations to help better describe the time varying mean and standard deviation as compared to the DC-MEAN and DC-STD.

Conclusions and future work

Traveling ionospheric disturbances generated by epicentral ground/sea surface motions, ionospheric disturbances associated with Rayleigh waves, and post seismic mono-periodic atmospheric resonance (i.e., acoustic gravity wave oscillations) between the lithosphere and the thermosphere were observed after several large earthquakes (Choosakul et al. 2009). In addition, tsunami generated from subduction earthquakes, such as the 2011 $M = 9.1$ Japan, the 2010 $M = 8.8$ Chile and the $M = 9.1$ Sumatra earthquakes, produced ionospheric holes which seem to manifest as sudden depletions of ionospheric TEC (Kahinami et al. 2012; Kamogawa and Kakinami 2013). However, several authors report potential contradictions in the observed behavior of the ionospheric TEC both before and after earthquakes occur. (Heki 2011) reports that for the 2011 $M = 9.1$ Japan earthquake, the TEC gradually enhanced for 40 min before the earthquake to the time when the co-seismic acoustic wave reached the ionosphere after which the TEC recovered to the normal state. Kahinami et al. (2012) reports that a tsunamigenic ionospheric hole occurred after the co-seismic acoustic wave reached the ionosphere creating TEC depletions with the TEC gradually recovering to its normal state after several minutes. Such apparent contradictions in observed TEC behavior, when considered carefully, seem to also point to definite commonalities between the reported results. It is possible to interpret the reports from Heki (2011) and Kahinami et al. (2012) as completing each other in the sense that upon the arrival of earthquakes, we typically observe enhancements in TEC while after a certain period of time, the TEC fluctuates well below its overall mean (DC-MEAN), leading to readily observable TEC depletions. Disagreements on the origin of TEC enhancements or the nature of the TEC depletions, as well as the potential source of related ionospheric holes, do not negate the important findings from these studies. Several authors have had critical responses to the real source and origin of ionospheric enhancements reported in Heki (2011) and questioned whether or not these enhancements are of seismic and pre-earthquake origin. Heki (2011) reports that these critical responses come in two stages: they first cast doubt on the TEC enhancements and often attribute them to possible artifacts. Second, when the TEC enhancements are accepted, doubts are raised on their significance when compared to other natural variations of space weather origin. For example, (Kahinami et al. 2012) attributed the enhancements to an artifact falsely detected by the combined effect of highly variable TEC under geomagnetic conditions and the occurrence of a tsunamigenic ionospheric hole. Masci et al. (2014) reports that the ionospheric enhancements are artifacts induced by the definition of the reference line adopted in analyzing TEC variations. Pulinets et al. (2004) reports significant deviations from monthly median values that are observed from time to time in ionospheric records during completely quiet solar and geophysical conditions. Yet, upon further examination of the time series of vertical TEC before and after the 2011 $M = 9.1$ Japan earthquake by Heki and Enomoto (2013) reveals that the tsunami did not make an ionospheric hole. Heki and Enomoto (2013) further confirms the validity of the ionospheric enhancements using ionosondes and magnetometer data. Therefore, it suffices to say that while a lot of good work was done on the potential correlation between ionospheric disturbances and seismic and pre-earthquake activities, there are significant disagreements on the importance, significance, and quite often, the validity of the results.

In this paper, we have developed a first-order framework for using the proposed UTEC data as an earthquake precursor. The underlying assumption supporting this framework is that ionospheric variations, due to interaction between traveling charges from redox reactions created from rocks under stress, can be observed in the UTEC data. The mode of travel of these charges, still under study, has thus far been attributed to gravity waves and/or post seismic mono-periodic atmospheric resonance. As shown in Fig. 5, these ionospheric variations can be summarized as

noticeable enhancements in UTEC data, well above an average UTEC background, for a time duration Δt_1 before the earthquake begins. These enhancements are followed by a UTEC depletion below the average UTEC background at time Δt_1, and UTEC fluctuations for a time duration $(\Delta t_2 - \Delta t_1)$ after the earthquake begins. Finally, we see the UTEC data slowly going back to an expected average level for a time duration $(\Delta t_3 - \Delta t_2)$ well after the earthquake started. Many aspects of the UTEC behavior are consistent with observations by many authors in the last 5–6 years. One interesting set of facts that seem to completely set the behavior in the UTEC data under study apart from other known TEC behaviors are the discontinuities and fluctuations seen in the UTEC data at the time of the earthquake. These discontinuities are inconsistent with the known physics of the ionosphere and must, therefore, be attributed to causes, other than known ionospheric dynamics that can be directly associated with seismic and pre-earthquake activities. However, the complete precursory capability of the UTEC data, more specifically its ability to provide a precise timeline for changes in UTEC before earthquakes has not been defined by the results of this paper. Further studies are required to better understand the local average behavior of the ionosphere and to better define the characteristic differences between the UTEC background and seismic and pre-earthquake UTEC levels. These studies might provide opportunities for defining some parameters that will eventually capture the changes in the UTEC as soon as they begin. Such parameters would be of significant utility as part of an overall scheme for earthquake forecasting.

Acknowledgements We would like to thank the Geographical Survey Institute of Japan for convenient and free use of their GEONET GPS data. Thanks are also due to A. Saito, Kosuke Heki, K. Hocke, and Y. Otsuka for their invaluable support to the field. Special Thanks to Dr. Friedemann Freund for his many years of devotion and dedication to earthquake theory and forecasting.

References

Astafyeva E, Afraimovich EL (2004) Long-distance traveling ionospheric disturbances caused by the great Sumatra-Andaman earthquake on 26 December 2004, Institute of Solar-Terrestrial Physics SD RAS, P. O. Box 4026, Irkutsk, 664033, Russia

Astafyeva E, Heki K, Kiryushkin V, Afraimovich E, Shalimov S (2009) Two-mode long-distance propagation of coseismic ionosphere disturbances. J Geophys Res 114(A10307):2009. https://doi.org/10.1029/2008JA013853

Chakrabarty D, Bagiya M, Thanpi S, Iyer KN (2012) Solar EUV flux (0.1–50 nm), F10.7 cm flux, sunspot number and the total electron content in the crest region of equatorial ionization anomaly during the deep minimum between solar cycle 23 and 24. Indian J Radio Space Phys 41:110–120

Choosakul N, Saito A, Iyemori T, Hashizume M (2009) Excitation of 4-min periodic ionospheric variations following the great Sumatra-Andaman earthquake in 2004. J Geophys Res 114:A10313. https://doi.org/10.1029/2008ja013915

Cornely P-RJ (2003) Flexible prior models: three-dimensional ionospheric tomography. Radio Sci. 38:1087. https://doi.org/10.1029/2002rs002703

Cornely P-R, Daniell R (2013) Anomalies in the Ionosphere around the Southern Faults of Haiti near the 2010 Earthquake. Natural Hazards NH13A-1589-2013, American Geophysical Union, December 2013

Freund F (2010) Toward a unified solid state theory for pre-earthquake signals. Acta Geophys 58:719–766

Freund F (2011) Pre-earthquake signals: underlying physical processes. J Asian Earth Sci 41:383–400

Freund F, Takeuchi A, Lau BWS (2006) Electric currents streaming out of stressed igneous rocks: a step towards understanding pre-earthquake low frequency EM emissions. Phys Chem Earth 31:389–396

Hammerstrom J, Cornely P-R (2016) Total electron content (TEC) variations and correlation with seismic activity over Japan. J Young Investig (JYI) 3. https://doi.org/10.22186/jyi.31.4.13-16

Hasbi AM, Momani MA, Ali MAM, Misran N, Shiokawa K, Otsuka Y, Yumoto K (2009) Ionospheric and geomagnetic disturbances during the 2005 Sumatra earthquake. J Atmos Solar Terr Phys 71:1992–2005

Hayakawa M, Fujinawa Y (1994) Electromagnetic phenomena related to earthquake predication. Terra Sci. Pub. Co., Tokyo

Hayakawa M, Molchanov OA (eds) (2002) Seismo electromagnetics: lithosphere-atmosphere-ionosphere coupling. Terra Sci Pub. Co., Tokyo

Heki K (2011) Ionospheric electron enhancement preceding the 2011 Tohoku-Oki earthquake. Geophys Res Lett. https://doi.org/10.1029/2011gl047908

Heki K, Enomoto Y (2013) Preseismic ionospheric electron enhancements revisited. J Geophys Res Space Phys 118:6618–6626. https://doi.org/10.1002/jgra.50578

Ho Y-Y, Liu J-Y, Parrot M, Pinçon J-L (2013) Temporal and spatial analyses on seismo-electric anomalies associated with the 27 February 2010 M = 8.8 Chile earthquake observed by DEMETER satellite. Natl Hazards Earth Syst Sci. 13:3281–3289. https://doi.org/10.5194/nhess-13-3281-2013. http://www.nat-hazards-earth-syst-sci.net/13/3281/2013

Jin R, Jin S, Feng G (2012a) M_DCB: Matlab code for estimating GNSS satellite and receiver differential code biases. GPS Solut 16:541–548. https://doi.org/10.1007/s10291-012-0279-3 **(Received: 19 April 2012/Accepted: 30 June 2012/Published online: 18 July 2012)**

Jin R, Jin S, Feng G (2012b) M_DCB: Matlab code for estimating GNSS satellite and receiver differential code biases. GPS Solut. 16:541–548. https://doi.org/10.1007/s10291-012-0279-3

Jin S, Occhipinti G, Jin R (2015) GNSS ionospheric seismology: recent observation evidencesand characteristics. Earth Sci Rev 147(2015):54–64

Kahinami Y, Kamogawa M, Tanioka Y, Watanabe S, Gusman AR, Liu J-Y, Watanabe Y, Mogi T (2012) Tsunamigenic ionospheric hole. Geophys. Res. Lett 39:L00G27. https://doi.org/10.1029/2011gl050159

Kamogawa M, Kakinami Y (2013) Is an ionospheric electron enhancement preceeding the 2011 Tohoku-Oki earthquake a precursor. J Geophys Res Space Phys 118:1751–1754. https://doi.org/10.1002/jgra.50118

Karato S-I (1999) Seismic anisotropy of the Earth's inner core resulting from flow induced by Maxwell stresses. Nature 402:871–873. https://doi.org/10.1038/47235

Kennett BLN, Engdahl ER (1991) Traveltimes for global earthquake location and phase identification. Geophys J Int 105:429–465

Kennett BLN, Engdahl ER, Buland R (1995) Constraints on seismic velocities in the earth from traveltimes. Geophys J Int 122:108–124

Liu JY, Tsai YB, Chen SW, Lee CP, Chen YC, Yen HY, Chang WY, Liu C (2006a) Giant ionospheric disturbances excited by the M9.3 Sumatra earthquake of 26 December 2004. Geophys Res Lett 33:L02103. https://doi.org/10.1029/2005GL023963

Liu JY, Tsai YB, Ma KF, Chen YI, Tsai HF, Lin CH, Kamogawa M, Lee CP (2006b) Ionospheric GPS total electron content (TEC) disturbances triggered by the 26 December 2004 Indian Ocean tsunami. J Geophys Res 111:A05303. https://doi.org/10.1029/2005JA011200

Liu JY, Tsai HF, Lin CH, Kamogawa M, Chen YI, Lin CH, Huang BS, Yu SB, Yeh YH (2010) Coseismic ionospheric disturbances triggered by the Chi-Chi earthquake. J Geophys Res 115:A08303. https://doi.org/10.1029/2009JA014943

Ma G, Maruyama T (2003) Derivation of TEC and estimation of instrumental biases from GEONET in Japan. Ann Geophys 21:2083–2093 **(c European Geosciences Union 2003, April 2003)**

Mannucci AJ, Wilson BD, Yuan DN, Ho CH, Lindqwister UJ, Runge TF (1998) A global mapping technique for GPS-derived ionospheric total electron content measurements. Radio Sci 33(3):565–582

Masci F, Thomas JN, Villani F, Secan JA, Rivera N (2014) On the onset of ionospheric precursors 40 min before strong earthquakes. J Geophys Res Space Phys 120:1383–1393. https://doi.org/10.1002/2014/ja020822

Ng KK (2016) Prediction methods in solar sunspots cycles. Sci Rep 6:21028. https://doi.org/10.1038/srep21028

O'Brien M, Cornely P-R (2015) Analyzing Anomalies in the Ionosphere Above Haiti Surrounding the 2010 Earthquake. J Young Investig

Ohl AI (1966) Wolfs number prediction for the maximum of the cycle 20. Soln Dannye 12:84

Otsuka Y, Ogawa T, Saito A, Tsugawa T, Fukao S, Miyazaki S (2002) A new technique for mapping of total electron content using GPS network in Japan. Earth Planets Space 54:63–70

Oyama K-I, Kakinami Y, Liu JY, Abdu MA, Cheng CZ (2011) Latitudinal distribution of anomalous ion density as a precursor of a large earthquake. J Geophys Res 116:A04319. https://doi.org/10.1029/2010JA015948

Parrot M, Tramutoli V, Liu TJY, Pulinets S, Ouzounov D, Genzano N, Lisi M, Hattori K, Namgaladze A (2016) Atmospheric and ionospheric coupling phenomena related to large earthquakes. Nat Hazards Earth Syst Sci. https://doi.org/10.5194/nhess-2016-172 **(Published: 23 June 2016)**

Poupinet G, Pillet R, Souriau A (1983) Possible heterogeneity of the Earth's core deduced from PKIKP travel times. Nature 305:204–206

Pulinets SA, Liu JY (2004) Ionospheric variability unrelated to solar and geomagnetic activity. Adv Space Res 34:1926–1933

Pulinets SA, Gaivoronskaya TV, Leiva Contreras A, Ciraolo L (2004) Correlation analysis technique revealing ionosphere precursors of earthquakes. Nat Hazards Earth Syst Sci 4:697–702

Russell CT, Lugmann JG, Jian LK (2010) How an unprecedented a solar minimum? Rev Geophys 48:RG2004. https://doi.org/10.1029/2009rg000316

Simon SJ, Zharkov SI, Zharkova VV (2014) Prediction of solar activity from solar background magnetic field variations in cycles 21–23. Astrophys J 795:46

Song X, Helmberger DVA (1995) P wave velocity model of Earth's core. J Geophys Res 100:9817–9830

Song Q, Ding F, Yu T et al (2015) GPS detection of the coseismic ionospheric disturbances following the 12 May 2008 M7.9 Wenchuan earthquake in China. Sci China Earth Sci 58:151–158. https://doi.org/10.1007/s11430-014-5000-7

Souriau A, Poupinet G (1991) The velocity profile at the base of the liquid core from PKP(BC + Cdiff) data: an argument in favor of radial inhomogeneity. Geophys Res Lett 18:2023–2026

Souriau A, Roudil P (1995) Attenuation in the uppermost inner core from broad-band GEOSCOPE PKP data. Geophys J Int 123:572–587

Yu W-C, Wen L, Niu F (2005) Seismic velocity structure in the earth's outer core. J Geophys Res 110:B02302. https://doi.org/10.1029/2003jb002928

Zou Z, Koper KD, Cormier VF (2008) The structure of the base of the outer core inferred from seismic waves diffracted around the inner core. J Geophys Res 113:B05314. https://doi.org/10.1029/2007jb005316

Acta Geophysica (2018) 66:71–80
https://doi.org/10.1007/s11600-017-0107-9

RESEARCH ARTICLE - APPLIED GEOPHYSICS

Improving waveform inversion using modified interferometric imaging condition

Xuebao Guo[1,2] · Hong Liu[1,2] · Ying Shi[3] · Weihong Wang[3] · Zhen Zhang[4]

Received: 20 July 2017 / Accepted: 7 December 2017 / Published online: 12 December 2017

Abstract

Similar to the reverse-time migration, full waveform inversion in the time domain is a memory-intensive processing method. The computational storage size for waveform inversion mainly depends on the model size and time recording length. In general, 3D and 4D data volumes need to be saved for 2D and 3D waveform inversion gradient calculations, respectively. Even the boundary region wavefield-saving strategy creates a huge storage demand. Using the last two slices of the wavefield to reconstruct wavefields at other moments through the random boundary, avoids the need to store a large number of wavefields; however, traditional random boundary method is less effective at low frequencies. In this study, we follow a new random boundary designed to regenerate random velocity anomalies in the boundary region for each shot of each iteration. The results obtained using the random boundary condition in less illuminated areas are more seriously affected by random scattering than other areas due to the lack of coverage. In this paper, we have replaced direct correlation for computing the waveform inversion gradient by modified interferometric imaging, which enhances the continuity of the imaging path and reduces noise interference. The new imaging condition is a weighted average of extended imaging gathers can be directly used in the gradient computation. In this process, we have not changed the objective function, and the role of the imaging condition is similar to regularization. The window size for the modified interferometric imaging condition-based waveform inversion plays an important role in this process. The numerical examples show that the proposed method significantly enhances waveform inversion performance.

Keywords Boundary region wavefield-saving strategy · Modified interferometric imaging condition · Storage · Random boundary condition

✉ Xuebao Guo
guoxuebao@mail.iggcas.ac.cn

Hong Liu
liuhong@mail.igcas.ac.cn

Ying Shi
shiying@nepu.edu.cn

Weihong Wang
wwhsy@sina.com

Zhen Zhang
zzhen-tlm@petrochina.com.cn

[1] Key Laboratory of Petroleum Resources Research, Institute of Geology and Geophysics, Chinese Academy of Sciences, Beijing 100029, China

[2] University of Chinese Academy of Sciences, Beijing 100049, China

[3] School of Earth Science, Science and Technology Innovation Team on Fault Deformation, Sealing and Fluid Migration, Northeast Petroleum University, Daqing 163318, China

[4] Research Institute of Exploration and Development, Tarim Oilfield Company, PetroChina, Korla 841000, Xinjiang, China

Introduction

RTM is recognized as a powerful but high-cost imaging method. However, the cost of FWI far exceeds that of RTM. Even for today's powerful computing capacity, the cost of 3D waveform inversion is prohibitive even for a regular model size, which is one of the main factors limiting the application of FWI. The calculation process of the two methods is similar: forward propagation of the source wavefield, backward propagation of the residual wavefield at the receiver positions, and zero-lag cross-correlation of the two wavefields. Since we need to cross-correlate two wavefields with different directions at the same moment, we have to save or reconstruct all the source wavefields or receiver wavefields. The requirement is therefore to seek more effective wavefield reconstruction strategies to reduce the storage requirement as much as possible. The most commonly used approaches are the boundary wavefield-saving strategy (Dussaud et al. 2008) and the checkpointing technique (Anderson et al. 2012; Symes 2007). The boundary region wavefield-saving strategy requires the boundaries to be saved at every time step and the wavefields stored at the two final steps. The storage requirement of this method is significantly less than saving all the wavefields but it still cannot be ignored when the model is large. The checkpointing technique requires a series of wavefields to be saved during the propagation process; similarly, the storage requirement is not negligible for large models.

Clapp (2009) proposed the random boundary condition (RBC) to make the wavefields from the boundary region incoherently scattered, which also allows the construction of time-reversible wavefields. By padding the boundary regions of the velocity model with random velocity anomalies, it effectively scatters the coherent waves and conserves energy in the propagation process, guaranteeing time-reversible wave propagation. The imaging condition is applied by first propagating the source wavefield from zero to maximum time, then simultaneously propagating it with the receiver wavefield from maximum time to zero, such that we only need to save the two source wavefields at the maximum time step. However, the RBC (Clapp 2009) has lower validity in cases of low-frequency wavefields in the waveform inversion.

Shen and Clapp (2015) proposed a RBC wavelength-dependent design that is more effective than the traditional method. Regardless of the boundary condition, however, it is inevitable that some wavefield information must be stored. If memory capacity is limited, it may be necessary to store the wavefields on disk, which means that the input/output (I/O) cost associated with disk reading/writing determines the efficiency of the approach. The greatest advantage of the RBC is improved computational efficiency by avoiding the I/O cost associated with transferring wavefields; the latter is also the primary reason for seeking to minimize wavefield storage.

For RTM, high-resolution imaging is dictated to a large degree by the accuracy of the velocity model and the imaging condition. Cross-correlation imaging condition (Claerbout 1985) is widely used in RTM, mainly because of its speed and robustness. Where random fluctuations in the true model are not reflected in the migration velocity, the image obtained by traditional cross-correlation imaging condition shows some noise because RTM has a high demand for an accurate velocity model. Sava and Poliannikov (2008) proposed interferometric imaging condition which uses the Wigner distribution function (WDF) to suppress random noise in the receiver wavefields. Guo et al. (2017) derived a modified interferometric imaging condition, which directly applies the WDFs to both source and receiver wavefields. This not only reduces the artifacts caused by random fluctuations, but also improves the continuity of the boundary image and deep illumination. The RTM process is very similar to that of waveform inversion gradient calculation. Although the information represented by their imaging profiles is different, it is equally applicable to the gradient calculation in terms of the imaging process. We expect that it will play a positive role both in FWI and RTM.

In addition to the wavefield storage problem, the wave propagation process represents a large proportion of waveform inversion. Therefore, parallel computing methods require our attention. Li et al. (2009) included a graphic processing unit (GPU) to accelerate pre-stack time migration, which greatly improves computational efficiency and dramatically saves power and maintenance cost. Then, Li et al. (2010) and Liu et al. (2010) presented GPU implementation of pre-stack reverse-time migration. Shin et al. (2014) implemented the Laplace-domain full waveform inversion on a single GPU card, which efficiently parallelized the preconditioned conjugate gradient method for a number of threads in the GPU card. Yang et al. (2015) also realized a time-domain full waveform inversion on GPU. The global memory of a single GPU card is usually limited, however, restricting the model size. Liu et al. (2013) adopted a domain decomposition technique to implement the reverse-time migration with production scale, the size of which depends on the number of GPU cards.

In this article, we first give a brief introduction to the random boundary condition and illustrate the advantages of this boundary compared with the absorbing boundary. Since the traditional RB is less valid for low-frequency wavefields, the new random boundary design of Shen and Clapp (2015) was adopted. We then describe the normalized wavefield inversion method and how to apply

modified interferometric imaging condition to the gradient calculation. We also discuss the advantages of this new imaging condition and why it improves the gradient. Due to the advantages of GPU in parallel computing, we then apply it to accelerate the wave propagation process. Because there are many previous works on this topic, we introduce only the techniques relevant to this article. Multi-scale inversion strategy is also adopted in the inversion process. Experimental results demonstrate the effectiveness of the proposed method and we discuss the parameter settings that influence the effect.

Random boundary condition

The absorbing boundary condition (ABC) undoubtedly performs better than RBC because no reflection information associated with the boundary region is introduced in ABC. Both methods recalculate the wavefields rather than saving them all; however, ABC experiences wavefield information loss in the propagation process due to attenuation of boundary reflections, so that its reversibility is conditional. ABC requires more storage than RBC to save information about wavefields from boundary regions at every moment because saving only the wavefields of the last two slices is insufficient. The required storage size is related to the model size and the time recording length. In this respect, RBC is obviously more efficient than ABC, and therefore more attractive for practical applications.

For RTM, results obtained by RBC perform similar to those using ABC. However, RBC shows poor performance at the initial stage of waveform inversion. Since low-frequency seismic waves have a longer wavelength, the effective speed for such waves is the average speed over the distance that roughly equals the dominant wavelength of the seismic waves. This effect makes the RB less effective in the initial stages of waveform inversion, which usually start with ultra-low frequencies. Shen and Clapp (2015) suggested that the RB effect can be improved by adjusting the spatial scale of randomness. This means that the random velocity anomalies in the boundary region must be larger than a single cell. The size of velocity anomalies is determined from the maximum frequency of the seismic wave. The random boundary design in the present study adopted the irregular shape of each velocity anomalous body as stated by Shen and Clapp (2015). The Butterworth filter was also used when applying the multi-scale inversion strategy. By setting a series of frequency ranges, gradient information at different scales was obtained. However, the frequency range does not accurately determine the maximum frequency of the filtered seismic wave. For lower frequency ranges, the maximum frequency of the filtered signals was higher than the upper limit of current frequency range: for example, the maximum frequency > 2 Hz when a 2 Hz low-pass filter was used. This information helped in determining the size of the velocity anomalous body. Figure 1 shows an example of the boundary design.

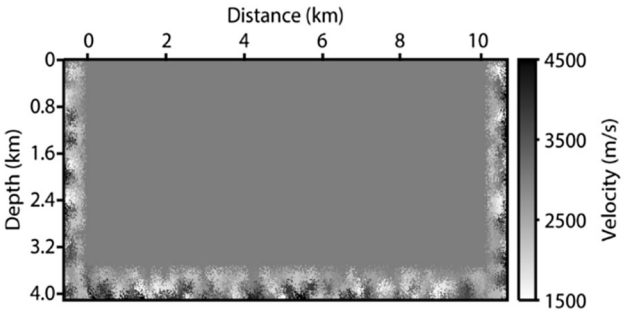

Fig. 1 Illustration of random boundary condition

Normalized wavefield-based waveform inversion

Because traditional waveform inversion is usually sensitive to amplitude, the normalized wavefield-based misfit function (Choi and Alkhalifah 2013) was adopted in this study. The objective function is expressed as follows:

$$E_{\mathrm{NW}} = \frac{1}{2}\sum_{i}^{\mathrm{ns}}\sum_{j}^{\mathrm{nr}} ||\hat{\boldsymbol{u}}_{i,j} - \hat{\boldsymbol{d}}_{i,j}||^2 = \mathrm{const} - \sum_{i}^{\mathrm{ns}}\sum_{j}^{\mathrm{nr}} \left\langle \hat{\boldsymbol{u}}_{i,j} \cdot \hat{\boldsymbol{d}}_{i,j} \right\rangle, \quad (1)$$

where $\hat{\boldsymbol{u}}_{i,j} = \boldsymbol{u}_{i,j}/||\boldsymbol{u}_{i,j}||$ and $\hat{\boldsymbol{d}}_{i,j} = \boldsymbol{d}_{i,j}/||\boldsymbol{d}_{i,j}||$; $\boldsymbol{u}_{i,j}$ and $\boldsymbol{d}_{i,j}$ are the traces from the modeled and observed data, respectively, at the ith source position and at the jth receiver position; $||\boldsymbol{u}||$ indicates the norm of $\boldsymbol{u}$; and $\langle\cdot\rangle$ denotes the inner product. In a similar form to the traditional methods, taking the derivative of Eq. (1) with respect to the mth velocity parameter gives the gradients of objective function:

$$\frac{\partial E_{\mathrm{NW}}}{\partial p_m} = \sum_{i}^{\mathrm{ns}}\sum_{j}^{\mathrm{nr}} \left\{ \frac{\partial \boldsymbol{u}_{i,j}}{\partial p_m} \cdot \frac{\left[\hat{\boldsymbol{u}}_{i,j}\hat{\boldsymbol{u}}_{i,j} \cdot \hat{\boldsymbol{d}}_{i,j} - \hat{\boldsymbol{d}}_{i,j}\right]}{||\boldsymbol{u}_{i,j}||} \right\}, \quad (2)$$

where $\langle\cdot\rangle$ denotes the dot-product of vectors. The corresponding adjoint source term is

$$\delta \mathrm{s}_{i,j} = \frac{\left[\hat{\boldsymbol{u}}_{i,j}\hat{\boldsymbol{u}}_{i,j} \cdot \hat{\boldsymbol{d}}_{i,j} - \hat{\boldsymbol{d}}_{i,j}\right]}{||\boldsymbol{u}_{i,j}||}. \quad (3)$$

The flowchart of the normalized wavefield-based waveform inversion using the random boundary condition is shown in Fig. 2.

```
fread source wavelet, initial model and shot gathers;
// Implementing the inversion under different frequency ranges
for (irange=1; irange<=N_range; irange ++) {
    // Setting the termination condition of the iteration
    iter=1;
    while (iter <=N_iter  && obj>=termination condition) {
        for (ishot=1; ishot<=N_shot; ishot++) {
            a) Construct random boundary for the current velocity model;
            b) By forward propagating source wavefields using absorbing boundary
            condition to generate synthetic data;
            c) Forward propagating source wavefields using random boundary
            condition and recording last two source wavefields;
            d) Calculating adjoint source using the synthetic and observed data;
            e) Backward propagating the adjoint source using absorbing boundary,
            and the source wavefield using random boundary, generating gradient
            on the fly;
        }
        Calculating step length and objective function;
        Update the velocity model;
        iter ++;
    }
}
fwrite the final velocity model;
```

Fig. 2 Pseudocode of waveform inversion using random boundary

Modified interferometric imaging condition-based gradient calculation

For the acoustic wave equation with constant density, using the adjoint state method, Eq. (2) can also be expressed as follows (Bunks et al. 1995; Yang et al. 2015):

$$\frac{\partial E_{\mathrm{NW}}}{\partial p_m} = \sum_i^{\mathrm{ns}} \sum_j^{\mathrm{nr}} \int_0^{t_{\max}} \frac{2}{v^3(\boldsymbol{x})} \cdot u^{\mathrm{tt}}(\boldsymbol{x}, t; \boldsymbol{x}_{\mathrm{s}}) \cdot u_{\mathrm{res}}(\boldsymbol{x}, t; \boldsymbol{x}_r) \mathrm{d}t, \tag{4}$$

where $u(\boldsymbol{x}, t; \boldsymbol{x}_{\mathrm{s}})$ is the source wavefield by the point source excited at the $\boldsymbol{x}_{\mathrm{s}}$ position; $u_{\mathrm{res}}(\boldsymbol{x}, t; \boldsymbol{x}_{\mathrm{r}})$ is the corresponding receiver wavefield by the adjoint source excited at the $\boldsymbol{x}_{\mathrm{r}}$ position, which propagates in the reverse-time direction; u^{tt} denotes the second derivative of u with respect to time; and p_m refers to the mth velocity parameter. Equation (4) is the weighted zero-lag cross-correlation of the two wavefields. In the present study, the modified interferometric imaging condition replaces the zero-lag cross-correlation operation. The resulting gradient calculation equation is expressed as

$$\frac{\partial E_{\mathrm{NW}}}{\partial p_m} = \sum_i^{\mathrm{ns}} \sum_j^{\mathrm{nr}} \int_0^{t_{\max}} \frac{2}{v^3(\boldsymbol{x})} \cdot \int_{|h_{\mathrm{x}}, h_{\mathrm{z}}| \le X} \mathrm{d}h[u_{\mathrm{s}}(x - h_{\mathrm{x}}, z - h_{\mathrm{z}}, t) u_{\mathrm{r}}(x + h_{\mathrm{x}}, z + h_{\mathrm{z}}, t)] \cdot W_{\mathrm{h}} \mathrm{d}t. \tag{5}$$

Here, some symbols are ignored and u_{s} and u_{r} used to denote u^{tt} and u_{res}, respectively. In Eq. (5), h_* is the shift in space; X is the size of the window in space; W_h is the weight function; and $\sum_h W_h = 1$. The interferometric imaging condition proposed by Sava and Poliannikov (2008) is effective in suppressing the noise caused by small-scale random variations of the true velocity. Using WDFs to pre-process the wavefields reconstructed from the observed data, random fluctuations in the wavefields are removed and coherent components are retained. However,

when the background velocity is not accurate enough, interferometric imaging condition suppresses weak scattering information, which is unsatisfactory for imaging the minor structures. Although this does not pose a problem for gradient calculation at the initial stage of waveform inversion, processing of receiver wavefields increases the high-frequency components [as seen in the Guo et al. (2017) results] and is not conducive to waveform inversion. Guo et al. (2017) used the source wavefields to replace one of the receiver wavefields, implicitly increasing the coverage range of each imaging point because the modified interferometric imaging condition extracts the cross-correlation of different spatial lags at every location, replacing zero-lag cross-correlation in conventional cross-correlation imaging condition. Compared with the result obtained by traditional imaging condition, the image of each point obtained by the proposed method contains increased symmetrical lag information.

Sava and Vasconcelos (2011) introduced extended imaging conditions for common image-point gathers constructed as a function of the space- and time-lag extensions at sparse points in the image, which has advantages as an analysis tool. The modified interferometric imaging condition is very similar to extended cross-correlation imaging condition, and may be considered as the weighted average of the extended imaging condition. The extended imaging gathers obtained in this way focus the energy at the origin of the space- and time-lag axes when the velocity is sufficiently accurate. Therefore, weighted averaging increases the imaging energy. Although the FWI and RTM utilize similar imaging process, the RTM image represents reflectivity distribution, whereas the FWI image denotes the wavepath that define the model parameter regions. This significantly influences the residuals of the events recorded at the corresponding receivers. The construction of the wavepath is based on the background model parameters, but like RTM, its energy is influenced by geometric spreading, becoming weak at edges and at depth. Therefore, the same principle, which is based on interferometric imaging condition, can also be applied to strengthen the wavepath of FWI and enhance the continuity of the image. This is because it focuses the energy of the extended imaging gathers on a single point. As concluded by Guo et al. (2017), both the image continuity and the deep illumination are obviously improved—probably because the longer wavelengths at depth than in shallow regions produce lower resolution images in the corresponding extended imaging gather. Therefore, for the same window size, the image constructed in the deep regions may contain more energy, which strengthens this effect. The primary role of the weighting function is to balance the range of coverage of each image point with different wavelengths. When the window size is much smaller than the wavelength, its role can be neglected. The advantages of modified interferometric imaging condition are that both random noise is suppressed and the image is improved.

Actually, the influences of RBC on the image are often reflected in deep parts and in areas of low illumination, whereas it is not obvious in other regions after multiple-shot stacking. In fact, modified interferometric imaging condition plays a complementary role in this situation. Since a series of adjacent points contributes to every point on the gradient, the coherent information is strengthened and improves the gradient focus. As shown in Eq. (5), the effect of the modified interferometric imaging condition is controlled by two parameters: window size and the weighting function. The window size will be illustrated in the following section. The three weighting functions used are:

$$\begin{cases} \text{The first: } W_h^1(h_x,h_z) = \dfrac{1}{(2X+1)^2} \\ \text{The second: } W_h^2(h_x,h_z) = \dfrac{2-h_x^2/X^2-h_z^2/X^2}{\sum_{ix=-X}^{ix=X}\sum_{iz=-X}^{iz=X}(2-ix^2/X^2-iz^2/X^2)} \\ \text{The third: } W_h^3(h_x,h_z) = \dfrac{\exp\left(-\left(h_x^2/X^2+h_z^2/X^2\right)\right)}{\sum_{ix=-X}^{ix=X}\sum_{iz=-X}^{iz=X}\exp(-(ix^2/X^2+iz^2/X^2))} \end{cases}. \tag{6}$$

Here, these forms are examples only, but it is not limited to these forms. It should be noted that we have not changed the objective function, because the form of the adjoint source associated with the objective function has not been changed. The function of the modified interferometric imaging condition is to improve the gradient image by applying it to the gradient calculation directly, such that its role is similar to regularization.

Implementation on GPU

There are many differences between CPU and GPU threads (Micikevicius 2009). First, context switching between threads is essentially free—the state does not have to be stored/restored because GPU resources are partitioned. Second, while CPUs execute efficiently when the number of threads per core is small (often one or two), GPUs achieve high performance when thousands of threads execute concurrently. GPU is a set of multiprocessors each with its own stream processors and shared memory. The global device memory is available to all multiprocessors. By executing thousands of threads at the same time, memory latency is hidden. Register and shared memory are partitioned among the currently executing threads.

Compute unified device architecture (CUDA) divides threads into different thread blocks. All threads contained in a block read and write the shared memory allocated for that block. Therefore, threads within a block communicate

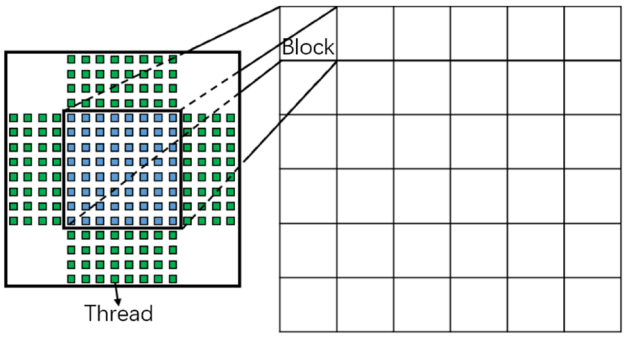

Fig. 3 8 × 8 data tile and halos for eight-order stencils in shared memory

with each other either using the shared memory or by taking the shared memory as the cache, because shared memory latency is two orders of magnitude lower than that of global memory. The key to efficiently implement an algorithm on GPUs is to take full advantage of memory bandwidth. In general, we used memory access redundancy (the ratio of the number of elements accessed to the number of elements processed) as a metric to assess implementation efficiency. The direct method of computing a k-order finite difference requires $(2k + 1)$ input elements for every output value, which leads to $(2k + 1)$ read redundancy.

Implementing the calculations from shared memory is an effective way of reducing the redundancy. Because the shared memory available for each multiprocessor is not sufficient to store the whole computational domain, all threads are divided into 2D blocks to match data tiling, assigning one thread per output element (Fig. 3). Given the k-order finite difference and $n \times m$ blocks and output tiles, an $(n + k) \times (m + k)$ shared memory array is needed to accommodate the data, in addition to the four halo regions. Because the halo elements are read by at least two blocks, the read redundancy of loading the data into shared memory arrays is $(n{\cdot}m + k{\cdot}n + k{\cdot}m)/(n{\cdot}m)$. Once a 2D tile and associated halos are loaded into shared memory, each thread block straightforwardly computes its output tile because all the data are acquired from shared memory rather than global memory.

Numerical examples

In the first example, the Marmousi2 model was used to test the random boundary by normalized wavefield-based waveform inversion. The data were generated by finite difference modeling with shot spacing of 400 m, receiver spacing of 20 m, and there are 24 shots and 500 receivers in total. The true model and the initial model are shown in Fig. 4a, b, respectively. Consideration of computational cost limited the size of the velocity anomalous body to the range of 2–32 grid points. The conjugate gradient method was adopted, and the source normalization was applied to enhance deep illumination. No regularization method was applied. Apart from the imaging condition, there was no difference between tests. The inversion was commenced at low frequencies using 1, 3 and 5 Hz low-pass filters. A maximum of ten iterations were used for each inversion stage.

The inversion results in Fig. 5a, b show that most of the structural shapes were recovered well, although some artifacts appear (mainly concentrated at the edges, as shown in the circles) due to the introduced random boundary. Figure 5c, d compares traces extracted from Fig. 5a, b. Figure 5c shows some fluctuation in the shallow region; Fig. 5d shows the effect in the deep region.

In the second example, the modified interferometric imaging condition-based inversion was tested for different weighting functions. The inversion results and single trace record are shown in Fig. 6. It was noted that the default window dimension of five grid points may not be optimal, because computational efficiency should also be taken into account. On the whole, the illumination of the deep region has been effectively improved, and the layers are more continuous and focused than in Fig. 5b. The results for different weighting functions also show different effects. The result for constant weight W_h^1 is smoother than for variable weighting functions W_h^2 and W_h^3 and have produced a closer fit to the true curve. However, the variable weighting functions show better resolution than the constant weight function, indicating some shortfalls.

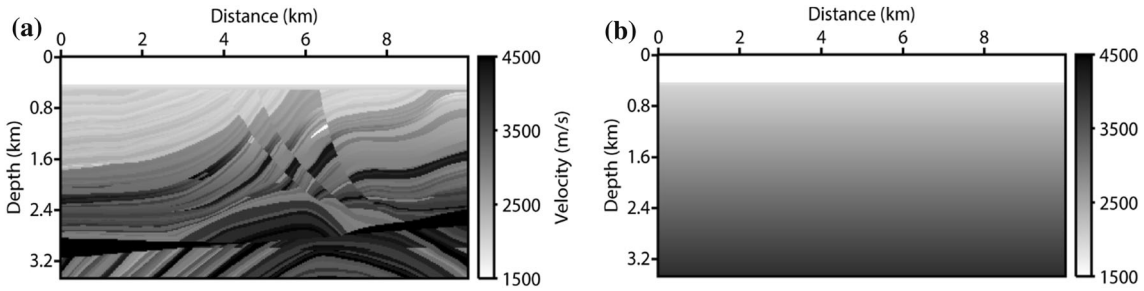

Fig. 4 The Marmousi2 model: **a** true model; **b** initial model

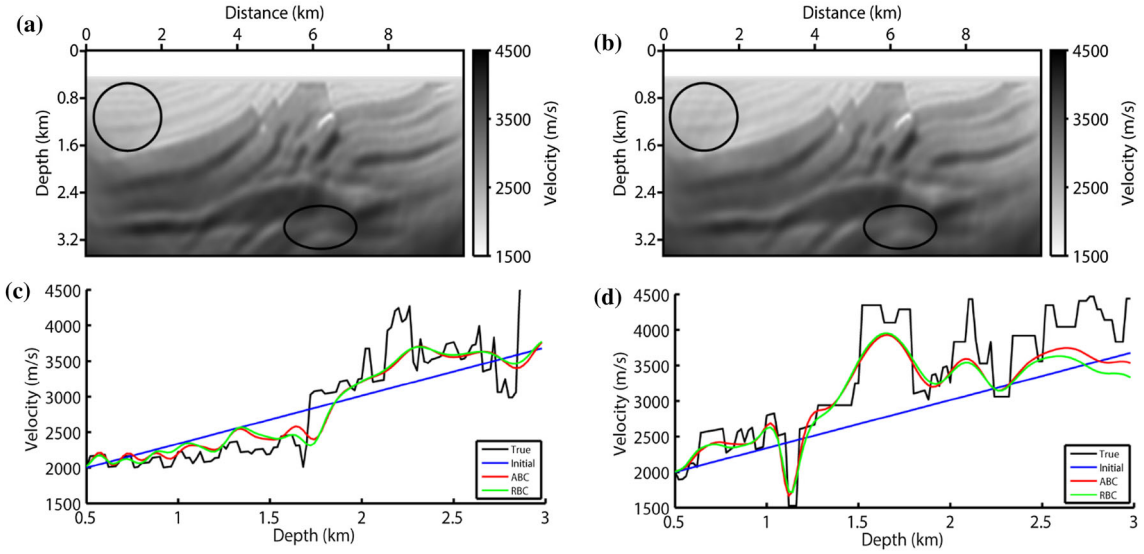

Fig. 5 Inversion results using different boundary conditions: **a** absorbing boundary condition; **b** random boundary condition; **c** comparison of single trace records for **a** and **b** at 1 km depth; **d** comparison of single trace records for **a** and **b** at 6.4 km depth

For the extended imaging gathers, the events are concentrated in the zero-lag position, and also show different sizes associated with the wavelength. The role of modified interferometric imaging condition is to give a weighted average image based on the extended imaging condition. The weighted average operation smooths the result, but because the variable weight functions give more weight to points around the zero-lag position, the smoothing effect is weakened.

To reduce computational cost, large window sizes should be avoided. Small window sizes, which are usually smaller than the size of the focused event displayed in the extended imaging gathers, more energy is contained in the image obtained by the constant weight function than that obtained using the variable weight functions. When the window size is larger than the wavelength, the weighting function is needed to balance the coverage of each image point when there are large wavelength differences between the shallow region and the deep region. The result is that no weighting function is needed when the window is sufficiently small.

The new imaging condition was then tested using different window sizes. In this example, the constant weighting function was applied. The window sizes were 2, 5 and 10 grid points and variable, or 'dynamic', numbers of grid points. The dynamic window size, X_f, is determined by the maximum frequency in each frequency range, using the following empirical formula:

$$X_f = \frac{1}{5dh}\frac{v_{ref}}{2f_{max}}, \tag{7}$$

where v_{ref} is the reference velocity (here $v_{ref} = 3500$ m/s); dh is the grid size; and f_{max} is the frequency of the low-pass filter, and we take the $2f_{max}$ as the maximum frequency of the current frequency range. As the inversion continues, more details of the velocity model are restored. This reveals some fluctuation which causes dramatic changes in the wavelength associated with the velocity. Based on this point, one fifth of the wavelength was selected in this example. To avoid the window size is too large or too small, the window size was limited to lie within the range 2–20 grid pints (This wide range was chosen to avoid unnecessary calculation).

Figure 7 shows that smoother results were obtained with greater window size, with most structures being basically unchanged. Figure 7e, f shows the effects of window size in terms of the contrast in a single trace record. For a fixed window size, the curves for $X = 2$ and $X = 5$ show better effects (2.1 km depth) than for $X = 10$. The recovered images of the structures when using these two window sizes are more focused and produce an improved match to the true curve. For $X = 10$, the high-velocity body at 2.1 km depth has become weaker than the original curve, even though the other structures are well recovered; this also indicates that value of X is too large, and that the window size also should be related to the wavelength of the seismic wave. The layers near the high-velocity body

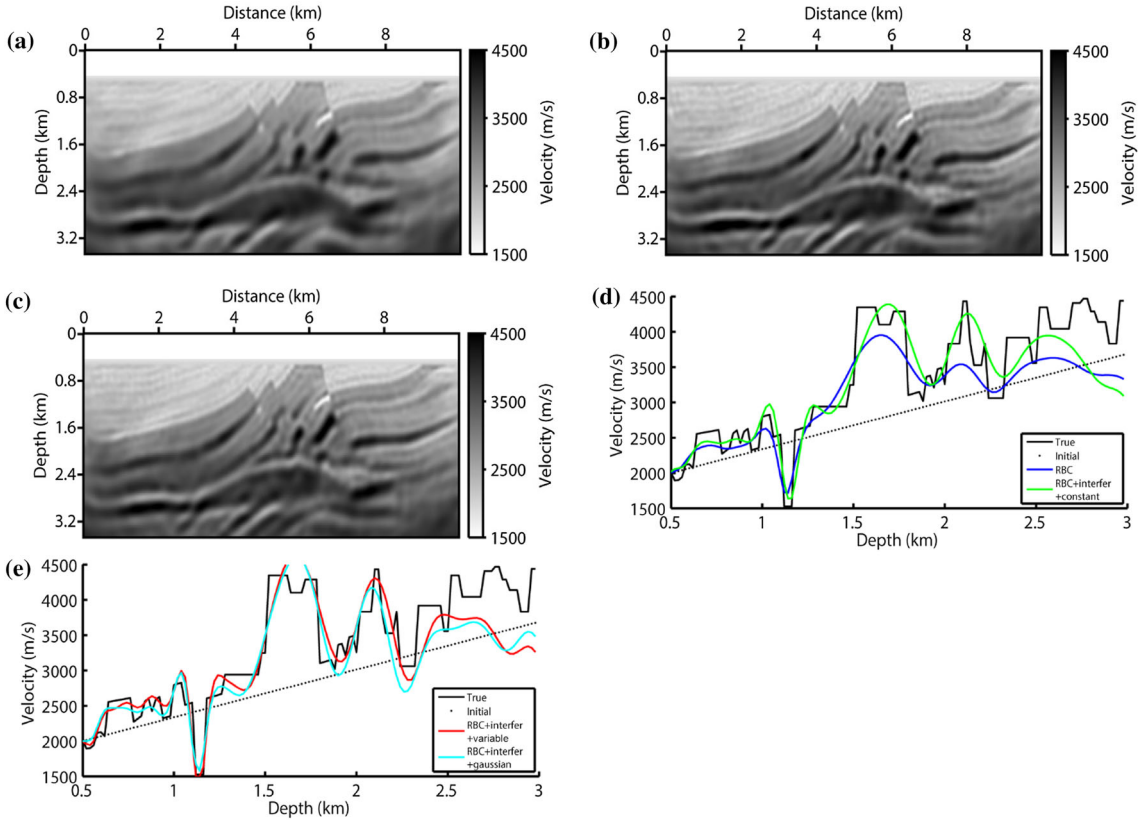

Fig. 6 Modified interferometric imaging condition-based inversion results using different weighting functions (window size = 5). **a** constant weighting W_h^1 from Eq. (6); **b** variable weighting W_h^2 from Eq. (6); **c** Gaussian weighting W_h^3 from Eq. (6); **d**, **e** contrast of single traces at 6.4 km depth

displayed at the depth of 2.1 km are slower, which means that the corresponding wavelength is smaller than the wave propagated in the high-velocity body, indicating that $X = 10$ may be too large in this region. For the regions with drastic velocity change, oversized window sizes will introduce the effects of surrounding areas.

When the window size is dynamic, the curve matches the true curve better than the curves for fixed window size. Since the wavelength depends both on velocity and frequency range, the dynamic window size shows better behavior because it takes this point into consideration. However, the dynamic curve shows some deficiency in the shallow region because the wavelength changes with velocity and also with frequency change, and the constant window size calculated from the average velocity is therefore not accurate enough. The average velocity was used rather than the local velocity, mainly because the variable window size is not conducive to GPU implementation. Since the velocity in the shallow region was generally lower than at depth, the window size appropriate for the deep region may be too large for the shallow region.

Conclusions

The RBC is efficient in reducing the storage requirement for wavefield information. For areas with enough illumination, the influence of RBC may be neglected after multiple shots stacking, whereas for areas with lower illumination, the noise introduced by RBC distorts the image. In this study, we have used modified interferometric imaging condition to improve the calculation of the waveform inversion gradient which weakens the influence of the noise such that the events become more continuous and focused than before, including in the deep region. The effects of the proposed imaging condition are controlled by weighting function and window size. For small window size, the constant weighting function is adequate. Constant weighting was adopted as the reference for testing different window sizes. The numerical examples show that changing the window size with wavelength produced improved results. Window size should not be too large or too small. Ideally, window size is related to the size of the focused events displayed on the zero-lag of the extended imaging gathers, but the situation becomes more complicated in practice because the wavelength changes sharply with

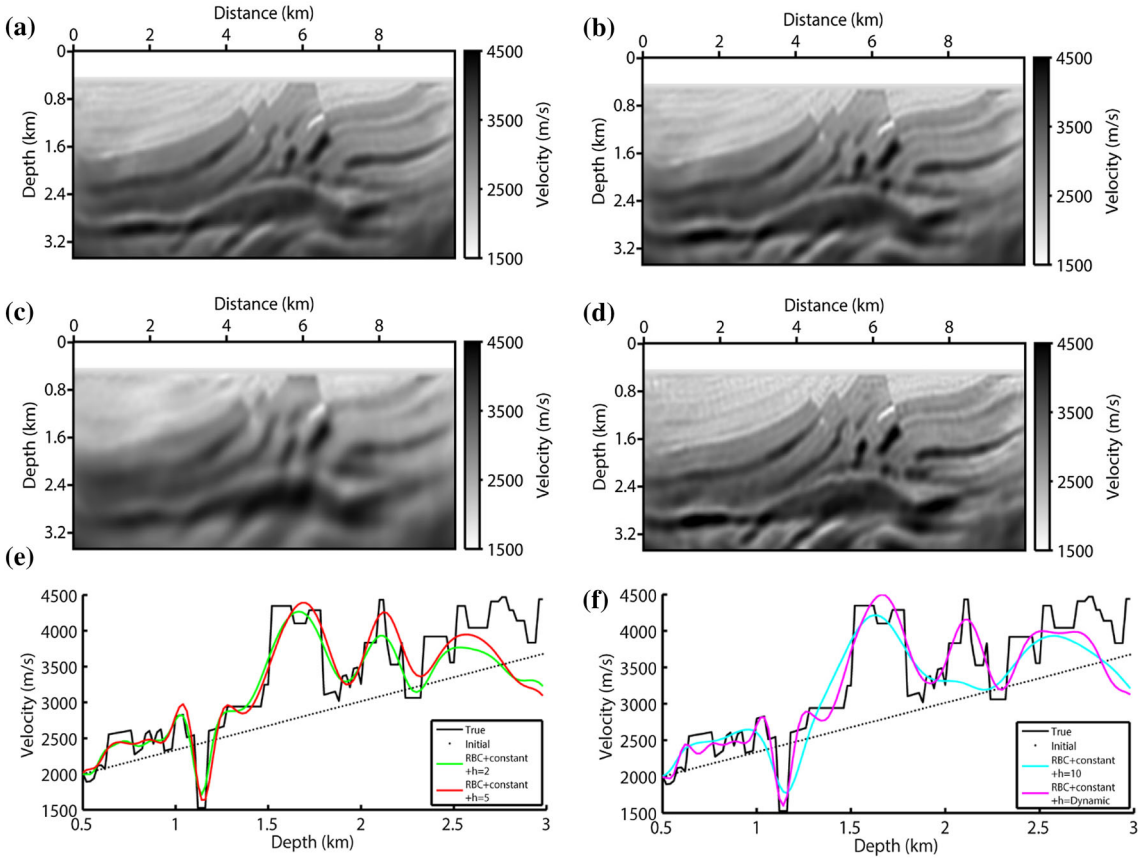

Fig. 7 Modified interferometric imaging condition-based inversion results using constant weighting with different window sizes: **a** $X = 2$; **b** $X = 5$; **c** $X = 10$; **d** dynamic X from Eq. (7); **e**, **f** contrast of single traces at 6.4 km depth

velocity change as the inversion proceeds. It is therefore difficult to choose the optimum parameter. Since the desired window size is usually larger at great depths than at shallow depths, a small window size may not be ideal, but in practice, it is the best compromise.

Acknowledgements This research was supported by Elastic Wave Seismic Imaging Technology Cooperation R & D Project of China National Petroleum Corporation, Major State Research Development Program of China (Grant No. 2016YFC0601101), the Project of National Natural Science Foundation of China (Grant Nos. 41574117 and 41474118), Heilongjiang Province Natural Science Fund for Distinguished Young Scholar (Grant No. JC2016006), and the Open Project of State Key Laboratory of Coastal and Offshore Engineering of Dalian University of Technology (Grant No. LP1509).

Compliance with ethical standards

Conflict of interest On behalf of all authors, the corresponding author states that there is no conflict of interest.

References

Anderson J, Tan L, Wang D (2012) Time-reversal checkpointing methods for RTM and FWI. Geophysics 77:S93–S103

Bunks C, Saleck FM, Zaleski S, Chavent G (1995) Multiscale seismic waveform inversion. Geophysics 60:1457–1473

Choi Y, Alkhalifah T (2013) Multisource waveform inversion of marine streamer data using normalized wavefield. Geophysics 78:R197–R206

Claerbout JF (1985) Imaging the earth's interior. In: Clapp RG (ed) Reverse time migration with random boundaries. 79th annual international meeting 2009, SEG, expanded abstracts, Blackwell Scientific Publications, pp 2809–2813

Clapp RG (2009) Reverse time migration with random boundaries. In: 79th Annual International Meeting, SEG, expanded abstracts, pp 2809–2813

Dussaud E, Symes WW, Lemaistre L, Singer P, Denel B, Cherrett A (2008) Computational strategies for reverse-time migration. In: 78th Annual international meeting, SEG, expanded abstracts, pp 2267–2271

Guo XB, Liu H, Shi Y (2017) Modified interferometric imaging condition for reverse-time migration. Explor Geophys. https://doi.org/10.1071/EG16116

Li B, Liu G, Liu H (2009) A method of using GPU to accelerate seismic pre-stack time migration. Chin J Geophys 52:245–252

Li B, Liu HW, Liu GF, Tong X, Liu H, Guo J, Pei JY (2010) Computational strategy of seismic pre-stack reverse time migration on CPU/GPU. Chin J Geophys 53:2938–2943

Liu HW, Li B, Liu H, Tong X, Liu Q (2010) The algorithm of high order finite difference pre-stack reverse time migration and GPU implementation. Chin J Geophys 53:1725–1733

Liu SW, Wang HZ, Chen SC, Kong XY (2013) Implementation strategy of 3D reverse time migration on GPU/CPU clusters. Chin J Geophys 56:3487–3496

Micikevicius P (2009) 3D finite difference computation on GPUs using CUDA. In: Proceedings of 2nd workshop on general purpose processing on graphics processing units, ACM, pp 79–84

Sava P, Poliannikov O (2008) Interferometric imaging condition for wave-equation migration. Geophysics 73:S47–S61

Sava P, Vasconcelos I (2011) Extended imaging conditions for wave-equation migration. Geophys Prospect 59:35–55

Shen X, Clapp RG (2015) Random boundary condition for memory-efficient waveform inversion gradient computation. Geophysics 80:R351–R359

Shin J, Ha W, Jun H, Min DJ, Shin C (2014) 3D Laplace-domain full waveform inversion using a single GPU card. Comput Geosci 67:1–13

Symes WW (2007) Reverse time migration with optimal checkpointing. Geophysics 72:SM213–SM221

Yang P, Gao J, Wang B (2015) A graphics processing unit implementation of time-domain full-waveform inversion. Geophysics 80:F31–F39

Acta Geophysica (2018) 66:81–91
https://doi.org/10.1007/s11600-017-0102-1

RESEARCH ARTICLE - HYDROLOGY

A study on the Wilkins and Forchheimer equations used in coarse granular media flow

Ashes Banerjee[1] · Srinivas Pasupuleti[1] · Mritunjay Kumar Singh[2] · G.N. Pradeep Kumar[3]

Received: 25 May 2017 / Accepted: 1 December 2017 / Published online: 13 December 2017

Abstract
Complexity of the pore geometry and the random nature of flow velocity make it difficult to predict and represent post laminar flow through porous media. Present study experimentally investigates the applicability of Forchheimer and Wilkins equations for post laminar flow where Darcy's law is invalid due to predominant inertial effect. It is observed that both porosity and media size have significant influence over the coefficients of the Forchheimer coefficients. To incorporate the effect of porosity and media size, behaviour of Forchheimer coefficients are investigated with hydraulic radius as characteristic length. An inversely proportional variation trend is found for all the present and earlier reported data. A new empirical relation between Forchheimer coefficients and hydraulic radius is obtained which can be universally applicable for all media size and porosity. Coefficients of the Wilkins equation are found to be non-deviating for different hydraulic radius in the present study and in the reported literature validating its applicability in predicting the non laminar flow through porous media. Further the Wilkins equation is modified after incorporating the correction factors for better applicability on the field.

Keywords Non-laminar flow · Porous media · Forchheimer equation · Wilkins equation

Introduction

Understanding non laminar flow phenomenon through porous media is primarily essential to analyse and model groundwater flow. Its study includes number of engineering applications such as flow through aquifer, flow through rock fill dams, flow through water filters, etc. Traditionally flows in aforementioned situations were solved using Darcy's law, which would predict flow behaviour satisfactorily when Reynolds number of flow is less than 10 (Kovacs 1971, 1981). With increasing Reynolds number inertial effect increases, resulting in a deviation from Darcy's linear relationship between superficial velocity and hydraulic gradient for coarse granular media. Understanding and modelling this deviation is one the most important concerns in porous media flow. Due to large complexities involved with the geometry, it has never been possible to identify a single equation to model non-Darcy flow through porous media. Hence, the search for an equation to predict the flow in the non laminar regime remains relevant up to date (Dukhan et al. 2014; Hellström and Lundström 2006).

Over the years numerous empirical models were reported to describe non-Darcy flow. Among them two types of equations are mostly used and supported by a large number of experimental data. First one is Forchheimer equation where hydraulic gradient is a second-order polynomial function of velocity and is expressed as

$$i = aV + bV^2, \tag{1}$$

where i is hydraulic gradient, V (m/s) is the seepage velocity, a (s/m) and b (s^2/m^2) are the Darcy and non-Darcy coefficients, respectively. Equation (1) was derived from

✉ Ashes Banerjee
ashes742@gmail.com

[1] Department of Civil Engineering, Indian Institute of Technology (Indian School of Mines), Dhanbad, Jharkhand 826004, India

[2] Department of Applied Mathematics, Indian Institute of Technology (Indian School of Mines), Dhanbad, Jharkhand 826004, India

[3] Department of Civil Engineering, SVU College of Engineering, Sri Venkateswara University, Tirupati, AP 517502, India

Navier–Stokes equation (Ward 1964; Ahmed and Sunada 1969; Hassanizadeh and Gray 1987; Whitaker 1996; Du Plessis and Masliyah 1988) providing it with a theoretical background.

The first-order term (aV) of the equation represents the viscous resistance (similar to Darcy's law) and when the flow is in the laminar regime the equation transforms itself to Darcy's law with a being equal to the inverse of coefficient of permeability (scaled with viscosity). Later it is established that inertial contribution on the flow friction is proportional to the square of the velocity (Reynolds et al. 2000; Hill and Koch 2002; Trykozko et al. 2016) and hence second-order term can be considered as a correction to the first-order term for non Darcy flow.

For precise modelling of non-Darcy flow with Forchheimer equation, proper definition of the coefficients is a prerequisite. Large amount of literature is dedicated towards exploring the behaviour of these coefficients with varying field, media and fluid conditions (Subramanya and Madav 1978; Kumar and Venkataraman 1995; Comiti et al. 2000; Reddy and Rao 2006; Kumar et al. 2004; Huang et al. 2013; Srinivas et al. 2014). Equation (1) is modified by various researchers after incorporating a and b as function of parameters such as media size, porosity, viscosity, etc. (Ergun 1952; Irmay 1958; Scheidegger 1960; Ward 1964; Ahmed and Sunada 1969). But expressions relating a and b with aforementioned parameters are purely empirical and of very limited use. Therefore, it is very difficult to model and predict non-Darcy flow using Forchheimer equation without proper realtion of a and b with the aforementioned parameters.

The second type relation is called Izbash equation (Sedghi-Asl et al. 2014; Wen et al. 2006), power law or missbach equation (Kumar and Venkataraman 1995), which presents hydraulic gradient as a power law function of the seepage velocity. The equation is written as

$$i = pV^j, \tag{2}$$

where p and j are empirical coefficients which depend on flow and media properties. Equation (2) represents Darcy's law for laminar regime when $j = 1$ and a fully turbulent regime when $j = 2$ (Kumar and Venkataraman 1995). At any value of j between 1and 2 it represents a transition regime. Mentioned the flow condition is fully turbulent Eq. (2) can be characterised as a special form of Eq. (1), since in the flow resistance the contribution of first-order viscous term of the Forchheimer equation is negligible compared to the inertial term (Thiruvengadam and Kumar 1997).

Though a number of researchers have suggested using Eq. (2) for analysis of non-Darcy flow (Bordier and Zimmer 2000; Yamada et al. 2005), but since it has only one coefficient p to account for all possible variations, it is not very reliable for modelling and predicting non-Darcy behaviour. Wilkins (1955) proposed an equation for wide range of aggregates (20–80 mm) in the following form:

$$V_v = C\mu^{\alpha} r^{\beta} i^{\gamma}, \tag{3}$$

where V_v is the pore velocity (m/s), C, α, β, γ are the coefficients of Wilkins equation, μ is the dynamic viscosity (Pa–s) and r is the hydraulic radius (m).

Equation (3) is a modified version of Eq. (2). As a majority of fluid and media properties are incorporated with separate identity, coefficients of Wilkins equation are found to be relatively non-deviating as reported in the literature (Garga et al. 1990; Kumar and Venkataraman 1995; Wilkins 1955). But supporting literature about the applicability and behaviour of the Wilkins equation for non linear flow through porous media is very less.

The present study is initiated to experimentally investigate the applicability of Forchheimer and Wilkins equation for modelling the flow resistance in non Darcy flow through coarse granular media. In order to investigate their applicability, nature of the coefficients are examined for variation in media size and porosity at room temperature neglecting the effect of viscosity.

Methodology

Media properties

Seepage analysis is concerned with media properties such as porosity and characteristic length. Porosity is measured as the ratio of the volume of water filled inside the permeameter and the volume of permeameter, after closing all the outlet valves of the packed permeameter and filling it completely with known volume of water. Characteristic length, which represents pore size, has to integrate all the parameters influencing the resistance. Therefore, 'hydraulic radius'(r) (Scheidegger 1958) is used as the characteristic length which is expressed as

$$r = \frac{e}{s_0}, \tag{4}$$

where e is the void ratio $= \frac{f}{(1-f)}$ with f is the porosity and S_0 is the specific surface as per Carman's definition (/m). Specific surface of a particle is defined as the surface area per unit volume. For a regular shaped particle, specific surface can be determined directly. For spheres it is expressed as

$$s_0 = \frac{6}{d}, \tag{5}$$

where d is the diameter of the sphere (m). But when it comes to irregular shaped particle, the surface area of the

media should be determined first to obtain the specific surface. For surface area measurement of irregular shaped media (crushed stone in the present study) the process used by Thiruvengadam and Kumar (1997) is used as follows:

1. The material is sieved through standard IS sieves to separate them into three sizes of 29.8, 34.78, 41.59 mm average volume diameter.
2. Two hundred random samples are collected from each size and they are fully submerged in a colour solution and their impression is collected on a white background of known dimension (Fig. 1a).
3. Collected impressions are then photographed and the processed (Fig. 1b) using suitable image processing software.
4. Pixel area is calculated for the complete background and for the impression of the media section. Surface area is then calculated from the following relation:

$$\frac{\text{Surface area of the complete background}}{\text{Surface area of the media impression}} = \frac{\text{Pixel area of the complete background}}{\text{Pixel area of the media impression}}$$

Process is then repeated and the average surface area is calculated for given sizes. Specific surface of the media is then calculated by dividing the surface area by their volume. Obtained values are presented in Table 1.

Experimentation

Experimentations are carried out in a parallel flow permeameter of 250 mm internal diameter and 1100 mm length (Fig. 2). Accessories like manometer board, collecting tank, centrifugal pump are connected to the permeameter. A header tank attached to the permeameter ensured flow regulation and stabilisation. Flow rate (m^3/s) is measured by volumetric method. Porous medium is retained between two perforated plates, one placed at the entrance and the other at a distance of 150 mm from the exit. A set of piezometric tapings placed at a regular interval of 50 mm and connected to a manometric board is used to measure the head loss. All the turbulence is damped at the entrance, using the perforated plate placed at the entrance and a horizontal perforated pipe at the end of delivery pipe. Permeameter is filled with medium under gravity to ensure even packing. Crushed stones having volume diameter of 29.8, 34.78 and 41.59 mm are used to pack the test section. Each size of media is packed to three different porosities (Table 2) to understand the effect of porosity on flow behaviour. Water is allowed to flow through the test section at maximum possible discharge for about 4–5 h to avoid any further reorientation of media during the experimentation. After the entrapped air is removed using suitable system, volumetric flow rate (m^3/s) and corresponding piezometer readings are noted when a steady-state condition is achieved. Eight separate piezometric head differences (m) with an accuracy of $\pm$ 1.89% are recorded with different vertical distances to eliminate any error during the calculation of hydraulic gradient due to non uniformity of packing. Similarly to remove any error during flow measurement, an average of three readings is used as volumetric flow rate with an accuracy of $\pm$ 2.35%.

Correction factors

Simulating an exact field condition is not possible during laboratory experiments. Therefore, wall porosity and tortuosity corrections are applied to the results in order to make them applicable on the field.

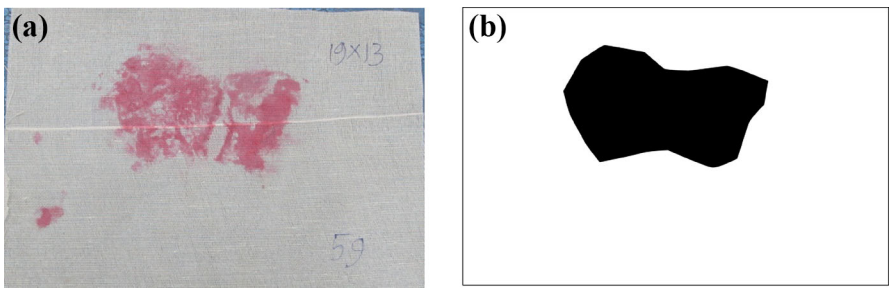

Fig. 1 **a** Impression **b** processed image of the crushed stone on white background for the measurement of the surface area

Table 1 Media properties

Media size (mm)	Volume diameter (mm)	Specific surface (surface area/volume) (/mm)	Shape factor (specific surface × volume diameter)
25.0–31.5	29.8	0.309	9.21
31.5–37.5	34.7	0.253	8.77
37.5–50.0	41.6	0.218	9.06

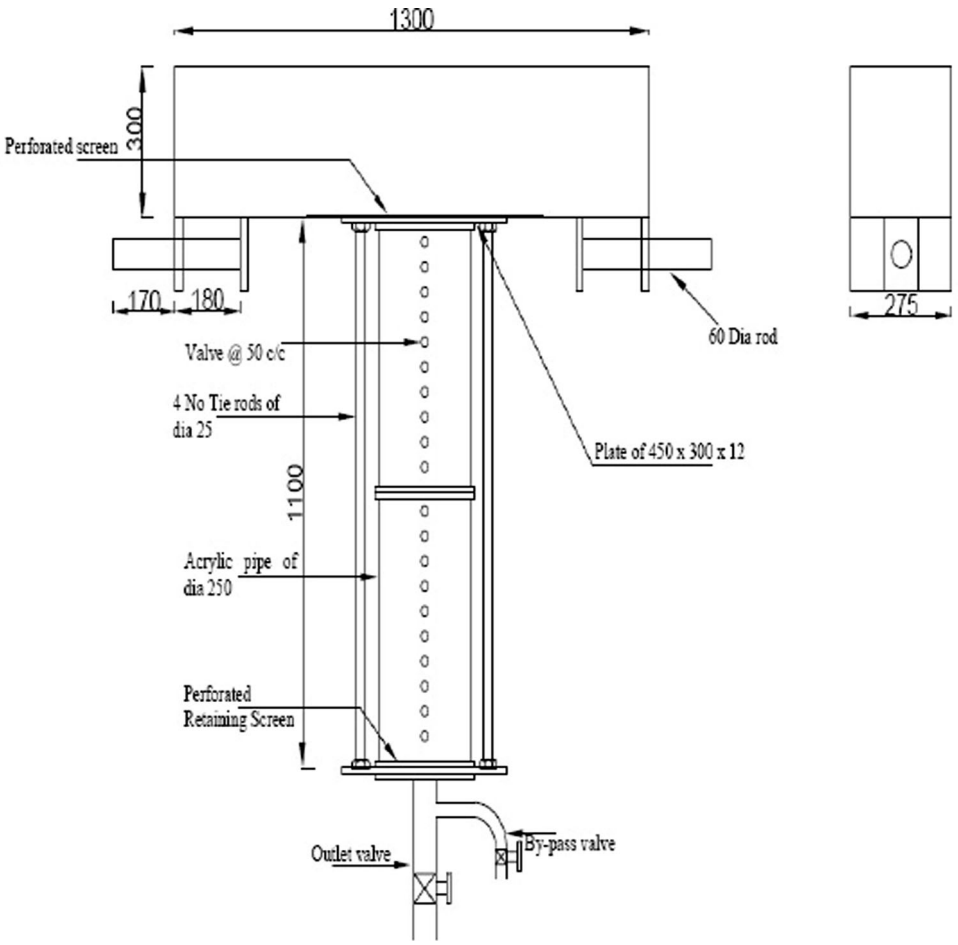

Fig. 2 Parallel flow permeameter test section

Table 2 Value of a and b for different media size and porosity after correction

Volume diameter (mm)	Porosity	a (s/m)	b (s^2/m^2)
29.8	0.405	0.056	3.725
	0.433	0.025	3.542
	0.456	0.045	3.304
34.78	0.417	0.083	3.444
	0.447	0.045	3.420
	0.463	0.068	3.025
41.59	0.410	0.057	2.606
	0.436	0.047	2.516
	0.461	0.046	2.322

Wall correction

Permeameters used in the laboratory are of confined dimensions which causes a loosely packed media near the wall compared to the media inside. Due to uneven packing, velocity of the flow is different at the centre compared to that near wall, causing variation in head loss. Impact of wall effect on flow properties depends on the ratio between sizes of the permeameter and the media (Dudgeon 1968; Mehta and Hawley 1969) and Reynolds number (Rose and Rizk 1949; Eisfeld and Schnitzlein 2001). Exact ratio of permeameter to media size for simulating a no wall effect flow condition is not yet clear. Referring to the literature one may find some studies have reported no wall effect condition when permeameter size to media size ratio is greater than 50 (Mehta and Hawley, 1969; Rose and Rizk 1949), where for some others the ratio is greater than 10 (Winterberg and Tsotsas 2000; Eisfeld and Schnitzlein 2001).

The wall correction factor (C_w) can be defined as the ratio between the average velocity through the entire cross section to the velocity through the inner zone of the permeameter:

$$C_w = \left(\frac{V}{V_{in}}\right), \tag{6}$$

where V_{in} is the velocity of the flow at the inner zone of the permeameter. An expression of wall correction factor developed by one of the authors for parallel flow similar to

the one published for convergent flow (Thiruvengadam and Kumar 1997) is used for velocity correction.

$$C_w = \left[\frac{\left(D + 4.83 \times \frac{d}{2}\right)\left(D - 0.83 \times \frac{d}{2}\right)}{D^2}\right]^{-1}, \quad (7)$$

where D is the diameter of the permeameter (m) and d is the hydraulic diameter of the media (m) used.Hence, corrected velocity for wall effect (V_w) is

$$V_w = \frac{V}{C_w} \quad (8)$$

Porosity correction

Porosity exercises greatest influence over the flow resistance because the basic variable in determining flow resistance is the pore velocity and porosity is prerequisite to determine it. To consider the effect of porosity transformation of superficial velocity to pore velocity is required. Superficial velocity is calculated by dividing the volumetric flow rate (m^3/s) by the cross-section area of the permeameter (m^2):

$$V = \frac{Q}{A}, \quad (9)$$

where Q is the volumetric flow rate and A is the cross-section area of the permeameter.Pore velocity can be defined as the actual velocity of flow through the pores and can be defined as

$$V_v = \frac{Q}{A_v}, \quad (10)$$

where V_v as the pore velocity (m/s) and A_v is the area of the pore (m^2). From Eqs. (9) and (10) porosity correction is introduced to the superficial velocity as follows (Rose and Rizk 1949)

$$V_v = \frac{V}{f} \quad (11)$$

Tortuosity correction

Tortuosity can be defined as the length of the actual flow path of particle divided by the average flow path. Conventionally hydraulic gradient in porous media is calculated assuming that flow takes a straight and undeviating path through it. However, in real situations, flow path of the fluid depends on the interlinking of the void spaces inside the media making the flow path non-linear and causing some errors in calculated hydraulic gradient and velocity.

Though tortuosity merely provides a qualitative representation of the actual flow dynamics occurring inside the complex geometry of porous structure, the use of this parameter provides an extra degree of freedom to account for the largely complex porous geometry. Similarity of the numerical values calculated by various definitions indicate its usefulness in flow modelling though porous media (Koponen et al. 1996).

Generally tortuosity is presented as (Bo-Ming and Jian-Hua 2004; Bear 1972):

$$\tau = \frac{l_e}{l}, \quad (12)$$

where l_e and l are the actual (m) and average or straight length (m) of the flow path. Hence, velocity (Comiti and Renaud 1989) can be modified for tortuosity as

$$V_\tau = V \cdot \tau \quad (13)$$

Similarly hydraulic gradient is corrected for tortuosity according to Carman (Thiruvengadam 2010) as

$$i_\tau = \frac{i}{\tau} \quad (14)$$

Due to very complex geometry of porous structure it has been challenging to derive an expression for the tortuosity correction factor. Therefore, most of the tortuosity corrections are calculated from experiments and then presented as empirical relations. Model proposed by Bo-Ming and Jian-Hua (2004) represents a simple mathematical correlation between tortuosity and porosity considering both overlapped and non-overlapped conditions without any empirical constant. Tortuosity correction factor is presented as

$$\tau = \left[1 + \frac{1}{2}\sqrt{1-f} + \sqrt{1-f} \times \frac{\sqrt{\left(\frac{1}{\sqrt{1-f}} - 1\right)^2 + \frac{1}{4}}}{1 - \sqrt{1-f}}\right], \quad (15)$$

where f is the porosity of the media.

Finally, after incorporating all the corrections, corrected velocities and hydraulic gradients are presented as

$$V_c = \frac{V \cdot \tau}{f C_w} \text{ and } \quad i_c = \frac{i}{\tau}, \quad (16)$$

where V_c and i_c are the corrected velocity and hydraulic gradient.

Results and analysis

Experimentations are performed at a higher range of Reynolds number (1736–7194) calculated as per definition of Kovacs (1971, 1981) (Eq. 17). Such high values are selected to make sure that the flow regime is non laminar. It

is defined that the flow regime is laminar when Reynolds number is less than 10 and turbulent when the Reynolds number is greater than 1000 (Kovacs 1971).

$$\mathrm{Re} = \frac{V d_k}{v}, \tag{17}$$

where v is the kinematic viscosity (m^2/s), d_k is the characteristic length defined by Kovacs as $= \frac{d\,(1-f)\,\alpha_s}{4f}$ with d as the volume diameter (mm) of the particle and α_s is the shape factor of the particle (Table 1). Data obtained from experiments are analysed using the Forchheimer and Wilkins equations. Effect of conditions such as porosity and media sizes are examined on both the equations.

Effect of porosity and media size on Forchheimer equation

After incorporating corrected velocities and hydraulic gradients in Forchheimer equation (Eq. 1), it is modified as

$$\frac{i_c}{V_c} = a + bV_c \tag{18}$$

Darcy (a) and non Darcy coefficients (b) are obtained after plotting Eq. (18) in the Fig. 3 and their values are presented in Table 2. Values of a and b from Table 2 are plotted against porosity for all three media sizes in Fig. 4a and b and results are compared with the earlier studies of Niranjan (1973) (Fig. 5a, b). Coefficients of Forchheimer equation are found to be inversely proportional to the size and porosity of the media as mentioned by earlier researchers (Kumar et al. 2004; Sedghi-Asl et al. 2014; Li et al. 2017). Though the reported variation pattern of a and b with porosity and media size is similar for all the studies, obtained relations between them are found to be different for every set of experimental data. For further illustration let us assume the variation of a and b with the porosity follows the following empirical relation:

$$a = \frac{C_1}{m^{x_1}} \quad \text{and} \quad b = \frac{C_2}{m^{x_2}}, \tag{19}$$

where C_1, C_2, x_1, x_2 are empirical constants and m is a parameter representing porosity of the packing. The problem is, values of C_1, C_2, x_1, x_2 differ largely for every reported study making it quite impossible to predict the values of these coefficients. Similar behaviour is observed for media size.

In earlier studies, behaviour of Darcy and non Darcy coefficients was investigated for the variation of either

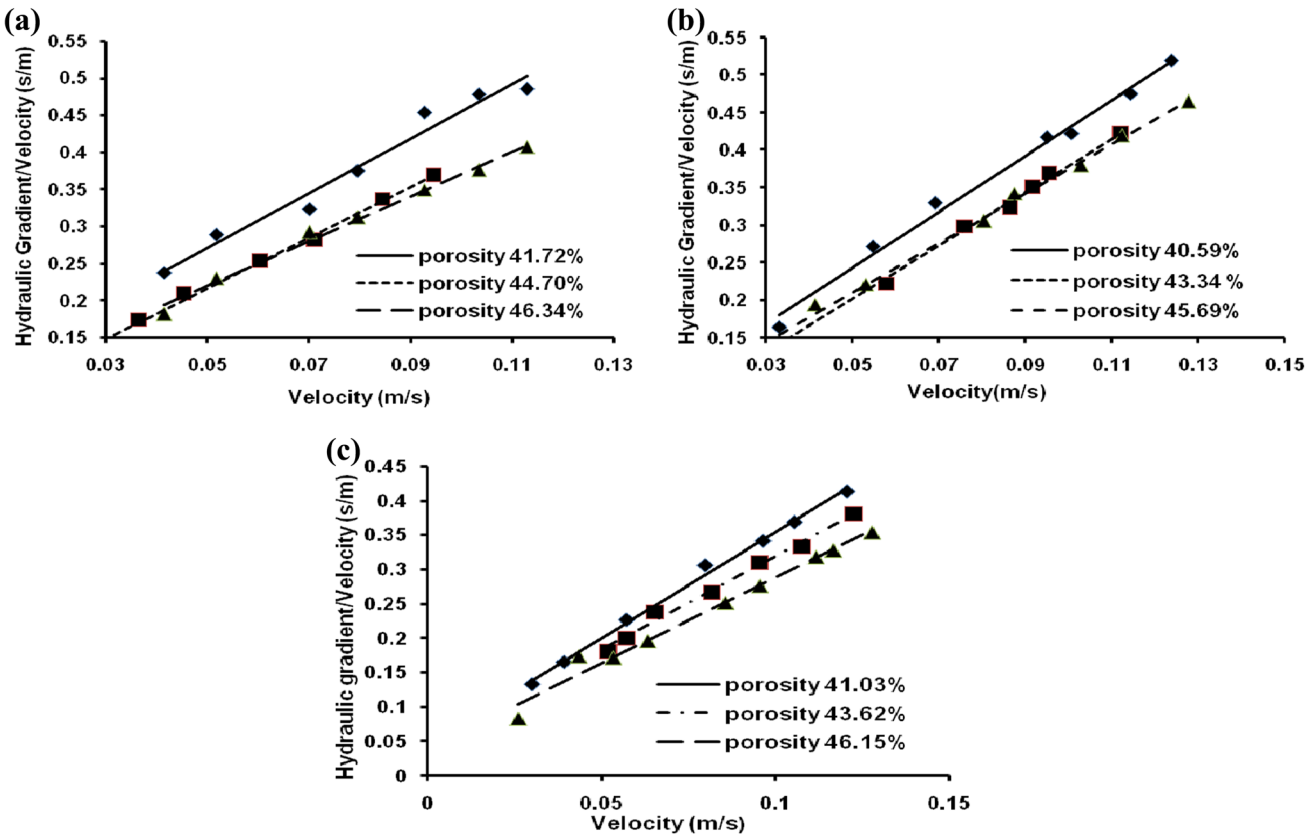

Fig. 3 Variation of Hydraulic Gradient/Velocity with Velocity for **a** 29.8 mm **b** 34.78 mm **c** 41.59 mm media size packed with three different porosities

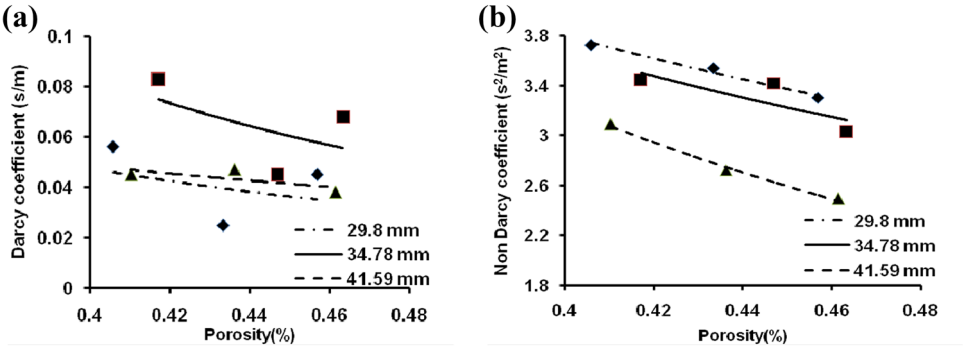

Fig. 4 Relation of **a** Darcy coefficient **b** Non-Darcy coefficient with porosity for different media size

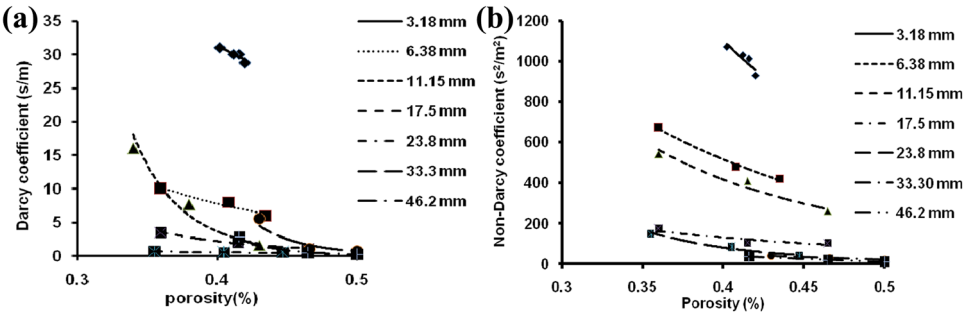

Fig. 5 Relation of **a** Darcy and **b** Non-Darcy coefficient with porosity for different media size data by Niranjan

porosity or size of the media separately ignoring the influence of the other parameter. This approach leads to further complexities because the Darcy and non Darcy coefficients are found to be influenced by both porosity and media size simultaneously (Figs. 4, 5).

Therefore, the present study takes special care in investigating the behaviour of Darcy and non Darcy coefficients with the hydraulic radius which incorporates the effect of both porosity and size of the media. When the values of Darcy and non Darcy coefficients are plotted against the hydraulic radius (Fig. 6), they are found to follow a similar trend for all the media sizes and porosities tested in the present study as well as in the earlier study reported by Niranjan (1973), Sedghi-Asl et al. (2014) Pradeep Kumar (1994), Nasser [Pradeep Kumar (1994)]. This indicates that if the effect of porosity and media size is considered simultaneously in the form of hydraulic radius, the variation of Darcy and non Darcy coefficient becomes much more simple and predictable. When all these results are combined and plotted together in a single graph, all the values are found to be in excellent correlation with each other (Fig. 7). From Fig. 7 a relation can be proposed between values of Darcy (a) and non Darcy coefficient (b) with the hydraulic radius of the media for non linear flow through porous media as:

$$a = \frac{0.000286}{r^{1.320438}} \quad \text{with} \quad R^2 = 0.7276 \tag{20}$$

$$b = \frac{0.069039}{r^{1.145820}} \quad \text{with} \quad R^2 = 0.85 \tag{21}$$

Equations (20) and (21) depict a much more predictable and simple variation pattern of Darcy (a) and non Darcy coefficient (b) with hydraulic radius compared to media size or porosity. Therefore, it can be further examined after applying the correction factors and a proper relation between Darcy (a) and non Darcy coefficient (b) with the hydraulic radius can be proposed. This may lead to an end to the age old problem concerning complex and unpredictable variation pattern of these coefficients and help in modelling the flow using Forchheimer equation.

Effect of porosity and media size on Wilkins equation

Very limited studies are reported on the Wilkins equation, but they present relatively non-deviating coefficients when subjected to non-laminar flow through porous media. Results obtained from the experimental set up are analysed in order to investigate the behaviour of parameters of the Wilkins equation. As discussed earlier, Wilkins equation is a modified version of Eq. (2). After modification, Eq. (2) can be presented as

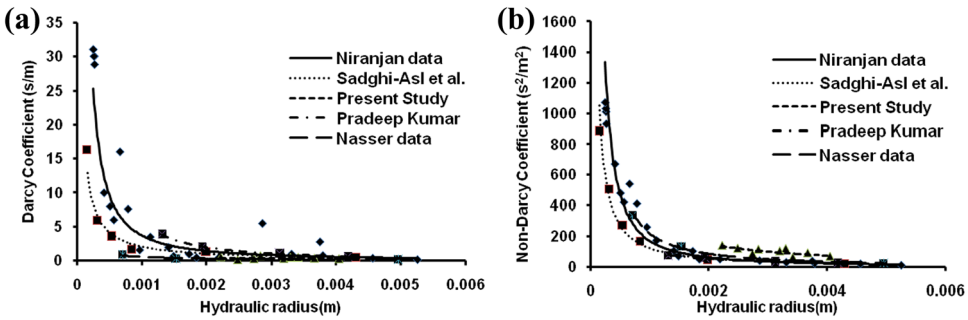

Fig. 6 Variation of **a** Darcy and **b** Non-Darcy coefficient with hydraulic radius

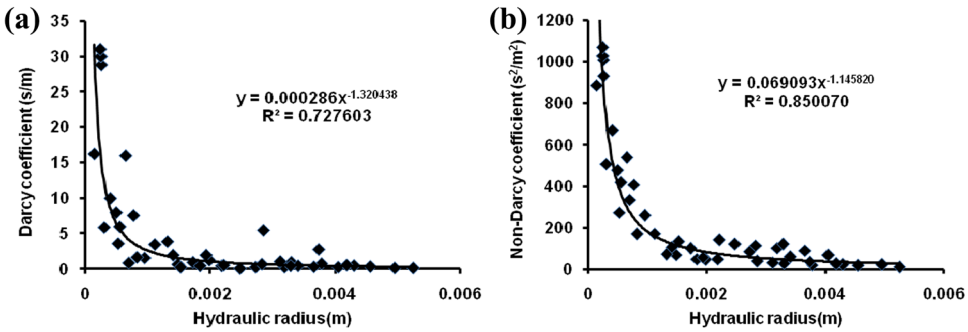

Fig. 7 Variation of **a** Darcy coefficient **b** Non-Darcy coefficient with hydraulic radius plotted together as a single variation trend

$$V = \frac{1}{\sqrt[j]{p}}(i)^{(1/j)} \tag{22}$$

and the Wilkins equation is in the form of

$$V_{\mathrm{v}} = Wr^{\beta} i^{\gamma} \tag{23}$$

In the earlier studies, there is no proper mention about the application of correction factors. In present study all the correction factors are incorporated in Eq. (23) as follows:

$$\frac{V \times \tau}{C_{\mathrm{w}} \times \eta} = \mathrm{Wr}^{\beta} \left(\frac{i}{\tau}\right)^{\gamma} \tag{24}$$

Judging by the similarity of Eq. (22) and (24) we can conclude

$$\frac{W \times C_{\mathrm{w}} \times \eta}{\tau^{\gamma+1}} r^{\beta} = \frac{1}{p^{1/j}} \text{ with } \gamma = \frac{1}{j} \tag{25}$$

Equation (25) can be written in the following logarithmic form:

$$\log W + \log C_{\mathrm{w}} + \beta \log r = \frac{1}{j} \log\left(\tau/p\right) + \log \tau - \log \eta \tag{26}$$

Equation (26) is plotted in the Fig. 8 with log r against 'x' axis and $\frac{1}{j}\log\left(\tau/p\right) + \log\tau - \log\eta$ against 'y' axis. Values of p and j are obtained after plotting the velocity and hydraulic gradient against the 'x' and 'y' axis, respectively, in Fig. 9. Almost similar values of W and β are obtained for all three sizes of media (Table 3). The reason for such behaviour may be incorporation of the hydraulic radius

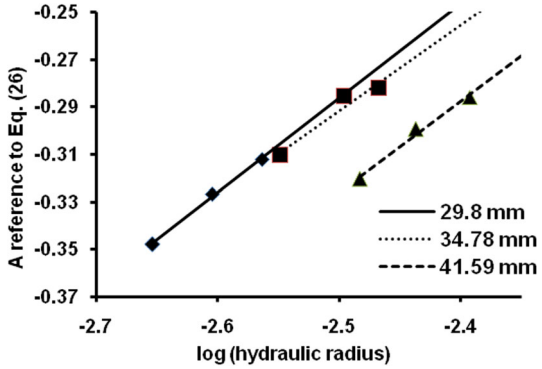

Fig. 8 Equation (26) plotted in the form of a straight line to obtain values of W and β

parameter in the equation which incorporates the variation of both media size and porosity. Value of γ in the Wilkins equation is said to be the representation of flow regimes. Value of γ is 1 when the flow is in laminar regime and gradually shifts towards its maximum value 0.5 when the flow is in completely turbulent regime (Chapokpour et al. 2013). Values of γ in the Table 3 indicate that the flow condition is not fully turbulent in the experimentation. However, experiments are performed at very high Reynolds number (1736–7194). The discrepancy suggests that unlike pipe flow, values of Reynolds number cannot precisely predict the flow regime in case of flow through porous media. This is due to the unavailability of proper definition of pore size and pore velocity but still it is essential as a tool to presume the flow regime inside large complexities of porous media with certain accuracy.

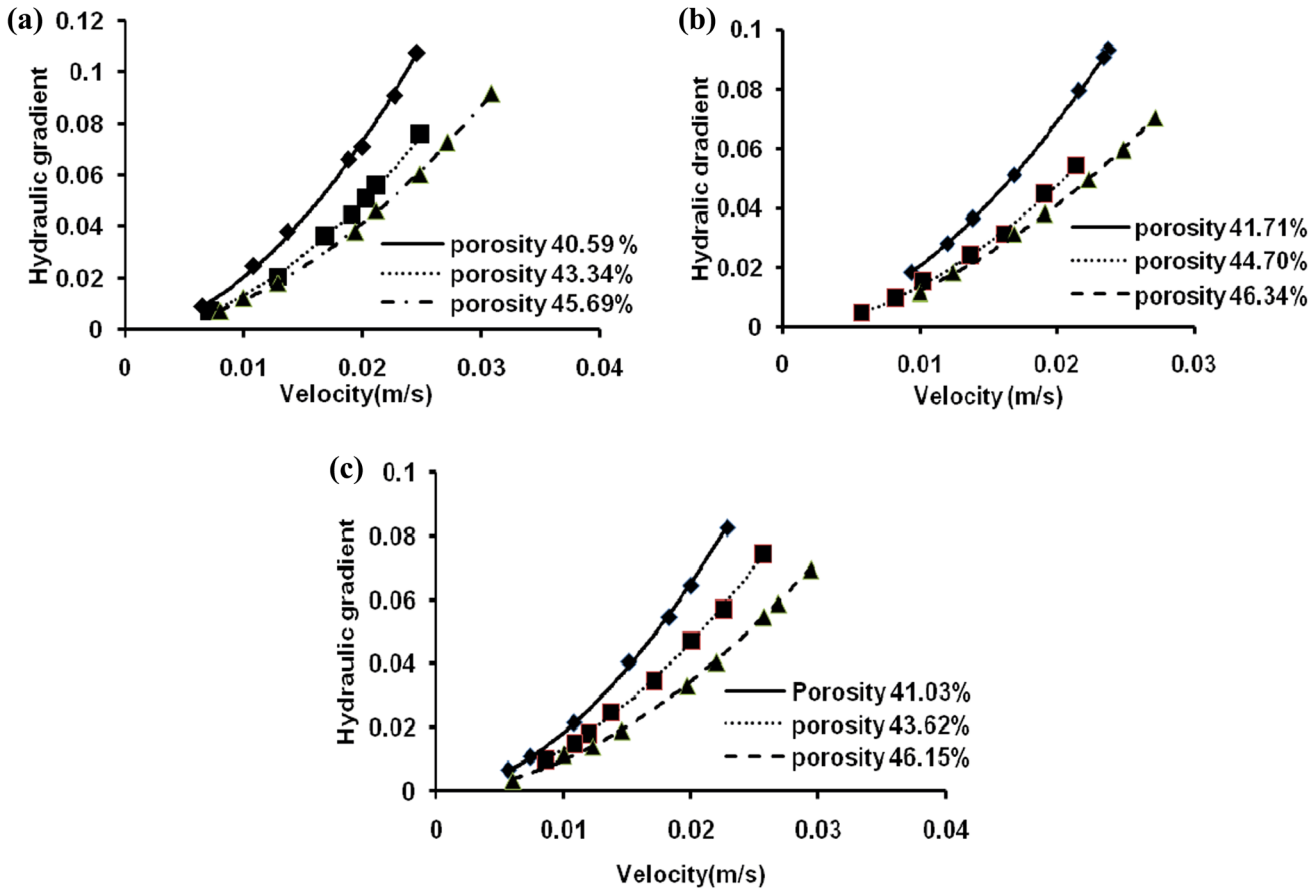

Fig. 9 Variation of hydraulic gradient with velocity for **a** 29.8 mm **b** 34.78 mm **c** 41.59 mm media size packed with different porosities

Table 3 Values of the Wilkins Coefficient with variation in media size and porosity

Volume diameter (mm)	W (m–s)	β	γ
29.80	5.11	0.397	0.541
34.78	4.12	0.362	0.562
41.59	4.30	0.384	0.546

It is observed from Eq. (6) that tortuosity is a function of porosity of the media (Bo-Ming and Jian-Hua 2004). In the earlier studies the variation of porosity was ignored as a constant tortuosity correction factor was used to correct the velocity and hydraulic gradient for all media packed with different porosities. This type of approach leads to some error in the values of W and β. The present study incorporates the variation of porosity in the tortuosity correction for all the media sizes experimented and modifies the Wilkins equation after applying the correction factors. Because of the reason discussed earlier, values of W and β obtained from the present study (Table 3) differ from the results reported by earlier researcher (Table 4).

Though the results obtained in present study differ a little from the earlier reported results, broadly all the studies point towards non-deviating coefficients of Wilkins equation for different media sizes and porosities. So, it is relatively easy to predict the non laminar parallel flow through porous media using the Wilkins equation.

Discussion and conclusion

Parallel flow through porous media for post laminar regime is studied using a parallel flow permeameter for three different media sizes each having three different porosities and using hydraulic radius as the characteristic length. Appropriate wall, porosity and tortuosity corrections are incorporated to the obtained velocity and hydraulic gradient. Applicability of the Forchheimer and Wilkins equations and the behaviour of the coefficients of these equations are studied for 29.80 mm crushed stones packed with 40.59, 43.34, 45.69% porosity, 34.78 mm crushed stones packed with 41.72, 44.70, 46.34% porosity and 41.59 mm crushed stones packed with 41.03, 43.62, 46.15% porosity. The findings are listed below:

Table 4 Values of Wilkins Coefficients reported by earlier researchers

Proposed by	Media type	Size (mm)	Porosity (%)	Boundary Condition	W(m-s)	B	γ
Wilkins (1955)	Crushed stone	51.0	40.0	Parallel flow	5.24	0.50	0.54
Garga et al. (1990)	Crushed stone	24.6	47.0	Parallel flow	5.39	0.50	0.53
Pradeep Kumar (1994)	Crushed stone	13.1	47.0	Parallel flow	4.94	0.51	0.52

1. Both Forchheimer and Wilkins type equations are found to be well fitted for representing the flow in the non-laminar regime.
2. Behaviour of Forchheimer coefficients are found to be very complex with variation in porosity and meida size analogous to the results reported in the literature. It is concluded that media size or porosity alone cannot represent the complete geometry of the pores. Therefore, hydraulic radius is introduced as characteristic length. The variation of a and b is investigated with hydraulic radius of the media;, both the coefficients are found to be inversely proportional to the hydraulic radius. Similar results are found from the data presented by earlier researchers.
3. The relationship of Darcy (a)/non Darcy coefficient (b) with the hydraulic radius (r) is derived after combining the results from the present study and some earlier reported data as

$$a = \frac{0.000286}{r^{1.320438}} \text{ with } R^2 = 0.7276$$

$$b = \frac{0.069039}{r^{1.145820}} \text{ with } R^2 = 0.85$$

Above relations suggest that the Darcy (a)/non Darcy coefficients (b) have a simple and predictable variation pattern with hydraulic radius which is valid for different experimental conditions. Further experimental works with proper correction factors are necessary to obtain readily applicable equations between Darcy (a)/non Darcy coefficients (b) and hydraulic radius to remove the complexity in the behaviour of these coefficients (a, b) with media properties and, therefore, help in modelling the flow using Forchheimer equation.

4. The coefficients of Wilkins equation are found to be non-deviating for all the media sizes and porosities as reported in the literature, pointing towards its applicability to model post linear flow through porous media.
5. In earlier studies either correction factors were not used or not properly defined. The present study used properly defined correction factors to correct the experimentally obtained velocity and hydraulic gradient and thus makes an effort to modify the Forchheimer and Wilkins equation to be applicable in the field conditions.

Hence both the Forchheimer and Wilkins equation are found be applicable for representing the flow in post laminar regime. The Wilkins equation is found to be suitable for modelling post laminar porous media flow due to the non deviating nature of its coefficients with variation in porosity and media size. However, for the modelling of Forchheimer coefficients it is suggested to use hydraulic radius instead of porosity and media size separately to make them applicable to predict the flow in numerous non linear situations such as water filters, aquifers, rock fill dams, oil and gas well, etc.

Acknowledgements The authors would like to thank the faculty of Civil Engineering, Mechanical Engineering and Chemical Engineering, IIT (ISM) Dhanbad. for their support and in utilising the facilities in the departments. The authors would like to acknowledge the funding received from IIT(ISM), Dhanbad, in Faculty Research Scheme (FRS), vide no: FRS (62)/2013-2014/CE utilised for fabrication of the permeameter experimental set up used in the study.

References

Ahmed N, Sunada DK (1969) Nonlinear flow in porous media. J Hydraul Div ASCE 95(6):1847–1858

Bear J (1972) Dynamics of fluids in porous media. Elsevier, New York

Bo-Ming Y, Jian-Hua L (2004) A geometry model for tortuosity of flow path in porous media. Chin Phys Lett 21(8):1569

Bordier C, Zimmer D (2000) Drainage equations and non-Darcian modelling in coarse porous media or geosynthetic materials. J Hydrol 228(3):174–187

Chapokpour J, Tokaldany EA, Sedghi-Asl M (2013) Estimation of friction coefficient in sediment contained flow through rockfill. Int J Eng Trans B 26(2):85–94

Comiti J, Renaud M (1989) A new model for determining mean structure parameters of fixed beds from pressure drop measurements: application to beds packed with parallelepipedal particles. Chem Eng Sci 44(7):1539–1545

Comiti J, Sabiri N, Montillet A (2000) Experimental characterization of flow regimes in various porous media-III: limit of Darcy's or creeping flow regime for Newtonian and purely viscous non-Newtonian fluids. Chem Eng Sci 55:3057–3061

Du Plessis P, Masliyah J (1988) Mathematical modelling of flow through consolidated isotropic porous media. Transp Porous Media 3(2):145–161

Dudgeon CR (1968) Relationship between porosity and permeability of coarse granular materials. In: Third Australasian Conference on Hydraulics and Fluid Mechanics, Sydney, pp 76–80

Dukhan N, Özer, Özdemir (2014) Experimental flow in various porous media and reconciliation of Forchheimer and Ergun relations. Exp Thermal Fluid Sci 57:425–433

Eisfeld B, Schnitzlein K (2001) The influence of confining walls on the pressure drop in packed beds. Chem Eng Sci 56(14):4321–4329

Ergun S (1952) Fluid flow through packed columns. Chem Eng Prog 48:89–94

Garga VK, Hansen D Townsend RD (1990) Considerations on the design of flowthrough rockfill drains. In: the Proceedings of the 14th Annual British Columbia Mine Reclamation Symposium, Cranbrook

Hassanizadeh SM, Gray WG (1987) High velocity flow in porous media. Transp Porous Media 2(6):521–531

Hellström GI, Lundström (2006) Flow through porous media at moderate Reynolds number. International Scientific Colloquium Modelling for Material Processing, Riga, pp 129–134

Hill RJ, Koch DL (2002) The transition from steady to weakly turbulent flow in a close-packed ordered array of spheres. J Fluid Mech 465:59–97

Huang K, Wan JW, Chen CX, He LQ, Mei WB, Zhang MY (2013) Experimental investigation on water flow in cubic arrays of spheres. J Hydrol 492:61–68

Irmay S (1958) On the theoretical derivation of Darcy and Forchheimer formulas. Trans Am Geophys Union 39(4):702–707

Koponen A, Kataja M, Timonen J (1996) Tortuous flow in porous media. Phys Rev E 54(1):406–410

Kovacs G (1971) Seepage through saturated and unsaturated layers. Hydrol Sci J 16(2):27–40

Kovacs G (1981) Seepage Hydraulics. ESPC, New York

Kumar GNP, Venkataraman P (1995) Non-Darcy converging flow through coarse granular media. J Inst Eng (India) 76(5):6–11

Kumar GNP, Thiruvengadam T, Murali M (2004) A further study on forchheimer coefficients as applied seepage flow. ISH J Hydraul Eng 10(2):1–13

Li Z, Wan J, Huang K, Chang W, He Y (2017) Effects of particle diameter on flow characteristics in sand columns. Int J Heat Mass Transf 104:533–536

Mehta D, Hawley MC (1969) Wall effect in packed columns. Ind Eng Chem Process Des Dev 8(2):280–282

Niranjan HS (1973) Non-Darcy flow through porous media. Master of Technology Thesis, Indian Institute of Technology, India

Pradeep Kumar GN (1994) Radial Non-Darcy flow through coarse granular media, unpublished PhD thesis, Sri Venkateswara University, Tirupati, India

Reddy BNP, Rao RM (2006) Effect of convergence on nonlinear flow in porous media. J Hydraul Eng 132(4):420–427

Reynolds A, Reavell S, Harral B (2000) Flow and dispersion through a close-packed fixed bed of spheres. Phys Rev E 62:3632

Rose HE, Rizk AMA (1949) Further researches in fluid flow through beds of granular material. Proc Inst Mech Eng 160(1):493–511

Scheidegger AE (1958) The physics of flow through porous media. Soil Sci 86(6):355

Scheidegger AE (1960) The physics of flow through porous media. University of Toronto Press, Toronto

Sedghi-Asl M, Rahimi H, Salehi R (2014) Non-Darcy flow of water through a packed column test. Transp Porous Media 101(2):215–227

Srinivas P, Kumar GNP, Jayachndra K (2014) Quantification of effect of convergence in porous media flow. In: 5th International Conference on Porous Media and Their Applications in Science, Engineering and Industry, Hawaii, pp 1–6

Subramanya K, Madav M (1978) Linear and Non-linear flow through porous media, submitted to central board of irrigation and power

Thiruvengadam M (2010) Experimental investigation on flow through porous media with an emphasis on characteristic parameters, unpublished PhD thesis, Sri Venkateswara University,Tirupati, India

Thiruvengadam M, Kumar GP (1997) Validity of Forchheimer equation in radial flow through coarse granular media. J Eng Mech 123:696–705

Trykozko A, Peszynska M, Dohnalik M (2016) Modeling non-Darcy flows in realistic pore-scale proppant geometries. Comput Geotech 71:352–360

Ward JC (1964) Turbulent flow in porous media. J Hydraul Div ASCE 90(5):1–12

Wen Z, Huang G, Zhan H (2006) Non-Darcian flow in a single confined vertical fracture toward a well. J Hydrol 330(3):698–708

Whitaker S (1996) The Forchheimer equation: a theoretical development. Transp Porous Media 25(1):27–61

Wilkins JK (1955) Flow of water through rockfill and its application to the design of dams. NZ Eng 10(11):382–387

Winterberg M, Tsotsas E (2000) Impact of tube to particle diameter ratio on pressure drop in packed beds. AIChE J 46(5):1084–1088

Yamada H, Nakamura F, Watanabe Y, Murakami M, Nogami T (2005) Measuring hydraulic permeability in a streambed using the packer test. Hydrol Process 19(13):2507–2524

Acta Geophysica (2018) 66:93–107
https://doi.org/10.1007/s11600-017-0109-7

RESEARCH ARTICLE - HYDROLOGY

Reinvestigation on mixing length in an open channel turbulent flow

Snehasis Kundu[1] · Manotosh Kumbhakar[2] · Koeli Ghoshal[2]

Received: 12 August 2017 / Accepted: 13 December 2017 / Published online: 19 December 2017

Abstract
The present study proposes a model on vertical distribution of streamwise velocity in an open channel turbulent flow through a newly proposed mixing length, which is derived for both clear water and sediment-laden turbulent flows. The analysis is based on a theoretical consideration which explores the effect of density stratification on the streamwise velocity profile. The derivation of mixing length makes use of the diffusion equation where both the sediment diffusivity and momentum diffusivity are taken as a function of height from the channel bed. The damping factor present in the mixing length of sediment-fluid mixture contains velocity and concentration gradients. This factor is capable of describing the dip-phenomenon of velocity distribution. From the existing experimental data of velocity, the mixing length data are calculated. The pattern shows that mixing length increases from bed to the dip-position, having a larger value at dip-position and then decreases up to the water surface with a zero value thereat. The present model agrees well with these data sets and this behavior cannot be described by any other existing model. Finally, the proposed mixing length model is applied to find the velocity distribution in wide and narrow open channels. The derived velocity distribution is compared with laboratory channel data of velocity, and the comparison shows good agreement.

Keywords Sediment and momentum diffusivity · Mixing length · Open channel flows · Velocity-dip-phenomenon · Settling velocity

Introduction

The investigation of longitudinal turbulent mean velocity profile in an open channel turbulent flow is a long-standing topic of research (Absi 2011; Yang 2009; Ballio and Tait 2012). The knowledge of velocity distribution helps to understand the flow dynamics and sediment transport mechanism. Though numerous models have been developed on vertical distribution of velocity (Absi 2011; Yang 2009; Kundu and Ghoshal 2012; Bialik et al. 2012; Bialik 2013), turbulence is such an irregular and unpredictable phenomenon that it does not allow any model to be universal. Some models are appropriate for some experimental or field data, whereas the same models may be inappropriate to fit some other types of measured data. So, the investigation on velocity distribution in an open channel turbulent flow is still in progress.

The present study analyses the vertical distribution of streamwise velocity in turbulent flows for both clear and sediment mixed water, and the analysis is done based on the application of mixing length formulation. Following the kinetic theory of gases, the mixing length l represents a small distance which a lump of fluid particle may randomly travel in a turbulent flow before mixing or colliding with surrounding fluid (Bialik et al. 2012, 2015; Bialik 2011, 2013), and the fluid parcel conserves all its properties before mixing. Prandtl (1932) originally developed two simple expressions on mixing length l out of which one was linear $l = \kappa y$ where κ is the von Karman constant and y is the distance from the bottom boundary wall and the other was parabolic $l = \kappa y\sqrt{1-y}$. Patel (1973) used a

✉ Manotosh Kumbhakar
manotosh.kumbhakar@gmail.com

Snehasis Kundu
snehasis18386@gmail.com

Koeli Ghoshal
koeli@maths.iitkgp.ernet.in

[1] Department of Basic Sciences and Humanities, IIIT Bhubaneswar, Bhubaneswar 751003, India

[2] Department of Mathematics, Indian Institute of Technology, Kharagpur 721302, India

mixing length of the type $l^* = \kappa y^* \tanh(\lambda^2 y^{*2})^{1/2}$ and claimed that it applies throughout the wall region. Launder and Priddin (1973) pointed out that many users adopt the expression of Van Driest (1956) for viscous damping of mixing length near the wall as $l = \kappa y(1 - \exp(-D))$ where D is the damping function. Nishioka and Iida (1973) reinvestigated the turbulent boundary layers developed by Prandtl (1960), Karman (1960) and Townsend (1961) and proposed a differential equation describing the mixing length. Galbraith et al. (1977) showed that when variations of shear stress are substantial, the choice of mixing length $l = \kappa y\sqrt{\tau/\tau_\omega}$, τ_ω being the wall shear stress, would be more appropriate.

Granville (1989) proposed a modified van Driest formula for the mixing length of turbulent boundary layers in pressure gradients as $l^* = \kappa y^* \sqrt{\tau^*}(1 - \exp(-\frac{y^*}{\lambda^*}))$ where λ^* is a function of pressure-gradient parameter. Umeyama and Gerritsen (1992a) proposed a mixing length for sediment-laden flow as $l = \kappa y\left(1 - \frac{y}{\delta}\right)^{\alpha}$ where δ is the boundary layer thickness and α was shown to be a function of sediment concentration. Kovacs (1988) developed a mixing length for sediment-laden flow as $l = l_0 D(C)$ where $D(C)$ is the damping function based on concentration of the flow which is given as $D = 1 - C^{1/3}$, C being the volumetric concentration. But its practical application on velocity distribution does not produce very satisfactory result. Buschmann and Gad-el Hak (2005) modified the damping function of van Driest's equation for mixing length and took the mixing length as $l^+ = \kappa(y^+ - D)[1 - \exp(-\frac{y^+}{\lambda})]^{3/2}$. Later on, Prandtl's mixing length model was revisited by Obermeier (2006) where he replaced the characteristic mixing length of Prandtl's model by different mixing lengths for velocity fluctuations parallel to the wall and normal to the wall, respectively. Castro-Orgaz et al. (2012) proposed mixing length model for sediment-laden flow as $l_m = \psi l_0$ and where the damping function ψ was determined by including the effect of density stratification through Richardson number R_i, wake parameter Π, velocity and concentration gradients. Few important mixing length models are summarized in Table 1.

Though the mixing length model of Castro-Orgaz et al. (2012) is a more generalized one than the existing previous models and can satisfactorily fit experimental observations on velocity distribution, still it fails to describe dip-phenomenon characteristic in velocity profile. The occurrence of maximum velocity below the free surface is known as velocity-dip-phenomena which is commonly found in narrow open channel flows where the aspect ratio of the channel (i.e., ratio of channel width b to flow depth h) is less than five (Nezu et al. 1993). Dip-phenomenon was observed both in laboratory open channels and rivers (Francis 1878; Murphy 1904; Keulegan 1938; Nezu et al. 1993). Yang (2009) stated that all open channel flows, regardless of the channel geometry, are three dimensional and vertical velocity is never zero due to the presence of secondary current which is considered as a significant reason for occurrence of maximum velocity below the free surface. Guo and Julien (2001, 2003) modified the log-wake-law of Coles (1956) with boundary correction to describe dip-phenomenon. Absi (2011) presented velocity distribution to predict dip-phenomenon based on an analysis of Reynolds-averaged Navier–Stokes equation and a log-wake modified eddy viscosity distribution. Kundu and Ghoshal (2012) proposed a velocity distribution based on an eddy viscosity with a modified wake correction and the dip-phenomenon was successfully described by the proposed model. Besides this, many analytical, semi-analytical and empirical equations have been proposed which describe the dip-phenomenon in open channels (Yang 2007; Bonakdari et al. 2008; Pu 2013; Guo 2013; Lassabatere et al. 2013). But none of these works dealt with the dip-correction through the behavior of mixing length.

The present study revisits the velocity distribution in narrow open channels where the dip-phenomenon comes from the formulation of mixing length. Apart from clear water flow, the study also formulates the mixing length for sediment-laden flow by including dip-phenomenon together with the effect of concentration gradient and density stratification, which are present in the damping function of the mixing length of sediment-laden flow (Rowinski and Lee 1993). Moreover, unlike Castro-Orgaz et al. (2012), the study considers sediment diffusivity ε_s to be different from momentum diffusivity ε_m which was actually considered by Hunt (1954) while dealing with high concentrated flow and both the coefficients are taken as functions of y. As the experimental data on mixing length are too limited in the literature, for the validation purpose, some of the mixing length data are extracted from the velocity data available in the literature and are compared with the model. It is also verified through velocity distribution like other researchers. Particularly, those experimental data of velocity are considered where dip-phenomenon is observed. The model of velocity is compared with the model of Castro-Orgaz et al. (2012) as the work is mostly a generalization, and the present model is found to predict the data better than the other.

Theoretical derivation

The primary objective of this study is to derive mixing length models for both clear water and sediment-laden flows. Theoretical formulations to derive the models are described in the following subsections.

Table 1 Summary of mixing length formulas in the literature

Serial	Literature	Model in clear water	Damping function
1	Prandtl (1925)	$l_0/h = \kappa\xi$	–
2	Prandtl (1932)	$l_0/h = \kappa\xi\sqrt{1-\xi}$	–
3	von Karman (1930)	$l_0/h = \kappa\dfrac{\mathrm{d}U/\mathrm{d}\xi}{\mathrm{d}^2U/\mathrm{d}\xi^2}$	–
4	Coles (1956)	$l_0/h = \dfrac{\kappa\xi\sqrt{1-\xi}}{1+\Pi_0\xi(\mathrm{d}W/\mathrm{d}\xi)}$	–
5	Umeyama and Gerritsen (1992b)	$l_0/h = \kappa\xi\sqrt{1-\xi}$	$\psi = (1-\xi)^{0.5\beta(C/C_a)}$
6	Kovacs (1988)	$l_0/h = \kappa\xi\sqrt{1-\xi}$	$\psi = 1 - C^{1/3}$
7	Yang (2007)	$l_0/h = \kappa\xi$	$\psi = 1 - \alpha_1[(0.74/C)^{1/3} - 1]$
8	Castro-Orgaz et al. (2012)	$l_0/h = \dfrac{\kappa\xi\sqrt{1-\xi}}{1+\pi\Pi_0\xi\sin(\pi\xi)}$	$\psi = 1 + \frac{u\rho_f(R+1-\beta)}{\rho_m}\left(\frac{\mathrm{d}u}{\mathrm{d}y}\right)^{-1}\frac{\mathrm{d}C}{\mathrm{d}y}\varphi_1$ where $\varphi_1 = \left[2 - \frac{\omega}{2u_*}(1-2C)\right]$
9	Present study	$l_0/h = \dfrac{\kappa\xi(1-\xi)^{3/2}}{\lvert 1-\xi-\lambda\xi\rvert\varphi_*}$ where $\varphi_* = [1+12\Pi_0\xi^2(1-\xi)]$	(i) For $0 \le y < y_d$, $\psi_1 = 1 + \frac{u\rho_f(R+1-\beta)}{\rho_m}\left(\frac{\mathrm{d}u}{\mathrm{d}y}\right)^{-1}\frac{\mathrm{d}C}{\mathrm{d}y}\varphi_1$ where $\varphi_1 = \left[2 + \frac{\phi\sqrt{1-\xi}}{2Au_*\lvert 1-\xi-\lambda\xi\rvert\varphi_*}\right]$ and $\phi = u_*\left[\omega_0^+(1-C)^{n_H}\{(2+n_H)C-1\} - A\kappa(1-2\xi) - (1-\gamma)\kappa\xi\frac{\mathrm{d}C}{\mathrm{d}y}\right]$ (ii) For $y_d < y \le h$, $\psi_2 = 1 - \frac{u\rho_f(R+1-\beta)}{\rho_m}\left(\frac{\mathrm{d}u}{\mathrm{d}y}\right)^{-1}\frac{\mathrm{d}C}{\mathrm{d}y}\varphi_2$ where $\varphi_2 = \left[\frac{\phi\sqrt{1-\xi}}{2Au_*\lvert 1-\xi-\lambda\xi\rvert\varphi_*}\right]$ and $\phi = u_*\left[\omega_0^+(1-C)^{n_H}\{(2+n_H)C-1\} - A\kappa(1-2\xi) - (1-\gamma)\kappa\xi\frac{\mathrm{d}C}{\mathrm{d}y}\right]$

Modification on mixing length in clear-water flows

In a clear water turbulent shear flow, the momentum transfer over a mixing length l_0 can be expressed using Prandtl's mixing length theory as (Kundu 1990):

$$\tau_t = \rho_f l_0^2 \left|\frac{\mathrm{d}u}{\mathrm{d}y}\right|\frac{\mathrm{d}u}{\mathrm{d}y} \tag{1}$$

where τ_t is the Reynolds shear stress, ρ_f is the fluid density, u_* is the shear velocity, u is the time-averaged velocity along longitudinal direction and y denotes the vertical coordinate. For a steady uniform flow, the Reynolds shear stress is expressed as (Muste and Patel 1997; Cellino and Graf 1999; Muste et al. 2005):

$$\tau_t = -\rho_f\overline{u'v'} = \tau_0(1-\xi) \tag{2}$$

where $\tau_0 = \rho_f u_*^2$ is the bed shear stress, and u' and v' are fluctuations of velocity in x and y directions, respectively.

In a boundary layer flow, the time-averaged velocity is expressed as (Coles 1956):

$$\frac{u_{\max} - u}{u_*} = -\frac{1}{\kappa}\ln\left(\frac{y}{\delta}\right) + \frac{2\Pi_0}{\kappa}\cos^2\left(\frac{\pi}{2}\frac{y}{\delta}\right) \tag{3}$$

where Π_0 is the Coles' parameter for clear water flow, κ is the von Karman coefficient taken as 0.4 for clear water flow and δ is the thickness of the boundary layer defined as the distance from bed to location of maximum velocity (Guo 2006). In a fully developed free surface flow, the maximum velocity appears at the free surface, i.e., where $\delta = h$. If the Reynolds shear stress is assumed by Eq. 2, the mixing length for clear water flow is obtained from Eq. 1 as:

$$\frac{l_0}{h} = \frac{\kappa\xi\sqrt{1-\xi}}{1+\pi\Pi_0\xi\sin(\pi\xi)} \tag{4}$$

where $\xi = y/\delta$ is the dimensionless vertical depth. Equation 4 was originally proposed by Coles (1956). Castro-Orgaz et al. (2012) used Eq. 4 as a basis to formulate the mixing length in sediment water mixture flow. Figure 1 shows the verification of the mixing length models of Prandtl (1925) (which is given as $l_0/h = \kappa\xi$) and Castro-Orgaz et al. (2012) for clear water flows. In Fig. 1a, data of mixing length are obtained from Umeyama and Gerritsen (1992b). From this figure, it can be observed that Eq. 4 agrees well with the experimental data. It can also be observed from the figure that the data points show a fluctuation when $\xi > 0.7$ which cannot be measured by the model of Prandtl and Castro-Orgaz et al. (2012). This fluctuation may be incorporated into the dip-phenomenon which causes the change in velocity gradient near the free surface. Since Eq. 1 contains the velocity gradient, it

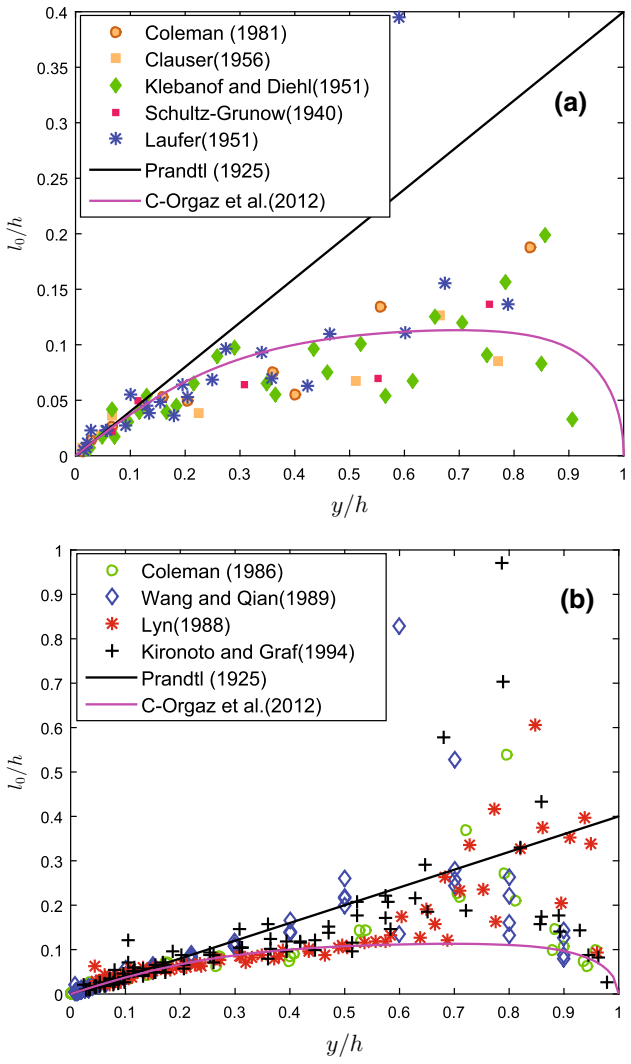

Fig. 1 Mixing length models for clear water flows. Please see Table 1 for corresponding theoretical models

indicates that the mixing length in clear water flow may be affected by the mean velocity distribution and its gradient near the free surface. Since in a narrow open channel flow, velocity gradient vanishes at the dip-position and then becomes negative up to the free surface, the distribution of mixing length may have significant effect on it from the dip-position to the rest of the maximum flow depth. To investigate this, the mixing length is computed from Eq. 1 using Eq. (3) for the experimental data of Coleman (1986) (runs 1, 21 and 32), Wang and Qian (1989) (runs CW1, CW2, CW3, CW4 and SW2), Lyn (1986) (runs C1, C2, C3 and C4) and Kironoto and Graf (1994) for clear water flows. For computation of mixing length, the velocity gradient is required which is calculated from the data set using the central difference approximation except for the starting and ending data points where velocity gradients are computed using forward and backward difference approximations, respectively. In all these data sets, the maximum velocity appears below the free surface and, thus, can be taken to verify the effect of velocity gradient in the mixing length model. For all data sets, computed values of mixing length (except three data points) are plotted in Fig. 1b together with the model of Prandtl (1925) and Castro-Orgaz et al. (2012). From the figure, it can be observed that mixing length follows a semi-normal type distribution that increases as one moves away from bed and approached to maximum value in the range $0.6 \leq \xi \leq 0.9$ and decreases when $\xi > 0.9$. More precisely, it can be observed that for each particular data set (e.g., data set of Wang and Qian 1989), the distribution of mixing length shows a peak where velocity gradient vanishes, i.e., where the dip occurs which can be checked from the measured velocity data. In other words, mixing length increases from bed to the dip-position and then decreases up to the free surface. This behavior cannot be described by the model of Castro-Orgaz et al. (2012) as suggested by the figure. Therefore, in this section we propose a modification on Castro-Orgaz et al. (2012) mixing length model for clear water flows through a modified velocity profile which incorporates dip-phenomenon.

In clear water flows through open channels, the complete time-averaged longitudinal velocity profile can be expressed including the effect of velocity dip-phenomenon by Kundu and Ghoshal (2012) as:

$$\frac{u}{u_*} = \frac{1}{\kappa}\ln\left(\frac{\xi}{\xi_0}\right) + \frac{\lambda}{\kappa}\ln(1-\xi) + \frac{2\Pi_0}{\kappa}(3\xi^2 - 2\xi^3) - \frac{4\lambda\Pi_0}{\kappa}\xi^3 \tag{5}$$

where u is the time-averaged velocity along main flow direction, u_* is the shear velocity, $\xi(= y/h)$ is the dimensionless vertical height, h is the maximum flow depth, y_0 is the vertical distance from the bed at which the velocity is hypothetically equal to zero, κ is the von Karman constant which is taken as 0.41 for clear water flow, Π_0 is the Coles' wake strength and λ is the dip-correction factor which is given as (Kundu and Ghoshal 2012):

$$\lambda = \frac{1}{\xi_d} - 1 \tag{6}$$

where $\xi_d(= y_d/h)$ denotes the dimensionless dip-position from channel bed. Equation 6 is obtained from Eq. 5 using the zero velocity gradient condition at dip-position, i.e., $\frac{d(u/u_*)}{d\xi} = 0$ at $\xi = \xi_d$. Solving Eqs. 1, 2 and 5, the mixing length in clear water flows is expressed as:

$$\frac{l_0}{h} = \frac{\kappa\xi(1-\xi)^{3/2}}{|(1-\xi-\lambda\xi)|\left[1+12\Pi_0\xi^2(1-\xi)\right]} \tag{7}$$

where λ is calculated from Eq. 6. Equation 7 represents clear water mixing length where $\kappa = 0.4$ and $\Pi_0 = 0.2$ are

taken. This equation gives a general form of mixing length in clear water flow. It reduces to a similar type of mixing length proposed by Castro-Orgaz et al. (2012) when $\lambda = 0$ and reduces to the mixing length for log-law when $\Pi_0 = 0$ (Umeyama and Gerritsen 1992b).

Modification on mixing length in sediment-laden flows

The schematic diagram of a steady two-dimensional turbulent sediment-laden flow in open channels without dip-phenomena and with dip-phenomena is shown in Fig. 2a, b, respectively. Suspended particles induce a mass density profile $\rho_m = \rho_m(y)$ with a velocity profile $u = u(y)$ as can be seen from the figures. Mixing length profile is derived throughout the water depth by dividing the whole depth into two regions, namely from the channel bed to the dip-position and then dip-position to the free surface. For that purpose, let two adjacent horizontal layers are separated by an elementary depth Δy and it is assumed that Δy is same as the mixing length scale l_m for sediment-laden flows (Fig. 2).

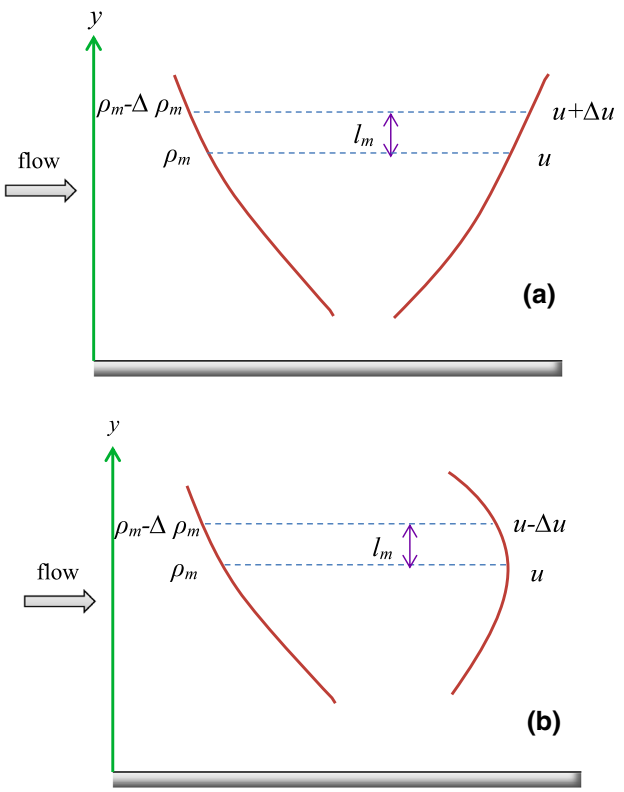

Fig. 2 Schematic diagram of exchange of momentum: **a** without dip-phenomena, and **b** with dip-phenomena

Mixing length in the region $0 \le y < y_d$

The momentum M of the flow at a distance $y + \Delta y$ can be expressed (by considering up to first order term in Taylor series expansion) as follows:

$$M(y + \Delta y) = M(y) + \Delta y \frac{\mathrm{d}M}{\mathrm{d}y} \tag{8}$$

From Eq. 8, one can express the change in momentum ΔM between the two layers as:

$$\Delta M = M(y + \Delta y) - M(y) = l_m \frac{\mathrm{d}}{\mathrm{d}y}(\rho_m u) = l_m u \frac{\mathrm{d}\rho_m}{\mathrm{d}y} + l_m \rho_m \frac{\mathrm{d}u}{\mathrm{d}y} \tag{9}$$

On the other hand, ΔM can also be obtained from velocity and mass density profiles (as can be seen from Fig. 2a) as:

$$\Delta M = (\rho_m - \Delta\rho_m)(u + \Delta u) - \rho_m u = \rho_m \Delta u - u\Delta\rho_m \tag{10}$$

where Δu, $\Delta\rho_m$ are the variations of velocity and density between the two layers separated by the distance l_m. Equation 10 is obtained by neglecting the second order term of small variation $\Delta u \Delta\rho_m$. The momentum transfer gets modified by the gradient of density which interacts with the velocity profile. From Eqs. 9 and 10, we get

$$\Delta u = l_m \frac{u}{\rho_m}\frac{\mathrm{d}\rho_m}{\mathrm{d}y} + l_m \frac{\mathrm{d}u}{\mathrm{d}y} + u\frac{\Delta\rho_m}{\rho_m} \tag{11}$$

Equation 11 includes both the velocity and density gradient effects in the momentum transfer. It can be seen that Eq. 11 simplifies to the classical Prandtl's theory in case of constant density. Further, the density variation $\Delta\rho_m$ can also be obtained as follows by expanding in Taylor's series expansion (considering up to second-order terms)

$$\Delta\rho_m = l_m \frac{\mathrm{d}\rho_m}{\mathrm{d}y} + \frac{l_m^2}{2}\frac{\mathrm{d}^2\rho_m}{\mathrm{d}y^2} \tag{12}$$

Substituting Eqs. 12 into 11, velocity variation is obtained as:

$$\Delta u = l_m \frac{\mathrm{d}u}{\mathrm{d}y}\left[1 + \frac{u}{\rho_m}\left(\frac{\mathrm{d}u}{\mathrm{d}y}\right)^{-1}\left(2\frac{\mathrm{d}\rho_m}{\mathrm{d}y} + \frac{l_m}{2}\frac{\mathrm{d}^2\rho_m}{\mathrm{d}y^2}\right)\right] \tag{13}$$

where ρ_m denotes the density of sediment-water mixture which can be expressed including the effect of added mass as:

$$\rho_m = (\rho_s + K\rho_f)C + \rho_f(1 - C) = \rho_f[1 + (R + 1 - \beta)C] \tag{14}$$

where C is the volumetric sediment concentration, $s_p = \rho_s/\rho_f$ is the specific gravity of particle, ρ_s denotes the density of solids/particles, $R = s_p - 1$ denotes the

submerged specific gravity of particles and $\beta = 1 - K$ with K as the added mass coefficient (Montes 1973). Equation 14 includes the effect of mass density of mixture on the momentum transfer. It also reveals that the turbulent momentum transfer is not only affected by density ρ_m and velocity u but also by their gradients. Therefore, the effect of suspended sediment particles must be relevant in near bed region where both du/dy and $d\rho_m/dy$ are large. Differentiating Eq. 14 and substituting into Eq. 13, velocity variation is expressed as:

$$\Delta u = l_0 \psi \frac{du}{dy} = l_0 \frac{du}{dy} \times \left[1 + \frac{u\rho_f(R+1-\beta)}{\rho_m}\left(\frac{du}{dy}\right)^{-1}\frac{dC}{dy}\left\{2 + \frac{l_0}{2}\frac{d^2C/dy^2}{dC/dy}\right\}\right] \quad (15)$$

Following Castro-Orgaz et al. (2012), the new mixing length l_m in sediment laden flows from the channel bed to the dip-position including the effect of added mass force can be written as:

$$l_m = l_0 \psi_1 \quad (16)$$

where ψ_1 denotes the damping function which is expressed as:

$$\psi_1 = 1 + \frac{u\rho_f(R+1-\beta)}{\rho_m}\left(\frac{du}{dy}\right)^{-1}\frac{dC}{dy}\left[2 + \frac{l_0}{2}\frac{d^2C/dy^2}{dC/dy}\right] \quad (17)$$

To derive a more appropriate form of the damping function in dilute as well as dense sediment laden flows, the Hunt's diffusion equation for the concentration of suspended sediment particles is considered. This equation is expressed as (Hunt 1954):

$$\varepsilon_s \frac{dC}{dy} + C(\varepsilon_m - \varepsilon_s)\frac{dC}{dy} + C(1-C)\omega = 0 \quad (18)$$

where ω is the settling velocity in mixture, ε_s denotes the sediment diffusivity and ε_m is the momentum diffusivity both being taken as function of y. According to the Reynolds analogy $\varepsilon_s = \gamma\varepsilon_m$ where γ is a proportionality constant which is the inverse of Schmidt number. Therefore, Eq. 18 can be rewritten as:

$$\varepsilon_m[\gamma + C(1-\gamma)]\frac{dC}{dy} + C(1-C)\omega = 0 \quad (19)$$

In sediment-laden flows, researchers (Lewis et al. 1949; Richardson and Zaki 1954) observed that due to increase of sediment concentration from free surface to the bed region, the settling velocity of a particle is reduced in comparison to the settling velocity in clear fluid which is known as 'hindered settling'. Richardson and Zaki (1954) proposed a formula to find the settling velocity in sediment-fluid mixture as:

$$\omega = \omega_0(1-C)^{n_H} \quad (20)$$

where ω_0 is the settling velocity of that particle in still clear fluid and n_H is the exponent of reduction which is generally considered as a function of particle Reynolds number $Re_p = (\omega_0 d_p)/\nu_f$ in which d_p is particle diameter and ν_f is the kinematic viscosity of fluid. Several authors proposed expressions for n_H (Richardson and Zaki 1954; Cheng 1997; Baldock et al. 2004; Pal and Ghoshal 2013; Kumbhakar et al. 2017). In this study, n_H is computed according to Richardson and Zaki (1954) as:

$$n_H = \begin{cases} 4.65, & Re_p < 0.2 \\ 4.4Re_p^{-0.03}, & 0.2 < Re_p < 1 \\ 4.4Re_p^{-0.1}, & 1 < Re_p < 500 \\ 2.4, & Re_p > 500 \end{cases} \quad (21)$$

Differentiating Eq. 19 with respect to y and using Eq. 20, the following equation is obtained as:

$$\frac{d^2C}{dy^2} = \frac{1}{A\varepsilon_m}\left(\frac{dC}{dy}\right)\left[\omega n_H C - A\frac{d\varepsilon_m}{dy} - \varepsilon_m\frac{dA}{dy} - \omega(1-2C)\right] \quad (22)$$

where $A = \gamma + C(1-\gamma)$. Substituting Eqs. 22 into 17, the damping function ψ can be rewritten as:

$$\psi_1 = 1 + \frac{u\rho_f(R+1-\beta)}{\rho_m}\left(\frac{du}{dy}\right)^{-1}\frac{dC}{dy}\left[2 + \frac{l_0\phi}{2A\varepsilon_m}\right] \quad (23)$$

where the function ϕ is expressed as

$$\phi = \omega_0 n_H C(1-C)^{n_H} - A\frac{d\varepsilon_m}{dy} - (1-\gamma)\varepsilon_m\frac{dC}{dy} - \omega_0(1-2C)(1-C)^{n_H} \quad (24)$$

It can be observed from Eq. 24 that the form of ϕ will be explicitly obtained if the momentum diffusivity is known. According to the Boussinesq formula, the momentum diffusivity is considered to be equal to the eddy viscosity which is described by the parabolic model as:

$$\frac{\varepsilon_m}{u_* h} = \kappa\frac{y}{h}\left(1 - \frac{y}{h}\right) \quad (25)$$

where u_* is the shear velocity, h is the flow depth. Yalin (1977) used Eq. 25 for deriving the streamwise velocity in sediment-laden flow. Inserting Eqs. 25 into 24, the function ϕ is obtained as:

$$\phi = u_*\left[\omega_0^+(1-C)^{n_H}\{(2+n_H)C - 1\} - A\kappa(1-2\xi) - (1-\gamma)\kappa\xi\frac{dC}{dy}\right] \quad (26)$$

Equation 23 together with Eq. 26 gives the general form of the damping function. For the simplicity of the

computation purposes, this damping function can be approximated to a simple form as considered by Castro-Orgaz et al. (2012). If $\gamma = 1$ is taken, sediment diffusivity near the bed is approximated as $\varepsilon_s = l_0 u_*$ (Montes 1973), there is no hindered effect in the settling velocity, i.e., $n_H = 0$, then Eq. 23 is simplified to

$$\psi_1 = 1 + \frac{u\rho_f(R+1-\beta)}{\rho_m}\left(\frac{du}{dy}\right)^{-1}\frac{dC}{dy}\left[2 - \frac{\omega}{2u_*}(1-2C)\right] \tag{27}$$

which was obtained by Castro-Orgaz et al. (2012).

Mixing length in the region $y_d < y \le h$

It can be seen from Fig. 2b that in case of narrow open channels, velocity takes maximum value at dip-position which is below water surface and then decreases up to the free surface. Thus, the change in momentum between the two layers can be obtained as:

$$\Delta M = \rho_m u - (\rho_m - \Delta\rho_m)(u - \Delta u) = u\Delta\rho_m + \rho_m \Delta u \tag{28}$$

Following the same steps like previous subsection, the velocity variation in this region can be obtained as:

$$\Delta u = l_0 \frac{du}{dy}\left[1 - \frac{u\rho_f(R+1-\beta)}{\rho_m}\frac{l_0}{2}\left(\frac{du}{dy}\right)^{-1}\frac{d^2C}{dy^2}\right] \tag{29}$$

Thus, the damping factor ψ_2 in mixing length can be written as:

$$\psi_2 = 1 - \frac{u\rho_f(R+1-\beta)}{\rho_m}\frac{l_0}{2}\left(\frac{du}{dy}\right)^{-1}\frac{dC}{dy}\frac{\phi}{A\varepsilon_m} \tag{30}$$

where ϕ is given by Eq. 26.

Equations 23 and 30 represent the damping functions in the modified mixing length in sediment-laden flows in two regions: from channel bed to before the position of maximum velocity and then from dip-position to the free surface, respectively. The mixing length at the dip-position has an infinite discontinuity. This is due to the fact that at the position of maximum velocity, velocity gradient becomes zero and hence a discontinuity occurs as can be understood from Eq. 1.

Derivation of velocity model

For sediment-laden flows, Eq. 1 becomes (Umeyama and Gerritsen 1992b)

$$\tau_t = \rho_m l_m^2 \left|\frac{du}{dy}\right|\frac{du}{dy} \tag{31}$$

where the density of the mixture is expressed as:

$$\rho_m = \rho_f(1 + (s_p - 1)C) \tag{32}$$

The second term in Eq. 32 can be considered as a perturbation to the density ρ_f. The presence of density perturbation will inevitably change the flow characteristics. Therefore, the total turbulent shear stress is expressed as (Lyn 1988; Mazumder and Ghoshal 2006):

$$\tau_t = \rho_f u_*^2\left(1 - \xi + R\int_\xi^1 C d\xi\right) \tag{33}$$

Combining Eqs. 31–33, the differential equation for the time-averaged velocity profile is obtained as:

$$\frac{dU}{d\xi} = \frac{h}{l_m}\left(\frac{1 - \xi + R\int_\xi^1 C d\xi}{1 + RC}\right)^{1/2} = \frac{h}{l_m} I(\xi) \tag{34}$$

where $U = u/u_*$ is the dimensionless time-averaged velocity, l_m can be calculated from Eq. 16 along with the damping functions as given in Eqs. 23 and 30 and $I(\xi)$ is the function which is

$$I(\xi) = \left(\frac{1 - \xi + R\int_\xi^1 C d\xi}{1 + RC}\right)^{1/2} \tag{35}$$

and l_0 and ϕ is taken from Eqs. 7 and 26, respectively.

Evaluation of proposed model with experimental data

Description of unknown parameters

To compute velocity profile from Eq. 34, a proper form of the suspension concentration distribution needs to be considered. Generally, the suspension profile is described by the well-known Rouse equation (Rouse 1937; Graf 1971) due to its simple form. But this equation produces very large value of sediment concentration at the reference level (Kundu 2016) and also concentration gradient approaches to infinity as ξ_a is very small. Due to these unreal wall boundary conditions, the Rouse equation is not considered in this study. An exponential-type suspension concentration proposed by Montes (1973) is adopted here as:

$$\frac{C}{C_a} = e^{-A_0\xi}\left(\frac{1 + e^{-2D\xi}}{2}\right)^{-A_0/D} \tag{36}$$

where C_a is the concentration at the reference level ξ_a which is the common boundary of bed-load and suspended-load, and A_0 and D are model parameters which are determined from experimental data. Montes (1973) suggested the value of D to be 30 approximately. Many researchers (Umeyama and Gerritsen 1992b; Castro-Orgaz et al. 2012) considered Eq. 36 for suspension study.

Apart from suspension concentration, Eq. 34 contains dip-correction parameter λ, reference concentration C_a, reference level ξ_a, proportionality parameter γ and settling velocity ω_0. The values of these parameters are computed as follows.

Guo (2013) analyzed the Modified log-wake law for smooth rectangular flows through open channels. He found that the location of dip-position shifts exponentially from the water surface to half of the flow depth as the aspect ratio decreases from infinity to zero and suggested an empirical formula to predict the dip-position. Therefore, the dip-position is calculated from Guo (2013) model as follows:

$$\xi_d = \left[1 + \exp\left\{-\left(\frac{\mathrm{Ar}}{\pi}\right)^{1.5}\right\}\right]^{-1} \tag{37}$$

where $\mathrm{Ar}(= b/h)$ is the aspect ratio of channel and b is the width of the channel. This formula is adopted in this study to calculate parameter λ from Eq. 6.

Following the work of Mazumder and Ghoshal (2006), the reference level ξ_a is taken as the lowest available height for each observed data set. The reference concentration C_a at ξ_a is computed from the formula proposed by Sun et al. (2003) as it uses three basic probabilities: incipient motion probability, non-ceasing probability and pick-up probability of the sediment particle. The reference concentration is given by

$$C_a = M_* P_* \frac{F(\cdot)}{1 + F(\cdot)} \tag{38}$$

where M_* denotes the density coefficient of bed material, P_* denotes the grain size class percentage of bed material and equal to unity for uniform sediments and the function $F(\cdot)$ is expressed as:

$$F(\cdot) = \frac{10^{-5}\tau^2 d_*^{1.84}\alpha_n\lambda_n}{(1-\gamma_n)(1-\lambda_n)(1+\gamma_n\lambda_n)} \tag{39}$$

where d_* is the dimensionless sediment particle diameter defined as $d_* = [(Rg)/v_f^2]^{1/3} d_p$, τ is the Shields parameter defined as $\tau = u_*^2/[Rgd_p]$, g is the gravitational force and α_n, γ_n and λ_n are incipient motion probability, non-ceasing probability and pick-up probability of sediment particles which are given by

$$\alpha_n = 1 - \frac{1}{\sqrt{2\pi}} \int_{-2.7\left(\sqrt{0.0822/\tau}+1\right)}^{2.7\left(\sqrt{0.0822/\tau}-1\right)} e^{-x^2/2} \mathrm{d}x \tag{40}$$

$$\gamma_n = 1 - \frac{1}{\sqrt{2\pi}} \int_{-2.7\left(\sqrt{0.0571/\tau}+1\right)}^{2.7\left(\sqrt{0.0571/\tau}-1\right)} e^{-x^2/2} \mathrm{d}x \tag{41}$$

$$\lambda_n = \frac{2}{\sqrt{2\pi}} \int_{\omega/u_*}^{\infty} e^{-x^2/2} \mathrm{d}x, \tag{42}$$

respectively.

In the model Eq. 34, the parameter A contains the parameter γ which is computed from the equation proposed by Pal and Ghoshal (2016). They studied the effect of particle concentration on turbulent diffusion and using several data sets proposed a regression equation for γ as:

$$\gamma = 0.33\left(\frac{\omega_0}{u_*}\right)^{0.931} \xi_a^{-1.196} C_a^{-0.118} \tag{43}$$

where settling velocity ω_0 of particles in still fluid is calculated from the formula proposed by Zhiyao et al. (2008). Based on the relationship between particle Reynolds number and the dimensionless particle diameter, Zhiyao et al. (2008) proposed a formula for calculating the settling velocity of a single particle which is applicable for a wide range of particle Reynolds number. Therefore, to compute settling velocity of the sediment particles, the formula given by Zhiyao et al. (2008) is used which is given as:

$$\omega_0 = \frac{\nu_f}{d} d_*^3 \left(38.1 + 0.93 d_*^{12/7}\right)^{-7/8} \tag{44}$$

where d_* is the dimensionless sediment particle diameter defined as $d_* = [(Rg)/v_f^2]^{1/3} d$.

Description of experimental data

The proposed model of velocity distribution (Eq. 34) is validated for both wide and narrow channels with a wide range of experimental data. As in this study the effect of secondary current is considered, the experimental data which have this effect on velocity profile are also considered. Therefore, experimental data of Coleman (1981) and Wang and Qian (1989) for narrow open channel flow and experimental data of Vanoni (1940) for wide open channel flow have been used in this study.

Coleman (1981) did experiments in a smooth flume which was 356 mm wide and 15 m long. During the experiments, the energy slope S was kept to be 0.002 except the last three test cases where S was 0.0022. The flow depth was nearly constant and about 1.71 m. Among 40 test cases, test cases 1, 21, and 32 were performed in clear water flow. Test cases, 2–20 were performed over sediment bed of sand diameter $d = 0.105$ mm; 22–31 with medium sands of diameter $d = 0.21$ mm; and 33–40 with coarse sands of diameter $d = 0.42$ mm. The temperatures were between 19.5 and 25.3 °C. The test cases (or run) 7 (fine sand), 29 (medium sand) and 37 (coarse sand) of Coleman (1981) have been selected to verify the model.

Wang and Qian (1989) did a series of experiments with plastic particles. The experiments were conducted in a recirculating, tilting flume which was 20 m long, 30 cm wide and 40 cm high. The bed slope, $S = 0.01$, was kept

Table 2 Summary of experimental data

Literature	Run	Ar	d_p (mm)	ρ_s/ρ_f	ω_0 (cm/s)	A_0	C_a
Coleman (1986)	7	2.082	0.105	2.65	0.66	5.78	0.059
	29	2.119	0.210	2.65	2.16	4.6	0.068
	37	2.132	0.420	2.65	5.49	4.4	0.057
Wang and Qian (1989)	SF4	3.000	0.268	2.64	3.10	6	0.014
	SM3	3.000	0.960	2.64	11.55	5	0.003
	SC7	3.000	1.42	2.64	15.00	5.1	0.043
Vanoni (1940)	5	5.593	0.16	2.65	1.39	7	0.008
	12	9.280	0.16	2.65	1.39	7.1	0.018
	15	10.054	0.16	2.65	1.39	9	0.01

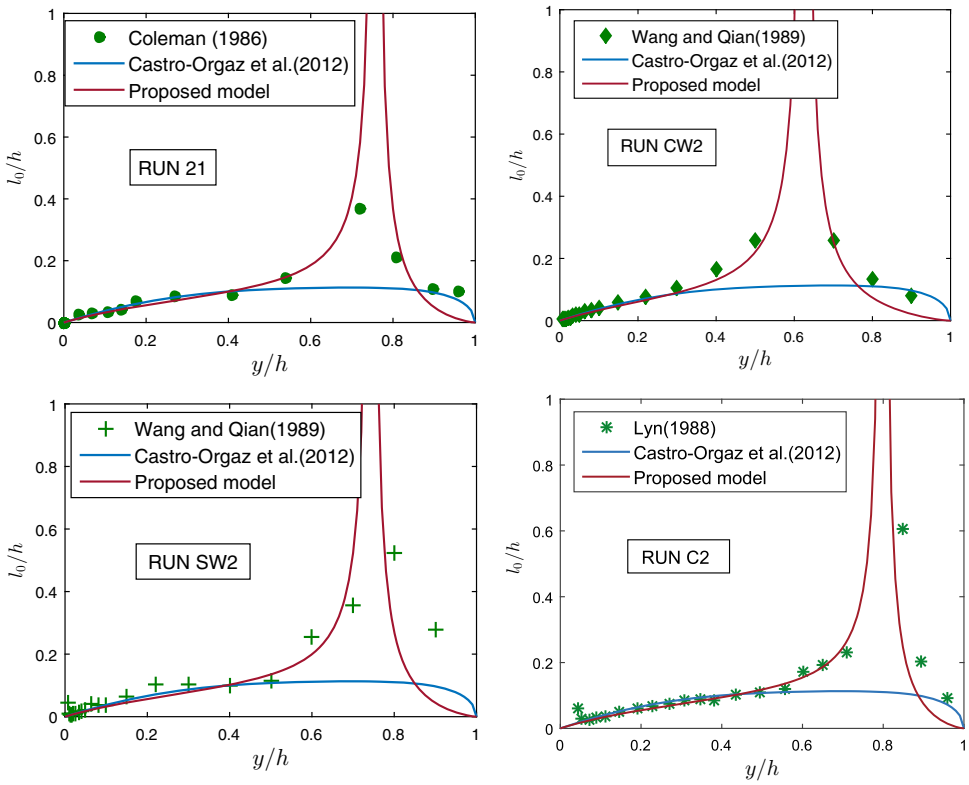

Fig. 3 Validation of proposed mixing length model Eq. (7) for clear water flows

same for all test cases. During the experiment, a uniform flow was maintained. To study the effect of density gradient on flow parameters, experiments with water + plastic particles with specific gravity 1.05 were selected. Test cases, SF, correspond to experiments with fine plastic particles having diameter $d = 0.268$ mm, SM with medium plastic particles having diameter $d = 0.96$ mm and SC with coarse plastic particles having diameter $d = 1.42$ mm. Among all test cases, SF4, SM3 and SC7 are arbitrarily considered here.

Vanoni (1940) performed experiments in two series. The experiments were done in a flume which is 33.25 inches wide and 60 feet long with adjustable bed slope. The bottom of the channel was made of steel sheet plate with artificially roughened by sand particles. Experiments were carried out in two series for both clear water and sediment-water mixture. In series I, experiments on clear water (test cases 1, 2 and 3) and sediment-water mixture (test cases 1–13) were performed where the slope was kept as $S = 0.0025$. In series II, experiments on clear water (test cases 14a, 14b, 21) and sediment-water mixture (test cases 14–22) were performed. In all the test cases, the aspect ratio varies from 5 to 11.90 and maximum velocity appears at the free surface. Here, test cases 5, 12 and 15 are chosen for validation of the models.

In all the selected test cases, aspect ratio has the range from 2.082 to 10.054 and maximum volumetric sediment concentration varies from 0.027 to 24%. Flow characteristics of all test cases or Runs are shown in Table 2.

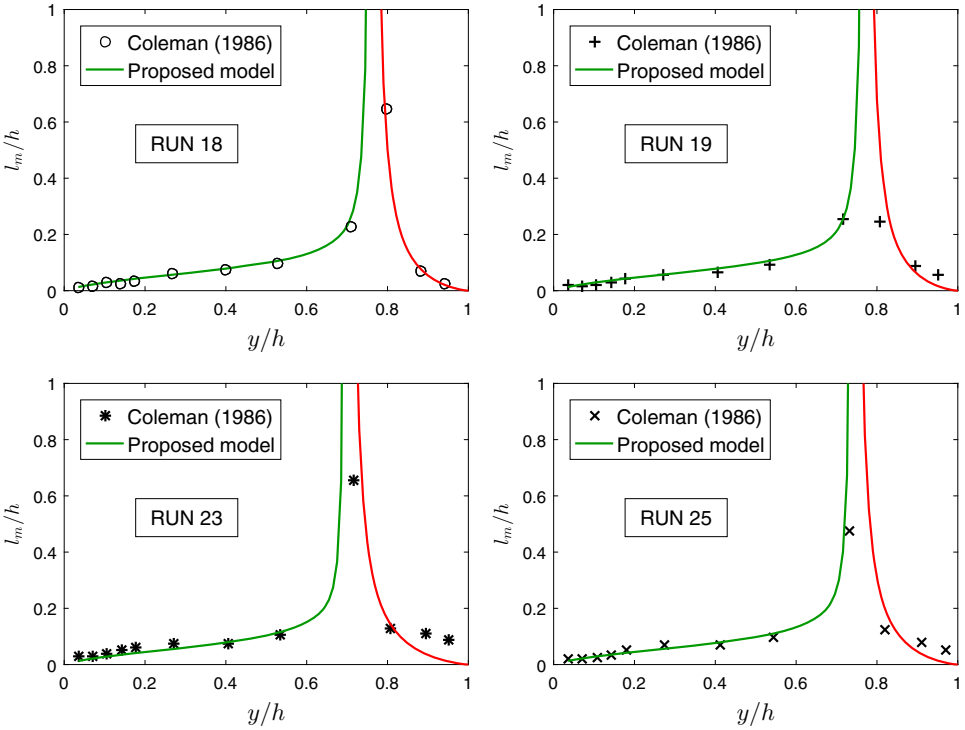

Fig. 4 Validation of proposed mixing length model for sediment-laden flows with data from Coleman (1986)

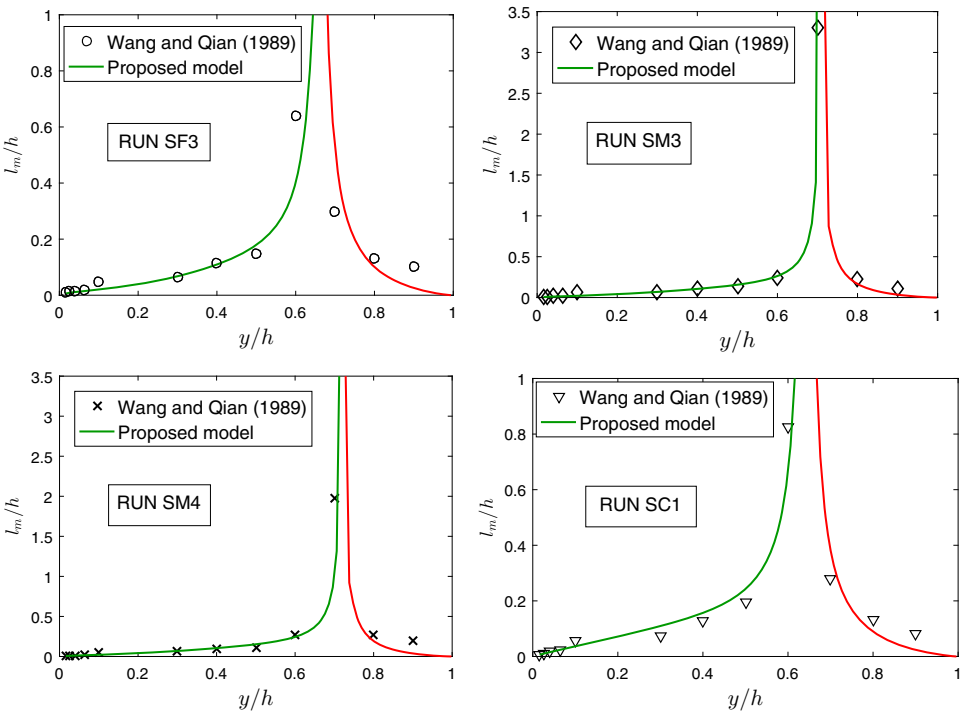

Fig. 5 Validation of proposed mixing length model for sediment-laden flows with data from Wang and Qian (1989)

Results and discussion

Mixing length results

Figure 3 shows the validity of the proposed mixing length model (Eq. 7) for clear water flows with the experimental data of Coleman (1986) (run 21), Wang and Qian (1989) (run CW2 and SW2) and Lyn (1986) (run C2). From the figure, it can be observed that initially mixing length increases from bed surface to the dip-position where it reaches the maximum value then decreases towards the free surface with zero value thereat. It can also be observed from Eq. 7 that when $\xi \rightarrow \xi_d$,

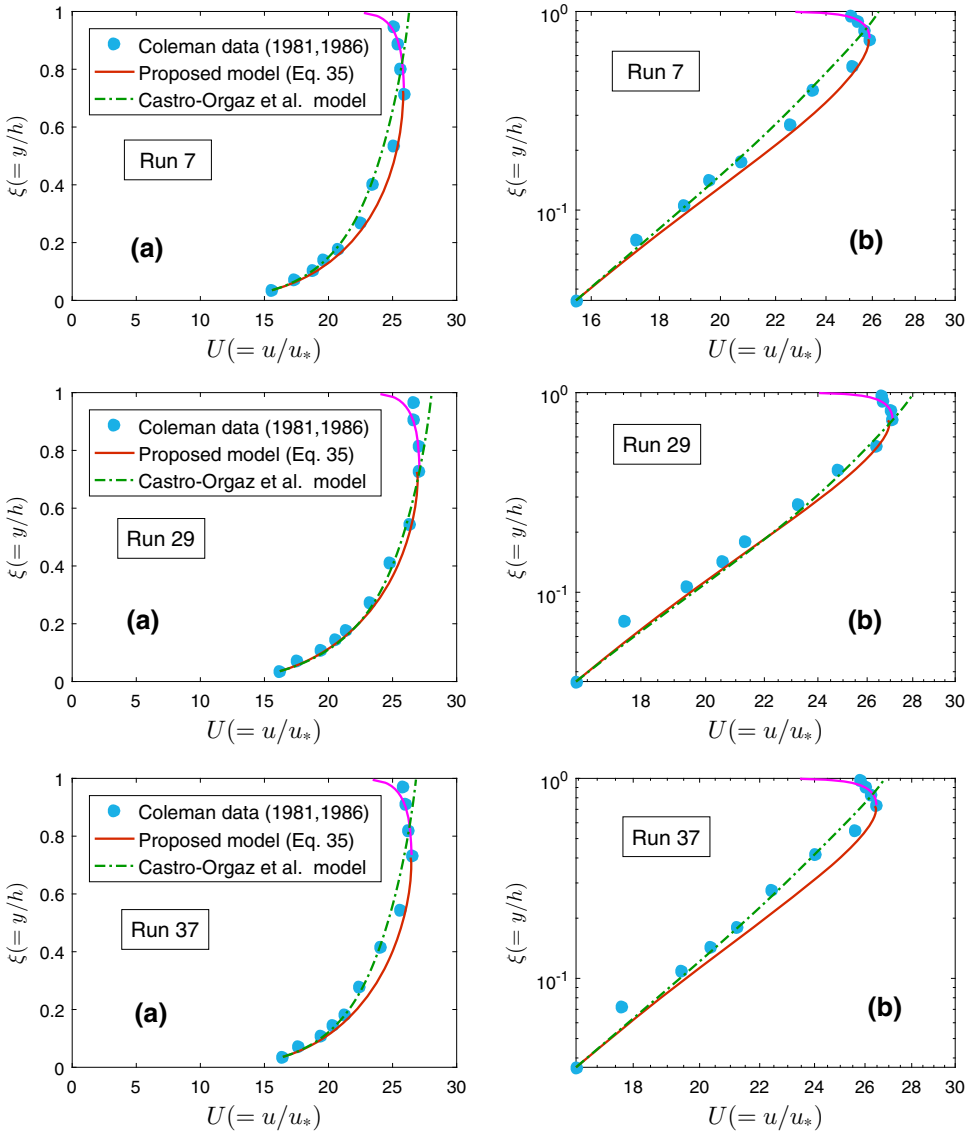

Fig. 6 Comparison of the proposed velocity model with data of Coleman (1981) and the model of Castro-Orgaz et al. (2012)

the factor $|(1-\xi-\lambda\xi_d)| \to 0$. Therefore, the value of l_0/h approaches to a high peak value. In the figure, Eq. 7 is plotted together with the model of Castro-Orgaz et al. (2012). In Eq. 7, the value of λ was taken from the considered experimental data sets. It is observed from the figure that the proposed model Eq. 7 predicts the mixing length well with the experimental data, whereas the model of Castro-Orgaz et al. (2012) underestimated the value of mixing length in the region where dip-position occurs. The proposed model can also be used to predict mixing length in wide open channels with $\lambda = 0$.

Figures 4 and 5 show the validity of the proposed mixing length model for sediment-laden flows with the data of Coleman (1986) and Wang and Qian (1989), respectively. Four different runs of Coleman's experiment as well as Wang and Qian's experiments are plotted in Figs. 4 and 5, respectively. In both the figures, the mixing length is computed from Eq. 16 where the functions ψ_1 and ψ_2 are computed from Eqs. 23 and 30, respectively, on the basis of Eqs. 34 and 36. It can be observed from runs 18, 23 and 25 of Fig. 4 that, at the dip-position, the mixing length takes a higher value. Also it follows that in the neighborhood of dip-position the decrease in mixing length occurs symmetrically. Similar observation is also observed in Fig. 5. More precisely, in Runs SM3 and SM4, mixing length shows a high value at the dip-position. These facts indicate that the exchange of momentum over a mixing length distance may not always decrease due to the presence of sediment particles. From the figure, it can be observed that the proposed model agrees well with the data points which shows the significance of this study.

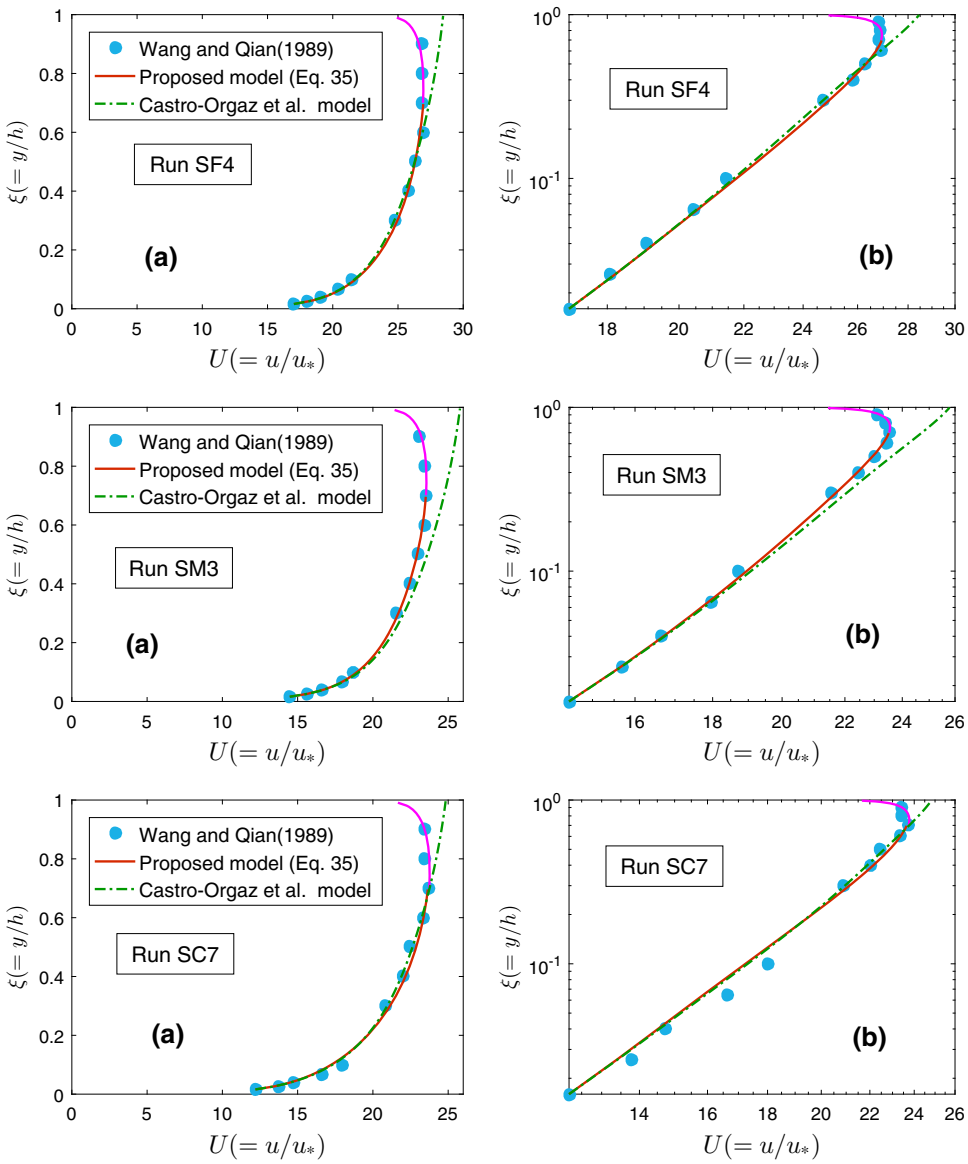

Fig. 7 Comparison of the proposed velocity model with data of Wang and Qian (1989) and the model of Castro-Orgaz et al. (2012)

Velocity distribution results

Figure 6 shows the validity of the proposed model (Eq. 34) with the experimental data of Coleman (1981). In the experiments, the aspect ratio Ar has the range from 2.05 to 2.13 and, therefore, the velocity-dip-phenomenon occurs. Figure 3a presents the results from selected runs in a linear scale and Fig. 3b in a logarithmic scale. The computed velocity profile $U = U(\xi)$ from Eq. 34 is plotted. The 4th order Runge–Kutta method is used to solve 34 with the initial condition $U(\xi_a) = U_a$. The singularity at $\xi = 1$ is removed by approximating the highest value of ξ as 0.9999. Since in literature, no formula or procedure is available to estimate the value U_a at the reference level ξ_a; therefore, these are chosen from experimental data in this study. To obtain the value of $I(\xi)$, standard recursive adaptive Lobatto quadrature technique is adopted which counts error of order 10^{-6} in MATLAB. The value of the parameter A_0 is obtained by fitting Eq. 36 with concentration data of Coleman (1981). Figure 6 shows that the model is able to predict the dip-phenomena and agrees well with the data points over the entire flow depth. The model of Castro-Orgaz et al. (2012) is also plotted in the figure and it can be observed that it fails to predict dip-phenomenon.

The proposed model is also validated with the experimental data of Wang and Qian (1989). Runs SF4, SM3 and SC7 are plotted in Fig. 7 together with the model of Castro-Orgaz et al. (2012). The model parameters are calculated in a similar manner as done previously. From the figure, it can be seen that proposed model gives a more appropriate result than model of Castro-Orgaz et al. (2012).

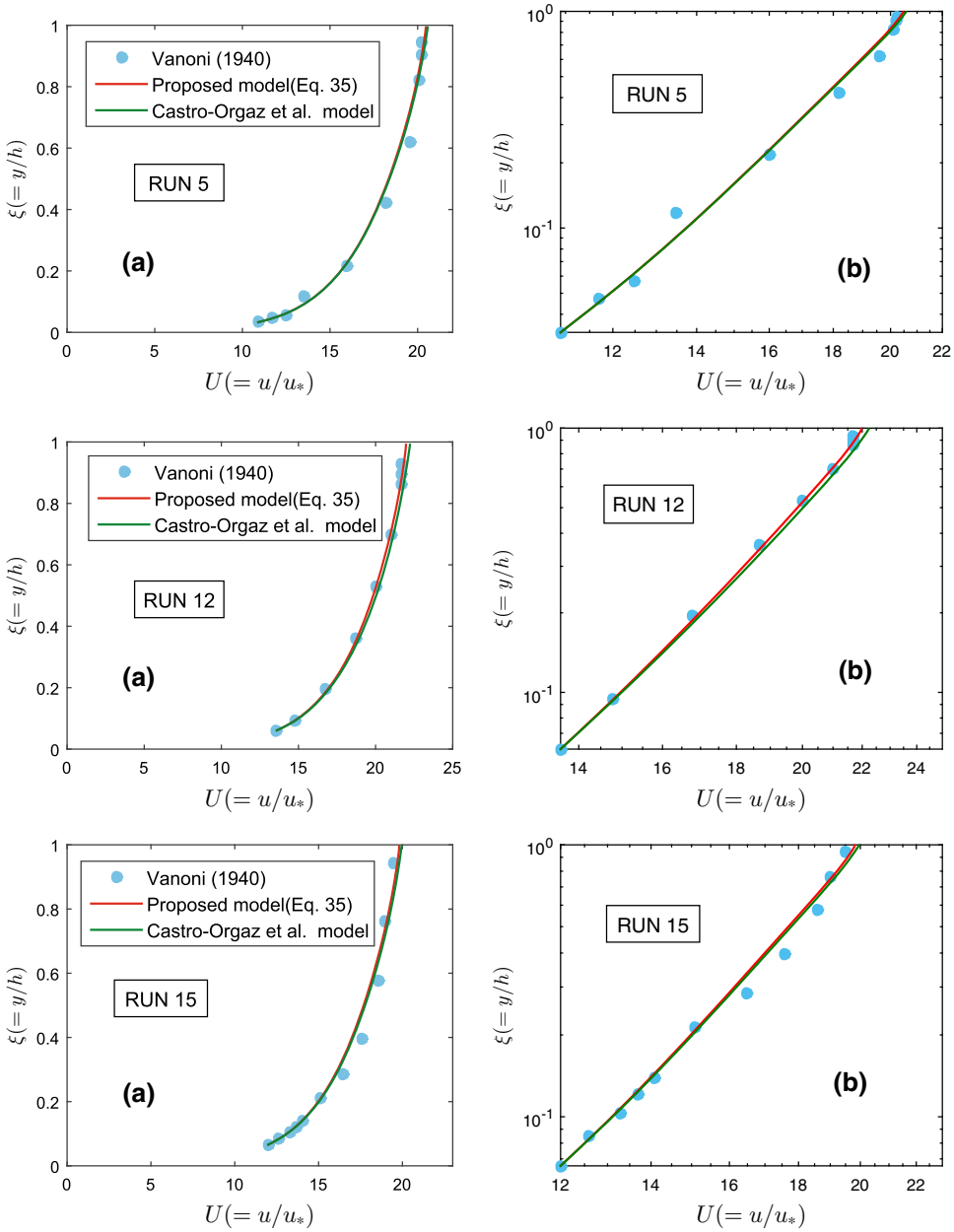

Fig. 8 Comparison of the proposed velocity model with data of Vanoni (1940) and the model of Castro-Orgaz et al. (2012)

To test the validity in wide open channel flows, the model is tested with the experimental data of Vanoni (1940). Runs 5, 12 and 15 are plotted in Fig. 8. From the figure, it can be observed that results from the present model are in good agreement with the model of Castro-Orgaz et al. (2012) as well as with the experimental data. This occurs because for wide open channel flows, the value of parameter λ becomes zero and both the mixing length models of this study and of Castro-Orgaz et al. (2012) give similar results.

Conclusions

In this study, streamwise turbulent velocity profile is investigated in an open channel through mixing length concept. Models on mixing length are proposed for both clear water and sediment-laden flow for the first time which include the dip-phenomenon. As direct data of mixing length are not available in the literature, for the validation purpose mixing length data are calculated from the available velocity data using finite difference approximations in the Prandtl's mixing length equation. The calculated mixing length data show that it follows a semi-normal type distribution that increases as one moves away from the bed, approaches a maximum value where the velocity is

maximum and then decreases. Unlike the previous models of mixing length, the present models are capable to describe this distribution pattern with a discontinuity at a point where the maximum velocity occurs.

The model of mixing length in sediment-laden flow contains a damping factor and this factor is calculated by differentiating diffusion equation with both sediment diffusivity and momentum diffusivity as functions of vertical height y. The velocity profile determined by using this mixing length model is capable of predicting dip-phenomenon. The ratio of sediment diffusivity to momentum diffusivity present in the model is determined through a regression equation proposed in a recent work which is a function of normalized settling velocity, reference height and reference concentration rather than treating it as a free parameter like many other researchers; as such, there is no free parameter present in the model. The plotting of mixing length in sediment mixed fluid shows that the presence of sediment may not damp the mixing length throughout the flow depth rather damping occurs from bed region to dip-position and in the neighborhood of dip-position mixing length decreases symmetrically.

Acknowledgements The first author is thankful to the Center for Theoretical Studies at the Indian Institute of Technology, Kharagpur, for providing a fellowship to visit the Institute and conduct the research reported in this paper. The second author acknowledges PhD fellowship from IIT Kharagpur.

Compliance with ethical standards

Conflict of interest The authors declare that they have no conflict of interest.

References

Absi R (2011) An ordinary differential equation for velocity distribution and dip-phenomenon in open channel flows. J Hydraul Res 49(1):82–89

Baldock TE, Tomkins MR, Nielsen P, Hughes MG (2004) Settling velocity of sediments at high concentrations. Coast Eng 51(1):91–100

Ballio F, Tait S (2012) Sediment transport mechanics. Acta Geophys 60(6):1493–1499

Bialik R, Nikora V, Rowiński P (2012) 3d lagrangian modelling of saltating particles diffusion in turbulent water flow. Acta Geophys 60(6):1639–1660

Bialik RJ (2011) Particle-particle collision in lagrangian modelling of saltating grains. J Hydraul Res 49(1):23–31

Bialik RJ (2013) Numerical study of near-bed turbulence structures influence on the initiation of saltating grains movement. J Hydrol Hydromech 61(3):202–207

Bialik RJ, Nikora VI, Karpiński M, Rowiński PM (2015) Diffusion of bedload particles in open-channel flows: distribution of travel times and second-order statistics of particle trajectories. Environ Fluid Mech 15(6):1281–1292

Bonakdari H, Larrarte F, Lassabatere L, Joannis C (2008) Turbulent velocity profile in fully-developed open channel flows. Environ Fluid Mech 8:1–17

Buschmann M, Gad-el Hak M (2005) New mixing-length approach for the mean velocity profile of turbulent boundary layers. J Fluids Eng 127(2):393–396

Castro-Orgaz O, Giraldez JV, Mateos L, Dey S (2012) Is the von karman constant affected by sediment suspension? J Geophys Res 117(F04002):1–16

Cellino M, Graf WH (1999) Sediment-laden flow in open-channels under noncapacity and capacity conditions. J Hydraul Eng 125(5):455–462

Cheng NS (1997) Effect of concentration on settling velocity of sediment particles. J Hydraul Eng 123(8):728–731

Coleman NL (1981) Velocity profiles with suspended sediment. J Hydraul Res 19(3):211–229

Coleman NL (1986) Effects of suspended sediment on the open-channel velocity distribution. Water Resour Res 22(10):1377–1384

Coles DE (1956) The law of the wake in the turbulent boundary layer. J Fluid Mech 1:191–226

Francis JB (1878) On the cause of the maximum velocity of water flowing in open channels being below the surface. Trans Am Soc Civ Eng 7(1):109–113

Galbraith RM, Sjolander S, Head M (1977) Mixing length in the wall region of turbulent boundary layers. Aeronaut Q 28(02):97–110

Graf WH (1971) Hydraulics of sediment transport. McGraw-Hill, New York

Granville P (1989) A modified van driest formula for the mixing length of turbulent boundary layers in pressure gradients. ASME Trans J Fluids Eng 111:94–97

Guo J (2006) Self-similarity of mean flow in pipe turbulence. In: 36th AIAA fluid dynamics conferences and exhibit, AIAA paper 2885, San Francisco

Guo J (2013) Modified log-wake-law for smooth rectangular open channel flow. J Hydraul Res 52(1):121–128

Guo J, Julien PY (2001) Turbulent velocity profiles in sediment-laden flows. J Hydraul Res 39(1):11–23

Guo J, Julien PY (2003) Modified log-wake law for turbulent flow in smooth pipes. J Hydraul Res 41(5):493–501

Hunt JN (1954) The turbulent transport of suspended sediment in open channels. Proc R Soc Lond A 224:322–335

von Karman T (1930) Mechanische Ähnlichkeit und turbulenz. Nachrichten von der Gesellschaft der Wissenschaften zu Göttingen: Mathematisch-physische Klasse, pp 58–76

Karman VT (1960) see H Schlichting, Boundary layer theory. McGraw-Hill, New York

Keulegan CH (1938) Laws of turbulence flow in open channels. J Res Natl Bureau Stand 21:707–741

Kironoto BA, Graf WH (1994) Turbulence characteristics in rough uniform open-channel flow. Proc ICE Water Marit Energy 106(12):333–344

Kovacs AE (1988) Prandtl's mixing length concept modified for equilibrium sediment-laden flows. J Hydraul Eng 124(8):803–812

Kumbhakar M, Kundu S, Ghoshal K (2017) Hindered settling velocity in particle-fluid mixture: a theoretical study using the entropy concept. J Hydraul Eng 143(11):06017019 (1–8)

Kundu PK (1990) Fluid mechanics. Academic, New York

Kundu S (2016) Effect of lateral bed roughness variation on particle suspension in open channels. Environ Earth Sci 75(8):1–18

Kundu S, Ghoshal K (2012) An analytical model for velocity distribution and dip-phenomenon in uniform open channel flows. Int J Fluid Mech Res 39(5):381–395

Lassabatere L, Pu HJ, Bonakdari H, Joannis C, Larrarte F (2013) Velocity distribution in open channel flows: analytical approach for the outer region. J Hydraul Eng 139(1):37–43

Launder BE, Priddin C (1973) A comparison of some proposals for the mixing length near a wall. Int J Heat Mass Transf 16(3):700–702

Lewis W, Gilliland E, Bauer W (1949) Characteristics of fluidized particles. Ind Eng Chem 41:1104–1127

Lyn DA (1986) Turbulence and turbulent transport in sediment-laden open-channel flows. PhD thesis, California Institute of Technology, California

Lyn DA (1988) A similarity approach to open-channel sediment laden flows. J Fluid Mech 193(1):1–26

Mazumder BS, Ghoshal K (2006) Velocity and concentration profiles in uniform sediment-laden flow. Appl Math Model 30:164–176

Montes JS (1973) Interaction of two dimensional turbulent flow with suspended particles. PhD thesis, Massachusetts Institute of Technology, Cambridge

Murphy C (1904) Accuracy of stream measurements. Water Supply Irrigation Pap 95:111–112

Muste M, Patel VC (1997) Velocity profiles for particles and liquid in open-channel flow with suspended sediment. J Hydraul Eng 123(9):742–751

Muste M, Yu K, Fujita I, Ettema R (2005) Two-phase versus mixed-flow perspective on suspended sediment transport in turbulent channel flows. Water Resour Res 41(W10402). https://doi.org/10.1029/2004WR003595

Nezu I, Tominaga A, Nakagawa H (1993) Field measurements of secondary currents in straight rivers. J Hydraul Eng 119(5):598–614

Nishioka M, Iida S (1973) The mixing length derived from krmns similarity hypothesis. Aeronaut Q 24:71–76

Obermeier F (2006) Prandtl's mixing length model-revisited. PAMM 6(1):577–578

Pal D, Ghoshal K (2013) Hindered settling with an apparent particle diameter concept. Adv Water Resour 60:178–187

Pal D, Ghoshal K (2016) Effect of particle concentration on sediment and turbulent diffusion coefficients in open-channel turbulent flow. Environ Earth Sci 75(18):1245

Patel VC (1973) A unified view of the law of the wall using mixing-length theory. Aeronaut Q 24(01):55–70

Prandtl L (1925) Bericht ber untersuchungen zur ausgebildeten turbulenz. Zeitschrift für Angewandte Mathematik und Mechanik 5:136–139

Prandtl L (1932) Recent results of turbulence research. Technical Memorandum 720, National Advisory Committee for Aeronautics

Prandtl L (1960) see H Schlichting, Boundary layer theory. McGraw-Hill, New York

Pu JH (2013) Universal velocity distribution for smooth and rough open channel flows. J Appl Fluid Mech 6(3):413–423

Richardson JF, Zaki WN (1954) Sedimantation and fluidization part I. Trans Inst Chem Eng 32:35–53

Rouse H (1937) Modern concepts of the mechanics of turbulence. Trans ASCE 102:463–543

Rowinski P, Lee SL (1993) Equilibrium profile of suspended sediment concentration. Acta Geophysica Polonica 41(2):163–176

Sun ZL, Sun ZF, Donahue J (2003) Equilibrium bed-concentration of nonuniform sediment. J Zhejiang Univ Sci 4(2):186–194

Townsend AA (1961) Equilibrium layers and wall turbulence. J Fluid Mech 11:97–120

Umeyama M, Gerritsen F (1992a) Velocity distribution in uniform sediment-laden flow. J Hydraul Eng 118(2):229–245

Umeyama M, Gerritsen F (1992b) Velocity distribution in uniform sediment-laden flow. J Hydraul Eng 118(2):229–245

Van Driest ER (1956) The problem of aerodynamic heating. Aeronaut Eng Rev 15(10):26–41

Vanoni VA (1940) Experiments on the transportation of suspended sediment by water. PhD thesis, California Institute of Technology, Pasadina

Wang X, Qian N (1989) Turbulence characteristics of sediment-laden flows. J Hydraul Eng 115(6):781–799

Yalin MS (1977) Mechanics of sediment transport, 2nd edn. Pegramon Press, New York

Yang SQ (2007) Turbulent transfer mechanism in sediment-laden flow. J Geophys Res 112(F01005). https://doi.org/10.1029/2005JF000452

Yang SQ (2009) Mechanism for initiating secondary currents in channel flows. Can J Civ Eng 36(9):1506–1516

Zhiyao S, Tingting W, Fumin X, Ruijie L (2008) A simple formula for predicting settling velocity of sediment particles. Water Sci Eng 1(1):37–43

Acta Geophysica (2018) 66:109–119
https://doi.org/10.1007/s11600-018-0110-9

RESEARCH ARTICLE - HYDROLOGY

Simulation of relationship between river discharge and sediment yield in the semi-arid river watersheds

Mohammad Reza Khaleghi[1] · Javad Varvani[2]

Received: 14 September 2017 / Accepted: 4 January 2018 / Published online: 25 January 2018

Abstract

Complex and variable nature of the river sediment yield caused many problems in estimating the long-term sediment yield and problems input into the reservoirs. Sediment Rating Curves (SRCs) are generally used to estimate the suspended sediment load of the rivers and drainage watersheds. Since the regression equations of the SRCs are obtained by logarithmic retransformation and have a little independent variable in this equation, they also overestimate or underestimate the true sediment load of the rivers. To evaluate the bias correction factors in Kalshor and Kashafroud watersheds, seven hydrometric stations of this region with suitable upstream watershed and spatial distribution were selected. Investigation of the accuracy index (ratio of estimated sediment yield to observed sediment yield) and the precision index of different bias correction factors of FAO, Quasi-Maximum Likelihood Estimator (QMLE), Smearing, and Minimum-Variance Unbiased Estimator (MVUE) with LSD test showed that FAO coefficient increases the estimated error in all of the stations. Application of MVUE in linear and mean load rating curves has not statistically meaningful effects. QMLE and smearing factors increased the estimated error in mean load rating curve, but that does not have any effect on linear rating curve estimation.

Keywords SRC · MVUE · Logarithmic transformation

Introduction

The transmission forms of sediments and deposits in open channels are wash load (near the top of the flow), suspended load (almost never has connection with the bed) and bed load (move in still connection with the channel bed) (Aberle et al. 2012; Singh et al. 2012; Bialik and Czernuszenko 2013; Bialik et al. 2012, 2014). The study of suspended sediment transport in rivers (Liu and Chiew 2012) has a past more than 100 years (Walling and Webb 1981). The first sample of suspended loads measured in the Mississippi River was in 1845 AD. In this regard, development of measured activities has been in line with increased need for information about suspended load (Ballio and Tait 2012) and its variations in management programs of reservoirs and water structures (Crawford 1991). The dynamic and complex nature of river load makes difficult the estimation of sediments entered into reservoirs and also long-term sediment production to determine the service life of structures (Haynes et al. 2012; Link et al. 2012). Correct estimation of sediment volume carried by a river is very important for water resource project management. Several methods of river suspended load estimation have been proposed and have been discussed in terms of different aspects. In general, the estimation of suspended load in rivers is divided into two categories: the first category, the methods based on dynamic and fluid mechanics laws have been presented by specialists and experts in science hydraulics, generally. The second method based on direct measurements and statistical analysis proposed by hydrologic scientists. Preston and Bierman (1989) suggested an integer classification based on hydrological method that its components are averaging estimator, ratio estimator, and

✉ Mohammad Reza Khaleghi
drmrkhaleghi@gmail.com

Javad Varvani
varvani_55@yahoo.com

[1] Department of Range and Watershed Management, Torbat-e-Jam Branch, Islamic Azad University, Torbat-e-Jam, Iran

[2] Department of Range and Watershed Management, Arak Branch, Islamic Azad University, Arak, Iran

regression estimator. Since suitable distribution for sediment density and flow is biennial log-normal distribution, hence, regression estimators (rating curves) are used as logarithmic. In the use of SRCs, there are two types of bias in related to the linear regression model. The first type of bias is related to a method used for obtaining of the regression equation. The second type of bias is resulted of changing the log mode to normal mode. The first type of bias may be somewhat reduced by applying a least-squares fit method that is unbiased somewhat but the second type of bias, such as adding the additional independent variables in the equation. In an unbiased model, an overestimation or an underestimation has the same probability and chance. According to Degens and Donohue (2002), accuracy is defined as the closeness of the load estimates to the actual load in the river in the period of interest and also precision is the variation of the measured values relative to the true variation of the target (or true) population. The most popular method for monitoring SRCs is the passing of a line (or more than a line) among the cloud points of flow discharge and sediment discharge its results will be a linear SRCs. Boning (2001) concluded that calculated sediment discharge without bias correction factor is 13% less than calculated sediment discharge used from MVUE method. In addition, estimation sediment using QMLE method is 4% more than MVUE method. In addition, the methods of MVUE and smearing disagreed with each other only 0.6%. In addition, MVUE method would be appropriate only if the statistical distribution of errors follows a normal distribution, an otherwise smearing method is the appropriate method. Cohn et al. (1989) investigated the bias and variance of the three methods of linear rating curve, transformed rating curve and unbiased estimator with minimum variance (MVUE) and their results showed that in most cases, old and transformed estimators can be achieved to acceptable values. However, in situations such as the small number of samples and flood conditions, the standard error of this method is high. While the MVUE method is unbiased, it provides a more acceptable solution than other methods. Blanco et al. (2010) investigated the temporal variations of suspended sediment load in the scales of monthly, seasonal, and annual storm in a 3-year period in the northwest of Spain and found that rating curves have no acceptable performance in estimating the amount of sediment yield particularly in the case of flood events. Their results also showed that the most sediment yield occurs during the events in 70% of cases which the peak discharge of sediment occurred earlier than the peak flow discharge. However, discharge–sediment patterns in the events are generally clockwise and this shows that the suspended sediment sources are close together and in-stream. Hu et al. (2011) analyzed the SRCs based on monthly data of flow discharge and suspended sediment concentration hydrometer at stations in the upper, middle, and lower reaches of the changing in different periods from 1955 to 2007. They also analyzed the temporal and spatial variations of the SRCs with respect to the impact of human activities and watershed characteristics. Their results indicate that human disturbances have had a substantial impact on sediment rating parameters, with the magnitude of the impact related to the scale of the river sections. In general, the past studies showed the error due to the logarithmic transformation and the effect of applying correction factors in connection with the methods of SRCs estimating in most cases; they are not definitive and more studies are needed. In general, there is a relation between sediment concentration (C) and water discharge (Q) for a hydrologic event. Hereof, a few types of C–Q relations are well known such as the hysteresis loop. Williams (1989), to identify and classify the major types of single-event C–Q relations, using models and field examples, studied qualitatively these relations (discharge and concentration vs. time) and concluded that comparing C–Q ratios at a given discharge provides a consistent, reliable method for categorizing C–Q relations (loop achievement). C–Q hysteresis loops are frequently analyzed in terms of temporal-graph mode, spread, and skewness to facilitate the understanding of sediment transport processes (Campagnol et al. 2012; Aich et al. 2014; Szilo and Bialik 2017). These indexes reveal five major classes of C–Q relations. These classes are single-valued (straight or curved), clockwise loop, counter-clockwise loop, single-valued plus a loop, and figure eight. The type and magnitude of C–Q relation for a particular site are function of rainfall–runoff and also sediment behavior features (Williams 1989). Clockwise hysteretic floods are characterized by their long duration and the highest hydrological and sedimentological responses; This loop (Class II) has been attributed to depletion of available sediment before the water discharge has peaked (Leopold and Maddock 1953; Arnborg and Walker 1967; Walling and Teed 1971; Walling 1974); counter-clockwise hysteretic floods are characterized by their short duration and moderate hydrological and sediment responses; finally, figure-eight hysteretic floods are related to multiple peaks in suspended sediment, coinciding with oscillations in discharge associated with the highest rainfall intensities within each event and moderate hydrological and sediment responses (Nadal-Romero et al. 2008). For single hydrologic events, figure-eight C–Q relations that it does not much matter (Arnborg et al. 1967). In addition, Nu-Fang et al. (2011) founded three different types of SSC-Q relationships (hysteretic loops): clockwise, figure eight, and complex. Lloyd et al. (2016) to characterize and quantify the storm behavior, used a range of metrics about loop characters such as loop direction, loop area and a hysteresis index (HI). Arnborg et al. (1967), in their investigation

about suspended Load in the Colville River, Alaska, founded that load per unit volume increased at a more rapid rate than discharge, such that the peak sediment load preceded peak discharge. The rate of increase of concentration was greater than that of water, and concentration peaked first. The SRC technique has been widely used by scientists and engineers for a large variety of purposes (Meade et al. 1990; Syvitski et al. 2000; Hu et al. 2011; Fan et al. 2012). The SRC is defined as the statistical relationship between suspended sediment concentration (sediment load) and stream discharge (Fan et al. 2012). Recently, hydrologists have used sediment rating (sediment transport) curves to estimate (predict) actually suspended sediment concentrations (SSCs) for subsequent flux calculations in the absence of actual SSC data (Walling and Webb 1981; Phillips et al. 1999; Horowitz 2003; Moreno and Bombardelli 2012). Ferguson (1986) and Asselman (2000) compared the actual and estimated suspended sediment concentrations from flow discharge using the constructed SRCs and concluded that SRCs are likely to underestimate actual concentrations (Horowitz 2003; Fan et al. 2012). To compensate for the above problem, various methods have been applied and several forms of bias correction factors have been suggested in recent years (Ferguson 1986; Asselman 2000; Iadanza and Napolitano 2006; Fan et al. 2012). The non-linear regression equations not only are used to construct the SRCs, but also are used to study the effect of the decreasing flow discharge and the suspended sediment concentration during the flooding on the shape of the SRC (Ferguson 1986; Phillips et al. 1999; Asselman 2000; Holtschlag 2001; Horowitz 2003; Fan et al. 2012). Numerous studies on the evaluation of bias correction factors in SRCs have been conducted in many regions around the world. Xu (1999, 2004) and Fang et al. (2008, 2011) analyzed the spatial and temporal scale dependences of sediment concentration and discharge relationship and concluded that when the discharge is larger than the critical value, the suspended sediment concentration has a little change. According to Asselman (2000), instantaneous sediment transport rates are not only a function of the transport capacity of a river, but also a function of sediment availability and this property illustrates it as a non-capacity load. Horowitz (2003) investigated the SRCs for estimating suspended sediment concentrations and concluded that over periods of 20 or more years, errors of $< 1\%$ can be achieved using a single SRC based on data spanning the entire period and also when error limits must be kept under 20%, temporal resolution probably should be limited to quarterly or greater. Bajcsy et al. (2007) used a simulation framework for evaluating sampling strategies and determining load accuracies in suspended sediment loads and concluded that watershed hydrologic and morphologic characteristics, sampling method, and frequency, along with the method used to develop sediment–discharge rating curves, can substantially affect the accuracy and precision at which sediment load estimates are made. The variation in suspended sediment concentration can be explained by sediment flushing, sediment concentration diluted during high discharge events and sediment exhaustion after event sequences (Hudson 2003; Lecce et al. 2006; Marttila and Kleve 2010). Riverbed morphology, slope, and stream power are the factors that have a close association with the distribution of sediment rating parameters (Asselman 2000; Syvitski et al. 2000; Morehead et al. 2003; Yang et al. 2007; Wang et al. 2008). Nowadays, computer programs are being developed that allows one to estimate sediment loads using several sediment–discharge rating curves and bias correction factors. Jain (2001) used the ANN approach to establishing an integrated stage–discharge–sediment concentration relation for two sites on the Mississippi River. Based on the comparison of the results for two gauging sites, it was shown that the ANN results are much closer to the observed values than the conventional technique. In addition, correct estimation of sediment volume being carried by a river was very important for many water resources projects. In addition, conventional SRCs, however, are not able to provide sufficiently accurate results. Barzegari et al. (2015) estimated suspended sediment by Artificial Neural Network (ANN), Decision Trees (DT), and SRC Models. They concluded that the accuracy of ANN with Levenberg–Marquardt backpropagation algorithm was more than the two other models, especially in high discharges. Arabkhedri et al. (2010) compared the effect of Adaptive Cluster sampling designs on the accuracy of SRC estimation performed a study for Gorgan-Rood River, Iran by synthesizing sample sets from daily rain and sediment records. They concluded that among tested methods, LMLWDC produced the most accurate results with only 3% overestimation and a coefficient of variation in the order of 14% when the sampling frequency was semiweekly and also the inclusion of more samples from high load periods is likely the cause of the more accurate estimates from adaptive sample sets.

The aim of this study is to evaluate the bias correction factors in SRCs and also to investigate the correlation between sediment rating parameters and to study their controller factors.

Materials and methods

Characteristics of the study hydrometric stations

Study area

Table 1 presents the characteristics of the selected hydrometric stations of Kale-Shour and Kashafrud. The selected

Table 1 Characteristics of the study stations

Average slope (%)	Average precipitation (mm)	Watershed area (km^2)	Elevation (m)	*Y*	*X*	Station code	River-station
3.1	263	9410	1563	3,990,444.2	629,075.5	47-045	Kale-Shour-Hossein Abad Jangal
3.2	260	4160	1664	3,993,109.0	674,079.4	47-039	Kale-Shour-Ruh Abad
10.6	275	535	2102	4,104,196.8	544,439.8	47-059	Bidvaz-Esfarayen
8	275	8770	1529	4,013,559.2	756,138.1	64-033	KashafRud-OlangAsadi
6.9	260	16,800	1335	3,986,122.8	334,121.1	64-039	KashafRud-Pole Khatoon
9	260	202	1260	4,023,165.6	698,984.5	64-019	Zoshk-SarAsiabeShandiz
6.8	260	16,300	1352	3,993,389.8	306,249.0	64-037	KashafRud-AghDarband

stations in terms of area range from 202 to 16,800 km^2, which show a good variety in terms of area factor. Watershed area, as a physical factor, can be effective in most hydrological processes. If the correction coefficients for the SRC are affected by the physical characteristics of the watershed, it is possible to identify their variations with changing of the area.

Precipitation rates in the study stations, not much change, so that rainfall rate ranges from 260 to 275 mm. In addition, elevation ranges from 1260 to 2102 m. Average slope ranges from 3.1 to 10.6%. Precipitation data have achieved based on rain gauge stations in the region and have an average value; obviously, in the mountainous regions of the study area, compared to the plain areas, changes in precipitation will be greater.

Used methods and models

According to Jansson (1996), flow discharges with a specific development to be divided into several categories, and for the average discharge per category, the average sediment related the same category to be determined and finally the SRC to be mapped using these estimated data. This method is called as mean load within discharge classes. Jones et al. (1981) used the parallel linear equation that was based on the passing of a line among the average of sediment points and their g to corresponding discharge. This method has been proposed as FAO method and in practice is calculated as a coefficient and applied in linear SRC. The other SRCs in which the bias problem result of changing into logarithmic mode (Dey et al. 2012) has been modified are Quasi-Maximum Likelihood Estimator (QMLE) (Ferguson 1987; Duan 1983) and smearing estimator (Thomas, 1985).The general equation of QMLE method is as follows (Eq. 1):

$$L^{\wedge}_{\mathrm{QMLE}} = L_{\mathrm{Rc}} . \exp\left(\frac{S^2}{2}\right) \tag{1}$$

where $L^{\wedge}_{\mathrm{QMLE}}$ is estimated sediment discharge (load) using the quasi-maximum likelihood estimator (m^3/s), LRC is the estimated sediment load from the rating curve and S^2 is mean square error of the regression. This method has also been called as a CF_1 parametric method. Smearing estimator is a nonparametric method (CF_2) and its general equation is (Eq. 2)

$$L_{\mathrm{s}} = L_{\mathrm{Rc}} \frac{\sum_{i=1}^{N} \exp(ei)}{N} \tag{2}$$

where L_{s} is estimated sediment discharge (load) using the smearing estimator (m^3/s), N is number of data points in the regression, and ei is residuals from least-squares regression and is the differences in the natural logarithms of measured and computed sediment discharge. Another important statistical method for each possible value of a parameter gives unbiased estimation or has a variance less than other methods and is MVUE method. In this method, the bias correction is used for each of the daily discharge values (Cohn et al. 1989). This method has the following equations (Eqs. 3, 4, 5):

$$\hat{L}_{\mathrm{MVUE}} = L_{\mathrm{Rc}(t)} \cdot g_{\mathrm{m}} \tag{3}$$

$$g_{\mathrm{m}} = \frac{m+1}{2m}\left\{(1-V)S^2\right\} \tag{4}$$

$$V = \frac{1}{N} + \left[\frac{(\ln(Q_x) - \overline{\overline{\ln(Q)}}^2}{\sum_{i=1}^{N}(\ln(Q_i) - \overline{\overline{\ln(Q)}}^2}\right] = \frac{1}{N} + \left[\frac{(\ln(Q_x) - Q_{\mathrm{Bar}})^2}{Q_{\mathrm{var}}}\right] \tag{5}$$

where $L^{\wedge}_{MVUE}$ is estimated sediment discharge (load) for the day using MVUE, $LR_{\mathrm{c(t)}}$ is sediment load estimated from the rating curve for each day (t), m is degrees of freedom of the regression equation, V is an estimation of the variability of a given value off-stream-flow discharge, gm is a function used by Bradu and Mundlak (1970), Q_x is daily mean stream flow for the day loads that are being predicted, Q is instantaneous stream flow in the regression, N is number of data points in the regression, Q_{var} is variance of flow discharges, Q_{Bar} is the flow average discharge, and S is SRC standard error.

Statistical population, sampling, and drawing of SRCs

Statistical population formed according to simultaneous flow discharge data and suspended sediment load. The sampling process was carried out as random by dividing the simultaneous data into two groups of 70 and 30% (Arabkhedri et al. 2010). The first group was used for drawing of the SRCs and also for estimating of correction coefficients and the second group was used for the validation of methods. This section was done using the SPSS software. After sampling in Excel, linear SRCs and mean load within discharge classes were drawn with various coefficients of CF_1, CF_2, and FAO. To use the coefficients of MVUE (minimum-variance unbiased estimator) method, first, the required parameters for this coefficient were earned from each of the linear SRCs and mean load within discharge classes, and then to facilitate complex calculations, it was used from FORTRAN program (Boning 2001). Finally, desired data were estimated using flow discharge rates and various SRCs in the 30% group.

Evaluation of the efficiency correction coefficients

To evaluate the efficiency of SRCs, the estimation for each method was evaluated using the statistical index of the proportion of estimated rate ratio to observed rate (base value) as the accuracy index and the coefficient of estimation variations as the precision index (Ferguson 1987; Duan 1983).

Results

Table 2 presents the amounts of accuracy index (the proportion of estimated sediment to observed sediment) of various factors related to bias (Inaccuracy) correction in the study stations. In addition, the values of the precision index or coefficient of variation related to the estimation of different methods that have been involved in this table. As this table shows, the amounts of accuracy index in the Kale-Shour–Hossein Abad Jangal station vary from 1.9 in linear rating curve without applying a correction factor up to 8.59 in FAO coefficient or combination of FAO correction factor and linear rating curve. Figure 1, which presents the location of the selected hydrometric stations, indicates this topic. The amounts of accuracy index in Kale-Shour-Ruh Abad and Bidvaz-Esfarayen stations in mentioned methods, vary from 8.2 to 45.26 and 3.62–23, respectively. This variation for KashafRud-Olang Asadi station in mentioned methods varies from 3.39 to 35.25.

Figure 2 shows the variations of the accuracy index in related to various methods (linear and mean) and their combination with FAO coefficient (F), CF1, CF2, and

Table 2 Amounts of accuracy indices related to the estimation of various factors affecting rating curve bias correction in the Kale-Shour and Kashafrud stations

Mean load within discharge classes				Linear sediment rating curve				Mean load within discharge classes	Linear sediment rating curve	Method	Station
FAO coefficient	CF1	CF2	MVUE	FAO coefficient	CF1	CF2	MVUE				
6.28	4.00	3.74	3.32	8.59	3.51	3.42	2.05	3.19	1.90	Accuracy Index	Kale-Shour-Hossein Abad Jangal
4.94	4.94	4.94	4.93	5.09	5.09	5.09	5.08	4.94	5.09	Precision Index	
29.25	25.39	23.84	18.98	45.26	16.86	15.91	9.26	18.5	8.20	Accuracy Index	Kale-Shour-Ruh Abad
3.94	3.94	3.94	3.89	4.10	4.10	4.10	4.09	3.94	4.10	Precision Index	
17.67	18.76	16.1	12.07	23.00	10.99	12.27	4.46	11.98	3.62	Accuracy Index	Bidvaz-Esfarayen
1.84	1.84	1.84	1.84	1.95	1.95	1.95	1.95	1.84	1.95	Precision Index	
14.17	9.15	8.66	6.78	35.25	10.74	11.18	4.17	6.52	3.39	Accuracy Index	KashafRud-OlangAsadi
5.79	5.79	5.79	5.74	5.72	5.72	5.72	5.71	5.79	5.72	Precision Index	
16.75	10.06	10.08	9.10	17.78	10.23	12.03	4.66	8.91	3.91	Accuracy Index	KashafRud-Pole Khatoon
3.40	3.40	3.40	3.40	3.73	3.73	3.73	3.72	3.40	3.73	Precision Index	
76.17	56.3	54.41	25.78	72.60	13.19	24.67	5.45	29.84	4.58	Accuracy Index	Zoshk-SarAsiabeShandiz
12.68	12.68	12.68	12.66	12.45	12.45	12.45	12.44	12.68	12.45	Precision Index	
30.37	65.46	55.06	43.92	11.14	21.41	15.8	8.07	43.13	7.33	Accuracy Index	KashafRud-AghDarband
3.31	3.31	3.31	3.22	8.33	8.33	8.33	8.01	3.31	8.33	Precision Index	

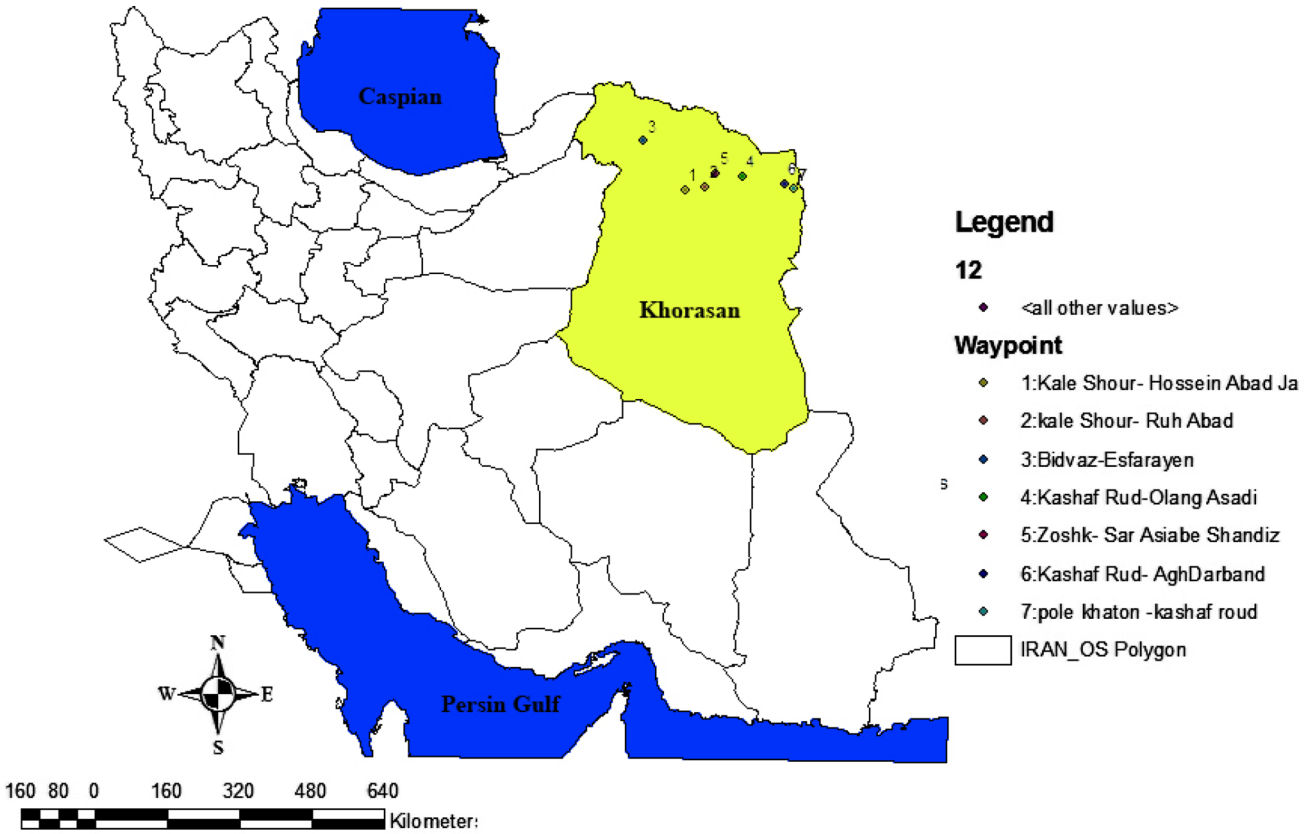

Fig. 1 Location of the study stations in Iran

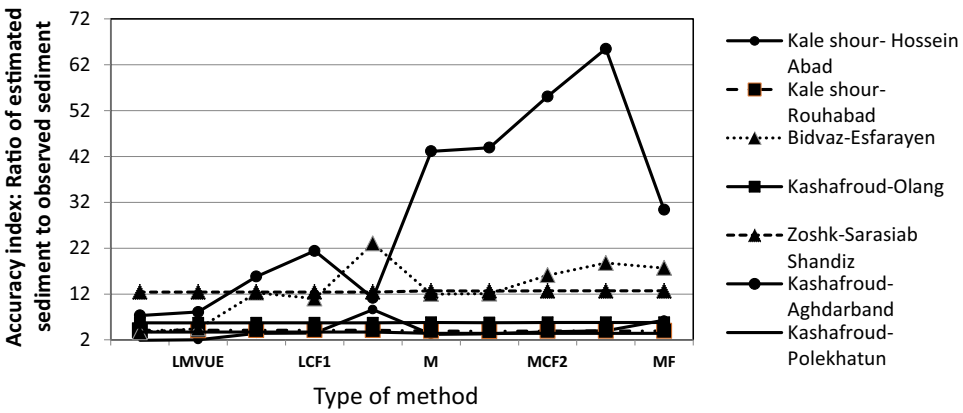

Fig. 2 Variations of the accuracy index in related to various methods (linear and mean) and their combination with FAO coefficient (*F*), CF1, CF2, MVUE in the study stations

MVUE in the study stations. Evaluation of the accuracy indices (the proportion of estimated sediment load to observed sediment load) and the precision index of the different methods can assist in selecting the appropriate method. The accuracy index was at the best equal to the unit and getting away from this index value from the unit indicates that the calculation is different from the observations. In the stations of Kashaf Rud-Pole Khatoon, Zoshk-Sar Asiabe Shandiz, and Kashaf Rud-AghDarband, the minimum and maximum amounts of the accuracy index are 3.91 to 17.78, 4.58 to 72.6, and 7.33 to 43.92, respectively. The results of Table 2 and Fig. 2 show that the minimum amount of the accuracy index, namely, the ratio of the estimated sediment load to the observed sediment load in linear SRC without applying a correction factor (1.9) has been seen in the station of Kale-Shour-Hossein Abad Jangal. However, we can say the amount of accuracy index in linear SRC method in all the stations is less than other methods. The amount of accuracy index in mean load within discharge class's method (M) in the study stations varies from 3.19 in Hossein Abad Jangal to 43.13 in Kashaf Rud-Agh Darband. In general, in all cases,

applying the correction factors of Cf_1, Cf_2 (parametric and nonparametric smearing estimators, respectively), MVUE, and FAO coefficient has been reduced the accuracy of the estimations.

Therefore, an exact method must necessarily have a high coefficient of variation. In most cases, the values of the coefficients are in agreement with the accuracy index, so the maximum amount of precision is belonged to linear SRC without applying a correction factor. Figure 3, which presents the variations of the precision index in related to various methods (linear and mean) and their combination with FAO coefficient (*F*), CF1, CF2, and MVUE in the selective stations, indicates this topic clearly. Primary data related to sediment concentration and flow discharge have been many changes as for a specific discharge class; variation of sediment concentration is very high. This is due to irregular nature of the sediment concentration and sedimentation in rivers. For further investigation findings, it was used from the accuracy and precision index methods. Tables 3 and 4 show that the results of a significant test of the various methods differ that indicators were done using Fisher's least significant difference method.

Discussion

Comparison of the accuracy index estimation in each method in the various stations using LSD statistical criterion (least significant difference) shows that with a confidence level of 99%, the mean accuracy related to the different methods is different from each other and this is extractable using the analysis of variance table. Tests for statistical significance indicate whether observed differences between assessment results occur because of sampling error or chance. Such "insignificant" results should be ignored, because they do not reflect real differences ("Significance" here does not imply any judgment about the absolute magnitude or educational relevance. It refers only to the statistical nature of the difference and indicates the difference is worth taking note of). In this test, the null hypothesis indicates that the mean accuracy of methods is equal to each other. To test this hypothesis, if the variance of the accuracy index between groups is greater than variance associated within groups and also have enough magnitude to be statistically acceptable, it can be concluded that the means are not equal, and there are significant differences between them. On the contrary, if variance associated with the methods is greater than the variance of the accuracy index between methods, it can be concluded that variance caused by the differences in the mean is statistically insignificant, and as a result, there is no significant difference between the means. It is worth mentioning that there are always differences between the means, but the difference is debatable that its magnitude is statistically significant and otherwise it can be ignored. Analysis of variance (ANOVA) table shows that the within groups mean square (256) is less than the between groups mean square (585) and statistically is significant at the 99% level. Therefore, with distinguishing the accuracy indexes methods, they can be divided into different groups. Based on the results, the first group included the methods of L, LMVUE, LCF1, LCf2, M, and MMVUE and the second

Table 3 Analysis of variance between different methods (ANOVA)

	Sum of Squares	*df*	Mean square	*F*	Sig.
Between groups	5265.04	9	585.00	2.25	0.030
Within groups	15,564.48	60	259.40	–	–
Total	20,829.52	69	–	–	–

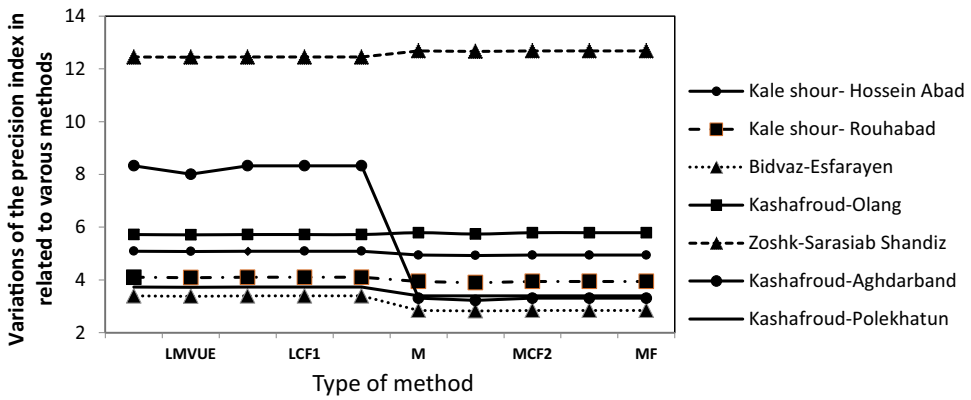

Fig. 3 Variations of the precision index in related to various methods (linear and mean) and their combination with FAO coefficient (*F*), CF1, CF2, MVUE in the selective stations. Primary data related to sediment concentration and flow discharge have been many changes as for a specific discharge class; variation of sediment concentration is very high. This is due to irregular nature of the sediment concentration and sedimentation in rivers

Table 4 Significant test related to efficiency difference between different methods of bias correction in related to various methods (linear and mean) and their combination with FAO coefficient (*F*), CF1, CF2, and MVUE in the study stations

Significant	Standard error	The mean difference	Method	
0.932	8.6	− 0.74	LMVUE	L
0.305	8.6	− 8.91	LCF2	
0.374	8.6	− 7.71	LCF1	
0.004	8.6	− 25.81	LF	
0.144	8.6	− 12.73	M	
0.154	8.6	− 12.43	MMVUE	
0.025	8.6	− 19.85	MCF2	
0.012	8.6	− 22.31	MCF1	
0.011	8.6	− 22.53	MF	
0.932	8.6	0.74	L	LMVUE
0.347	8.6	− 8.16	LCF2	
0.421	8.6	− 6.97	LCF1	
0.005	8.6	− 25.07	LF	
0.169	8.6	− 11.99	M	
0.18	8.6	− 11.69	MMVUE	
0.03	8.6	− 19.11	MCF2	
0.015	8.6	− 21.57	MCF1	
0.014	8.6	− 21.79	MF	
0.305	8.6	8.9	L	LCF2
0.347	8.6	8.16	LMVUE	
0.89	8.6	1.19	LCF1	
0.054	8.6	− 16.9	LF	
0.658	8.6	− 3.82	M	
0.684	8.6	− 3.52	MMVUE	
0.209	8.6	− 10.94	MCF2	
0.125	8.6	− 13.4	MCF1	
0.119	8.6	− 13.62	MF	
0.374	8.6	7.71	L	LCF1
0.421	8.6	6.97	LMVUE	
0.89	8.6	− 1.19	LCF2	
0.04	8.6	− 18.09	LF	
0.562	8.6	− 5.02	M	
0.586	8.6	− 4.71	MMVUE	
0.164	8.6	− 12.13	MCF2	
0.095	8.6	− 14.59	MCF1	
0.09	8.6	− 14.81	MF	
0.004	8.6	25.81	L	LF
0.005	8.6	25.07	LMVUE	
0.054	8.6	16.9	LCF2	
0.04	8.6	18.09	LCF1	
0.134	8.6	13.07	M	
0.125	8.6	13.38	MMVUE	
0.491	8.6	5.96	MCF2	
0.686	8.6	3.5	MCF1	
0.705	8.6	3.28	MF	

group (precision indexes) included that the methods of MCf2, MCf1, MF, and LF. In fact, we can say that despite the differences between the amounts of the accuracy index related to linear rating curve without applying a correction factor, the mentioned values statistically is not significant and locate in the first group.

Conclusion

Since in the sediment curve rating regression equations, only one independent variable is entered; therefore, these curves are not enabled to estimate the actual sediment load of a river accurately and this is determined well by the results of this study and other research (Ferguson 1987; Waling 1977; Asselman 2000). Easiness in the application of these equations has caused to have a frequency of use in estimation of sediment load. Accurate estimation of sediment load in rivers requires sampling at short intervals of discharge and suspended sediment concentration. However, in present time, the mentioned operation is performed rarely, and only for certain specific stations so from the standpoint of daily sediment, the selected stations in this study have a relatively good condition. This issue is important in the selection of the basis for evaluation and comparison of estimation of sediment curve curves. The implemented accuracy index is the ratio of estimated sediment to the actual sediment content of different periods in the studied stations. The statistical population which according to it the sampling is done, and finally, SRCs are drawn based on those samples, has a great influence on the accuracy of the curves. In addition, beyond the sample size, moreover, the type of sampled data affects the accuracy of the curves, so that the more scattered the primary data, the estimation of SRCs is encountered at greater error. In addition, the estimated error rate will decrease if the sediment curve is drawn in such a way that it contains a lot of information from the primary statistical society. In the case of the MVUE coefficient, this is true and this regulation applies to the MVUE coefficient, because it earns too much information from the original data and individual flow data that estimation is done based on them. Mean load within discharge classes that is a transform of linear rating curve has not only a better performance than linear LMUE, but also even in some cases shows a high estimation error than mentioned method. Application of the MVUE coefficient in this method has been reduced the estimation error as well and to some extent has been improved the estimations of this method. Since the coefficients of FAO, CF_1, and CF_2 include only a little of calibration data, therefore, their performance is low in the estimation of average sediment load in considered periods and has low accuracy and precision than MVUE method. In general, to improve SRC relations at various stations, we need a lot of studies to clarify the nature and complexity of the regression estimators and/or other models. What is important in this regard is to have an appropriate target (or true) population consist of simultaneous data from the sediment concentration and flow discharge. Flow discharge as an auxiliary variable has an important role in the application of SRCs and it is the only independent variable that enters the SRC regression equations. In addition to checking the flow rates, it is necessary to test the application of other variables in the plotting of sediment curves. In other words, multivariable sediment curves should be plotted for this purpose. In the next research, to estimate the sediment curves (to estimate the sediment load of rivers and catchment areas), it is suggested to use variables such as time, time series functions, seasonal changes, and so on. The application of logarithmic transformation correction coefficients in single-variable sediment curves, in most cases, has scattered results; hence, their application should be more cautious.

Acknowledgements We thank TAMAB (Water Resources Research Organization of Iran) for providing the data for discharge and sediment and for helping us with the data preprocessing.

References

Aberle J, Coleman SE, Nikora VI (2012) Bed load transport by bed form migration. Acta Geophys 60(6):1720–1743. https://doi.org/10.2478/s11600-012-0076-y

Aich V, Zimmermann A, Elsenbeer H (2014) Quantification and interpretation of suspended-sediment discharge hysteresis patterns: how much data do we need? CATENA 122:120–129. https://doi.org/10.1016/j.catena.2014.06.020

Arabkhedri M, Noor-Akma I, Mohamad-Roslan MK (2010) Effect of adaptive cluster sampling design on accuracy of SRC estimation. J Hydrol Eng 15(2):142–151. https://doi.org/10.1061/(ASCE)HE.1943-5584.0000171

Arnborg L, Walker HJ, Peippo J (1967) Suspended Load in the Colville River, Alaska, 1962. Geografiska Ann: Ser A Phys Geogr Landsc Process Essay Geomorphol 49(2–4):131–144. https://doi.org/10.2307/520882

Asselman NEM (2000) Fitting and interpretation of SRCs. J Hydrol 234(3–4):228–248. https://doi.org/10.1016/S0022-1694(00)00253-5

Bajcsy P, Li Q, Crowder D, Markus M (2007) A simulation framework for evaluating sampling strategies and determining load accuracies in suspended sediment loads, Union. American Geophysical Union, Fall Meeting 2007 (**abstract id H53A-0962**)

Ballio F, Tait S (2012) Sediment transport mechanics. Acta Geophys 60(6):1493–1499. https://doi.org/10.2478/s11600-012-0074-0

Barzegari F, Yosefi M, Talebi A (2015) Estimating suspended sediment by artificial neural network (ANN), decision trees (DT) and SRC (SRC) models (case study: Lorestan Province, Iran). Civ Eng Infra J 48(2):373–380. https://doi.org/10.7508/ceij.2015.02.011

Bialik RJ, Czernuszenko W (2013) On the numerical analysis of bedload transport of saltating grains. Int J Sediment Res 28:413–420

Bialik RJ, Nikora VI, Rowinski PM (2012) 3D Lagrangian modelling of saltating particles diffusion in turbulent water flow. Acta Geophys 60(6):1639–1660. https://doi.org/10.2478/s11600-012-0003-2

Bialik RJ, Karpinski M, Rajwa A, Luks B, Rowinski PM (2014) Bed form characteristics in natural and regulated channel: a comparative field study on the Wilga River, Poland. Acta Geophys 62:1413–1434

Blanco MLR, Castro MMT, Palleiro L, Castro MTT (2010) Temporal changes in suspended sediment transport in an Atlantic

catchment, NW Spain. Geomorphology 123:181–188. https://doi.org/10.1016/j.geomorph.2010.07.015
Boning WC (2001) Recommendations for use of retransformation methods in Regression, models used to estimate sediment loads. http://water.Usgs.Gov
Bradu D, Mundlak Y (1970) Estimation in lognormal linear models. J Am Stat Assoc 65(329):198–211. https://doi.org/10.1080/01621459.1970.10481074
Campagnol J, Radice A, Ballio F (2012) Scale-based statistical analysis of sediment fluxes. Acta Geophys 60(6):1744–1777. https://doi.org/10.2478/s11600-012-0028-6
Cohn TA, Delong LL, Gilroy EJ, Hirsch RM, Wells DK (1989) Estimating constituent loads. Water Resour Res 25(5):937–942. https://doi.org/10.1029/WR025i005p00937
Crawford CG (1991) Estimation of suspended and SRCs and mean suspended sediment loads. J Hydrol 129:331–398. https://doi.org/10.1016/0022-1694(91)90057-O
Degens BP, Donohue RD (2002) Sampling mass loads in rivers—a review of approaches for identifying, evaluating and minimizing estimation errors. Water and Rivers Commission, Water resource technical series No WRT 25, pp 1–43. www.wrc.wa.gov.au/public/feedback/
Dey S, Das R, Gaudio R, Bose SK (2012) Turbulence in mobile-bed streams. Acta Geophys 60(6):1547–1588. https://doi.org/10.2478/s11600-012-0055-3
Duan N (1983) Smearing estimate, a nonparametric retransformation method. J Am Stat Assoc 78(383):605–610. https://doi.org/10.1080/01621459.1983.10478017
Fan X, Shi C, Zhou Y, Shao W (2012) SRCs in the Ningxia-Inner Mongolia reaches of the upper Yellow River and their implications. Quat Int 282:152–162. https://doi.org/10.1016/j.quaint.2012.04.044
Fang HY, Cai QG, Chen H, Li QY (2008) Temporal changes in suspended sediment transport in a gullied loess watershed: the lower Chabagou Creek on the Loess Plateau in China. Earth Surf Process Landf 33(13):1977–1992. https://doi.org/10.1002/esp.1649
Fang H, Li QY, Cai QG, Liao YS (2011) Spatial scale dependence of sediment dynamics in a gullied rolling loess region on the Loess Plateau in China. Environ Earth Sci 64(3):693–705. https://doi.org/10.1007/s12665-010-0889-4
Ferguson RI (1986) River loads underestimated by rating curves. Water Resour Res 22:74–76. https://doi.org/10.1029/WR022i001p00074
Ferguson RI (1987) Accuracy and precision of methods for estimating river loads. Earth Surf Process Landf 12:95–104. https://doi.org/10.1002/esp.3290120111
Haynes H, Ockeleford AM, Vignaga E, Holmes WM (2012) A New Approach to define surface/sub- surface transition in gravel beds. Acta Geophys 60(6):1589–1606. https://doi.org/10.2478/s11600-012-0067-z
Holtschlag DJ (2001) optimal estimation of suspended-sediment concentrations in streams. Hydrol Process 15:1133–1156. https://doi.org/10.1002/hyp.207
Horowitz AJ (2003) An evaluation of SRCs for estimating suspended sediment concentrations for subsequent flux calculations. Hydrol Process 17:387–3409. https://doi.org/10.1002/hyp.1299
Hu BQ, Wang HJ, Yang ZS, Sun XX (2011) Temporal and spatial variations of SRCs in the Changjiang (Yangtze River) watershed and their implications. Quat Int 230(1–2):34–43. https://doi.org/10.1016/j.quaint.2009.08.018
Hudson PF (2003) Event sequence and sediment exhaustion in the lower Panuco Watershed, Mexico. Catena 52(1):57–76. https://doi.org/10.1016/S0341-8162(02)00145-5
Iadanza C, Napolitano F (2006) Sediment transports time series in the Tiber River. Phys Chem Earth Parts A/B/C 31(18):1212–1227. https://doi.org/10.1016/j.pce.2006.05.005
Jain S (2001) Development of Integrated SRCs Using ANNs. J Hydraul Eng 127(1):30–37. https://doi.org/10.1061/(ASCE)0733-9429(2001)127:1(30)
Jansson MB (1996) Estimating a SRCs of the Reventon river at Palomo using logged mean loads within discharge classes. J Hydrol 183(4):227–241. https://doi.org/10.1016/0022-1694(95)02988-5
Jones KR, O Berney DP, Barret EC (1981) Arid zone hydrology for agricultural development, FAO Irrigation and Drainage Paper, 37, 271. ISBN 10: 925101079X/ ISBN 13: 9789251010792
Lecce SA, Pease PP, Gares PA, Wang JY (2006) Seasonal controls on sediment delivery in a small coastal plain watershed, North Carolina, USA. Geomorphology 73(3–4):246–260. https://doi.org/10.1016/j.geomorph.2005.05.017
Leopold LB, Maddock T (1953) The hydraulic geometry of stream channels and some physiographic implications. USGS professional paper No. 252, Hydrodynamics, pp 1–57
Link O, Gonzalez C, Maldonado M, Escauriaza C (2012) Coherent structure dynamics and sediment particle motion around a cylindrical pier in developing scour holes. Acta Geophys 60(6):1689–1719. https://doi.org/10.2478/s11600-012-0068-y
Liu XX, Chiew YM (2012) Effect of seepage on initiation of cohesionless sediment transport. Acta Geophys 60(6):1778–1796. https://doi.org/10.2478/s11600-012-0043-7
Lloyd CEM, Freer JE, Johnes PJ, Collins AL (2016) Using hysteresis analysis of high-resolution water quality monitoring data, including uncertainty, to infer controls on nutrient and sediment transfer in catchments. Sci. Total Environ 543(A):388-404. https://doi.org/10.1016/j.scitotenv.2015.11.028
Marttila H, Kleve B (2010) Dynamics of erosion and suspended sediment transport from drained peat-land forestry. J Hydrol 388(3–4):414–425. https://doi.org/10.1016/j.jhydrol.2010.05.026
Meade RH, Yuzyk TR, Day TJ (1990) Movement and storage of sediment in rivers of the United States and Canada. Surface Water Hydrol Boulder Colorado 3:255–280. https://doi.org/10.1007/978-94-009-3071-1_8
Morehead MD, Syvitski JPM, Hutton EWH, Peckham SD (2003) Modeling the temporal variability in the flux of sediment from ungauged river watersheds. Glob Planet Change 39(1–2):95–110. https://doi.org/10.1016/s0921-8181(03)00019-5
Moreno PA, Bombardelli FA (2012) 3D Numerical simulation of particle-particle collisions in saltation mode near stream beds. Acta Geophys 60(6):1661–1688. https://doi.org/10.2478/s11600-012-0077-x
Nadal-Romero E, Regüés D, Latron J (2008) Relationships among rainfall, runoff, and suspended sediment in a small catchment with badlands. CATENA 74(2):127–136. https://doi.org/10.1016/j.catena.2008.03.014
Nu-Fang F, Zhi-Huaa S, Lu L, Cheng J (2011) Rainfall, runoff, and suspended sediment delivery relationships in a small agricultural watershed of the Three Gorges area, China. Geomorphology 135(1–2):158–166. https://doi.org/10.1016/j.geomorph.2011.08.013
Phillips JM, Webb BW, Walling DE, Leeks GJL (1999) Estimating the suspended sediment loads of rivers in the LOIS study area using infrequent samples. Hydrol Process 13:1035–1050. https://doi.org/10.1002/(SICI)1099-1085(199905)
Preston SV, Bierman J (1989) An evaluation of methods for the estimation of tributary mass loads. Water Resour Res 25(6):1379–1390. https://doi.org/10.1029/WR025i006p01379
Singh A, Guala M, Lanzoni S, Foufoula-Georgio E (2012) Bedform effect on the reorganization of surface and subsurface grain size distribution in gravel bedded channels. Acta Geoph. 60(6):1607–1638. https://doi.org/10.2478/s11600-012-0075-z
Syvitski JPM, Morehead MD, Bahr DB, Mulder T (2000) Estimating fluvial sediment transport: the rating parameters. Water Resour Res 36(9):2747–2760. https://doi.org/10.1029/2000WR900133

Szilo J, Bialik RJ (2017) Bed load transport in two creeks at the ice-free area of the Baranowski Glacier, King George Island, West Antarctica. Pol Polar Res 38(1):21–39. https://doi.org/10.1515/popore-2017-0003

Thomas RB (1985) Estimating total suspended sediment yield with probability sampling. Water Resour Res 21:1381–1388. https://doi.org/10.1029/WR021i009p01381

Waling DE (1977) Assessing the accuracy of suspended SRCs for a small watershed. Water Resour Res 13:531–538. https://doi.org/10.1029/WR013i003p00531

Walling DE (1974) Suspended sediment and solute yields from a small catchment prior to urbanization. In: Gregory KJ, Walling DE (eds), Fluvial processes in instrumented watersheds, Inst. Br. Geogr., London Inst Br Geogr Spec Publ 6:169–192

Walling DE, Teed A (1971) A simple pumping sampler for research into suspended sediment transport in small catchments. J Hydrol 13:325–337

Walling DE, Webb BW (1981) The reliability of suspended sediment load data. In: Walling D, Tacconi P (eds) Erosion and sediment transport measurement, IAHS Publication no. 133. IAHS Press, Wallingford, pp 177–194

Wang HJ, Yang ZS, Wang Y, Saito Y, Liu JP (2008) Reconstruction of sediment flux from the Changjiang (Yangtze River) to the sea since the 1860s. J Hydrol 349(3–4):318–332. https://doi.org/10.1016/j.jhydrol.2007.11.005

Williams GP (1989) Sediment concentrations versus water discharge during single hydrologic events in rivers. J Hydrol 111:89–106. https://doi.org/10.1016/0022-1694(89)90254-0

Xu JX (1999) Erosion caused by hyper-concentrated flow on the Loess Plateau of China. CATENA 36:1–9. https://doi.org/10.1016/S0341-8162(99)00009-0

Xu JX (2004) Hyper-concentrated flows in the slope-channel systems in gullied areas on the Loess Plateau, China. Geografiska Ann Ser A Phys Geogr 86:349–366. https://doi.org/10.1111/j.0435-3676.2004.00237.x

Yang GF, Chen ZY, Yu F, Wang Z, Zhao Y, Wang Z (2007) Sediment rating parameters and their implications: Yangtze River, China. Geomorphology 85(3–4):166–175. https://doi.org/10.1016/j.geomorph.2006.03.016